Neuromorphic behaviour in nanoparticle films

A thesis submitted in partial fulfilment
of the requirement for the Degree of

Doctor of Philosophy in Physics
at the
University of Canterbury

by

Shota Shirai

School of Physical and Chemical Sciences
University of Canterbury
2019

Abstract

Conventional computer power has increased dramatically over the last 50 years due to reduction in the physical size and increased areal density of the fundamental electrical components, but this is now facing physical and economical limitations. Neuromorphic computing is a novel computing framework inspired by the biological brain. Advances in neuromorphic computing are expected to make it possible to overcome these limitations.

This study aims to explore electrical properties in percolating nanoparticle devices as candidates for neuromorphic hardware. The devices are fabricated in a cluster deposition system under optimised conditions to stabilise the devices. The electrical properties of the devices fabricated near the percolation threshold are characterised by measuring their conductance.

Sn-based devices show switching behaviour. This is observed as a change in conductance, induced by atomic-scale wire formation and destruction under application of voltage stimuli. Switching behaviour is investigated using voltage pulses, voltage amplitude and temperature. Also, the results of the analysis of the switching dynamics and temporal correlation indicate that the devices exhibit burst activity, scale-free dynamics as well as long-range temporal correlation (LRTC). In neuroscience, these features are associated with memory functions and information processing in cortex. The LRTC in the Sn-based devices originates from the underlying scale-free network structure.

As an alternative device, Ag/Ag_2S-based devices are fabricated by the sulphidisation of Ag nanoparticles. The switching behaviour in the Ag/Ag_2S devices originates from the electrochemical process of Ag filament formation and dissolution. Also, the device exhibits a stimulus frequency dependent plasticity which is similar to the synaptic activity which characterises the learning abilities of brains.

These brain-like characteristics can be exploited within the context of a neuromorphic computing framework. One example is reservoir computing: this allows practical signal processing such as voice recognition and time series prediction.

Contents

1 Introduction **1**

1.1 Neuromorphic Computing . . . 2

1.1.1 Biological Brain and Computation . . . 3

1.1.2 Artificial Neural Networks . . . 5

1.1.3 Neuromorphic Architectures . . . 7

1.2 Self-assembled Percolating Nanoparticle Films . . . 10

1.2.1 Nanoclusters and Nanoparticles . . . 10

1.2.2 Percolation Theory . . . 11

1.3 Fractals, Scale-free Behavior and Power-laws . . . 12

1.4 Thesis Outline . . . 14

2 Experimental techniques **17**

2.1 Materials . . . 17

2.1.1 Tin (Sn) . . . 18

2.1.2 Silver (Ag) . . . 18

2.2 Substrates . . . 19

2.3 Nanocluster Deposition . . . 20

2.4 Scanning Electron Microscopy (SEM) . . . 24

2.5 Electrical Measurement Systems . . . 25

2.6 Data Processing in MATLAB . . . 27

2.6.1 Raw Data Processing . . . 27

2.6.2 Analysis of Raw Data . . . 29

3 Sn-based Percolating Neuromorphic Networks (PNNs) **31**

3.1 Summary of Previous Research at UC . . . 31

3.1.1 Switching Behaviour in Tunnel Junctions . . . 32

3.1.2 Quantised Conductance . . . 32

3.1.3 The Switching Mechanism . . . 34

3.2 Fabrication of Sn-based PNNs . . . 36

3.3 Results: Switching Dynamics . . . 39
3.3.1 Activation of Switching Sites . . . 39
3.3.2 Network Activity for Applied Voltage Pulses . . . 44
3.4 Summary . . . 52

4 Temporal Dynamics and Correlations **55**
4.1 Time Series Analysis . . . 56
4.1.1 Methodology in Neuroscience and Event-trains . . . 56
4.1.2 Inter-event Interval (IEI) . . . 58
4.1.3 Autocorrelation Function (ACF) . . . 61
4.1.4 ACF and LRTC . . . 62
4.2 Fitting Procedure . . . 64
4.2.1 Linear Regression . . . 64
4.2.2 Maximum Likelihood Estimation . . . 67
4.2.3 Goodness-of-Fit Test and Kolmogorov-Smirnov (KS) Test . . . 68
4.2.4 Fitting Model Comparison . . . 72
4.3 Event Detection . . . 73
4.3.1 Measurement Noise-floor and Threshold . . . 74
4.3.2 Threshold Selection for Slow Sampling . . . 76
4.3.3 Results of Event Detection . . . 78
4.4 Simulation of Effects of Sub-sampling and Thresholding . . . 80
4.4.1 Construction of Simulated G trace . . . 80
4.4.2 Effects of Sub-sampling . . . 81
4.4.3 Effects of Thresholding . . . 83
4.4.4 Summary of Effect of Thresholding . . . 84
4.5 Switching Activity and Network Structure . . . 85
4.5.1 Self-similar Switching Activity . . . 85
4.5.2 Network Structure . . . 87
4.6 Fits to IEI Distributions . . . 90
4.6.1 Power-law . . . 90
4.6.2 Other Heavy-tailed Distributions . . . 93

4.7 Scale-free Temporal Dynamics and Correlations . . . 94
4.7.1 Long-range Temporal Correlation (LRTC) . . . 95
4.7.2 Hierarchical Burst Model . . . 96
4.7.3 LRTC and Underlying Network Structure . . . 98
4.7.4 Scale-free Dynamics and LRTC in Multiple Devices . . . 99
4.7.5 Voltage Dependence of Scale-free Dynamics . . . 101
4.8 Correlations and Critical Dynamics . . . 104
4.9 Summary . . . 106

5 Ag/Ag_2S-based PNNs 109
5.1 Previous Research of Memristive Ag/Ag_2S Devices . . . 110
5.1.1 Memristor . . . 110
5.1.2 Ag/Ag_2S-based Single Atomic Switches . . . 111
5.1.3 Atomic Switch Networks . . . 115
5.1.4 Switching Mechanisms . . . 117
5.2 Fabrication of Ag/Ag_2S-based PNNs . . . 120
5.2.1 Deposition of Ag NPs . . . 121
5.2.2 Sulphidisation of Ag NPs . . . 122
5.3 Properties of Ag/Ag_2S-based PNNs . . . 124
5.3.1 Network Activation . . . 124
5.3.2 Bias Polarity Dependence of the Filament Formation . . . 125
5.3.3 Stimulus Frequency Dependent Plasticity . . . 127
5.4 Summary . . . 129

6 Conclusion and Future Work 131

Bibliography 134

Acknowledgment 163

A MATLAB codes 165
A.1 The List of the MATLAB Codes . . . 165
A.1.1 Raw Data Analysis . . . 165

A.1.2 Analyzing and Plotting Data 165
A.1.3 Simulation code 166
A.1.4 Functions 167

List of Figures

1.1 Moore's law and energy consumption as a function of clock frequency. 2
1.2 Mammalian brain, biological neural network, neurons and synapse 4
1.3 A diagram of an artificial neuron and a simple artificial neural network 5
1.4 General structure of reservoir computing 7
1.5 von Neumann architecture and unconventional architecture used in the model of TrueNorth in IBM 8
1.6 Energy consumption for conventional hardware and neuromorphic hardware. 9
1.7 Schematic illustrations of various types of percolating networks 12
1.8 Examples of fractal objects and self-similar temporal patterns of a signal . . . 13

2.1 Substrate with a pair of NiCr/Au electrode and shadow mask used in thermal evaporation 19
2.2 The cluster deposition system 21
2.3 Deposition chamber and cryostat 23
2.4 Schematics of measurement systems 26
2.5 Raw data processing with spike-replacement filter and local median filter . . 28
2.6 Comparison of effects between in-built median filter in MATLAB and local median filter 29

3.1 The first results of switching activity in Sn percolating device at UC 32
3.2 Quantised conductance in quantum point contact in 2-dimensional electron gas 33
3.3 Schematic illustration of atomic-scale wire formation process 35
3.4 Onset curves and morphology in SEM for different deposition pressures . . . 37
3.5 A typical onset curve of G in Sn devices 38
3.6 The first sweep of voltage in Sn device 39
3.7 Activation of the device for high G and low G devices 41
3.8 Voltage dependence of switching rate 42
3.9 Temperature dependence of switching activity 44
3.10 Switching activity in archetype A and archetype B 46

3.11 Rate of linked-events at leading edges and trailing edges of voltage pulses . . 47
3.12 Rate of Linked-up-events for up-events and pulses 48
3.13 The event-structure associated with up-down events 49
3.14 The stimulus frequency dependence of the conductance and the network potentiation 51

4.1 Neuronal signal, a spike train and definition of the event-train and inter-event intervals 57
4.2 The difference in the activity patterns between a Poisson process and a power-law distribution 60
4.3 Examples of autocorrelation funcion 62
4.4 An example of long-range slow decay in ACF 63
4.5 The effect of the binning methods in the standard linear regression for an exponential and a power-law 65
4.6 Event detection in neuronal signal and the electrical current noise in our measurements 73
4.7 Event detection by thresholds determined by the noise-floor for slow and fast sampling 74
4.8 Event detection in slow measurement at the noise-floor 75
4.9 Multi-barcode plot in slow measurement 77
4.10 Detected events with the alternative threshold value and generated event-train in slow measurement. 78
4.11 The IEI distributions for various threshold values in slow sampling data and for different sampling speeds. 79
4.12 Simulated G and ΔGtraces based on the power-law distributions of IEI and ΔG 81
4.13 The effect of sub-sampling in G_{sim} and ΔG_{sim} 82
4.14 The effect of sub-sampling in distributions of IEI and ΔG 83
4.15 The effect of choice of threshold values before and after sub-sampling. 84
4.16 Self-similar switching activity 86
4.17 Heavy-tailed ΔG distribution in switching activity 87

4.18 Simulated network structures for different coverage and the degree distributions 89
4.19 Maps of the exponents by MLE and p-values of the KS test for various lower and higher cut-off value . . . 91
4.20 The IEI distributions examined with MLE and KS test . . . 92
4.21 PDF and CDF of the IEI distributions with various fitting models . . . 94
4.22 ACFs and LRTCs in our experimental data. . . . 95
4.23 Hierarchical Burst Model . . . 97
4.24 Hierarchical burst simulation . . . 98
4.25 The exponent values obtained from the IEI distributions and ACFs for multiple devices devices as a function of voltage . . . 101
4.26 Voltage depenence of the IEI distribution and ACF . . . 103
4.27 The critical dynamics in PNNs demonstrated by avalanche profiles and the characteristic exponents . . . 105

5.1 Circuit diagram and a typical I-V characteristic in memristor . . . 111
5.2 Memristive behaviour in a Ag/Ag_2S based single atomic switch and Ag filament formation process . . . 113
5.3 Inorganic synaptic behavior in the Ag/Ag_2S single atomic junction. . . . 114
5.4 Properties of atomic switch networks consisting of Ag/Ag_2S nanowires . . . 116
5.5 Schematics of the electrochemical process for Ag filament formation process in the $Ag/Ag_2S/W$ single junction. . . . 118
5.6 Ag filament formation and self-dissolution at $Ag/Ag_2S/Ag$ junctions . . . 119
5.7 Resistance change in Ag NPs deposition and sulphidisation . . . 120
5.8 Deposition of Ag NPs . . . 121
5.9 Sulphidisation of Ag NPs . . . 123
5.10 Activation of the $AgAg_2S$ PNN . . . 125
5.11 Bias polarity and corresponding resistance change . . . 126
5.12 Stimulus Frequency Dependent Plasticity in Ag/Ag_2S-based PNNs . . . 128

List of Tables

4.1 List of the parameters for the power-law and the exponential distributions . . 71

4.2 The exponent values obtained from the IEI distributions and ACFs for multiple devices devices 100

5.1 Electric properties of Ag and Ag_2S 117

List of Abbreviation

ACF	Autocorrelation Function
AIC	Akaike Information Criterion
ANN	Artificial Neural Network
BIC	Bayesian Information Criterion
BNN	Biological Neural Network
CDF	Cumulative Density Function
CMOS	Complimentary Metal-Oxide-Semiconductor
CPU	Central Processing Unit
DFA	Detrended Fluctuation Analysis
EEG	Electroencephalogram
EFIE	Electric Field-Induced Evaporation
EFISD	Electric Field-Induced Surface Diffusion
fMRI	functional Magnetic Resonance Imaging
FNN	Feedforward Neural Network
IC	Integrated Circuit
IEI	Inter-Event Interval
IGA	Inert Gas Aggregation
ISI	Inter-Spike Interval
KS test	Kolmogorov-Smirnov test
LE	Leading Edge
LMF	Local Median Filter
LR	Linear Regression
LRTC	Long-Range Temporal Correlation
LTD	Long-Term Depression
LTP	Long-Term Potentiation
MCBJ	Mechanically-Controlled Break Junction
MEG	Magnetoencephalographic
MIM	Metal-Insulator-Metal
MLE	Maximum Likelihood Estimation
NP	Nanoparticle
PDF	Probability Density Function
PNN	Percolating Neuromorphic Network
PSD	Power Spectral Density
RC	Reservoir Computing
RNN	Recurrent Neural Network
SEM	Scanning Electron Microscopy
SRF	Spike-Replacement Filter
STDP	Spike-Timing Dependent Plasticity
STM	Scanning Tunnelling Microscope
STP	Short-Term Plasticity
TE	Trailing Edge
UHV	Ultra High Vacuum

Chapter 1

Introduction

The traditional computer architecture, known as *von Neumann architecture*, has had great advances in terms of increasing the processing speed while reducing the physical size and the increased areal density of such fundamental electrical components such as processors and memory. In particular, the number of transistors in an integrated circuit (IC) has doubled every two years, as predicted by *Moore's Law* [1] (see Fig. 1.1(a)). However, the conventional architecture is now meeting the fundamental and critical limitations which affect transistor dimensions and processing speed. As shown in Fig. 1.1(a), the single-thread performance and clock frequency which corresponds to the computational speed has already started to saturate. Furthermore, economic limitations (capital investments, research costs, electrical power) are also problematic. To overcome these limitations, new computer architectures are urgently required.

Neuromorphic computing is an unconventional computing paradigm inspired by the biological brain. As shown in Fig. 1.1(b), while the operation speed of the brain is very slow compared to conventional computer processors operated with the clock frequency of ∼GHz, the energy consumption is almost 4 orders of magnitude lower than that of the latest processors. Therefore, neuromorphic computing architectures are expected to have better energy efficiency and allow a paradigm shift in traditional computation methods.

This chapter provides a general introduction to neuromorphic computing in Section 1.1, the basics of nanoparticles as well as percolation theory in Section 1.2 and the concept of fractals and power-laws in Section 1.3. Section 1.4 gives the main aim of this work and a

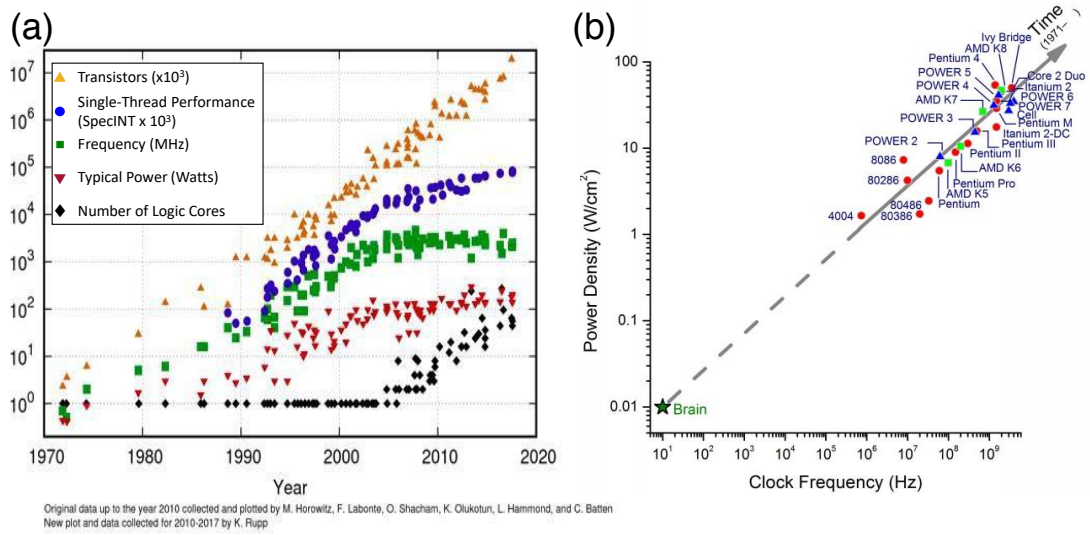

Fig. 1.1. (a) 42-year evolution of the number of transistors, performance of single-thread in a processor, clock frequency, typical power consumption and the number of logic gates in a single processor (adapted from ref. [2]). The number of transistors has doubled every two years as predicted by Moore's law, but the clock frequency and the single-thread performance, which correspond to computational speed, have already started to saturate. (b) Power density as a function of clock frequency. Compared to the conventional processors operated with clock frequency of ∼GHz, the processing speed of brains is very slow (∼10 Hz), but the required energy density is almost 4 orders of magnitude below than that of the latest processor. Also, the brain has a great advantage in image and pattern recognition (adapted from ref. [3]).

layout of the thesis summarising the content of each chapter.

1.1 Neuromorphic Computing

Neuromorphic computing envisages building computer architectures inspired by mammalian brains. In addition to low energy consumption (∼25 W [4]), the mammalian brains have a great advantage in pattern and image recognition such as finding a certain face or voice in a crowded place. These tasks cannot be immediately achieved even by supercomputers which consume ∼MW of electrical energy and can carry out raw numerical calculations much faster than the human brain.

This section briefly describes the basics of biological brains and brain-inspired computing. The focus is on artificial neural networks and unconventional computer architectures.

1.1.1 Biological Brain and Computation

Biological brains are very complex organic systems which have evolved over millions of years in nature. Brains contain massive hierarchical networks, called *biological neural networks* (*BNNs*), which enable efficient information processing [5–7]. Fig. 1.2 shows (a: bottom) a network of complex structural connections in a brain [8] and (b) a highly-interconnected neural network [9]. The estimated number of the neurons in the brain of a typical adult human is ∼100 billion [10–12]. As shown in Fig. 1.2(c), a typical neuron consists of three parts: a *cell body* (also called *soma*), *dendrites* and an *axon*. Neurons receive signals from other neurons and produce a response signal, which is a communication between the neurons. The cell body has a nucleus and an *axon hillock*. As shown in Fig. 1.2(c), the axon hillock is connected to the axon and integrates the incoming signals from other neurons through the dendrites which have tree-like branches [4]. When the total strength of the signals integrated in the axon hillock exceeds the threshold, the axon transmits the signal towards the neighbouring connected neurons.

Neurons transmit information using electrical signals, known as *action potentials*. Action potentials travel along the axon and are transferred to other neurons by *synapses*. Since a single neuron may form ∼1000 synapses with other neurons, the number of synapses in the brain is estimated to be ∼100 trillion [4, 14]. Information transmission between neurons is mainly operated by chemical signalling of synapses (although there exist electrical synapses) [4]. When an action potential arrives at a synapse, the synapse releases neurotransmitters (i.e. messenger chemicals) to transfer the signal from pre-synaptic cell to post-synaptic cell (see the inset in Fig. 1.2(c)).

A critical mechanism of memory formation and learning in the brain is *synaptic plasticity* which represents the modulation of synaptic connectivity of BNNs [15, 16]. Synaptic plasticity is governed by various factors, including the firing rate, spike timing and synaptic cooperativity [7, 17, 18]. For example, the simultaneous or rapid sequential activation of two neurons connected via synapses strengthens the synaptic connection between them. This particular characteristic is known as *spike-timing dependent plasticity* (*STDP*) [18]. Also, the synaptic connection is enhanced with repeated stimulation of the post-synaptic neurons, and conversely, when neurons are inactive for a long time, the synaptic connectivity is re-

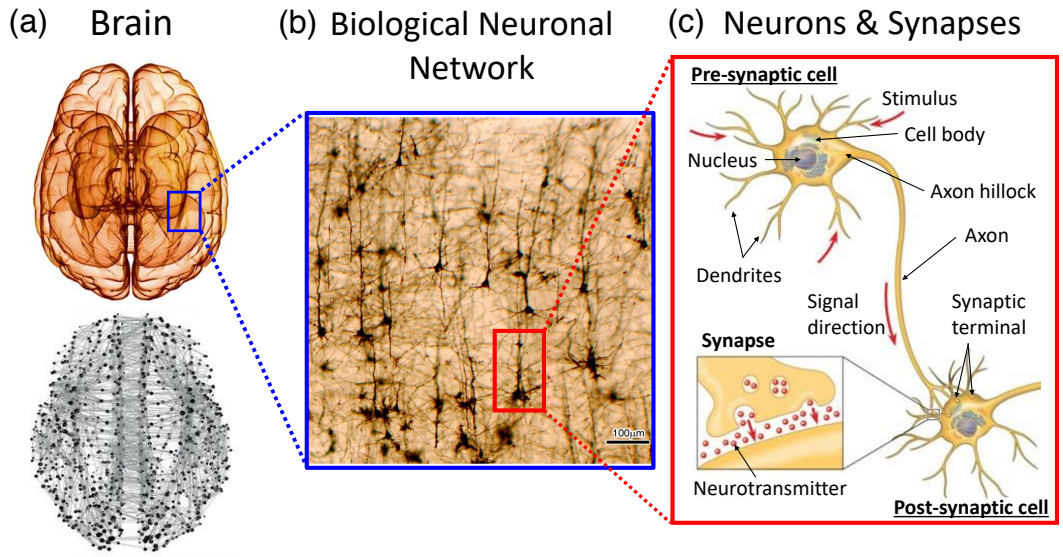

Fig. 1.2. (a: top) A schematic illustration and (a: bottom) a network of structural connections of a brain. The complex network structure of the brain consists of hierarchically organized *biological neural network*. (b) Golgi-stained cortical neurons in a human brain represent a highly connected neural network. (c) A schematic illustration of neurons consisting of *dendrites*, *cellbody* (*soma*) and *axon*. Each neuron is connected via synapses (the inset) which release neurotransmitter between pre-synaptic cell and post-synaptic cell. The signals in brains propagate on neurons as electrical signals and processed in the network (the figure is compiled from ref. [8, 9, 13]).

duced. Lasting strengthening and weakening synaptic connections are known as *long-term potentiation* (*LTP*) and *long-term depression* (*LTD*), respectively [15, 16, 19–21].

Patterns of neural activities corresponding to brain functionalities originate from the global activity of self-organised complex systems rather than local activity of a single neuron or small groups of neurons. Such complex self-organised system composed of the massive non-linear elements exhibits *emergent phenomena* which are spatiotemporal patterns arising from an underlying collective behaviour in large complex systems [22]. Neural network models incorporate the insights obtained from the perspective of individual neurons but also attempt to explain such phenomena as consciousness and the cognitive states of the brain which cannot be easily explained within single-neuron frameworks [22, 23].

Despite developments in methodology and technological advances [23], the exact mechanism of brain computation and signal processing mechanisms is still not fully understood. However, the ongoing efforts to understand properties of the brain provide important inspiration for the development of unconventional computer architectures. The next section summarises brain-inspired computing system based on BNNs.

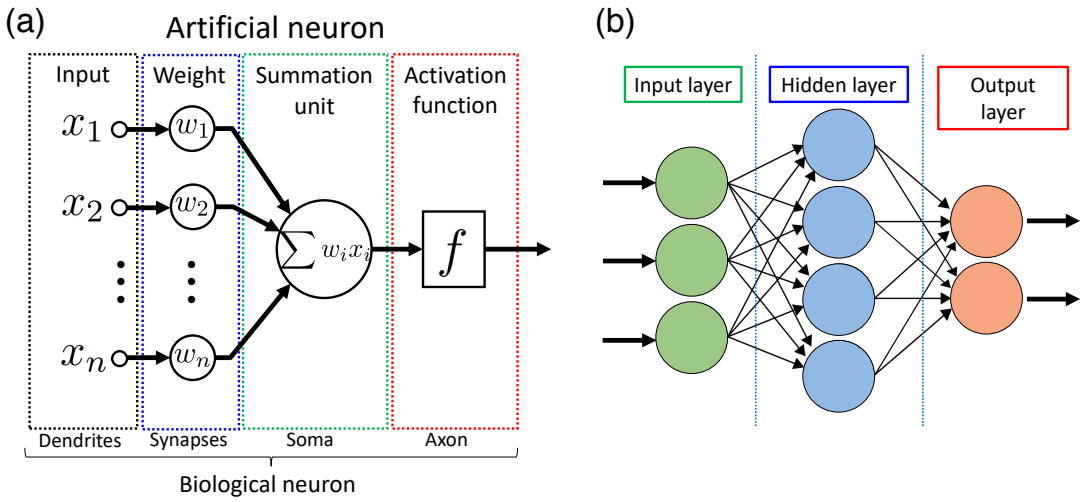

Fig. 1.3. (a) A diagram of artificial neuron mimicking a biological neuron. Typical mathematically modelled artificial neuron is composed of input nodes, weights, a summation unit and an activation function (e.g. step function or sigmoid function), which respectively represent the parts of the biological neuron i.e. dendrites, synapses, soma and axon. (b) A simple artificial neural network consisting of the artificial neurons. The artificial neural networks are divided into three layers: an input layer, hidden layers and an output layer.

1.1.2 Artificial Neural Networks

Artificial neural networks (*ANNs*) are computing systems that model the information processing capabilities of BNNs and have massive parallelism and redundancy [24, 25]. It is very important to note that ANNs are not a replica of BNNs, but the processing components (*artificial neurons*) are inspired by (but not identical to) biological neurons and synapses. There are two approaches to demonstrate ANNs i.e. software-based emulation and hardware-based emulation.

In the software-based ANN emulations, a mathematically modelled artificial neuron is often used as an elementary unit. Fig. 1.3(a) shows a representative model of the artificial neuron: it is composed of input nodes, weights, a summation unit and activation function that respectively correspond to dendrites, synapses, soma and axon in a biological neuron (Fig. 1.2(c)).

Fig. 1.3(b) shows the simplest model of an ANN consisting of an input layer, a hidden layer and an output layer. The signals on the input layer are transferred to the hidden layer where the signals propagate with respect to the weights of each node (i.e. the artificial neuron). The structure of ANNs is generally classified into two types: *feedforward neural*

networks (*FNNs*) [26] and *recurrent neural networks* (*RNNs*) [27]. In FNNs, the information flows in only one direction from the input nodes to the output nodes through the hidden layer (Fig. 1.3(b)) without cycles or loops in the network. The FNNs are suited for processing *static* data which is neither sequential nor time-dependent.

One of the most successful learning algorithms in software-based FNNs is *deep learning* [26] using multiple hidden layers, called *deep neural networks*. For example, AlphaGo, a gaming program for the board game "Go", is trained with deep neural networks by Google DeepMind, defeated a human top-ranking player [28]. Since Go is a much more complex game than chess due to the larger board and larger number of possible steps per move, traditional algorithms without ANNs are not able to calculate all possibilities to find optimised solutions.

In contrast to FNNs, RNNs are characterised by feedback (recurrent) connections which generate history-dependent dynamical responses to input signals, and hence are used for *dynamic* data processing such as temporal and sequential pattern recognition [27]. A crucial issue is the high learning cost (i.e. long computational time) due to the complexity of the process, leading to high energy consumption [29]. However, there is a simplified model based on software-based RNNs: it is described below.

Reservoir Computing (RC)

Reservoir computing (*RC*) is originally developed from a framework of the software-based RNNs [29–32]. Fig. 1.4 shows a typical reservoir computing system which also consists of three layers i.e. (red) an input layer, (green) a reservoir and (blue) an output layer. The essential role of the reservoir in RC maps input signals into a high-dimensional space which allows effective pattern analyses of the input information [30, 31]. The reservoir is usually fixed and only weights of the output signals are trained with linear regression and classification, which allows to simplify learning algorithms leading to lower training cost (i.e. time and energy) than other RNNs [29].

The fundamental requirements for the reservoir is a collection of non-linearly connected units, and the exact internal network connectivity and adaptive updating are not needed [29, 30]. Hence, the interest in RC has been increasing as an approach to developing cost-efficient neuromorphic hardware implementation using a variety of physical systems, sub-

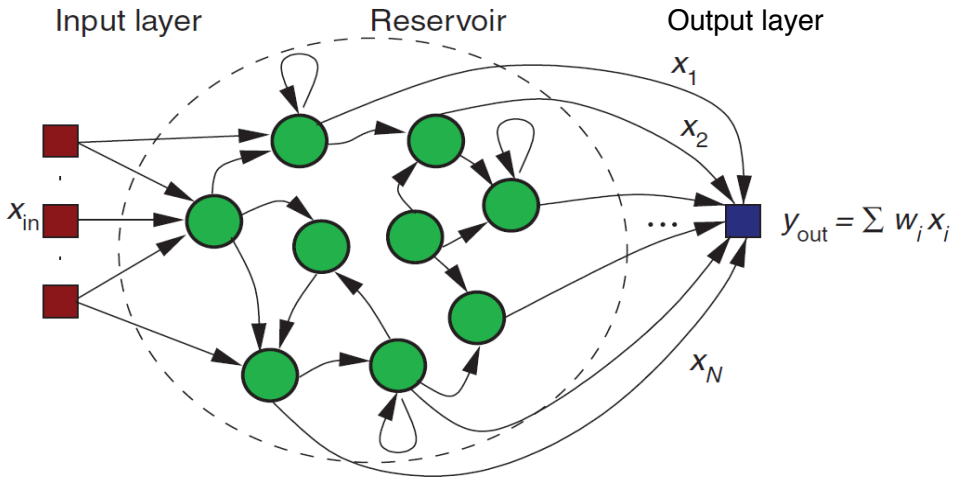

Fig. 1.4. A standard layout of the reservoir computing (adapted from ref. [32]). The reservoir computing also consists of three parts: (red) an input layer, (green) a reservoir and (blue) an output layer. The reservoir is a collection of non-linearly connected units with recurrent loops and plays a role in mapping input signals into a high-dimensional space which allows effective pattern analyses of the input information. The reservoir is fixed without the exact internal connectivity and only weights of the output signal are trained with linear regression and classification resulting in fast learning.

strates and devices [29, 31, 33–36]. An interesting example of a physical systems is "water in a bucket" presented in an early study of fluidic RC [37]. This system performed an XOR task and a spoken digit recognition task (see more technical detail in the literature [37]).

Behind the recent great success in software-based emulation of ANNs, there are ongoing developments of powerful computers with fast processing speeds and a large number of parallel processing units. However, the software emulation using supercomputers consumes a lot of electrical energy e.g. AlphaGo consumes approximately 500 MWh (1 MW×3 weeks [28, 32]) for training the network. Thus, the development of the neuromorphic hardware with low operation energy also has gained a lot of attention in recent research [38, 39], as described in the next section.

1.1.3 Neuromorphic Architectures

The software emulation of ANNs described in the previous section still relies on the traditional von Neumann architecture and does not solve fundamental problems in processing

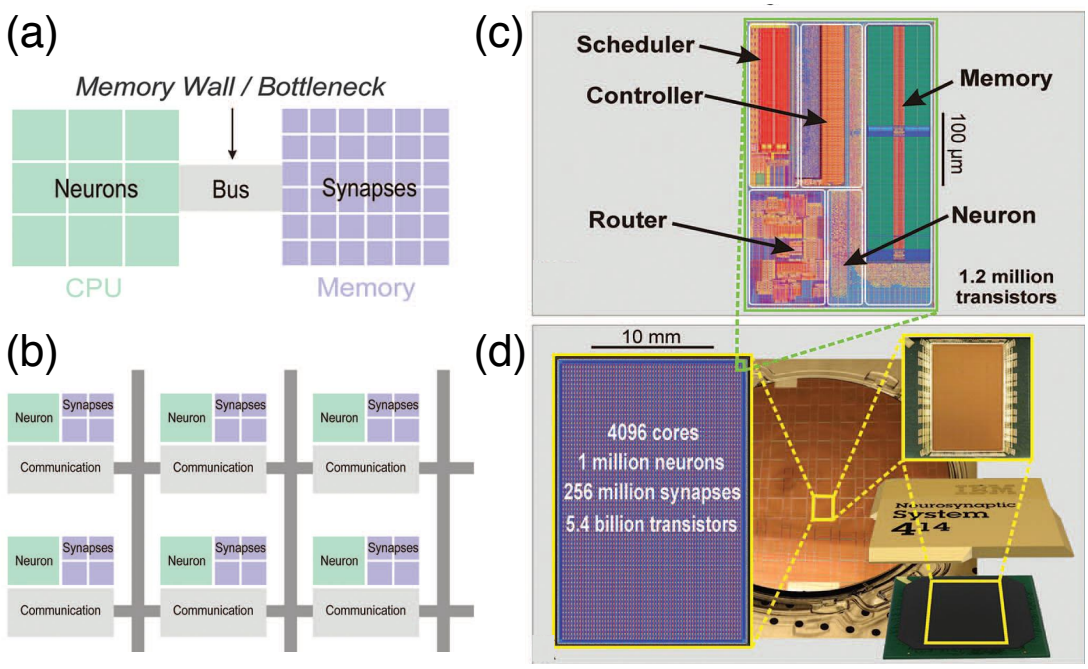

Fig. 1.5. (a) The von Neumann architecture consisting of the external memory and processor. The *von Neumann bottleneck*, which is a fundamental limit of the conventional architecture, is caused by communication between processor and memory and results in the limitation of the processing speed and high power consumption. (b) A new computer architecture used in the computer chip in TrueNorth in IBM. In this brain-inspired architecture, memory, computation and communication are integrated into the single module, as shown in (c), and distributed in a chip, as shown in (d). The single chip contains 1 million neurons and 256 million synapses with 5.4 billion transistors and is operated in parallel and communicate through an event-driven network. The chip of TrueNorth achieved significant low power consumption of ∼70 mW. (adapted from ref. [3])

speed and energy consumption. As shown in Fig. 1.5(a), the von Neumann architecture consists of a central processing unit (CPU) and memory, leading to the inevitable fundamental problem, called *von Neumann bottleneck*, which limits a processing speed [3]. To overcome this limitation, unconventional computer architectures are being investigated in scientific research and industry. This section summarises the recent progress in neuromorphic hardware emulating functionalities of brains.

In the hardware approach towards neuromorphic computing, the existing complementary metal-oxide-semiconductor (CMOS) technology has been used in various projects such as BrainScaleS [40], spiNNaker [41, 42], Neurogrid [43], SyNAPSE [44], Human Brain Project [45] and Loihi [46]. A representative example of the CMOS-based neuromorphic chip is "TrueNorth" in the SyNAPSE project in IBM [3, 44]. TrueNorth adopts a new

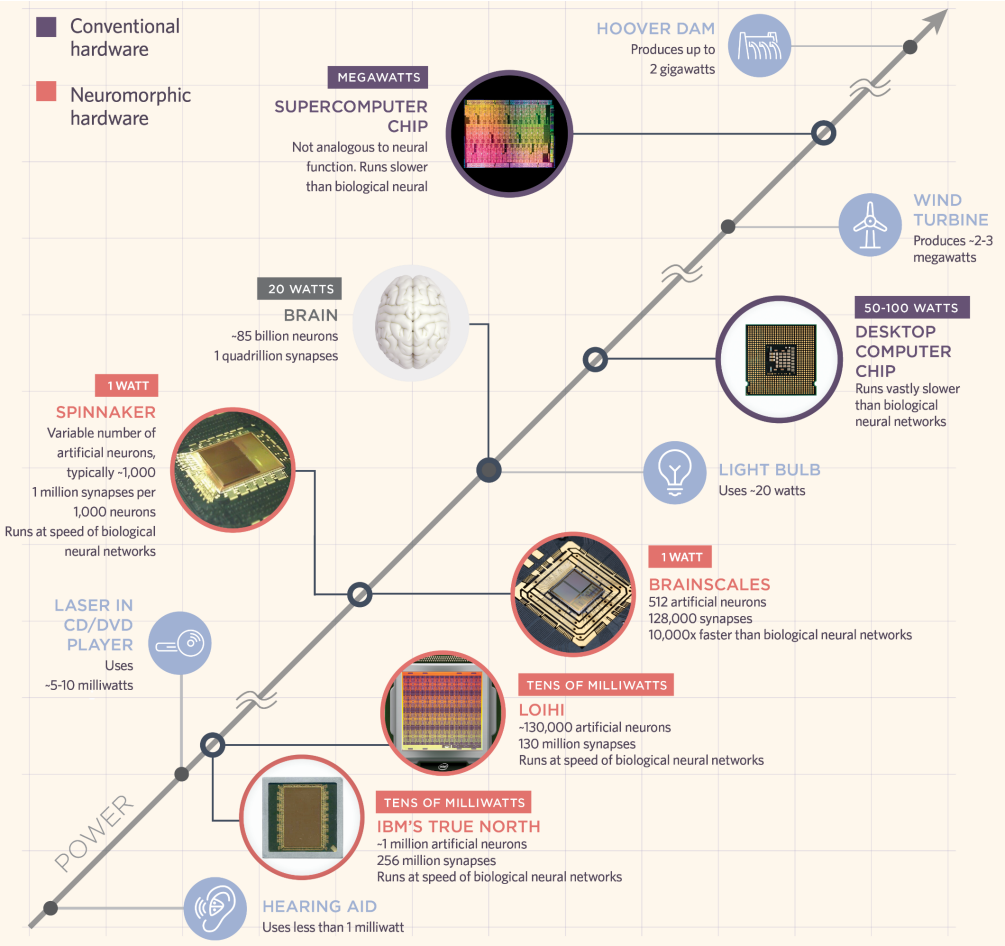

Fig. 1.6. Energy consumption for conventional hardware and neuromorphic hardware (adapted from ref. [47]). Compared to conventional hardware based on von Neumann architecture, neuromorphic architecture demonstrate very low energy consumption of <1 W.

architecture where memory, computation and communication are integrated as a unit (see Fig. 1.5(c)) and distribute the units on a chip (see Fig. 1.5(b)). As shown in Fig. 1.5(d), the single chip has 4096 neuro-synaptic cores with 1 million programmable neurons and 256 million synapses composed of 5.4 billion transistors. It should be acknowledged that these numbers are still much lower than the number of components of the brain (e.g. neurons and synapses). TrueNorth demonstrated event-based computation, which is inspired by the biological brain computation using neuron spikes, and achieved remarkable low energy consumption of ∼100 mW.

As shown in Fig. 1.6, the neuromorphic hardware using the CMOS technology can be operated with very low energy consumption compared to conventional computer chips. However, these approaches primarily focus on mimicking the structure or functionalities of

biological neurons and synapses at the individual level without the complexity of the network that is an inherent property of the brains (see Section 1.1.1).

Another approach to develop the neuromorphic hardware is the use of the complex network which exhibits functionalities similar to the biological brains [48–51]. The investigation of neuromorphic devices with complex networks is the main focus of this thesis. In the next section, the self-assembled neuromorphic devices are introduced with the basics of nanoclusters and percolation theory.

1.2 Self-assembled Percolating Nanoparticle Films

Self-assembled neuromorphic devices are fabricated without precise control of structure of the network elements, which includes sulphidised Ag nanowires [48, 49] and nanoparticles [50–52]. The main focus of this thesis is percolating films of nanoparticles and this section introduces the important concepts that are required to understand the neuromorphic behaviour in the devices discussed in the following chapters.

1.2.1 Nanoclusters and Nanoparticles

Nanoclusters, simply referred to as *clusters*, are aggregates of atoms or molecules with at least one dimension with the size in the range from 1 to 10 nm. Nanoclusters are generally included in the wider class of particles, called *nanoparticles* (*NPs*), which have sizes with the diameters between 1 and 100 nm [53, 54]. While there is no clear definition between nanoclusters and nanoparticles, particles smaller than 10 nm are called nanoclusters (or clusters) in this thesis for convenience.

The size-dependent properties also indicate the possibility of controlling the cluster properties by changing the cluster size with precisely controlled cluster formation process [54, 55]. Therefore, cluster production and stabilisation of the clusters also have acquired a great deal of attention and various chemical and physical methods for nanocluster production have been demonstrated [54, 56]. The clusters in this work are produced with *inert gas aggregation* (*IGA*) technique [56–58]. In IGA, vaporised or sputtered metal is introduced in a flow of cold gas, causing highly supersaturated vapour. Clusters are produced through a condensation-like process in a low-temperature inert gas environment. The size and proper-

ties of clusters can be controlled by changing the parameters, in particular, by changing the deposition rate, gas pressure and gas flow. Further details of the cluster deposition system used in this work are described in Chapter 2.

1.2.2 Percolation Theory

Percolation theory is a branch of probability theory originally introduced by Broadbent and Hammersley in 1957 [59] to explain the motion of liquid in a porous media. Since then, various percolation models have been introduced and investigated [60]. For example, Kirkpatrick extended the theory to explain the electrical conductivity in the random resistor network [61]. The percolation theory has successfully been used to describe critical phenomena, such as the phase transition of materials [62] and to understand phenomenon and problems in physics [63–66], chemistry [67–69] , biology [69–72] as well as network science [73, 74]. The main focus of this section is two-dimensional (2D) percolating network models. Fig. 1.7 shows some examples of 2D percolation models.

2D *bond percolation model* considers the system shown in Fig. 1.7(a) where each two nodes in a 2D square lattice are randomly connected with probability p independent of the neighbour nodes. A collection of connected nodes forms a pathway. Above a certain value of p_c, a single pathway is formed from one side of the system to the other (see Fig. 1.7(a)). p_c is called the *percolation threshold*. In the bond percolation model $p_c = 0.5$ [60], but p_c is not universal and depends on the model, the lattice structure and the dimensionality e.g. $p_c \sim 0.59$ in 2D *site percolation* (Fig. 1.7(c)) and p_c ~0.68 in 2D *continuum percolation* system (Fig. 1.7(d)) [60, 76]. While the threshold values have been investigated using both numerical simulation models and theoretical approaches [60, 76], rigorous proofs are still discussed in the community of mathematicians [77, 78].

Percolating nanoparticle films are discussed within a *percolating tunnelling* model [79], as shown in Fig. 1.7(e, f). This model has been investigated using a numerical simulation model based on continuum percolation model [79] and shows its capability as neuromorphic hardware [80]. The detail of the 2D continuum percolation model and percolating tunnelling model are described in Section 4.5.2. Since there are tunnelling gaps on pathways, the value of p in the percolating tunnelling model is close to but below p_c in the continuum percolation model [79, 80].

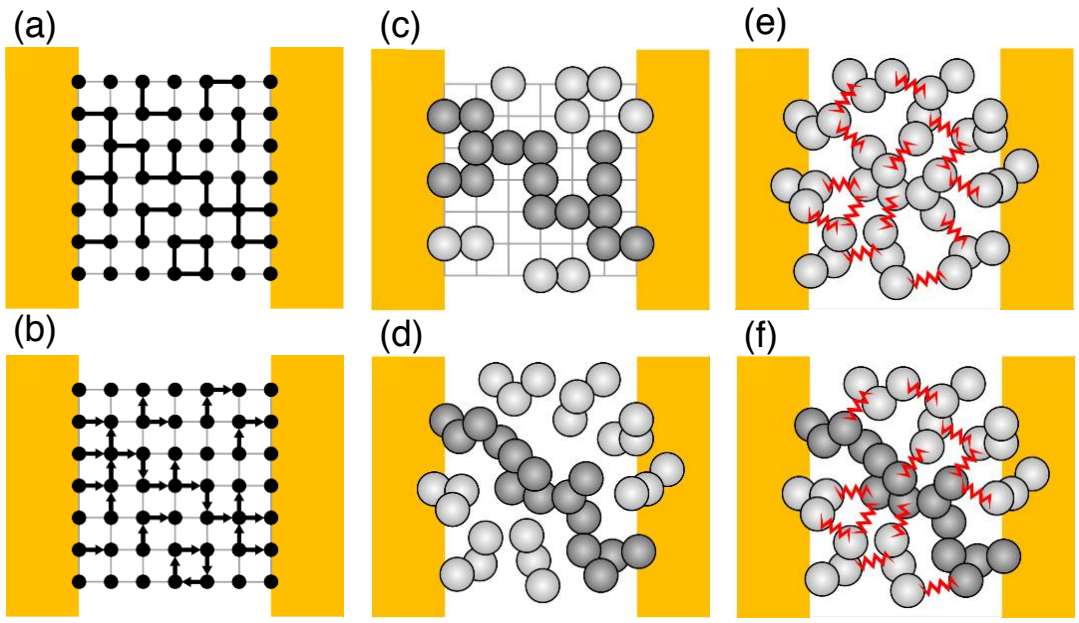

Fig. 1.7. Schematic illustrations of various types of 2-dimensional percolating networks (adapted from [75]). (a) Bond percolation is a model describing connection of bonds between nodes with probability p. Above $p > p_c = 0.5$ (p_c: the percolation threshold), a pathway between the contacts (yellow pads) exists for large system sizes. (b) Directed percolation is a model modified from the bond percolation in (a), where bonds are directional, allowing current flow in only one direction. (c) Site percolation considers sites occupied with probability $p \sim p_c$ (∼0.59). (d) Continuum percolation allows discs to overlap. p_c in large systems is rigorously estimated as the value of ∼0.68. (e) Percolation with tunnelling is developed based on the continuum percolating model. This model represents the conductance of the network of deposited nanoparticles with tunnelling gaps. In this model, the probability of the occupied area is near but below p_c of the continuum percolation and quantum tunnelling between particles (red symbols) allows conduction even without continuous pathways. (f) Percolation with tunnelling at $p \sim p_c$ has a continuous pathway coexisting with tunnelling connections.

1.3 Fractals, Scale-free Behavior and Power-laws

Fractals, introduced by Mandelbrot [81], are objects or quantities which display self-similar patterns on an infinite number of scales. Fractal objects are easily created by repeating the same process in multiple scales as shown in Fig. 1.8(a). There are many fractal objects in nature [82] e.g. roman cauliflower (romanesco broccoli) shown in Fig. 1.8(b). Since fractals do not have specific characteristic scales, such systems are usually referred to as *scale-free* [70]. Scale-free systems are characterised by *power-law* functions. In the romanesco broccoli, the frequency of the size follows a power-law [70, 83].

In network science, power-laws are known as evidence of the *scale-free networks*. The

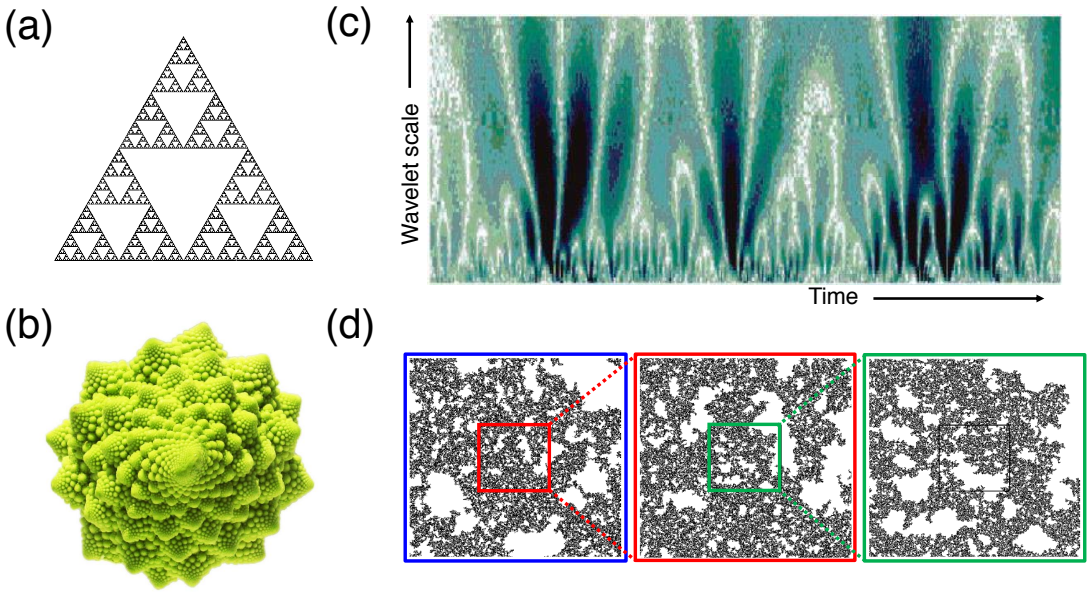

Fig. 1.8. Examples of fractal objects and time-series data. (a) Sierpinski Gasket (b) Roman cauliflower (Romanesco broccoli) (adapted from ref. [89]) The frequency of a certain size of triangles in (a) or flowers in (b) as a function of its size follows a power-law. (c) Colourized wavelet analysis of a heart rate time series (adapted from ref. [90]). a horizontal axis and a vertical axis represent time (∼1700 hearbeats) and the wavelet scale (5 - 300 s), respectively. The brighter colour indicates large heartbeat fluctuations resulting in the larger amplitude of the wavelet. This figure shows a tree-like, self-similar temporal structure in the cardiac dynamics. (d) Fractal structure observed in the percolating clusters (adapted from ref. [91]). Three different magnifications of the cluster network presents a very similar pattern for each other.

scale-free networks are characterised by power-law distributions of the degree (i.e. the number of links connecting to a node) and have attracted a lot of attention since A. Barabasi discovered the scale-free nature in the topology of the World Wide Web [84]. In the scale-free network, some nodes (called *hubs*) have many more nodes than other nodes, leading to the heavy-tail in the degree distribution. In studies of network topology, many real-world networks are said to be scale-free, including social networks, information networks and biological networks [6, 85–87]. Note however that the evidence of the scale-free nature and the validity of the power-laws are still being discussed by the scientific community [88]. The scale-free network structure in the percolating tunnelling networks is discussed in Chapter 4.

In neuroscience, fractal, self-similar pattern and power-law scaling in space and/or time can be found and considered as evidence of the functional integration among different levels of neuronal organisation [70, 92–94]. Fig. 1.8(c) shows an example of temporal self-similar patterns observed in wavelet analysis for heartbeat rate. The brighter colour indicates

larger heartbeat fluctuation and shows a tree-like self-similar structure. Also, power-laws are very important as a signature of *critical dynamics* in brains. The critical dynamics is discussed with scale-free neural avalanches [95, 96], spontaneous spatiotemporal patterns in functional magnetic resonance imaging (fMRI) [22, 97], $1/f$ noise in recordings of the brain signals [98, 99]. In a critical state of the brain, the brain capacity and information processing are maximised [100].

Percolation models also exhibit the rich fractal and scaling structure of the geometric features shown in Fig. 1.8(d) [101–105]. Percolating networks are important systems in the context of neuromorphic hardware. They emulate neural networks due to several reasons: (i) percolation theory is central to the concept of scale-free network [106], (ii) percolating NP systems have recently proposed as a platform of the neuromorphic computing [50–52, 80, 107] and (iii) at the critical point of the percolation threshold, the correlation length diverges, resulting in long-range spatial correlation [101]. Based on the background of percolating systems, this thesis focuses on the temporal correlation represented by self-similar temporal activity as well as the network structure of the percolating nanoparticle devices.

1.4 Thesis Outline

This chapter introduced the fundamental problems in the traditional von Neumann architecture and emphasised the necessity for developing neuromorphic computing, especially for neuromorphic hardware operating with low energy consumption. This thesis aims to investigate the neuromorphic behaviour in percolating nanoparticle films which are fabricated at a critical point (phase-transition) and are expected to have fractal geometry. The following chapters described below address the main research questions which must be answered for the development of neuromorphic devices.

Chapter 2 describes the basic experimental setup and methods used in this work, including materials, substrates, cluster deposition system and raw data processing. Some specific analysis methods are introduced in later chapters.

Chapter 3 and Chapter 4 focus on switching behaviour in Sn-based NP devices. Chapter 3 describes the recent progress in device fabrication technique with a summary of the previous research and discusses new results which are important to understand network prop-

erties under voltage stimuli. Chapter 4 explores temporal network dynamics and correlation that are fundamental functionalities to implement computation. The temporal correlation is discussed in terms of an underlying network structure, which was often ignored in the previous neuromorphic devices, using the numerical simulation for the percolating tunnelling network.

Chapter 5 investigates switching behaviour in Ag/Ag_2S-based NP devices fabricated with established cluster deposition technique described in Chapter 2. The previous research conducted by the other groups has reported that Ag/Ag_2S systems show properties similar to those observed in the biological brain.

Chapter 6 summarises the network dynamics discussed in the previous chapters and describes future work. A list of analysis codes in MATLAB with descriptions are also given in Appendix A.

Chapter 2

Experimental techniques

This chapter summarises the experimental setup and data analysis methods used in this work. In the beginning of this chapter, materials and substrates used in device fabrication are introduced in Section 2.1 and 2.2, respectively. The cluster deposition system used to deposit nanoclusters in well-controlled conditions is presented in Section 2.3. Section 2.4 provides a brief description of scanning electron microscope characterising the deposited nanoparticles on the substrates. In the later sections, Section 2.5 gives information about the measurement system used to obtain electrical properties of the fabricated devices and Section 2.6 summarises raw data processing used in the subsequent analysis in this work.

2.1 Materials

This section gives a brief introduction to the materials used in the cluster deposition system shown in Section 2.3. Most recent research in the group is focused on tin (Sn) clusters and shows promising properties [50, 52] (also see Section 3.1). Since the deposition process has already been well optimised [50], Sn is used as a target material for the deposition of clusters in this work as well. In addition to Sn, silver (Ag) is also used in this work in a new attempt to fabricate devices using the sulphidiation of Ag clusters (see Chapter 5). The following sections describes the basic properties of Sn and Ag.

2.1.1 Tin (Sn)

Tin (Sn) is a soft and malleable metal belonging to group 14 in the periodic table of elements. The atomic number of Sn is 50 and Sn has 10 stable isotopes because it has a magic number of protons which means electrons fill all of the nuclear shells, leading to this unique property [108]. It has two main oxidisation states, +2 (SnO) and +4 (SnO_2). The melting point is around 505 K (232 °C) in bulk, which is the lowest in group 14, but it is further lower to ∼450 K (177 °C) for 11 nm particles [108, 109]. Due to its low melting point, Sn alloy is also used as solder. Under atmospheric pressure and at room temperature, Sn has two common allotropes i.e. α-Sn and β-Sn. β-Sn, also known as white tin, is a silvery-white metal with a body-centred tetragonal crystal structure. On the other hand, α-Sn, known as grey tin, is a zero-band-gap semiconductor with a diamond cubic structure which does not exhibit metallic properties. β-Sn is stable above ∼286 K and below the temperature, only for high purity of Sn, the $\beta - \alpha$ phase transition spontaneously occurs ("tin pest"), leading to autocatalysis with volume expansion in α-Sn. As the other phase in Sn, both γ-Sn and σ-Sn exist at high temperature (∼432 K) and under GPa pressures. Metallic Sn naturally oxidises in the atmosphere and SnO_2 forms a thin layer on the surface, working as a protector for further oxidisation of the bulk. The oxidisation process can be controlled by humidity, as discussed in Section 3.2.

2.1.2 Silver (Ag)

Silver (Ag) is a well-known precious metal. It is characterised by the highest electrical conductivity, thermal conductivity and reflectivity at room temperature among all metals. Also, Ag is an extremely ductile metal and can be stretched to a monoatomic wire [110]. Historically, Ag has been used for jewellery, coins and tableware. Since Ag has various electrical and chemical properties, Ag has been the centre of a great deal of attention in physics, chemistry, biology and industry [55, 108]. Ag-ions have anti-bacterial properties and Ag nanoparticles are used in clothing and in deodorants to prevent the formation of unpleasant odours.

Ag easily reacts with sulphur (S) and forms a dark-grey silver sulphide (Ag_2S) causing silverware and silver objects to tarnish. Ag_2S has attracted the attention in research since

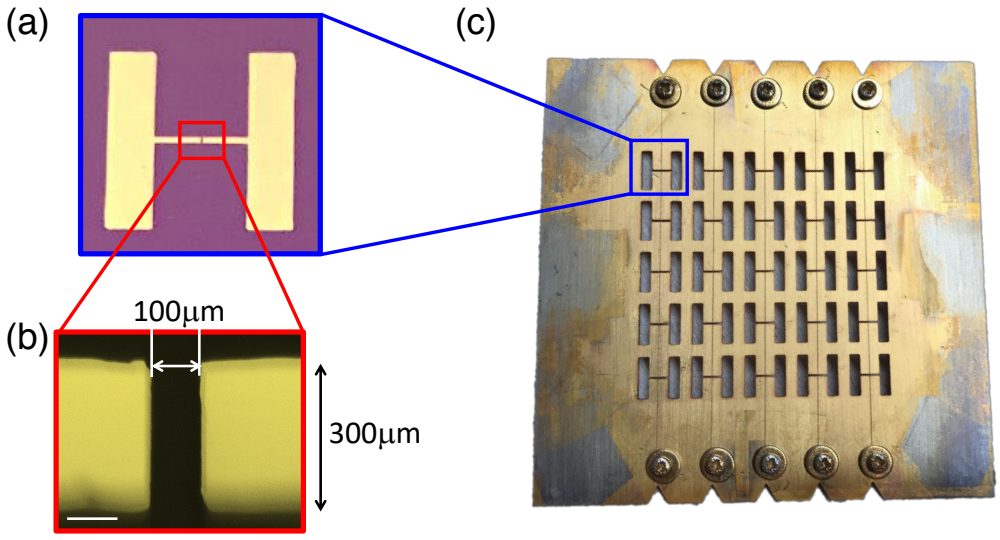

Fig. 2.1. (a)A simple H-shape two terminal electrode consisting of NiCr (5 nm)/Au (45 nm) on the 10 mm× 10 mm Si_3N_4 substrate. (b) SEM image of active area (100 μm × 300 μm) before cluster deposition (in false colours). The scale bar is for 100 μm (c) A shadow mask used in the evaporation of electrodes (5×5 array of perforates). The shadow is created tungsten wires crossing the center of the H-shape.

the first study of electric conduction of Ag_2S was performed by Faraday in the 19th century [111]. Ag_2S has good chemical stability and three stable phases: α, β and γ in the order of increasing temperature [112–114]. The detail of the property of α-Ag_2S and β-Ag_2S, which is related to the property of the device, is described in Chapter 5.

2.2 Substrates

The substrates used for cluster deposition are Si wafers with 100 nm Si_3N_4 passivation layer. Si_3N_4 has the advantage of low chemical reactivity and hardness [115]. The structure of the electrodes is designed to examine the electrical properties of the percolating nanoparticle films in two-terminal electrode configuration as shown in Fig. 2.1(a). The simple H-shape electrode with a 100 μm gap consists of 5 nm of NiCr (99.5%) and 45 nm of Au (99.99%) and is fabricated by thermal evaporation using a shadow mask technique in a high vacuum chamber (Edwards Auto 306 thermal evaporator) [116]. As shown in Fig. 2.1(c), the shadow mask has 5×5 array of H-shaped perforations and the 100 μm thick wires at the centre of each column provide the gaps which become the active areas of the nanoparticle networks.

The width of the electrodes is 300 μm and the dimension of the active area is 300 μm×100 μm as shown in Fig. 2.1(b).

The profile of the fabricated electrodes is measured by a surface profiler (Dektak 150). The profile usually exhibits a gradual slope in the 100 μm gap due to the round shape of wires. The slope enhances connections between the conducting network of metal nanoparticle and the edges of the electrode. Before deposition, the wafer is diced into 10 mm×10 mm samples and the samples are cleaned with acetone to remove any contaminants and isopropyl alcohol (IPA) for rinse. The substrates immediately after the IPA rinse are dried with 99.99% N_2 air blow. A final check of the substrate is done with an optical microscope and then the substrates are ready for the cluster deposition, as described in the next section.

2.3 Nanocluster Deposition

This section presents the nanocluster deposition system [116, 118, 119], which is used for the fabrication of the nanoparticle devices. Fig. 2.2(a) shows an overview of the deposition system consisting of four stages: *source chamber*, *differential pumping stage*, *mass selection chamber* and *deposition chamber*. Three different vacuum pumps are connected to different pumping stages (see Fig. 2.2(a)) and create the pressure gradient in the system, which allows the delivery of the clusters from the source chamber to the deposition chamber. Details of each chamber are provided below.

The Source Chamber

The source chamber, where clusters are produced using magnetron sputtering, is made up of a magnetron sputter head and a liquid nitrogen cooling system. Fig. 2.2(b) shows a schematic diagram of the interior of the source chamber [117]. The sputter target is a metallic disc (99.999% pure β-Sn or 99.999% pure Ag supplied by Kurt J. Lesker) and is mounted in front of a permanent magnet on the sputter head. As shown in Fig. 2.2(d), Ar gas is introduced from the back of the target and a DC bias produces the Ar plasma near the surface of the target which is the cathode. The Ar^+ ions are accelerated towards to the target source by the applied electric field and bombard the source surface, causing atoms to be ejected. The electrons produced during the ionisation of the Ar are trapped by the

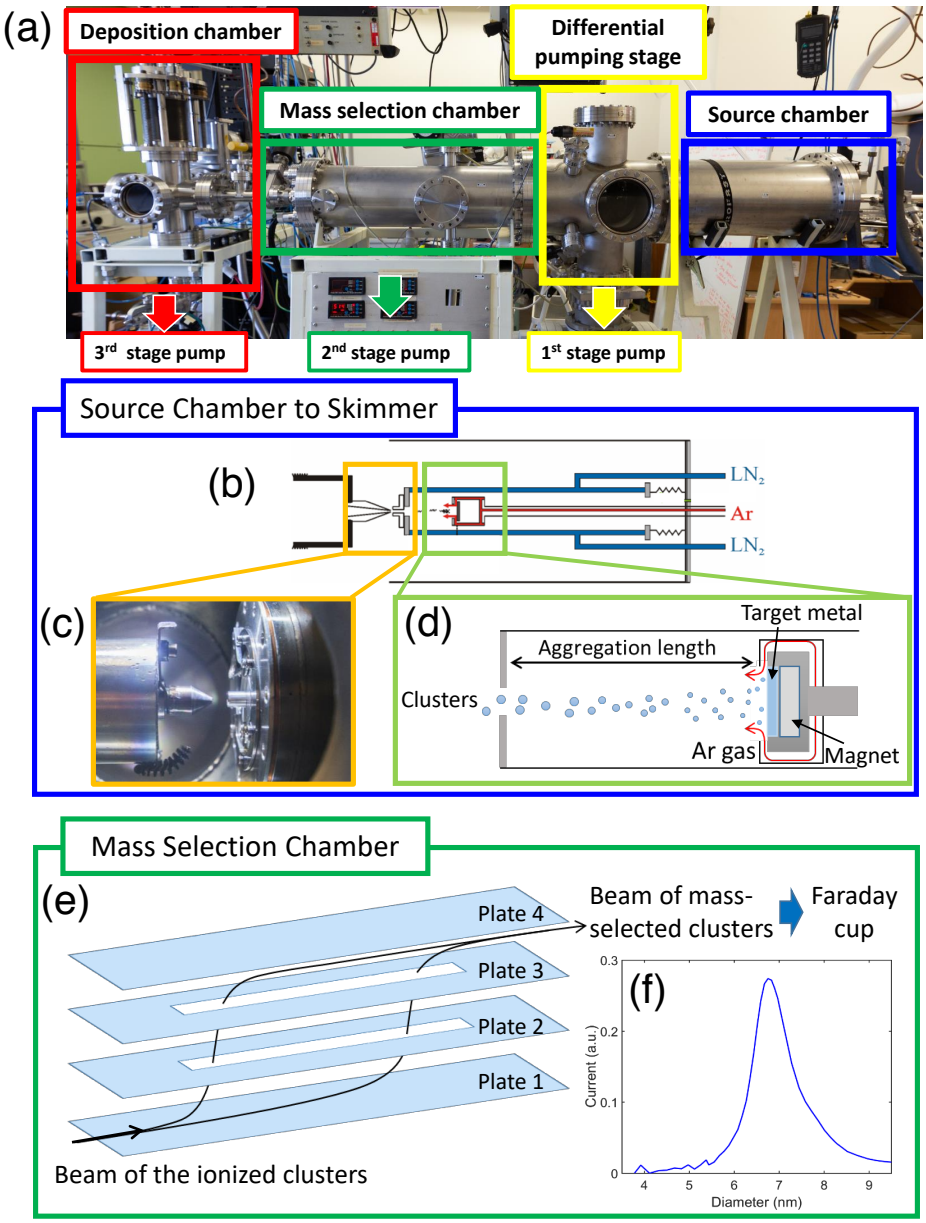

Fig. 2.2. (a) Overview of the cluster deposition system consisting of 4 stages: (blue) *source chamber*, (yellow) *differential pumping stage*, (green) *mass selection chamber* and (red) *deposition chamber*. Clusters produced in the source chamber are delivered by the pressure gradient in the system and are deposited on the device in the deposition chamber. (b) A schematic illustration of the interior of the source chamber (adapted from ref. [117]). Liquid nitrogen (LN_2) in the isolated part indirectly cools down the air in the chamber, leading to the growth of clusters. (c) A photograph of the nozzle and skimmer in the differential pumping stage. (d) A schematic illustration of the aggregation process. The cluster size in the beam can be controlled by adjustment of the aggregation length. (e) A schematic diagram of the mass selection filter. The mass-selected clusters enter the Faraday cup measuring the number of ions to obtain mass distribution. (f) A typical distribution of the cluster size converted from the mass obtained before deposition. The cluster size is ∼7 nm in this example.

magnetic field and move in helical trajectories near the surface of target source, resulting in more ionisation of Ar and promoting the sputtering. To avoid melting the surface of the metallic target due to the increase in temperature caused by the ionic bombardment, cooling water flows through the pipes on the back of the target source. Atoms detached from the target surface start forming nanoclusters. Liquid nitrogen (LN_2) cools down the gas in the source chamber (see Fig. 2.2(b)) to help the growth of the clusters. The size of clusters can be controlled by various parameters in the source chamber such as the Ar flow rate, the traveling distance of particles between the source and an exit nozzle (aggregation length, see Fig. 2.2(d)) and the sputter power e.g. the larger aggregation distance generally produce bigger clusters. The effect of each of these parameters on the cluster size distribution has been discussed previously in the literature [116, 120].

The Differential Pumping Stage

The clusters generated in the source chamber are guided to the exit nozzle and travel towards a skimmer (see Fig. 2.2(c)) thorough the differential pumping stage. In this stage, the pressure is lower than that in the source chamber, resulting in a pressure gradient and most of the gas is pumped out before the skimmer. Since clusters have higher mass than the gas, they can pass through the skimmer. The skimmer has a particular shape and plays an important role to collimate the clusters into a beam [118].

The Mass Selection Chamber

The clusters coming from the differential pumping stage enter the mass selection chamber through the skimmer. In this chamber, the mass distribution of the clusters is analysed by the mass selection filter [117, 118, 121]. The filter comprises two pairs of metallic plates parallel with the trajectory of the beam as shown in the schematic diagram in Fig. 2.2(e). When ionised clusters enter the space between plate 1 and plate 2, they gain vertical momentum due to the applied pulse voltage to plate 1. Then, the clusters enter between plate 3 and 4 through the holes on plate 2 and 3. In this region, the clusters lose the vertical component of the velocity gained during the first pulse due to the applied equal but opposite pulse. Since lighter clusters gain more energy than heavier clusters during the first pulse,

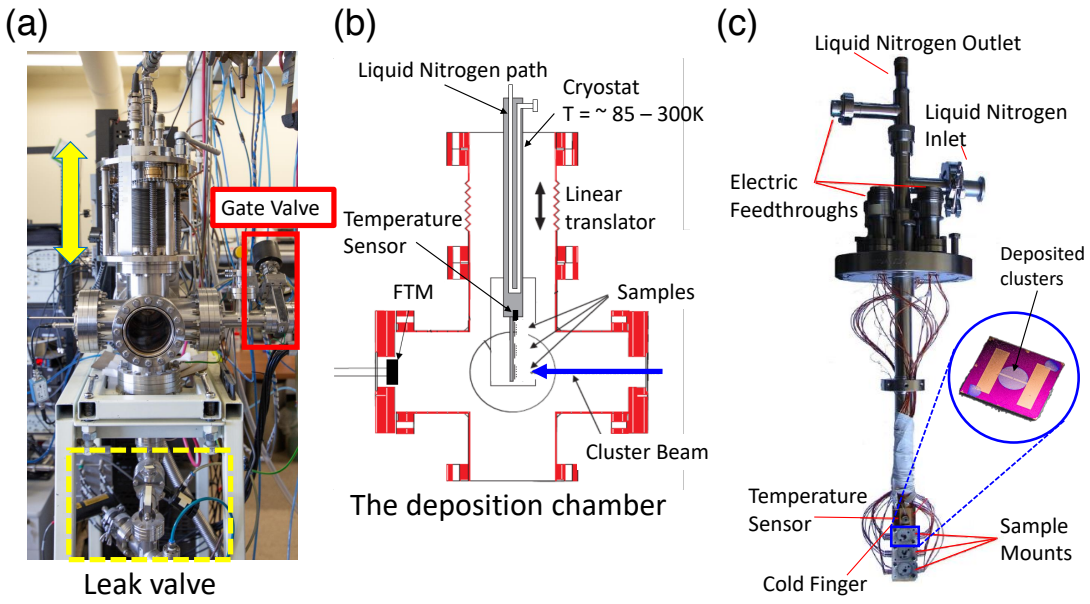

Fig. 2.3. (a) An overview of the deposition chamber and (b) the schematic structure of the deposition chamber (adapted from ref. [119]). The start and termination of the deposition are controlled using a gate valve in (a) between the mass selection chamber and the deposition chamber. The leak valve in (a) allows control of the pressure and humidity in the chamber during deposition. (c) The cryostat and sample mounts on the cold finger (adapted from ref. [116]). The cold finger can be cooled down to ∼85 K using liquid nitrogen. The sample holder can mount up to three samples and the deposition is operated one by one by changing the vertical location of the samples using the linear translator in (b). The inset in (c) shows the device after the deposition of Sn clusters.

light clusters travel upwards during the time between the pulses. The mass of clusters which can reach the Faraday cup depends on the magnitude of pulse and the aperture of the exit hole connected to the Faraday cup. Finally, only clusters with a particular mass are left on the axis and enter the Faraday cup to measure the number of ions. By changing the pulse voltages on the lengths, it is possible to measure the distribution of the cluster sizes. A mass distribution of the cluster beam (as in Fig. 2.2(f)) is obtained before each deposition in order to confirm whether the size of the clusters is within the desired range.

The Deposition Chamber

The deposition chamber is where the clusters are deposited on the target substrate. The chamber is smaller than the other chambers and connected to a molecular turbo pump with a rotary pump to maintain the pressure at $\sim 10^{-6}$ Torr. The pressure and humidity in the chamber during cluster deposition can be controlled by leaking air from the leak valve in

Fig. 2.3(a). Control of the deposition conditions is an essential factor to stabilise the devices [50], as discussed in Section 3.2. As shown in a schematic diagram in Fig. 2.3(b), there is a film thickness monitor (FTM; Sycon Instruments STM-100/FM) in the chamber in order to measure the deposition rate in Å/min. The start and end of deposition is controlled by a gate valve between the mass selection chamber and the deposition chamber (see Fig. 2.3(a)). Maximum of three target samples can be attached to the sample holders on the vertical cold finger shown in Fig. 2.3(c). *In-situ* electrical measurements such as voltage and current measurements with applied DC voltage or voltage pulses are conducted through a pair of electrodes for each device (see the inset in Fig. 2.3(c)). The temperature during the electrical measurements can be changed by using liquid nitrogen poured into the liquid nitrogen path in Fig. 2.3(b) and measured with a temperature sensor near samples on the cold finger (see Fig. 2.3(c)).

2.4 Scanning Electron Microscopy (SEM)

Scanning Electron Microscope (*SEM*) is a microscope which produces images by scanning a focused electron beam over a surface. While a traditional optical microscope has limitation of a maximum resolution of ∼0.3 μm due to the wavelength of visible light (400-700 nm) [122], SEM has wide areal range from 5 μm to 1 cm in width with spatial resolution of 1-100 nm depending on the magnification [123].

In SEM, accelerated electrons with an energy of a few keV interact with surface and produce various types of signals including secondary electrons, back-scattered electrons as well as X-rays. These signals contain information about the surface topography, morphology and composition as described below:

• **Secondary electrons** are emitted near the sample surface, allowing high resolution images to be produced with details of ∼1 nm in size. Typical SEM images are obtained from the secondary electrons.

• **Back-scattered electrons** are electrons reflected from the samples. While the accuracy is less than that obtained from secondary electrons, the back-scattered electrons have an advantage in imaging crystal orientation or channelling contrast in polycrystalline materials because the back-scattered electron is sensitive to small crystal tilts of the sample surface

[123].

• **X-rays** are emitted by inelastic collision of the incidental electrons with inner shell electrons of the atoms in the samples. The X-rays in SEM are used to identify the distribution of elements [123].

In this work, the SEM (JEOL JSM-7000F Field Emission SEM) is used for imaging the morphology of deposited nanoparticles in both Sn and Ag/Ag_2S devices (see Chapter 3 and Chapter 5, respectively).

2.5 Electrical Measurement Systems

The electrical properties of devices, represented by their conductance or resistance, are measured *in-situ* in the deposition chamber under ultra high vacuum (UHV) condition. The devices (up to three samples in a single deposition) are mounted on sample holders and UHV feedthroughs carry the electrical signals in and out of the chamber. Two different experimental configurations are used depending on the preferred sampling speed i.e. 120 ms "slow" sampling and 200 μs "fast" sampling. Slow sampling is suitable for long measurements (∼days) with low amplitudes of noise, and fast sampling is used for characterising devices with high resolution in time.

Fig. 2.4 depicts schematic illustrations for (a) the slow measurement setup and (b) the fast measurement setup. In the slow measurement in (a), the voltage across the device and the electric current flowing through the device are measured using a Keithley 2000 multimeter and a Keithley 6514 electrometer, respectively. A voltage source (IOtech digital-analog converter) is connected to one electrode and the other electrode is grounded through the electrometer. A LabVIEW program is used to control instruments and record the voltage and the current. The device resistance during deposition is measured with the slow measurement system.

The fast sampling measurement in (b) is operated with a digital oscilloscope (Tektronix TDS5032b) and pre-amplifier (Stanford SR570). Since the oscilloscope can measure only voltages, a pre-amplifier is needed to convert the current into a voltage signal. The current is recalculated from the amplified voltage. A TG function generator allows to apply the desired voltage stimuli. Although the oscilloscope can measure at a faster sampling speed,

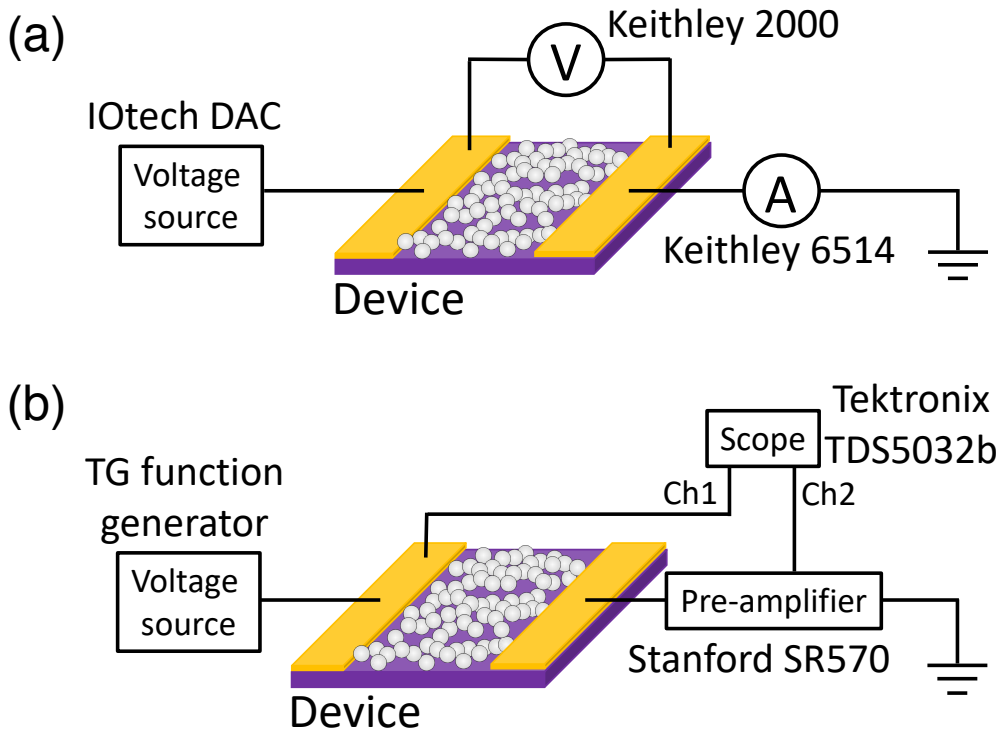

Fig. 2.4. Schematic diagrams of the measurement setups. (a) For 120 ms slow sampling measurements, voltage across device and the flowing electric current are measured by a Keithley 2000 multimeter and a Keithley 6514 electrometer which are controlled by a LabView program (b) In 200 μs fast sampling measurements, a oscilloscope (Tektronix TDS5032b) is used to measure voltage with a pre-amplifier (Stanford SR570). The current is also detected as voltage after pre-amplifier which allows current to be converted into voltage because the oscilloscope cannot directly measure the current.

the measurement duration is limited to 400 s due to the capability of the oscilloscope.

The electrical measurement begins from the start of cluster deposition in the fabrication process. The typical measurement duration of the fabrication process is more than 10 min and the resistance change from ∼GΩ to ∼kΩ. Therefore, the slow measurement system is used to monitor the device resistance under a DC bias of 0.1 V during the deposition because of its capability to measure long duration and wide range of current (see Section 3.2).

After the fabrication process, the electrical properties are characterised by pulsed voltage stimuli and DC voltages. The device properties under pulsed voltage stimuli are measured at slow sampling speed for the same reason as measurements during the deposition process. On the other hand, during DC voltage measurements, since the current range can be fixed with respect to the device resistance, both slow and fast sampling speeds are used. Further details of the effects of two sampling speeds on the results is discussed in Chapter 4.

2.6 Data Processing in MATLAB

Data analysis is performed in MATLAB, which is capable of handling large quantities of data and provides flexibility of coding with such in-built functions as a statistical analysis toolbox and a parallel computing toolbox. The developed codes to analyse the data in this work are summarised in Appendix A. This section focuses on the initial raw data processing required for the analysis that is described in the following chapters.

2.6.1 Raw Data Processing

The raw data comprises voltage ($V_{\mathrm{raw}}(t)$) and electrical current ($I_{\mathrm{raw}}(t)$) as a function of time are shown in Fig. 2.5(a). The procedure of the data processing is briefly described below.

1. Import the data

Measured data (text files) containing time, $I_{\mathrm{raw}}(t)$, $V_{\mathrm{raw}}(t)$ and temperature is imported using the in-built MATLAB function `importdata`. The raw data processing is automated by the MATLAB script (`DataAnalyzer` in Appendix A) and multiple text files can be processed and .mat files are generated for each dataset.

2. Calculate the conductance (G)

Raw conductance ($G_{\mathrm{raw}}(t)$, shown in Fig. 2.5(a)) as a function of time, is calculated from $I_{\mathrm{raw}}(t)$ and $V_{\mathrm{raw}}(t)$ with the equation:

$$G_{\mathrm{raw}}(t) = \frac{I_{\mathrm{raw}}(t)}{V_{\mathrm{raw}}(t)} \times \frac{1}{G_0} \tag{2.1}$$

where $G_0 = 2e^2/h \sim 7.748 \times 10^{-5}$ S is the quantum of conductance (see Section 3.1.2).

3. Implement the cleaning process for raw data

$I_{\mathrm{raw}}(t)$ has a lot of spikes induced by the electrometer (Keithley K6514) at the voltage pulse edge where the current range changes, resulting in spikes in $G_{\mathrm{raw}}(t)$ as shown in Fig. 2.5(a). In order to avoid the misidentification of switching events, it was necessary to remove the spikes from $G_{\mathrm{raw}}(t)$ using two kinds of filter. Fig. 2.5(d) shows the result of the first filter and Fig. 2.5(e) shows cleaned $G(t)$ after application of the second filter. Since the measurements with DC bias do not have the spikes in $G_{\mathrm{raw}}(t)$, this process can be skipped.

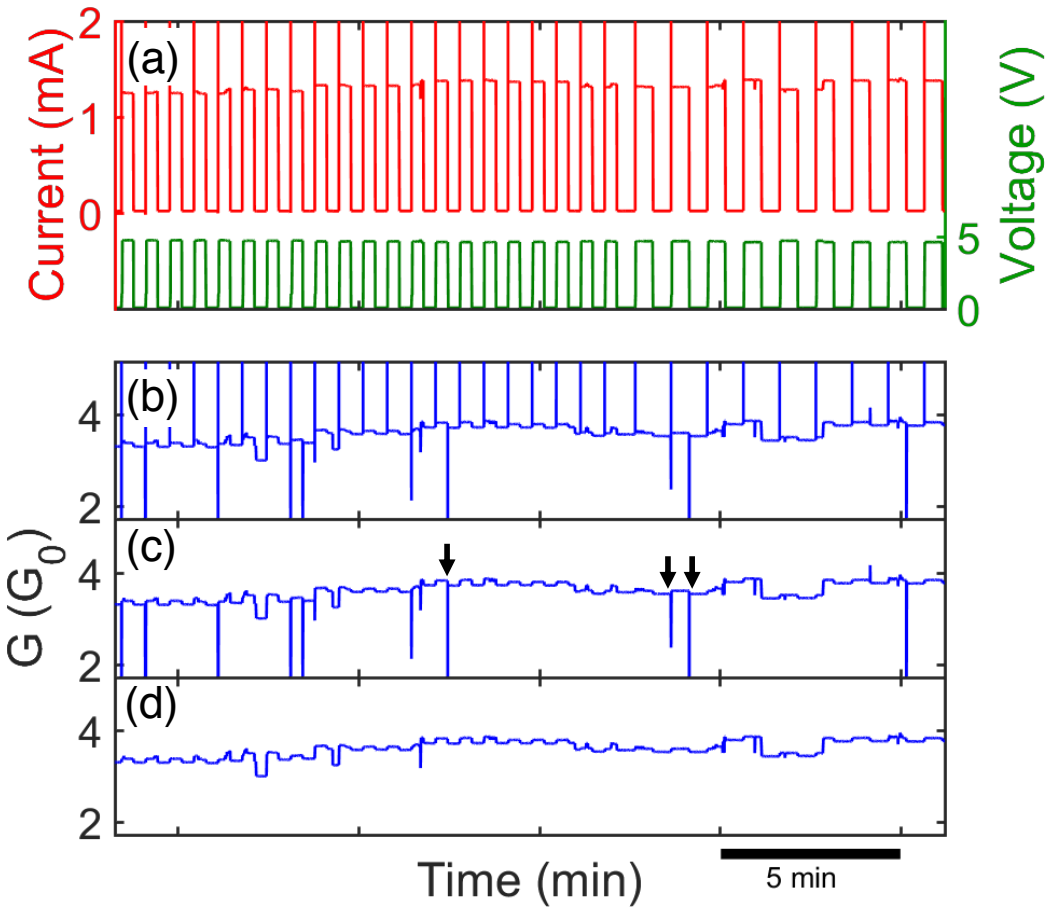

Fig. 2.5. (a) Raw measured data of (red) electrical current ($I_{\mathrm{raw}}(t)$) and (green) voltage ($V_{\mathrm{raw}}(t)$) as a function of time (B86R13). The current contains spikes at the edges of voltage pulses where the current range changes in an electrometer (Keithley K6514). (b) Raw G traces over time ($G_{\mathrm{raw}}(t)$) calculated from I_{raw} and V_{raw}. The $G_{\mathrm{raw}}(t)$ contains the current-induced spikes at the edges of the voltage pulse. (c) Most of the significant large spikes are removed using the *spike-replacement filter* (*SRF*). However, the small spikes similar in size to that of the switching events cannot be removed (see the black arrows for some examples) and another filter called *local median filter* (*LMF*) is needed. (d) After using two filters, cleaned $G(t)$ is obtained. The processed data is assessed one by one.

More details of the cleaning process are provided in the next section.

4. Detect switching events

After the cleaning process, switching events are detected with a detection threshold. When the change in G is above the threshold value, the change is recorded as a switching event corresponding to the network change in the devices. The threshold value depends on the types of applied voltage and sampling speed and is therefore discussed in each chapter.

5. Save the results in .mat file

The processed data is saved in a .mat file, which is a file format used in MATLAB. This

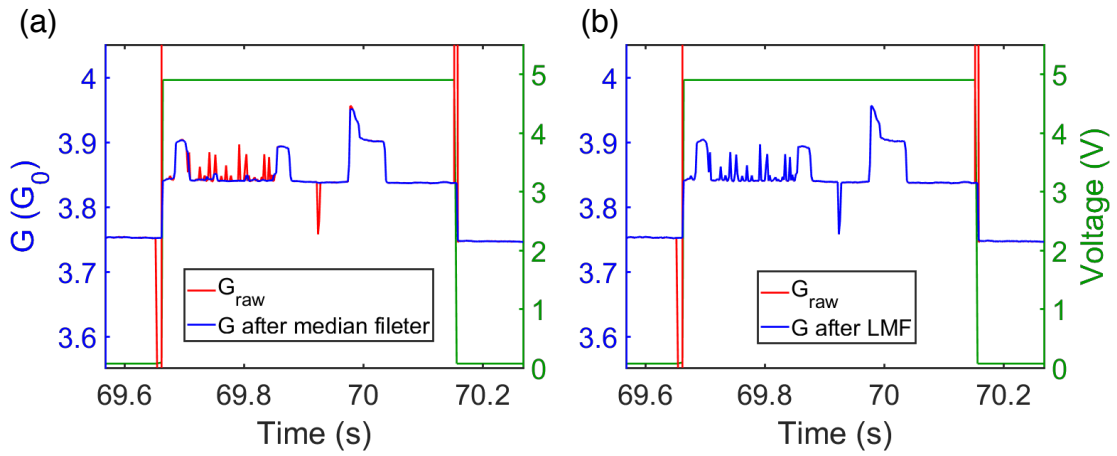

Fig. 2.6. Comparison of effects between (a) in-built median filter in MATLAB and (b) LMF after passing SRF. The red lines represents G_{raw} before applying two filters. While in-built median filter lost the real switching events, the LMF successfully removed only measurement induced spikes at the edges of pulses.

file allows access to cleaned data and also to information about detected switching events. It is used in various other analysis routines discussed in the following chapters.

2.6.2 Analysis of Raw Data

The data cleaning process is needed for $G_{\mathrm{raw}}(t)$ obtained in the voltage pulse measurements in order to remove the spikes (Fig. 2.5(b)). This process uses two original filters: *spike-replacement filter* (*SRF*) and *local median filter* (LMF). The majority of the spikes have very large values in G ($>100\mathrm{G}_0$) whereas typical G values in the device are smaller than $10\mathrm{G}_0$. The SRF detects the spikes which have G values above the spike threshold (Default: $G = 100\mathrm{G}_0$) and replaces the spikes to the value at the closest point of the next valid point. As shown in Fig. 2.5(c), the SRF replaces most of the significant large spikes, but cannot remove those spikes which are similar in sizes to the switching events as indicated by the black arrows in (c). These spikes originate from small measurement time lag due to the current range change. To remove these spikes, the LMF is used.

The LMF is based on the in-built 1-D median filter (`medfilt1`) in MATLAB and is applied only for G values at the voltage edges which are defined as data points within ± 2 points from a step of a voltage pulse. As shown in Fig. 2.5(d), after using the two different filters, both the big and small spikes are removed and a clean G trace is obtained. As

shown in Fig. 2.6(a, b), a great advantage of using the SRF and the LMF instead of in-built median filter in MATLAB is that neither of the filters affects the switching events and loses the information in the data. The effect of the two filters is validated in all data for voltage pulse stimuli by comparing between G_{raw} and G after filtering.

Chapter 3

Sn-based Percolating Neuromorphic Networks (PNNs)

Percolating nanoparticle networks have been extensively studied at the University of Canterbury (UC). The device fabrication procedure using cluster deposition has been well developed for the last decade [50, 116, 118, 119].

This chapter summarises previous research and then focuses on new results for the switching mechanism of the *individual* switch. This is essential to understand complex *collective* switching dynamics discussed in Chapter 4. Section 3.1 introduces the brief history of previous research at UC, with a summary of the progress made thus far and the basics of the atomic switches. Section 3.2 describes the fabrication of percolating nanoparticle networks. Section 3.3 discusses important properties of the devices for neuromorphic application. Finally, the summary is given in Section 3.4.

3.1 Summary of Previous Research at UC

The first percolating films at UC were fabricated using bismuth (Bi) nanoparticles (NPs) by Schmelzer [124] and their unusual conductance behaviour was studied by Schulze [125]. Since then, Bi NP films were used to investigate the mechanism of coalescence [126] and the electrical properties of the NP networks which were accurately described by percolation theory [127]. In terms of the application of the devices, tin oxide percolating NP films were used as hydrogen and ammonia gas sensors [128].

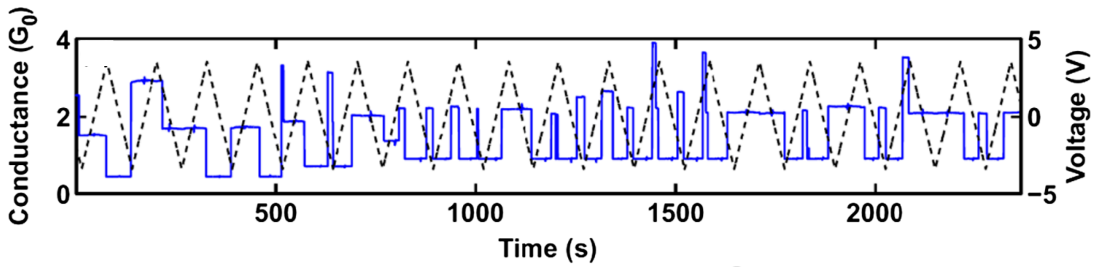

Fig. 3.1. The switching behaviour with multiple quantised conductance steps in the Sn percolating NP film (adapted from ref.[52]). Similar switching behaviour has been observed in different neuromorphic devices [48, 129].

More recently, research has focused on percolating tin (Sn) NP films as a neuromorphic device (*percolating neuromorphic networks* (*PNNs*)), as described in the next section.

3.1.1 Switching Behaviour in Tunnel Junctions

Switching behaviour in the Sn NP devices was observed as changes of the device conductance (G) with multiple quantised steps [52] as shown in Fig. 3.1. Sn NP devices deposited near the percolation threshold have tunnelling gaps on electrical pathways [52, 79]. The switching behaviour is understood as a consequence of the atomic wire formation and destruction in the gaps under voltage stimuli. Resistive switching activity induced by the atomic scale wires has been reported in self-assembled Au cluster thin films [107]. The detail of conductance quantisation and the switching mechanism at a single junction are described in the following sections. Similar switching behaviour has been observed in many different neuromorphic devices [48, 129].

3.1.2 Quantised Conductance

In the classical model in solid-state physics, it is well-known that the conductance (G) of a two-dimensional rectangular conductor is characterized with the width (W) and the length (L) [131] and follows the Ohmic scaling law:

$$G = \sigma \frac{W}{L} \tag{3.1}$$

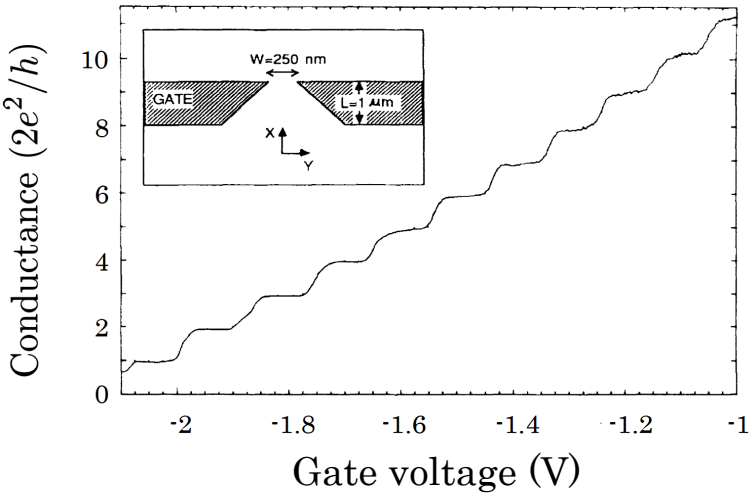

Fig. 3.2. Quantised conductance obtained by using quantum point contact (QPC) in two-dimensional electron gas in GaAs/AlGaAs heterostructure. The inset shows a schematic diagram of the electrical gate which allows to control constriction of the electric pathway with applied gate bias. Quantised conductance steps with clear plateaus at multiples of $2e^2/h$ are observed with applied negative gate bias (adapted from ref.[130]).

where σ is the conductivity characterising the material property, which is independent of the dimensions.

In an atomic-sized conductor, the Ohmic scaling law in Eq. (3.1) is no longer valid. During the 1980s, with the development of lithographic technologies, it became possible to explore the quantisation of conductance. The first observation of quantisation of G was reported in 1988 by two independent research groups [130, 132]. Their experiments were performed with two-dimensional electron gas in semiconductor (GaAs/AlGaAs heterostructure) with a pair of metallic gates, called the split gate configuration (see a schematic structure in Fig. 3.2 (the inset)). The width of constriction for an electron pathway is controlled by applying bias voltages to the gates. Fig. 3.2 shows the conductance changes as a function of applied negative gate bias and exhibits clear discrete steps with multiple plateaus at integer units of the conductance quantum:

$$G_0 = \frac{2e^2}{h} \sim 7.748 \times 10^{-5} S \tag{3.2}$$

where e is the charge of the electron and h is the Planck's constant.

Quantisation of G is observed in the full quantum limit satisfying two conditions. The

first condition is the *ballistic transport* of electrons, where the length of an electrical pathway is smaller than the mean-free-path that is the average distance travelled by an electron without scattering. In the ballistic regime, the electrons pass through the constriction with no momentum loss. The second condition is that the width of the electrical path must be comparable to the Fermi wavelength (λ_F) where the wave nature of electrons dominates their transport property in the wire, i.e. the number of conduction channels n depends on the width (w) of constriction ($n = 2w/\lambda_F$) [133]. The theoretical proof of conduction quantisation is given in the literature [131, 133].

Since the Fermi wavelength of electrons in a semiconductor is hundred times larger than that in metal [134, 135], in terms of the ease of fabrication of the device, a semiconductor with gates was used in the initial demonstration of the quantised conductance [130, 132]. With the development of the experimental techniques and equipment, quantised conductance has been observed in metal nanowires formed by mechanically-controlled break junctions (MCBJs) [135–137], scanning tunnelling microscope (STM) [134, 137–141] and electrochemical processes [129, 142–144]

3.1.3 The Switching Mechanism

STM and MCBJ techniques demonstrate not only the quantum nature of the electron but also the behaviour of the atoms at the microscopic scale. Previous studies of atomic motion give important insight to understand the switching mechanism in Sn PNN devices, as described in this section.

Atomic-scale Wire Formation The formation of the wire between two nanoparticles is induced by the local electric field across the tunnelling gap and can involve two possible processes, i.e. *electric field-induced surface diffusion* (*EFISD*) and *electric field-induced evaporation* (*EFIE*). Fig. 3.3 shows the schematic illustrations of the wire formation process. In EFISD in Fig. 3.3(a), since the surface atoms on the particle are mobile under the local electric field (~ 1 V/nm for Sn [145]) across a gap, the atoms are attracted towards the other side of the particle (electric field source metal), resulting in the formation of a protrusion, as shown in Fig. 3.3(b). This protrusion causes the gap between two particles to narrow and the strength of the electric field within the gap to increase. When the electric filed exceeds

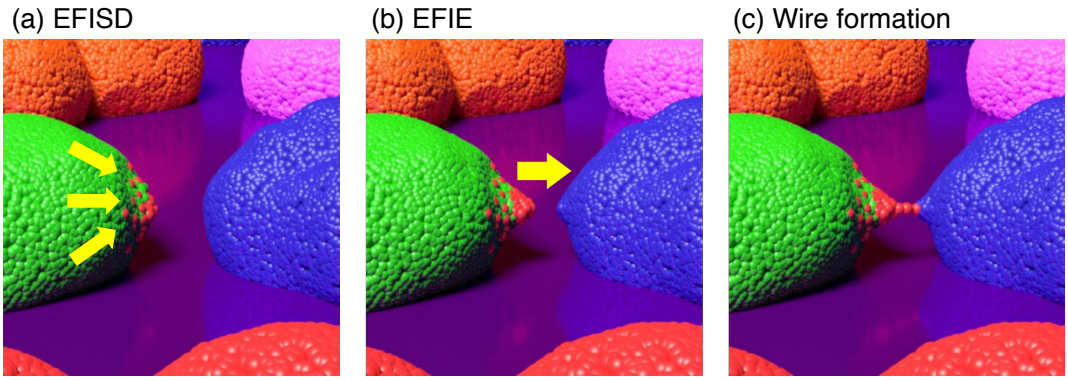

Fig. 3.3. Schematic illustration of the wire formation process at a single junction. A local electric field applied to the single junction induces (a) an *electric field-induced surface diffusion* (*EFISD*) and (b) *electric field-induced evaporation* (*EFIE*). In EFISD, mobile atoms on the surface of the particles move towards the other side of the particle and create protrusion within the gap, leading to the enhancement of the electric field across the gap. Then EFIE induced *jump to contact*, resulting in (c) wire formation within the gap. The electric fields required for EFISD and EFIE are ∼1 V/nm and ∼26 V/nm, respectively for Sn. The narrowing of the tunnelling gap with formation of the protrusion allows the local electric field to exceed the required strength for EFIE.

the strength required for EFIE (∼ 26 V/nm [146]), the surface atoms on one side jump to the other side, in a process known as *jump-to-contact* [135, 138], resulting in the formation of an atomic-scale wire, as shown in Fig. 3.3(c).

Atomic-scale Wire Destruction The atomic-scale wires are subject to very high current density, leading to the annihilation due to *electromigration* [147]. Electromigration is the momentum transfer from conduction electrons, resulting in the migration of atoms in the direction of electron flow. Electromigration reduces the size of the conducting wire and eventually breaks it. The required electrical current density is calculated as $\sim 2 \times 10^8$ A/m^2 for Sn [148]. Considering a typical measured device current range (∼mA) and the thickness of atomic-scale wire (∼nm), the current density in each Sn atomic wire can easily exceed the required value [52].

An atomic-scale wire has quantised conductance ($1G_0$) and switching results in discrete steps in G [52]. However, the observed changes in G are often not exact multiplication of G_0 due to the location of the switching sites in the PNNs. The details of this are discussed in Section 4.5.2.

3.2 Fabrication of Sn-based PNNs

Instability of the first-generation of devices was one of the biggest obstacles to overcome when investigating the basic properties of Sn PNNs. This section describes a solution to stabilise the devices and the deposition procedure used in this work.

The crucial problem in the device fabrication [52, 116] was to control the *coalescence* during and after deposition of Sn NPs. Coalescence is a process where two or more particles merge and form a compact structure. Since coalescence determines the structure of NPs, electrical properties and stability of the device, the control of the process is a critical factor in device fabrication. In Sn-based devices, deposited Sn NPs on the substrate are initially joined to neighbouring particles with fragile connections. At room temperature, the surface atoms have sufficient mobility and can be merged via coalescence, leading to the loss of electric pathways. To overcome this issue, S. K. Bose improved the deposition procedure and established the fabrication technique, described below, to provide stable devices with a rich variety of switching activities [50].

The main driving force for the coalescence of NPs is the minimisation of the total surface energy by the elimination of the interface, the grain boundary and the defects [149, 150]. Coalescence can be controlled by the partial pressure of air (P_{dep}) and relative humidity (RH) in the deposition chamber (see in Section 2.3): these are related to the oxidisation process of NPs. During fabrication, P_{dep} is precisely controlled by introducing the ambient air containing moisture through a leak valve (see Fig. 2.3). Fig. 3.4(a) shows the onset of conductance for different P_{dep} in the range from 6 μTorr (base pressure) to 600 μTorr. As shown in Fig. 3.4(b), the onset time (t_0: the initial time of observation of nonzero G) monotonically decreases with increase in P_{dep}. In contrast, the onset width (Δt: defined as time required to reach $6\mathrm{G}_0$ from t_0) is longer with higher P_{dep} (600 μTorr), compared to lower P_{dep} (< 100 μTorr).

As shown in Fig. 3.5(c), the particle sizes on the post-deposition device are greater than the originally deposited clusters ($\sim$7 nm) because the deposited clusters form NPs through coalescence (scale bar: 100 nm). The particle sizes for higher $P_{\mathrm{dep}} = 600$ μTorr in (d) are smaller than those of lower $P_{\mathrm{dep}} = 10$ μTorr in (c). This can be attributed to the prevention of the coalescence of the Sn NPs by the formation of tin-oxide shell [151] at higher P_{dep}.

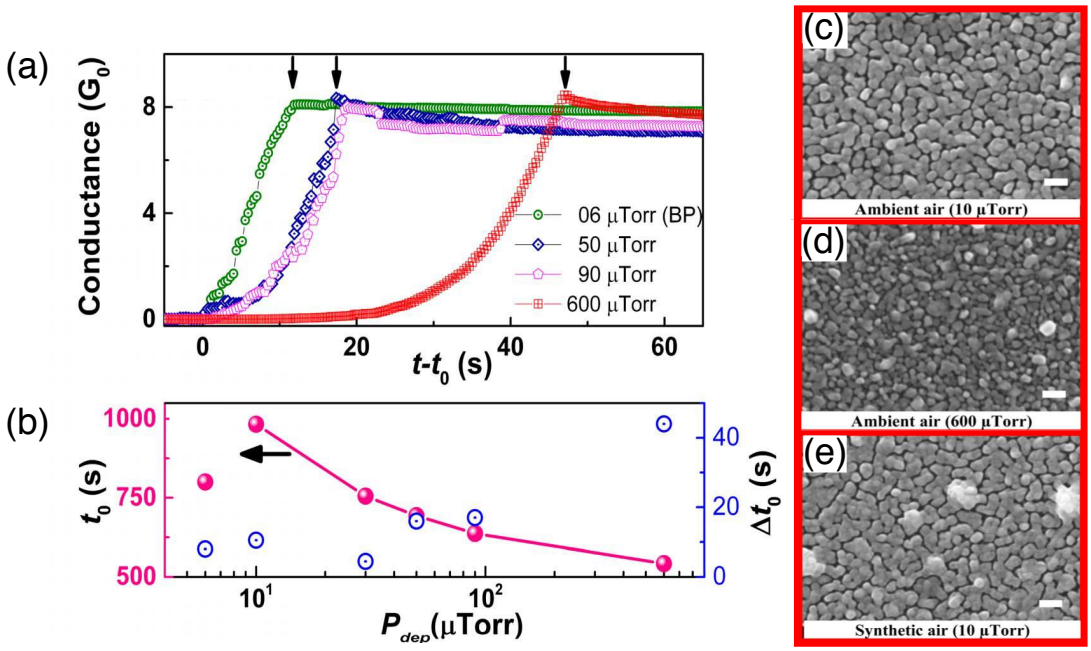

Fig. 3.4. The onsets of conductance and morphology obtained in SEM for different deposition conditions (adapted from ref.[50]). (a) Onsets of conductance for different P_{dep} (0.6-600 μTorr). (b) The onset time (t_0: the initial time of observation of nonzero G since the deposition started) for lower pressure ($<$ 100 μTorr) is relatively long, whereas the onset width (Δt: the time between t_0 and termination of deposition near $8G_0$) is shorter. On the other hand, the higher P_{dep} (600 μTorr) has short t_0 and long Δt due to reduced coalescence. An SEM image for the post-deposition devices under (c) lower P_{dep} = 10 μTorr show larger sizes of groups compared to (d) the case of higher P_{dep} = 600 μTorr. The white scale bars in (c-e) are 100nm. (e) The SEM image for the device fabricated with dry (RH $<$ 5% [50]) synthetic air. Since moisture also helps suppress coalescence, the device fabricated with synthetic air is not stable.

In addition to P_{dep}, high RH ($\sim$ 80%) also has an important role for stabilising the devices. According to the literature [152], the oxidation of pure Sn into tin-oxide (SnO and SnO_2) is accelerated under humid conditions. Since the deposition condition in this work is similar to the condition in the previous study of oxidation of Sn [152], it is assumed that only part of the surface of Sn NP is oxidised and that a tin-oxide shell is formed. The deposition with dry synthetic air shows different microstructure to the device deposited with the ambient air (Fig. 3.4(e): the particle sizes are slightly larger), even though the P_{dep} is the same value of 10 μTorr as in Fig. 3.4(c). In short, only when both P_{dep} and RH are precisely controlled, the devices are stabilised [50].

In this work, Sn-based PNN devices are fabricated using the optimised conditions (P_{dep} = 10 μTorr and RH $\sim$ 80%) with the deposition rate of 0.2 Å/min. Fig. 3.5(a) shows

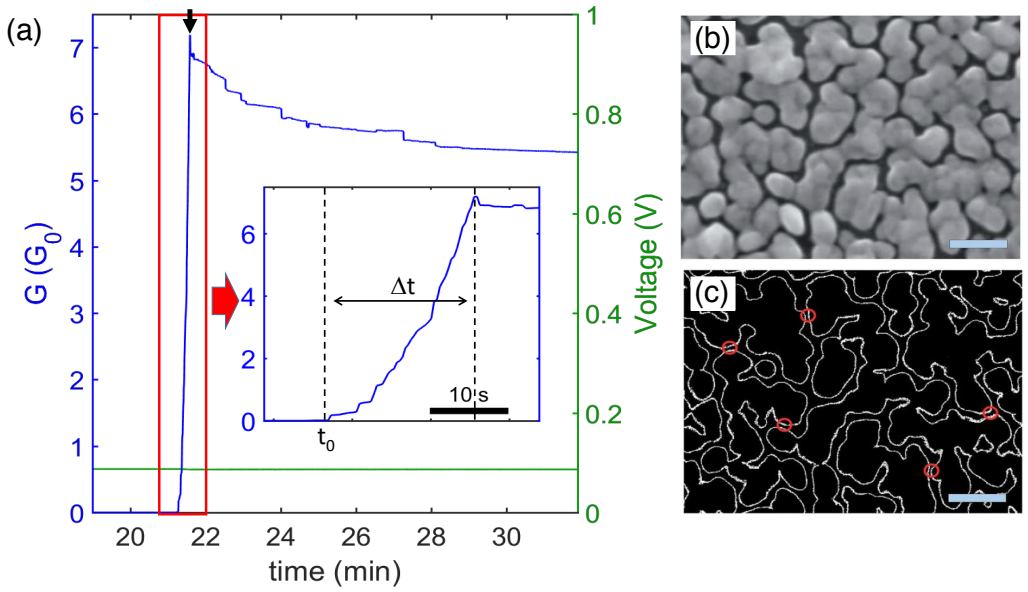

Fig. 3.5. (a) A typical onset of G measured on two-terminal device (B134, V = 0.1 V: read voltage, $P_{\text{dep}} = 10$ μTorr, RH∼80%) The inset is a high magnification of the onset showing steep change of G. Even after the termination of the deposition, the change of G is still observed for ∼5 min due to coalescence of particles. However, ambient air with high RH suppress the coalescence and the device finally stabilised at ∼5.5G_0. Once the device reaches the stable state, the G remains constant value for months unless the voltage stimuli is applied [50]. (b) A SEM image of the post-deposition device and (c) corresponding edge-marking exhibit the gaps (red circles) on the conducting pathways, which are potential switching sites where atomic wires are formed or broken. The scale bars are 100 nm in (b, c).

an onset curve in G with typical values of $t_0 \sim 20$ min and $\Delta t \sim 20$ s (see the inset). The deposition is terminated at ∼6G_0 (∼ 2 kΩ) near the percolation threshold [50, 51] (see the black arrow in (a)) whereas G at the termination of deposition may deviate ±1G_0 because of the very sharp onset curve. As shown in Fig. 3.5(a), the G values slightly decrease even after the termination of deposition due to coalescence of the particles, but the ambient air with high P_{dep} and high RH (∼80%) suppresses the coalescence, resulting in the stable G value. Once the device is stabilised, G remains the same for months, unless voltage stimuli are applied [50].

Each group of particles (Fig. 3.5(b)) works as an electrical pathway. Fig. 3.5(c) shows the corresponding edge-marking of the groups of particles in (b), which presents the gaps separating the groups that are potential switching sites (highlighted with red circles) for atomic-scale wire formation or annihilation (see Section 3.1.3). These switching sites can be activated with voltage stimuli, as described in the next section.

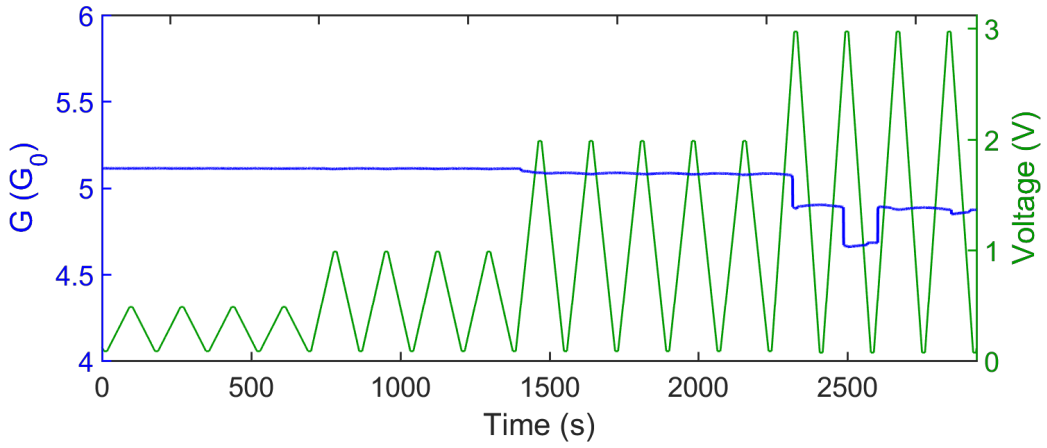

Fig. 3.6. Time evolution of G under the initial sweep of voltages in a post-deposition device (B134R01). In the first voltage stimuli to define an activation voltage (V_{th}), the voltage peaks slowly increase from 0.5 V until the G shows both increase and decrease. The voltage ramp suits to observe the activation of the device ($V_{th} = 3$ V in this example). The V_{th} depends on each device, but it is normally in the range between 2 V and 4 V.

3.3 Results: Switching Dynamics

While the switching dynamics in a single tunnelling junction is described in Section 3.1, the improvement of the device fabrication techniques described in the previous section allows further investigation of properties of PNNs, which is vital for understanding the complex switching dynamics discussed in Chapter 4. This section consists of two parts: *Activation of Switching Sites* and *Network Activity for Applied Voltage Pulses*. In brief, the first part describes switching activity as a function of voltages and temperature, and the second part discusses the network response to applied voltage pulses which corresponds to the controllability of the network configuration.

3.3.1 Activation of Switching Sites

Activation of the switching sites (i.e. tunnelling gaps) in PNNs depends on the external conditions, such as applied voltages and temperature, as described below.

(I) Voltage Threshold (V_{th})

The post-deposition devices are first examined with voltage ramps to obtain a threshold voltage at which the device starts switching. The voltage ramps are continuous changes of

voltage and allow the voltage threshold to be easily found. The peak voltage increases from 0.5 V until the device shows both increase and decrease of G several times. Fig. 3.6 shows a typical example of the time evolution of G for the voltage sweep in the post-deposition device. In this device, clear switching with $\sim 0.2 G_0$ steps was observed in the segment for the peak voltage of 3 V. While the threshold voltage (V_{th}) differs for each device, the V_{th} is normally found to be between 2 V and 4 V. Below V_{th}, the switching activity is not observed. Also, the V_{th} is dependent on the surface coverage of PNNs, as described below.

(II) V_{th} and Surface Coverage

To investigate the threshold voltage as well as switching activity in the different coverage of PNNs, high and low coverage devices were fabricated. The surface coverage of the network corresponds to G at the termination of deposition (G_{stop}). Fig. 3.7 shows switching activity for (a) a high coverage ($G_{\text{stop}} \sim 14 G_0$) device and (b) a low coverage ($G_{\text{stop}} \sim 0.5 G_0$) device with applied voltage stimuli (DC bias) up to 10 V. Compared to the typical device ($G_{\text{stop}} \sim 6 G_0$) deposited near the percolation threshold, the high coverage device in (a) is activated with a lower V_{th} $\sim$0.5 V. Under lower voltage stimuli (V $<$ 4 V) the device conductance mainly decreases. This can be understood as a consequence that in high coverage of the network, the number of conducting pathways exceeds the number of gaps, and thus the atomic-wires are predominantly destroyed, decreasing G. In contrast, in the low coverage device, V_{th} is much higher ($\sim$6 V) than that of the typical devices. This is because of the existence of wider gaps in the low coverage network [79, 80] which requires a higher electric field to form atomic-scale wires. As can be seen in Fig. 3.7(b), even at high voltages (6-8 V), the switching activity is limited and only small switching is observed.

Interestingly, both high and low coverage networks finally reached a stable state where the switching dynamics is self-balanced with multiple up and down switching events maintaining constant average G. While deviation of G_{stop} may not affect the switching behaviour after reaching to the self-balanced state, the optimised G in the typical devices is used because the devices near the percolation threshold naturally show the self-balanced switching dynamics with relatively low voltages.

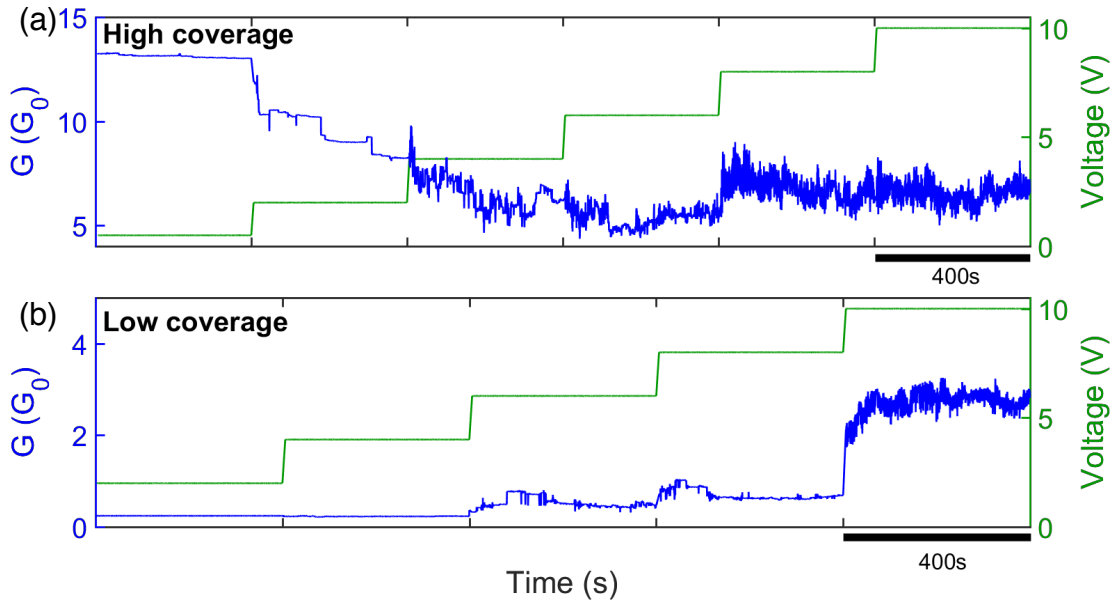

Fig. 3.7. The activation of the network elements for (a) high coverage (Gstop ∼14G_0) device (B177R01, R03, R05, R07, R09, R11) and (b) low coverage (∼0.5G_0) device (B176R02, R04, R06, R08, R10). The applied stimuli are DC bias in this example. The high coverage device in (a) can be activated at low voltage (∼0.5 V) whereas under the lower voltages (<4 V) the G mainly decreases. This is understood to be due to the destruction of the majority of the conducting pathways corresponding to high G until 4 V. Averaged G is relatively high compared to the device near the percolation threshold. In contrast, the low coverage device in (b) is active at only high V (>6 V) due to the existence of the wider tunnelling gaps which require the higher electric field to form atomic-scale wires. Both devices show the self-balanced switching activity with constant G at the higher voltage (< 6 V in (a) and ∼ 10 V in (b)).

(III) Voltage Dependence of Switching Rate

The switching activity of the activated devices increases under higher voltage stimuli above V_{th}. This section describes the relationship between the associated switching rate and the applied voltage amplitude.

Fig. 3.8(a) shows the switching activity under the range of voltage pulse amplitude (V_p) between 1 V and 10 V. Red markers represent switching events. Below V_{th} (2 V in this example), there is no switching event and for $V \sim V_{th}$ (2-3 V), only a limited number of switching events occur. In contrast, for higher V_p (> 4 V) many switching events with various switching sizes are observed. Fig. 3.8(b) shows the switching rate (the number of switching events per min) for 2 consecutive forward-backward voltage measurements (i.e. V_p = 1 V → 10 V → 1 V). The first forward voltage-sweep (red solid line) shows an ex-

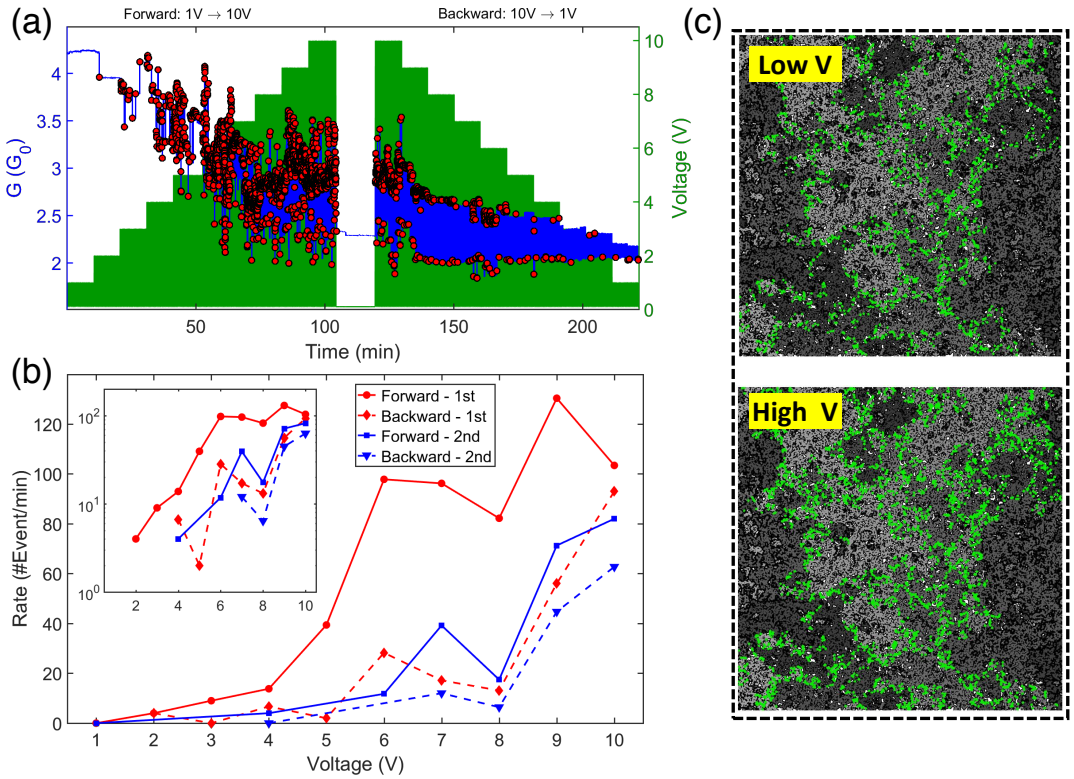

Fig. 3.8. Voltage dependence of (a) the switching activity in G with detected events (red markers) and (b) the corresponding switching rate (the number of events per min) (B148R03-R04, $\tau_p = 10$ s, 10 min for each V_p). Below V_{th} (2 V) there is no switching events and near V_{th} (2-3 V), only a few switching events are observed. The switching activity is enhanced in higher voltages ($V_p > 4$ V) and switching rate drastically increases as shown in (b), Above 6 V, the switching rate shows saturation (see the inset). (c) Numerical simulations of the switching activity in the network at (top) low and (bottom) high voltages (adapted from ref.[51]). The green dots in (a, b) represent the activated switching sites under voltage stimuli and the grey shades denote the groups of connected particles which are separated by tunnelling gaps (adapted from [153]). The increase of the activated switching sites and the spatial distribution at high voltage in (b) indicate activation of new sites that are not activated at low voltage in (top). Besides, multiple switching events in the same switching site may also contribute to enhancing the switching rate at higher voltages.

ponential increase of the rate until 6 V and then saturates (see the inset). In the first backward voltage-sweep (red dashed line), the switching rate drastically decreases and the second voltage-sweep (forward: blue solid line, backward: blue dashed line) has a similar rate to that of the first backward voltage-sweeps across V_p.

The enhanced switching activity for higher voltage originate from additionally activated switching sites and the increase of the activity at a single switching site. To investigate the voltage dependence of the switching rate, a numerical simulation is implemented due to the difficulty in accessing each switching site in the experimental setup [153]. Similar to the

two-terminal measurements, a voltage stimulus is applied to the left side of the network and the right side is grounded. Activated switching sites are denoted with green dots and the groups of connected particles which are separated by tunnelling gaps are represented by grey shades. Details of the simulation model are described in literature from the group at UC [79, 80, 153] (also see Section 4.5.2). High voltage (top in (c)) activates the new switching sites which are inactive under low voltage (bottom in (c)). In an intuitive understanding of the activation process, high applied voltage amplitude increases the local electric field across tunnel junctions which were previously below a minimum value required to cause switching. The increase in the number of the activated switching sites and their spatial distribution indicate the activation of previously inactive switching sites, contributing to the rise of the switching rate.

Higher voltage application ($V_p > 6$ V) may cause excessive Joule heating leading to opening the wider tunnelling gap or destruction of the gap. The formation of atomic-scale wires in the wider gaps requires a higher electric field. This results in a significant decrease in the switching rate for low voltage stimuli after the saturation in the first forward voltage-sweep while the network is still active for the high voltage stimuli (e.g. V_p = 9-10 V in the second voltage-sweep: blue line in Fig. 3.8(b)).

In short, higher voltage stimuli can activate more switching sites and enhance the switching rate, but also may cause fatigue of the devices (also see Section 4.7.5). As another factor of the network activation, the effect of temperature for the switching activity is investigated in the next section.

(IV) Temperature Threshold (T_{th})

As reported in the previous research for the other switching devices [143, 154], temperature is another possible parameter affecting the switching activity in Sn-based PNNs. To investigate the temperature dependence of switching activity, the device temperature is varied from the lowest possible temperature in the system (∼85 K) to room temperature. The temperature during voltage stimuli is measured with a temperature sensor near the device. Fig. 3.9(a, b) shows a typical example of switching activity with temperature and switching rate as a function of temperature, respectively. The switching rates are averaged every 10 K and the solid line in (b) shows a sigmoid-fit. At lower temperature below $T_{th} \sim 200$ K, no switching

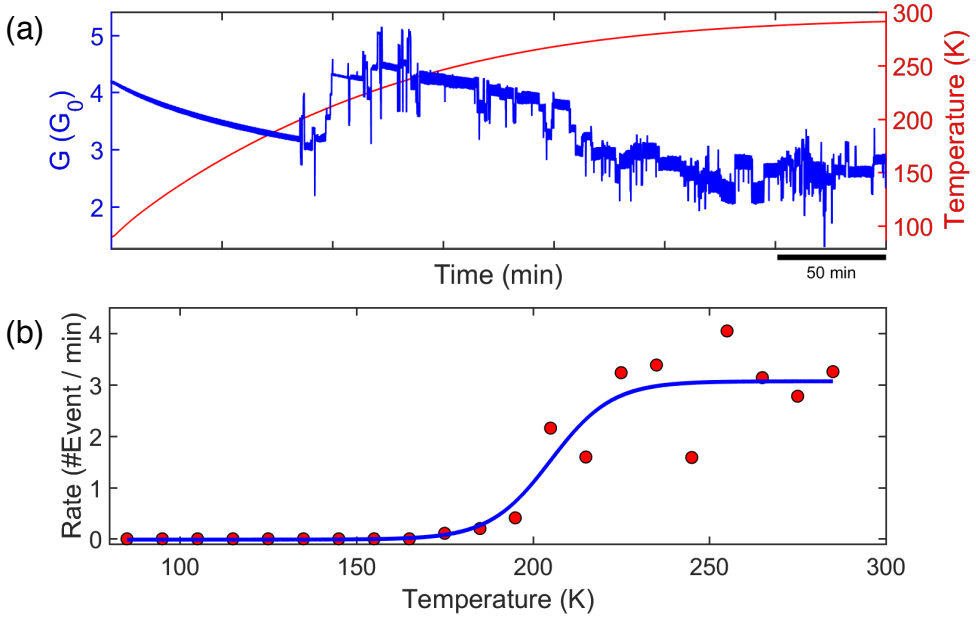

Fig. 3.9. Temperature dependence of the switching activity: (a) conductance change (B68R16, V = 8 V, τ_p = 10 s) and (b) corresponding switching rate with temperature (averaged rate from B67R20,B67R23, B68R16, V = 8 V, τ_p = 10 s). There is no switching activity below 200 K and above 250 K the event rate saturates. The event rates are averaged every 10 K and the solid line is sigmoid-fit. The typical energy scale calculated from T_{th} is ∼17 meV and matches to the Debye temperature of Sn [51].

events are observed even under high voltage stimuli (V = 8 V) above the V_{th} = 3 V. Above 250 K, the switching event rates saturate.

The typical energy scale required for atomic reconfiguration is estimated as $e/k_B T_{th} \sim$ 17 meV where e is the electron charge and k_B is the Boltzmann constant. This energy scale matches the Debye temperature of Sn [155]. The temperature dependence in Fig. 3.9 can be understood as a consequence of "freezing out" the atomic motion below 200 K and the diffusion of adatoms in the tunnelling gaps, which is necessary for wire formation, is effectively prevented [51]. This result also indicates the switching activity in Sn-based PNNs is not sensitive to small variations in room temperature.

3.3.2 Network Activity for Applied Voltage Pulses

In the previous section, the activation of the device and the switching rate under different voltage stimuli and temperature were discussed in terms of the individual switching activity. As described in Section 3.3.1 (III), the switching rate increases with excitation of the network under high voltage stimuli. This section investigates the detail of the switching dynamics

near and above V_{th} in terms of the response of the network for the voltage pulse stimuli.

(I) Switching Types: Linked-events and Unlinked-events

Any applied voltage pulses consist of four components:

- "On" phase where the voltage is constant above the read voltage (0.1 V)
- "Off" phase where the applied voltage is just the read voltage of 0.1 V
- Leading edge (LE) where the voltage increase from "off" to "on"
- Trailing edge (TE) where the voltage decrease from "on" to "off"

The read voltage used to measure the device conductance is 0.1 V, which is below the voltage threshold. Based on these components, the switching events are classified into two different types i.e. *linked-events* and *unlinked-events* (see examples in Fig. 3.10(a, b)). The linked-events occur at either LE or TE of voltage pulses. For convenience, the voltage edge is defined as ± 2 data points from a step of a voltage pulse. Unlinked-events occur not at pulse edges while unlinked-events are not observed in the "off" phase (i.e. $V = 0.1$ V). The classification of switching events are implemented in analysis of raw data described in Section 2.6.1 using MATLAB (`DataAnalyzer` in Appendix A.1).

(II) Archetype-A and Archetype-B

The classification of the switching event types allows to categorize the switching activity into two archetypes: *Archetype-A* and *Archetype-B*.

Archetype-A ($V_p \sim V_{th}$) When the voltage pulse amplitude (V_p) is near voltage threshold ($V_p \sim V_{th}$), the limited number of switching sites are activated in the network (Fig. 3.8(c)) and thus the switching activity simplifies. Fig. 3.10(a: top) shows a typical switching activity in G (blue line) with V_p close to but above V_{th}. Green markers and red markers represent linked-events and unlinked-events, respectively.

Histograms in Fig. 3.10(a) show distributions of switching size in (green) linked-events and (red) unlinked-events for different pulse widths ($\tau_p = 5$, 10 and 30 s). For $V \sim V_{th}$, increase in G i.e. up-events ($G_{\uparrow}$) are mainly linked-events and in contrast, most of the

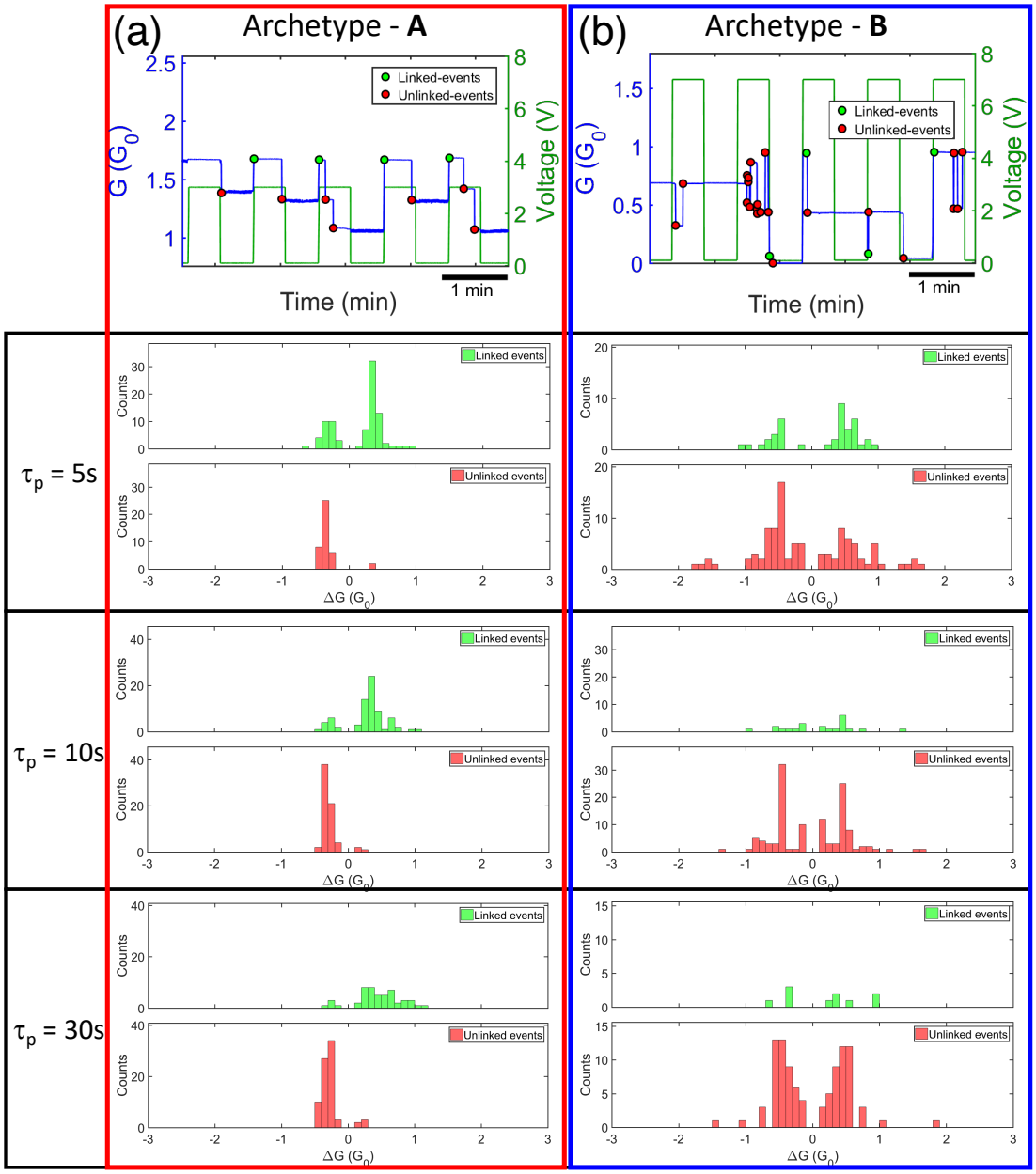

Fig. 3.10. Switching activity observed in G for two archetypes i.e. (a) archetype-A (B31R02, V_p = 3 V) and (b) archetype-B (B68R10, V_p = 7 V). Archetype-A is the switching behaviour at $V_p \sim V_{th}$ and as shown in histograms for three different pulse width (τ_p = 5, 10 and 30 s), linked-events (green) induce the increase of G (i.e. up-events: $G_\uparrow$) and unlinked-events (red) are observed as the decrease of G (i.e. down-events: $G_\downarrow$). On the other hand, in archetype-B, switching activity becomes complex due to multiple switching events. As shown in histograms in (b), the unlinked-events become dominant in both up and down events while linked-events corresponding to $G_\uparrow$ still can be seen at τ_p = 5 s.

decease in G i.e. down-events ($G_\downarrow$) are observed as unlinked-events.

Fig. 3.11(a) shows the rate of linked-event at LE (red line) and TE (blue line) for all

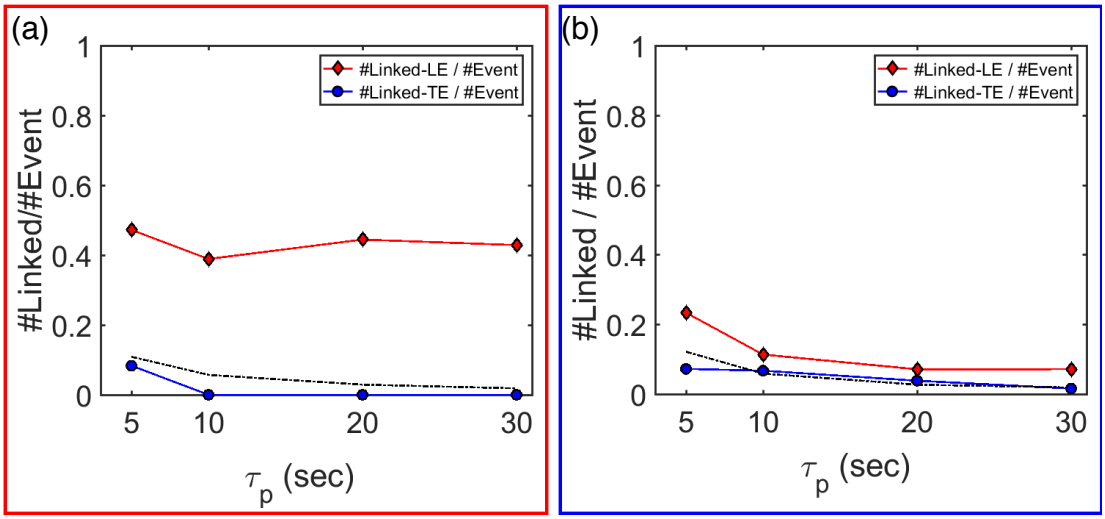

Fig. 3.11. Rate of linked-events at (red line) LE and (blue line) TE to all the switching events in (a) archetype-A (B68R02, V_p = 3 V) and (b) archetype-B (B68R10,V_p = 7 V). The dotted line represents the expected fraction for each τ_p in case of when the events are randomly distributed on "on" phase of pulses. In archetype-A in (a), the fraction of the linked-events at LE is much higher than the dotted line whereas the fraction of the linked-events at TE is consistent with the randomly distributed events. This indicates the linked-events at TE are just by chance and are not driven by a change of electric field. In contrast, the fraction of linked-events at LE in archetype-B decrease but above the dotted line. This is a consequence of the increase in the number of events due to additional unlinked-events.

the switching events. The dotted line indicates the rate of linked-events estimated from a random distribution of switching events. The fraction of the linked-events at LE is much higher than that of the random occurrence (the dotted line) whereas the rate of the linked-events at TE is consistent with the random occurrence, i.e. these events occur at the TE simply by chance and they are not driven by changes in the electric field.

Briefly, in archetype-A, $G_{\uparrow}$ predominantly occurs at LE (i.e. linked-events) and $G_{\downarrow}$ is mainly observed as unlinked-events after several seconds of current flow (see Fig. 3.10(a: top)), which is consistent with the idea of electromigration causing the destruction of atomic-scale wires.

Archetype-B ($V > V_{th}$) At higher voltages ($V > V_{th}$), the switching activity is enhanced (Section 3.3.1 (III)). Fig. 3.10(b: top) shows a typical snapshot of G trace (blue line) with two types of events, i.e. (green markers) linked-events and (red markers) unlinked-events. As shown in the histograms in Fig. 3.10(b), in addition to the $G_{\uparrow}$ in linked-events (green), multiple up and down unlinked-events (red) are observed, especially for longer τ_p = 5 and

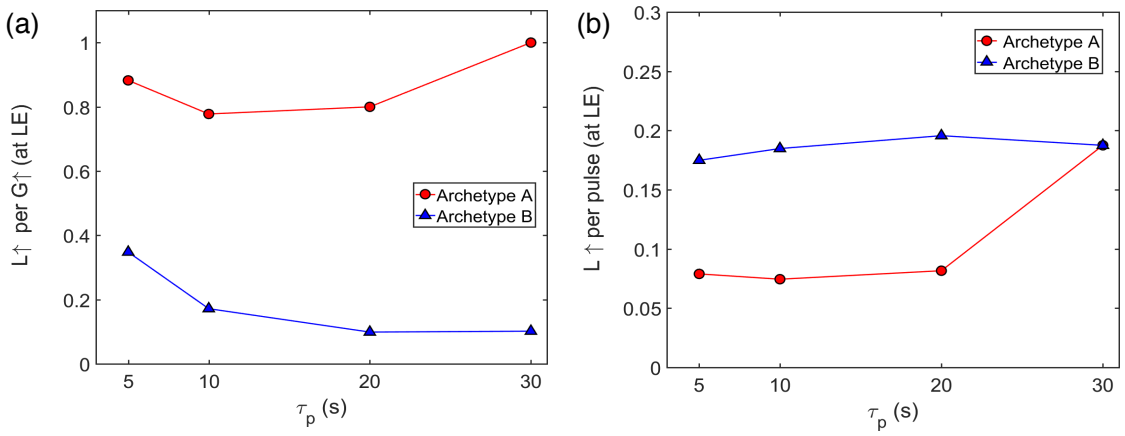

Fig. 3.12. (a) Linked-up ($L_\uparrow$) events at TE per up-events (i.e. $L_\uparrow$ + $U_\uparrow$) and (b) $L_\uparrow$ per pulse for (blue lines) archetype-A (B68R02, V_p = 3 V) and (red lines) archetype-B (B68R10, V_p = 7 V). As shown in (a) in archetype-A, almost 100% of up-events are observed as linked-events whereas the fraction of linked-events in archetype-B decreases due to additional unlinked-up events. However, the fraction of linked-up events per pulse remains similar range between 10% and 20% for both of archetypes, indicating at all applied voltages a similar fraction of the LE induces up-events.

10 s, the rate of the unlinked-events become dominant. As shown in Fig. 3.11(b), similar to archetype-A, the linked-events in archetype-B still preferably occur at LE, while the fraction of the linked-events at LE decrease due to the increase of the total number of events associated with additional unlinked-events.

Comparison between two archetypes (A and B) In both archetypes, the linked-events predominantly correspond to $G_\uparrow$ at the LE rather than the TE. Fig. 3.12(a) shows the number of linked-up ($L_\uparrow$) events at LE as the total number of $G_\uparrow$ (i.e. $L_\uparrow$ + $U_\uparrow$) for both archetypes. In archetype-A (red line), the fraction of $L_\uparrow$ is nearly 1, i.e. ∼100% of $G_\uparrow$ are $L_\uparrow$ at LE while $U_\uparrow$ is negligible for all τ_p. In contrast, the archetype-B (blue line) shows the decrease of $L_\uparrow/G_\uparrow$ with longer τ_p, e.g. at τ_p = 30 s, ∼10% of $G_\uparrow$ originate from $L_\uparrow$ events with ∼90% being $U_\uparrow$ events. Similar to Fig. 3.11(b), the fraction of the linked-events at LE decreases due to the increase of additional $U_\uparrow$ in archetype-B. However, as shown in Fig. 3.12(b), the number of $L_\uparrow$ per pulse remains in a similar range around 10 - 20% for both archetypes, indicating that at all applied voltages a similar fraction of the LE induces $L_\uparrow$.

A difference between archetype A and B is also observed in the network respond time characterised by $G_\uparrow$ preceded by unlinked-down ($U_\downarrow$) events. Fig. 3.13 shows histograms of

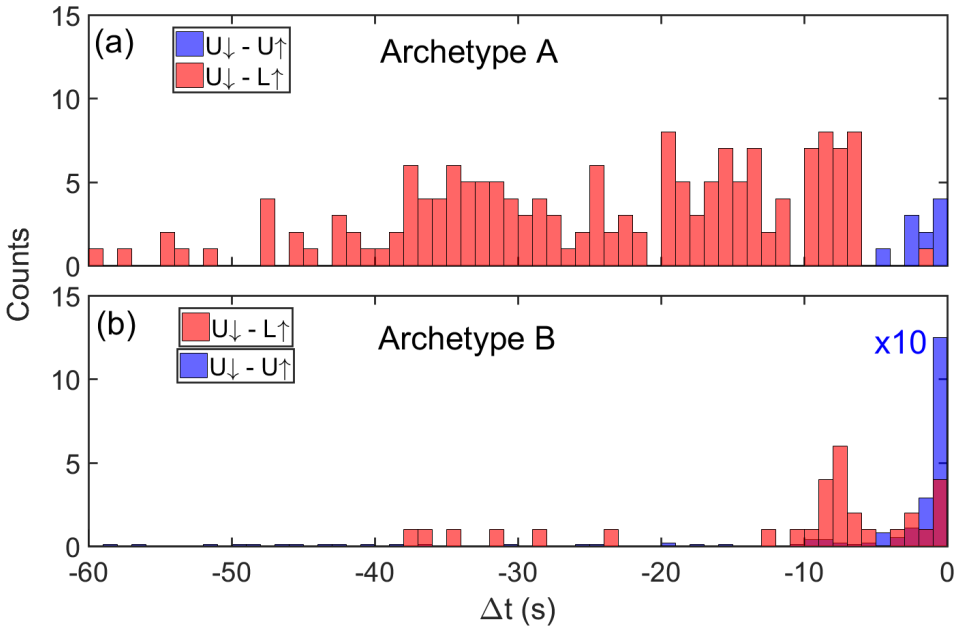

Fig. 3.13. The event-structure characterised with Δt (time between $U_{\downarrow}$ and up-events (i.e. $L_{\uparrow}$ or $U_{\uparrow}$)). (a) Archetype-A (B68R02, $V_p = 3$ V) shows the $L_{\uparrow}$ events are predominantly ($\sim$ 75%) preceded by an $U_{\downarrow}$ event and the Δt for $U_{\downarrow}$-$L_{\uparrow}$ is widely distributed. In contrast, (b) archetype-B (B68R10, $V_p = 7$ V) shows the $U_{\uparrow}$ events preceded by $U_{\downarrow}$ event occurs more frequently than $L_{\uparrow}$ with short Δt, indicating rapid response for the network changes in higher voltage stimuli.

counts of $L_{\uparrow}$ (red) and $U_{\uparrow}$ (blue) preceded by $U_{\downarrow}$ for (a) archetype-A and (b) archetype-B as a function of time (Δt) from $U_{\downarrow}$ to $G_{\uparrow}$ (i.e. $L_{\uparrow}$ or $U_{\uparrow}$). In archetype-A, the $L_{\uparrow}$ events are predominantly ($\sim$75%) preceded by a $U_{\downarrow}$ event and the Δt is widely distributed.

In contrast, in archetype-B, the $U_{\uparrow}$ events occur more frequently than $L_{\uparrow}$ and $U_{\uparrow}$ events are also predominantly preceded by $U_{\downarrow}$ with short Δt. Since higher applied voltage activates more switching sites (Fig. 3.8(c)) and also enhances the switching activity for each site, any change in the network configuration is likely to cause the next change in the network in a relatively short period of time, leading to the narrow distribution of Δt in Fig. 3.13(b). This result implies the switching events are spatially correlated in the network.

The difference between two archetypes originates from the accessibility of the network pathways and occurrence of switching at each tunnelling junction. In archetype-A, the activated network pathways at $V_p \sim V_{th}$ is limited to a small number of the main conduction pathways which connect the two electrodes. The applied voltage drops across the tunnelling gaps in these pathways, resulting in high local electric fields. Thus, a small number of available switching sites allows the rapid formation of atomic-scale wires, leading to $L_{\uparrow}$

events at the LE with large ΔG. In archetype-B, the additional network pathways are activated with higher voltages whereas the main pathways are still reconfigured. In other words, archetype-B is archetype-A plus additional $U_{\uparrow}$-$U_{\downarrow}$ of switching events from newly activated switching sites. Based on the insights obtained in this section, the next section investigates the overall network activity as an integrated behaviour of the switching activity in the individual site.

(III) Stimulus Frequency Dependence and the Network Connectivity

The two archetypes discussed in the previous section suggest the controllability of the network configuration. To investigate the stimulus frequency dependence of the switching activity, the voltage pulse widths (τ_p) are varied.

Fig. 3.14(a, b) shows stimulus frequency dependence of G (blue line) which represents the network connectivity. τ_p are varied in the range between 2 s and 30 s (green line corresponding to the right axis). In shorter τ_p (2 and 5 s), the averaged G (red line in (a, b)) is relatively high and in contrast the averaged G for $\tau_p > 10$ s becomes lower. Fig. 3.14(c) shows histograms of the switching sizes for $\tau_p = 2$, 10 and 30 s. At a larger values of τ_p, the number of $G_{\downarrow}$ (i.e. breaking atomic wires) is enhanced compared to that at smaller τ_p. Also, the broad peak of $G_{\downarrow}$ is observed in longer pulses. This can be attributed to the breakage of multiple wires during long pulses and the next pulse edge reconnects those wires at multiple switching sites, resulting in the bigger change in G (see a snapshot of such activity in Fig. 3.14(d)).

In the case of shorter pulses, there is less chance for the atomic wires to be broken by the current flow and the network connection is enhanced, leading to the relatively higher G in Fig. 3.14(a). On the other hand, in the case of longer pulses, the likelihood of breaking the atomic wires is higher, and thus the average conductance (G_{ave}) decrease. These results indicate the network configuration can be changed by tuning the voltage stimulus: this is essential functionality for neuromorphic applications [129, 142, 156, 157].

Also, a repetition of the network stimulation can enhance the overall connectivity in the network, i.e. increase in the G_{ave} due to the formation of robust conduction pathways in the network. Fig. 3.14(b) shows the second stimulus of the network activity after the first measurement shown in Fig. 3.14(a). The minimum value of the G_{ave} in (b) is higher than

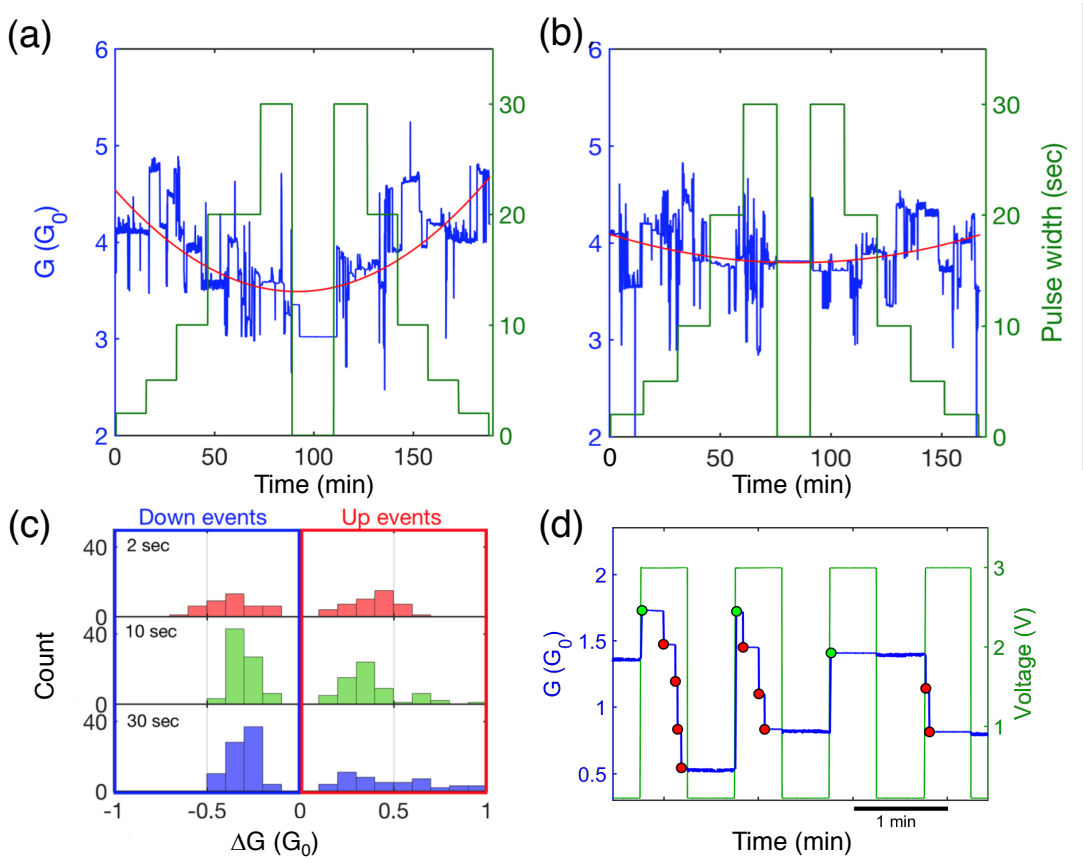

Fig. 3.14. The stimulus frequency dependence of the conductance ((a) B86R06, V_p = 6 V and (b) B86R11, V_p = 6 V) with various τ_p (2-30 s). Red lines in (a, b) indicate the averaged G. (a) The short pulse widths (e.g. 2 s and 5 s) enhance the wire formation resulting in the higher averaged G. On the other hand, the longer pulse widths (e.g. 20 s and 30 s) decrease the averaged G due to breaking wires. (b) Repetition of the voltage stimulus can enhance the overall connectivity in the network leading to an increase of the minimum averaged G. The number of events in (a) and (b) is the almost identical value (∼700) and thus the network is still active. (c) The distribution of the switching size for different τ_p shows the broad distribution of $G_\uparrow$ and enhanced $G_\downarrow$ events at larger τ_p. This can be attributed to the breakage of multiple broken wires by electromigration and their reconnection by the formation of new wires, as can be seen in (d) (B31R02, V_p = 3 V)

that in (a). Network connectivity enhancement is understood to occur when several cycles of the wire breaking and forming under voltage stimuli result in the formation of completely stable conduction pathways which increase the overall G. Since the total number of events for these measurements is almost identical (∼700), the change in the network response is not attributed to network fatigue, which may decrease the switching activity. Also, this result indicates that the overall network state depends on the history of the voltage stimuli. In other words, the information of the previous measurements is stored as the network state represented by G. Such stimuli dependent reconfiguration of the network connectivity is

discussed in the context of memory and learning abilities [142, 158].

3.4 Summary

This chapter summarised the switching behaviour in Sn-based PNN devices. The well-established deposition procedure allowed for the fabrication of stable devices and investigation of the network activity in terms of activation of switching sites under various conditions. Since the fabricated devices are stable for months, multiple measurements can be taken with various voltage stimuli.

The two archetypes of the switching activity provide the insight into the accessibility of the switching sites on the conduction pathways of the network. Voltage stimuli near the threshold V_{th} (archetype-A) only activate the switches on the main conduction pathways. Linked-events occur at the leading edges of voltage pulses. On the other hand, higher voltage above V_{th} (archetype-B) activates new switching sites and accesses a wider range of switching sites of a multitude of the switching sizes. In addition, the rapid response of the network to the previous network change was observed. While the sampling speed with voltage pulse were limited in this work, the expected response time for the former network changes is understood to operate on a timescale <10 ns, as reported in the literature [129, 159].

The reconfiguration of the overall network was accomplished with voltage pulse widths. The difference in the mechanisms of wire formation and annihilation allows the reconfiguring of the network state represented by G. When voltage pulses with shorter widths are applied, the effect of the electric field becomes dominant and the probability of a wire break is lower, leading to higher G. In contrast, the higher amplitude of the applied voltage or longer pulse width increases the probability of wire annihilation, resulting in a decrease of G, while the wire formation is still occurring. This ability to modulate the network configuration with the successive stimulus is a key requirement for the learning capability in neuromorphic systems [80, 129, 156].

The network connectivity enhancement observed between two consecutive voltage pulse stimuli (Fig. 3.14(a, b)) is considered to be due to the strengthening of each conduction pathway with the repetition of stimuli. A couple of cycles of wire destruction and reformation result in the formation of a strong wire and a consequent increase in overall G in

the subsequent voltage stimuli [51]. In neuroscience, the connectivity of biological neural networks is discussed in terms of the synaptic potentiation related to the learning ability of the brain and memory formation [15, 160, 161] (Section 1.1.1). Considering this analogy to biological networks, the stimuli history dependent network connectivity suggests that memory function exist in the network and that it is possible to train the network with respect to the type of voltage stimuli [50, 51, 142, 158]. While the results shown in this chapter were discussed from a perspective of the switching behaviour in individual tunnel junctions, the complex switching activity and memory function imply individual switching events are highly-interconnected. For real computation, temporal correlation, which arises from the interdependent activity, becomes another important factor [48, 49]. The next chapter focuses on the temporal dynamics and correlation in PNNs measured with DC bias stimuli which provide high signal-to-noise ratio and allow measurements for long duration.

Chapter 4

Temporal Dynamics and Correlations

The previous chapter described fabrication of the Sn-based PNNs and characterisation of the switching activity at *individual* switching sites in the network. Functions of the brain, like behavioural or cognitive states, arise from *collective* behaviour of activated groups of neurons [162]. For this reason, it is important for neuromorphic applications of PNNs to explore the emergent behaviour of switching across the network, and the resulting network dynamics in the devices. This is the focus of this chapter.

This chapter investigates the network dynamics using time series analysis based on the methodology used in neuroscience. Section 4.1 contains a brief introduction to the time series data, the analysis methods employed in neuroscience and also used to analyse our experimental data. Section 4.2 explains the fitting procedures for the data and the goodness-of-fit methodology based on the maximum likelihood estimation. Section 4.3 and 4.4 focus on the thresholding technique employed for analysing the time series including the effect of sub-sampling and thresholding. Section 4.5 discusses the relation between self-similar switching activity and the underlying network structure. Section 4.6 describes the fitting model of the experimental data and Section 4.7 presents the results of the temporal dynamics analysis and discusses the mechanisms. Finally, the conclusions for this chapter is drawn in Section 4.9.

4.1 Time Series Analysis

Time series analysis is a general term used for the analysis for *time series data*: it is defined as a series of data points indexed in time order (usually discrete time). The main purpose of time series analysis is to extract meaningful statistical information, understand the dynamics behind the temporal patterns and construct models for predicting values in a future time series from the current and past values. Nowadays, time series analysis is widely used in different fields (e.g. forecasting of the economy, stock market analysis, weather pattern analysis and seismic analysis) with a multitude of analysis methods employed [163–165].

Time series analysis can be divided into two main classes: frequency-domain analysis and time-domain analysis [165]. Frequency-domain analysis indicates how the time series variation is accounted for by different frequency components and includes the power spectral density (PSD) function obtained from Fourier transforms [166]. On the other hand, time-domain analysis refers to variation of the data in time and focuses on the autocorrelation function (ACF) (see detail in Section 4.1.3). According to the *Wiener-Khinchin theorem*, the Fourier transformation of the ACF is the PSD and conversely, the inverse Fourier transformation of the PSD is the ACF [167]. For the form of our data discussed in this chapter, frequency-domain analysis is not useful [1] and only time-domain analysis is used to characterised the data.

In the following sections, the relevant analysis methods used in neuroscience and analysis of temporal signals of PNN devices are described. For a detailed understanding of time series analysis and its applications, the literature [163–165] should be consulted.

4.1.1 Methodology in Neuroscience and Event-trains

This section briefly describes neuronal signal recording, the data analysis techniques and then explains how the relevant neuroscience methodology is utilised for the experimental data analysis.

Neurons in the brain fire signals to communicate with other neurons. When the neurons fire, this signal is recorded as a change of electrical potential, called an *action potential* or *spike*. These action potentials propagate from the cell body of a neuron through the axon

[1] The analysed data is binary sequence of 0s and 1s, leading to artefact in a PSD slope.

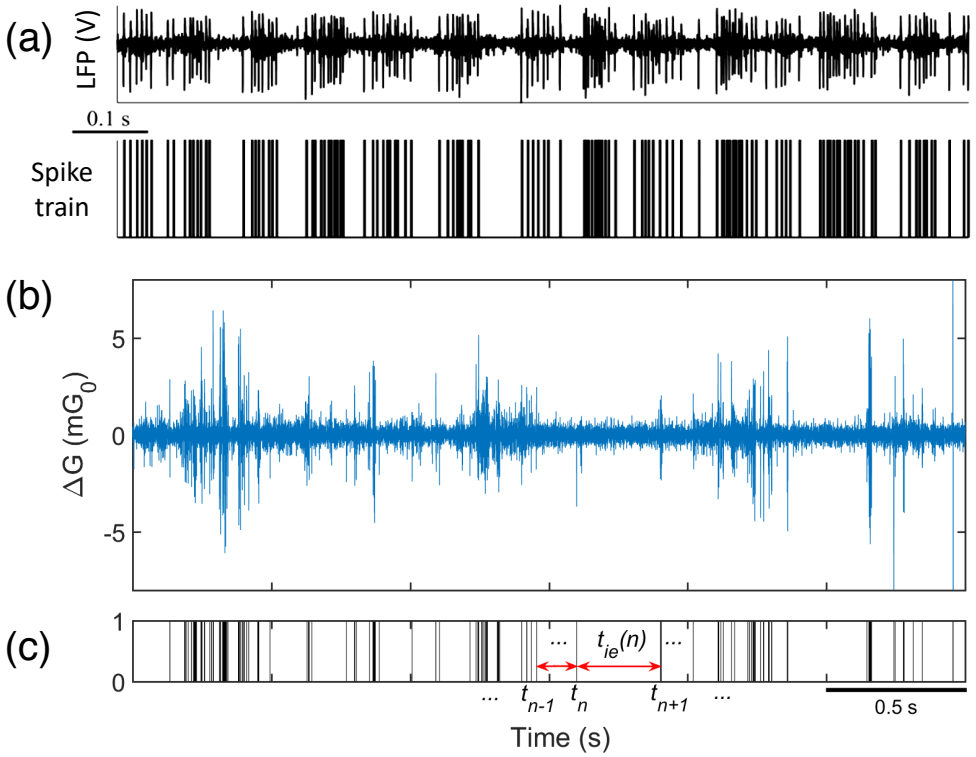

Fig. 4.1. Comparison between a typical neuronal signal recorded in brain (adapted from [168]) and the switching activity in our device (B189(R03), 200 μs sampling, V = 5 V). (a) The signal of action potentials (LFP: local field potential) observed as changes of voltages (upper figure) is converted into a *spike-train* (lower figure) by using a threshold to distinguish the spikes from the noise (see Section 4.3.1). (b) The signal in the network activity represented by ΔG which is qualitatively similar to the neuronal recording in (a). (c) An event-train where occurrence of an "event" is assigned a value 1 whereas "no-event" is assigned value 0. The events are detected using detection thresholds (see Section 4.3).

to synapses and hence to the next neuron (also see Section 1.1.1). Fig. 4.1(a: top) shows an example of a record of action potentials in a brain.

A popular method to analyse the neuronal signals is to digitise the action potentials and generate a binary sequence of 1s and 0s, called a *spike-train* (see an example in Fig. 4.1(a: bottom)), which assigns a value of 1 at the time of a spike and record 0 for no spike. Each spike in the spike-train is detected with the thresholding procedure described in Section 4.3.1.

The use of a spike-train has the advantage of replacing the complex waveform with a simple binary signal. Analysis of the spike-trains is used for understanding spatio-temporal correlations [169, 170], fractal patterns of neuronal firings [171, 172], estimation of entropy and information [173, 174], neural avalanches and criticality [96, 175] as well as neural coding [176, 177].

The switching activity in PNNs is recorded as changes in conductance (ΔG). Fig. 4.1(b) shows the temporal evolution of ΔG which is qualitatively similar to the neuronal signal shown in Fig. 4.1(a: top). The ΔG trace shows the point-to-point changes and removes drift in G. In order to apply the methodology from neuroscience, first, an *event-train* is obtained from the experimental ΔG trace.

The concept of the event-train is the same as that of the spike-train in neuroscience. The event-train assigns a value of 1 at the time when a switching event is detected beyond an event detection threshold (see the detail of the thresholding procedure in Section 4.3 and 4.4). Fig. 4.1(c) shows an example of an experimental event-train and t_n is the time at the n_{th} event. In the following sections, relevant analysis techniques to characterise the temporal dynamics are described.

4.1.2 Inter-event Interval (IEI)

One of the most frequently used measures to quantify the temporal activity is the distribution of *inter-event intervals* (*IEIs*) (often referred to as *inter-spike intervals* (*ISIs*) in neuroscience). The IEI is the time between two consecutive events, which is denoted as $t_{ie}(n) = t_{n+1} - t_n$, where $n = 1, 2, ..., (N_{\text{tot}} - 1)$ (N_{tot}: the total number of events) (see Fig. 4.1(c)). The probability density function (PDF) of the IEI distribution ($P(t_{ie})$) may characterise the process behind the activity and for the binned discrete time series is defined as:

$$P(t_{ie}) = \frac{N(t_{ie})}{N_{\text{tot}} \times W(t_{ie})} \tag{4.1}$$

where $N(t_{ie})$ is the number of counts in a bin represented by t_{ie} with a bin width $W(t_{ie})$. Different binning techniques are described in Section 4.2.1. In general, the PDF must mathematically satisfy the normalisation condition i.e.

$$\int_{x_{\text{min}}}^{x_{\text{max}}} P(x)dx = 1 \quad \text{(Continuous time series)} \tag{4.2}$$

$$\sum_{x=\ x_{\text{min}}}^{x_{\text{max}}} P(x) = 1 \quad \text{(Discrete time series)} \tag{4.3}$$

where x_{min} and x_{max} are the minimum (≥ 0) and maximum of the PDF range, respectively. $P(t_{ie})$ can provide a basic insight for the underlying process behind the events e.g. events

are random (i.e. Poisson process) or non-random (i.e. non-Poisson process).

Fig. 4.2(a-c) shows an example of random event activity obtained from a synthetic data generated from Poisson process [178]. The event-train in (a) shows successive events follow each other with a relatively narrow range of t_{ie} from 0 to 100 (see Fig. 4.2(b)). A characteristic of random events is the *exponential distribution* of $P(t_{ie})$ which results in a straight line on a log-linear plot as shown in (c). The exponential distribution is mathematically denoted as:

$$P(x) = C\exp(-\lambda x) \tag{4.4}$$

where λ is the exponent ($\lambda > 0$) and C is the normalisation constant determined from Eq. (4.2) or (4.3). Exponential IEI distributions describe random processes such as traffic flow patterns and accident frequencies [179] as well as the activity of single neurons [180, 181].

The differences between Poisson processes and non-Poisson processes are striking. While the IEI distributions for Poisson process are exponential, the non-Poisson processes are generally characterised by heavy-tailed IEI distributions. One of the well-known non-Poisson process is a *power-law*. Power-law distributions are mathematically denoted as:

$$P(x) = Cx^{-\gamma} \tag{4.5}$$

where γ is the power-law exponent and C is the normalisation constant satisfying Eq. (4.2) or (4.3). To characterise an experimental IEI distribution a robust fitting procedure is required [182–185]. This is described in Section 4.2.

Power-law distributions of IEIs are often observed in neuroscience [186] as well as in occurrence of earthquakes [187] and human dynamics [178, 188]. Power-law distributed IEIs have gained a lot of attentions as they are believed to be characteristics of *correlation* or *memory* in complex systems [189–191]. The correlations or memory determine the amount of information propagating from the previous states to the future states in the system over time [191]. Power-law IEI distributions are also recognised as a signature of inhomogeneous temporal activity, such as bursts [178, 189–192]. Bursts in neuron firings are described as a "neuronal avalanches" and since their discovery [175], they have been investigated in terms of underlying scale-free dynamics and associated criticality in the brain [95, 96].

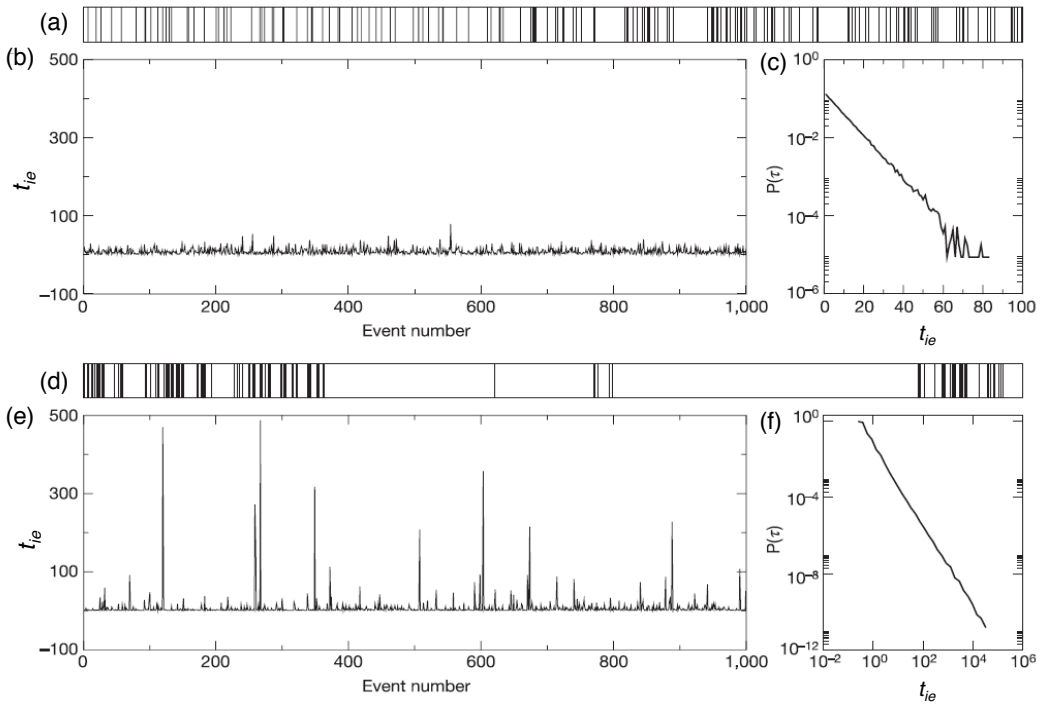

Fig. 4.2. The activity patterns observed in a Poisson process (a-c) and a power-law distribution (adapted from ref.[178]). (a, d) show the event-trains, and (b, e) and (e, f) present IEI values for the first 1000 events and the IEI distributions for all events, respectively. In the Poisson process, the event-train in (a) exhibits consecutive events relatively regular intervals and the obtained IEI values in (b) are within the narrow range. The Poisson process is characterised by the exponential distribution of IEI, resulting in a straight line on a log-linear plot in (c). In contrast, the power-law distributed events in (d) shows highly inhomogeneous pattern containing a few very long IEIs leading to the large spikes in the first 1000 events in (e). The power-law distributed events are characterised by a straight line on log-log plot as shown in (f).

Fig. 4.2(d-f) shows an example of a power-law distributed event activity generated from the stochastic priority list model [178]. The event-train (d) exhibits a highly inhomogeneous pattern and the IEI values (e) have some irregular large values (up to $t_{ie} \sim 500$ for the first 1000 IEIs). The IEI distribution on a log-log scale (f) spans ∼4 orders of magnitude in time and exhibits a straight line with a slope of $\gamma = 2$.

Although the PDF of the IEI distribution can characterise the temporal pattern in the event-trains in terms of a stochastic process as shown in Fig. 4.2, the IEI distribution alone does not give any information about correlations between events [189, 193] (also see Section 4.1.4). In order to obtain information about correlation or memory between events, another measure is required as described in the next section.

4.1.3 Autocorrelation Function (ACF)

Correlations and memory in the time series data (e.g. event-train) are usually characterised by the *autocorrelation function* (*ACF*). In general, the ACF is a measure of the correlation between the original observed signal and a delayed version of the signal, and helps to describe the temporal evolution of the process. For time series data ($y(t)$) with data length N, the ACF is defined as:

$$A(t_d) = \frac{\sum_{n=1}^{N-|d|} (y_n - \bar{y})(y_{n+d} - \bar{y})}{\sum_{n=1}^{N} (y_n - \bar{y})^2} \quad (|d| < N-1) \tag{4.6}$$

where t_d is the delay time and $y_n = y(t_n)$ $(n = 1, ..., N)$. The integer variable d is also known as the *lag* which determines the number of shifted data points between the original and the delayed data. $A(t_d)$ is also called as *lag-d autocorrelation*. $\bar{y}$ is the overall mean value of $y(t)$:

$$\bar{y} = \frac{1}{N} \sum_{n=1}^{N} y_n \tag{4.7}$$

If a signal is random, values of the ACF for $t_d \neq 0$ are expected to be within *confidence intervals* [164, 165], calculated by the standard deviation (95% confidence level) of the ACF for the white noise process. The confidence interval (Δ) for data with length N is denoted as

$$\Delta \sim 0 \pm \frac{1.96}{\sqrt{N}} \tag{4.8}$$

Fig. 4.3(a) shows an example of an ACF for random events generated by `gendata` in Appendix A.1. As anticipated in Eq. (4.8), $\sim$ 95% of points of the ACF (red dots) are within the confidence intervals (blue lines).

Non-random signals are characterised by the *correlation strength* and *correlation range* (also referred to as the *memory range*) of the ACF. The correlation strength is the amplitude of the ACF (often represented by $A(t_1)$ (i.e. *lag-1*) [194–196]) The correlation range is inferred from the slope of the ACF. The correlation ranges are classified into two types i.e. *short-range correlation* and *long-range correlation*. The short range correlation is char-

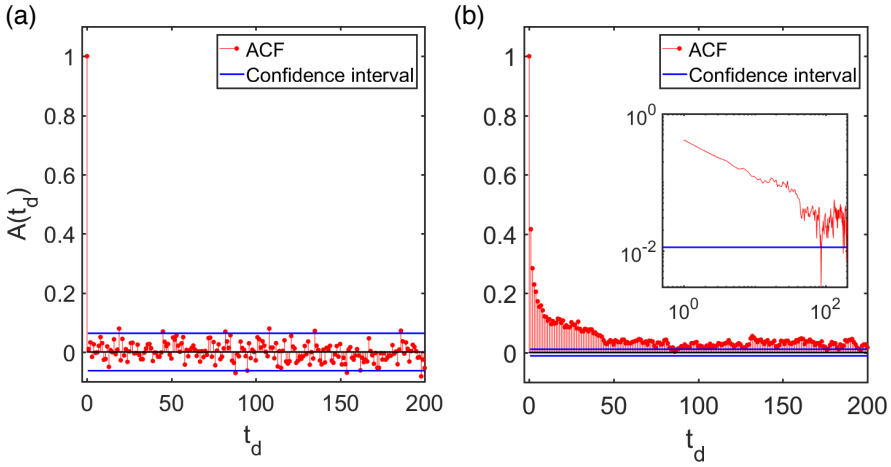

Fig. 4.3. Examples of autocorrelation function (ACF) for different event-trains: (a) random events, (b) a power-law distributed events which has a power-law IEI distribution. These event-trains are generated using `gendata` in Appendix A.1. Random events (a) show ∼95% of ACF values are within the confidence interval (blue lines). The power-law distributed events exhibits a power-law decay of ACF in (b) (also see inset of a log-log plot).

acterised by exponential decay of ACF slopes and the correlation drops to "0" (i.e. within the confidence interval) at a certain time delay [197–199].

Long-range correlation is typically quantified with a power-law-like decay of ACF and indicates a strong correlation in time series data. In neuroscience, *long-range temporal correlations* (*LRTCs*) are associated with learning ability, memory formation and rapid information transfer [83, 200–204]. More details of the mechanism of the LRTC are discussed in Section 4.7. In the next section, details of ACF and LRTC are described from the statistical point of view.

4.1.4 ACF and LRTC

In the previous section, it was explained that the ACF can reveal underlying memory process in time series data. While LRTC has been studied in various research fields [205–208], according to the previous statistical research [189, 193], the power-law slope of the ACF needs to be carefully evaluated, especially when the IEI distribution also follows a power-law.

Statistical studies have revealed that *renewal processes* [209], where power-law distributed IEI values are uncorrelated, exhibit power-law decay of the ACF. Renewal processes [189, 193] satisfy a scaling relationship between the power-law exponent γ in the IEI

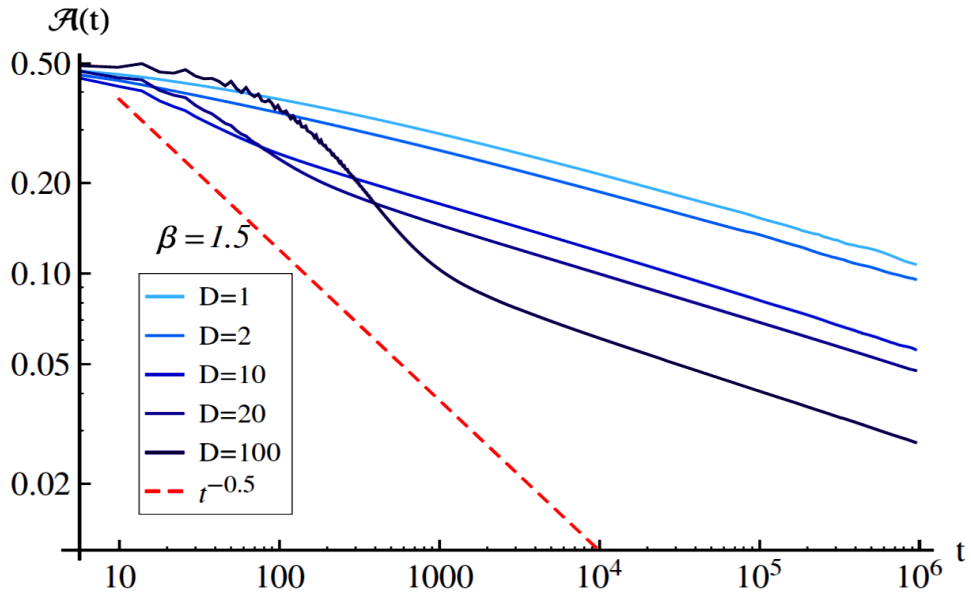

Fig. 4.4. The simulation results of ACF for correlated events in the time series [193]. In this simulation, the parameter D indicates the strength of correlation. The ACF for correlated events shows slow and long time range decay compared to the ACF of the non-correlated IEIs with the power law IEI exponent of 1.5 (dashed line).

distribution and the power-law ACF decay slope (β), which is derived as:

$$\gamma + \beta = 2 \quad \text{for} \quad 1 < \gamma < 2 \tag{4.9}$$

$$\gamma - \beta = 2 \quad \text{for} \quad 2 < \gamma < 3 \tag{4.10}$$

In contrast, when the successive IEIs are correlated, the ACF should exhibit a slower decay with lower exponent ($\beta < |\gamma - 2|$). Fig. 4.4 shows ACFs of correlated signals generated from the simulation model [193] where parameter D determines the strength of correlations, i.e. larger D corresponds to more correlation in the events. The ACF slopes for the correlated IEIs (solid lines) are lower than the slope (dashed line) calculated from the scaling relationship in Eq. (4.9). This slower decay suggests that the data retains correlations for a longer time and is clearly distinguished from the slope in the renewal process. In short, the slower decay of ACF than renewal processes is strong evidence of the existence of LRTC.

Detrended fluctuation analysis (DFA) and PSD In the neuroscience literature, analysis techniques such as detrended fluctuation analysis (DFA) and Fourier transform are also

used to analyse the time series data, especially when the form of the data makes it difficult to obtain reliable ACFs. The DFA is usually applied for detecting self-similarity in the non-stationary data (e.g. electroencephalogram (EEG) signals) and the obtained exponent, called the Hurst exponent (H), indicates the correlation in the time series [83, 200–203]. A value of H in the range of $0.5 < H < 1$ indicates the existence of LRTC in the time series and positive long-range decay in ACF. In contrast, a value of H in the range of $0 < H < 0.5$ indicates an anti-correlation ($A(t_d) < 0$) and in case of $H = 0$, a time series is uncorrelated.

On the other hand, Fourier transforms are used to obtain the PSD of the neuronal oscillation signals (e.g. EEG and magnetoencephalographic (MEG)) and when LRTC exists in the signal, PSD decay as $\sim f^{-\eta}$ [98, 203, 210, 211]. By using the Wiener-Khinchin theorem, it is possible to show that β, H and η are related [99, 188, 212, 213] as:

$$\beta = 2 - 2H = 1 - \eta \tag{4.11}$$

In this work, the quality of the data allows the ACF to be used to investigate correlations in our time series data [189, 193, 214], but Eq. (4.11) allows comparisons with results from other methods.

4.2 Fitting Procedure

The reliability of the fitting function and the fitting procedure is critical to understanding the mechanism of events. Hence, the statistical validation of the possible fitting procedures has been investigated in a great deal of detail [182–185]. This section describes the fitting procedure and methods to evaluate the fitting results using synthetic exponential and power-law distributions. The essential result is that linear regression can be used to fit ACFs, but is not reliable for PDFs, where the maximum likelihood method is required.

4.2.1 Linear Regression

Linear regression (*LR*) is an often used fitting procedure for all kinds of data [84, 178], including PDFs, but in this section it is shown to be problematic in some circumstances. A linear fit is implemented in histograms of PDFs which are generated by binning data with

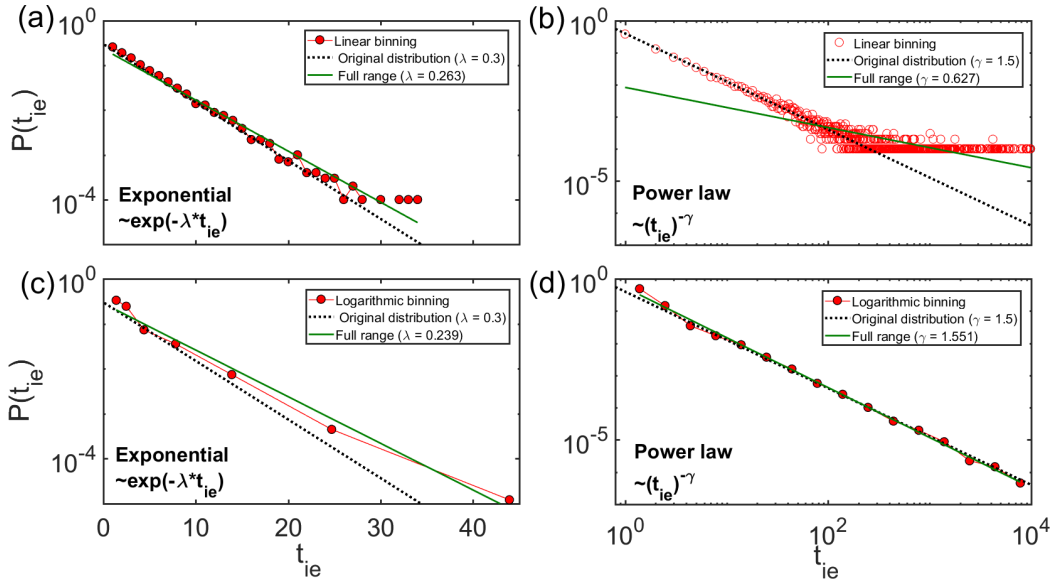

Fig. 4.5. An exponential distribution and a power law distribution with different binning techniques. The ideal fitting exponents here are the ones used to generate the synthetic data. (a) Linearly binned exponential distribution are well aligned on the ideal fitting line except for a few point on the tail. (b) The power-law distribution with linear binning shows a noisy tail due to the poor statistics in counts on the tail of the distribution. (c) The exponential distribution logarithmic binning deviates from the ideal fitting line, but (d) the tail of the power-law distribution can extend while reducing the noise.

bins of width ($W(t_{ie})$). Hence, the binning method and range of data that is fitted can affect the results. This section discusses two different binning techniques by using synthetic data and the results of the fitting procedure.

Linear Binning Linear bins have a constant linear bin width (W_{lin}) at a bin i:

$$W_{lin} = x_{i+1} - x_i$$

where x_i is a value of the i_{th} bin edge. The value of the bin i is represented by the centre of the bin (i.e. $(x_i + x_{i+1})/2$). For the IEI distributions, the linear bin width is determined by the data sampling speed, which means each bin counts the number of occurrences of a unique IEI value.

In order to investigate the effect of binning in the PDF, the synthetic distributions of the exponential and the power-law are generated by `gendata` in Appendix. A.1. The exponents for the synthetic data are $\lambda = 0.3$ for the exponential and $\gamma = 1.5$ for the power-law,

respectively. Fig. 4.5(a, b) shows examples of the linear binning for (a) the exponential distribution and (b) the power-law distribution. The dotted lines in Fig. 4.5 show the ideal fitting line based on the true exponents. In the exponential distribution in (a), the exponent obtained by LR is $\lambda = 0.263$ and the fitting line deviates from the ideal line. This deviation is obviously caused by data points on the tail and 4 points on the tail can be discarded to obtain an exponent close to the true value.

The deviation of data points in the tail becomes a critical issue in the power-law distribution. As shown in Fig. 4.5(b), since many bins in the tail have counts of 1 and there are many empty bins, the tail of the distribution is very noisy and deviates from the theoretical expected line. When linear regression is blindly applied for the full range (green line in Fig. 4.5(b)), the fit is completely wrong.

In order to reduce the noise on the tail and improve the fitting results, especially in a power-law distribution, another binning method is derived, as described below.

Logarithmic Binning In this technique, the bin widths are equally spaced on a logarithmic scale. The size of the i_{th} logarithmic bin ($W_{log}(i)$) is defined as

$$W_{log}(i) = 10^M \left(10^{i/n_{\text{step}}} - 10^{(i-1)/n_{\text{step}}}\right)$$

where 10^M is the minimum value of the bin edge and n_{step} is the number of steps per decade. The centre of bin i is $10^{M+i\times W_i/2}$.

In the logarithmic binning techniques, the bin width increases in the tail of the distribution, leading to more counts for the tail. In the power-law distribution, since the bin sizes vary, histograms of counts with the logarithmic binning have slope $\gamma + 1$ [185] instead of γ in PDFs, i.e. the PDF normalise the biased bin sizes (see Eq. (4.1)).

Fig. 4.5(c, d) shows the logarithmically binned exponential and power-law distribution, respectively. In the power-law distribution, logarithmic binning can dramatically improve the resolution of the tail of the distribution. The power-law exponent in LR is $\gamma = 1.55$, which is improved compared to the linear binning, whereas the exponential distribution in (d) still deviates from the ideal line.

Although logarithmic binning improves the linear regression, especially with regard to

the power-law, the number of bins decreases and the linear fit relies on a limited number of data points, i.e. only 16 points for 4 orders of magnitude in (d). In general, binning may lose information about the distributions of points within the bin [183] and there is dependence on the bin sizes [184]. Also, in logarithmic binning, the weights of the linear fit are not equal for the head and the tail of the distributions, i.e. one observed value on the tail strongly affects the overall fitting result [183].

Therefore, while the binning methods used for visualising histograms of the PDFs, the alternative approach is adopted to estimate the fitting parameters, as introduced in the next section.

4.2.2 Maximum Likelihood Estimation

An alternative estimation of fitting parameters is the *Maximum Likelihood Estimation* (*MLE*) [182–185]. The MLE determines the fitting parameters (α_{MLE}) which maximise the likelihood function for a model probability function $P(x)$ (e.g. an exponential or a power-law with an unknown exponent α). The likelihood function is defined as:

$$L(\alpha) = \prod_{i=1}^{N} P(x_i) \tag{4.12}$$

where x_i $(i = 1, ..., N)$ is i_{th} observed value (e.g. $t_{ie}(i)$) within the considered fitting range between x_{min} and x_{max}. Note that in the likelihood function, observed values x_i is constant values and the parameter α is varied whereas PDFs (e.g. Eq. (4.4) or Eq. (4.5)) focus on changing x with a constant exponent. In other words, MLE finds the parameter condition which more likely observes the values of x_i. In this thesis, following the literature [184, 215, 216], C is calculated for finite fitting range between the minimum (x_{min}) and the maximum (x_{max}) cut-offs (*doubly truncated distributions*). The double truncation takes into account the finite size effects which may originate from sub-sampling [217] and limited measurement duration [216].

In practical calculations, it is more convenient to use the log-likelihood (the natural logarithm of the likelihood function), mathematically given as:

$$l(\alpha) = \ln L(\alpha) = \sum_{i=1}^{N} \ln P(x_i) \tag{4.13}$$

In the log-likelihood function, the product of the probabilities in the likelihood function becomes a sum and the individual components can be maximised. This transformation reduce the amount of calculation, especially when the parameter is analytically obtained with differentiation [183, 184] while the maximum of the likelihood and log-likelihood coincide. The log-likelihood of an exponential distribution with an exponent of λ in Eq. (4.4) is:

$$l(\lambda) = N \ln C - \lambda \sum_{i=1}^{N} x_i \tag{4.14}$$

and for a power-law distribution with an exponent of γ in Eq. (4.5) it is written as:

$$l(\gamma) = N \ln C - \gamma \sum_{i=1}^{N} \ln(x_i) \tag{4.15}$$

where C in both cases is determined from the normalisation condition in Eq. (4.2) or Eq. (4.3) (see Table 4.1 at the end of Section 4.2.3).

While in continuous data, the maximum value in log-likelihood is analytically derived (see Table 4.1), in discrete data, the parameters cannot be calculated analytically and need to be implemented with numerical maximisation of the log-likelihood functions for each model (see Table 4.1). In this thesis, MATLAB codes (`plmle` and `exmle` in Appendix A.1) are used to estimate the parameters. For mathematically generated distributions shown in Fig. 4.5, MLE gave the values of $\lambda_{\text{MLE}} = 0.301$ and $\gamma_{\text{MLE}} = 1.500$ for the exponential and the power-law, respectively. These estimations were made for the full range of distributions and the exponents match the true exponents ($\lambda = 0.3$ and $\gamma = 1.5$) in Fig. 4.5.

MLE has been shown to provide unbiased fitting exponents [183]. However, for all empirical data, MLE always yields parameters for the hypothesised model distribution regardless of the validity of the fitting parameters. Therefore, determining the goodness-of-fit for the estimated parameters is necessary, as described in the next section.

4.2.3 Goodness-of-Fit Test and Kolmogorov-Smirnov (KS) Test

The goodness-of-fit test used along with MLE is the *Kolmogorov-Smirnov* (*KS*) test [182, 183, 218, 219], which is based on the calculation of a measure called *KS distance* (d_e). The KS distance is simply the maximum distance between the complimentary cumulative

distribution function (CDF) of the theoretical distribution ($S_o(x)$) and the empirical one ($S_e(x)$), and is denoted as:

$$d_e = \max |S_o(x) - S_e(x)| \quad (x_{\min} \leq x \leq x_{\max}) \tag{4.16}$$

where $x_{\min} \leq x \leq x_{\max}$ is the data range of the considered function. $S(x)$ is defined as:

$$S(x) = 1 - \int_{x_{\min}}^{x} P(x')dx' \quad \text{(Continuous time series)} \tag{4.17}$$

$$S(x) = 1 - \sum_{x'=x_{\min}}^{x} P(x') \quad \text{(Discrete time series)} \tag{4.18}$$

where $P(x)$ is the PDF of either synthetic data or experimental data. Some representative theoretical CDFs are given in Table. 4.1 [183–185, 220].

The KS distance in Eq. (4.16) indicates how much the empirical CDF deviates from the theoretical CDF and is an indicator of goodness-of-fit, i.e. small d_e means a "good" fit, whereas large d_e means a "bad" fit. A statistical test is required to determine the probability (p-value) that the KS distance for the fit has a value larger than the one obtained empirically. The p-value can be calculated from the theoretical formula, but since this analytical solution can overestimate the p-value, an alternative approach based on synthetic data is used in this thesis [184, 215].

Hence, the p-value is estimated by comparing the experimental d_e with the synthetic d_e obtained from randomly drawn model distributions (`gendata` in Appendix A.1):

$$p = \text{Prob}[\text{ experimental } d_e > \text{the synthetic } d_e \text{ }] \tag{4.19}$$

The p-value depends on the number of the generated distributions (500 distributions in this thesis).

The significance value (p_s) which determines the probability to reject the hypothesised model. p_s is a value between 0 and 1 and in this thesis the p_s is set to be the relatively stringent value of 0.2 [183, 184, 215, 221]. When the $p > p_s$, the KS test fails to reject the hypothesis (i.e. the hypothesis passes the KS test). Conversely, if $p < p_s$, the KS test rejects the hypothesis (i.e. the hypothesis fails the KS test).

While MLE and the KS test are stronger statistical tools to estimate and validate the parameters for the single hypothesised model, they do not prove that the hypothesis is the best of the possible models. The next section introduces a statistical method to compare likelihoods among candidates of the fitting models.

	Distribution	Range	C	MLE parameters	CDF $S(x)$
(a)	Continuous Power-law $Cx^{-\gamma}$ (Non-truncated)	$x_{\min} < x < \infty$	$\frac{(\gamma-1)}{x_{\min}^{\gamma-1}}$	$\gamma_{\text{MLE}} = 1 + N\left(\sum_{i=1}^{N} \ln \frac{x_i}{x_{\min}}\right)^{-1}$	$\frac{-x^{1-\gamma}}{x_{\min}}$
(b)	Continuous Power-law $Cx^{-\gamma}$ (Truncated)	$x_{\min} < x < x_{\max}$	$\frac{(\gamma-1)}{x_{\min}^{\gamma-1} - x_{\max}^{\gamma-1}}$	Numerical analysis for γ_{MLE} in $l(\gamma)$: $\frac{1}{\gamma-1} + \frac{x_{\max}^{1-\gamma}\ln(x_{\max}) - x_{\min}^{1-\gamma}\ln(x_{\min})}{x_{\max}^{1-\gamma} - x_{\min}^{1-\gamma}}$	$\frac{x_{\max}^{1-\gamma} - x^{1-\gamma}}{x_{\max}^{1-\gamma} - x_{\min}^{1-\gamma}}$
(c)	Discrete Power-law $Cx^{-\gamma}$ (Non-truncated)	$x = x_{\min}, x_{\min}+1, ..., \infty$	$\frac{1}{\zeta(\gamma, x_{\min})}$	Numerical analysis for γ_{MLE} in $l(\gamma)$: $-\ln(\zeta(\gamma, x_{\min})) - \frac{\gamma}{N}\sum_{i=1}^{N}\ln(x_i)$	$1 - \frac{\zeta(\gamma, x)}{\zeta(\gamma, x_{\min})}$
(d)	Discrete Power-law $Cx^{-\gamma}$ (Truncated)	$x = x_{\min}, x_{\min}+1, ..., x_{\max}$	$\frac{1}{\zeta(\gamma, x_{\min}, x_{\max})}$	Numerical analysis for γ_{MLE} in $l(\gamma)$: $-\ln[\zeta(\gamma, x_{\min}, x_{\max})] - \frac{\gamma}{N}\sum_{i=1}^{N}\ln(x_i)$	$1 - \frac{\zeta(\gamma, x)}{\zeta(\gamma, x_{\min}, x_{\max})}$
(e)	Continuous Exponential $C\exp(-\lambda x)$ (Non-truncated)	$x_{\min} < x < \infty$	$\lambda\exp(\lambda x_{\min})$	$\lambda_{\text{MLE}} = N\left(\sum_{i=1}^{N}(x_i - x_{\min})\right)^{-1}$	$\exp[-\lambda(x - x_{\min})]$
(f)	Discrete Exponential $C\exp(-\lambda x)$ (Non-truncated)	$x = x_{\min}, x_{\min}+1, ..., \infty$	$\frac{1-\exp(-\lambda)}{\exp(-\lambda x_{\min})}$	Numerical analysis for λ_{MLE} in $l(\lambda)$ $\ln\left(\frac{\exp(-\lambda x_{\min})}{1-\exp(-\lambda)}\right) - \frac{\lambda}{N}\sum_{i=1}^{N} x_i$	$\frac{\exp(-\lambda x) - \exp(-\lambda x_{\min})}{\exp(-\lambda) - 1}$

Note: $\zeta(\gamma, x) = \sum_{i=1}^{N} \frac{1}{(i+x)^{\gamma}}$ is the Hurwitz zeta function and $\zeta(\gamma, x_{\min}, x_{\max}) = \zeta(\gamma, x_{\min}) - \zeta(\gamma, x_{\max})$.

Table 4.1: A list of the parameters used in MLE and the KS test for the power-law and the exponential distribution [183–185, 220].

4.2.4 Fitting Model Comparison

In order to compare models, an *information criterion* (I) is often used. The general definition of I for a model is:

$$I = -2l(\alpha_i) + K_p \tag{4.20}$$

where $l(\alpha_i)$ is the maximum log-likelihood with MLE parameter α_i in the model and K_p is a penalty for the number of parameters (K_i). The term -2$l(\alpha_i)$ is known in the information theory as the deviance [222] and the term K_p compensates the advantage for having more parameters leading to a higher likelihood [222, 223].

The two commonly used criteria are *Akaike information criterion* (*AIC*) [222–224] and *Bayesian information criterion* (*BIC*) [223, 225–227]. While they originate from quite different theoretical frameworks, both equations are in the form of Eq. (4.20). The difference between these criteria is only the penalty values in Eq. (4.20). In the AIC, the penalty value is $K_p = 2K_i$ and the factor of 2 is fixed. On the other hand, the BIC has a penalty value of $K_p = \ln(N)K_i$ (N: the number of data points), leading to a larger penalty for models with more free parameters than the AIC when $N > e^2 (\sim 7)$. In short, compared to the AIC, the BIC favours a simpler model with fewer parameters.

The calculated information criterion for each model can be converted to a *weight* (w_i) (termed as *Akaike weight* in the AIC and *Schwartz weight* in the BIC) defined as

$$w_i = \frac{\exp[-(I_i - I_{\min})/2]}{\sum_{j=1}^{M} \exp[-(I_j - I_{\min})/2]} \tag{4.21}$$

where $I_{\min}$ is the smallest I among the candidate models (I_i ($i = 1, ..., M$)). The weights provide the probability that each model is the best among the candidates.

Along with the MLE and the KS test, the information criterion statistically supports the reliability of the fitting model. However, it is very important to note that there must be an underlying generative mechanism behind the hypothesised model. According to the literature [216, 228], the time series data always comes from a underlying generative process. If there is a hypothesis which describes the specific mechanism generating the data, the hypothesised model distribution should be considered as a candidate distribution. If there

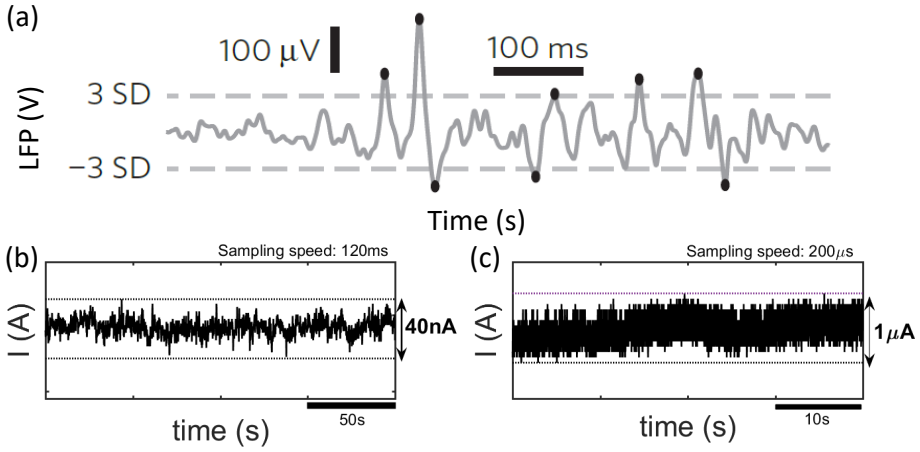

Fig. 4.6. (a) Event detection threshold by using the standard deviation of the noise in neuronal signal (LFP: local field potential measured with multiple electrode array) (adapted from ref.[229]). Only the peak above the threshold (grey dashed line: 3SD = $3\sigma_{\text{noise}}$) are detected as events (black dots) and used in the analysis. Typical electrical current noise in our experiments is measured in ordinary resistors (5 kΩ ∼ $2.6G_0$ as an example in (b, c)) at (b) 120 ms "slow" sampling and (c) 200 μs "fast" sampling. The conservative estimates of noise amplitudes are 40 nA and 1 μA in the current which are equivalent to ∼$0.1mG_0$ and ∼ $2.6mG_0$ in device conductance at V= 5 V for slow and fast sampling speeds, respectively. The current noise amplitudes are consistent for different resistances and voltages.

is no such hypothesis and the estimated fitting parameter do not have physical meanings, new physical insights cannot be gained and the underlying process cannot be explained even though another distribution can "perfectly" fit on the experimental data. In the model selection, not only the statistical support for the fitting but also the physical generative mechanism for the time series data must be considered.

4.3 Event Detection

Any data structure includes noise, and thresholding is required to distinguish real switching events from noise. The pulsed voltage measurements discussed in Chapter 3 present difficulties for event detection due to the low signal-to-noise (S/N) ratio during the off-pulses and at pulse edges. The DC voltage measurements described in this chapter do not have those problems and permit lower detection threshold values and more straightforward detection of switching events. This section reconsiders thresholding for the time series analysis.

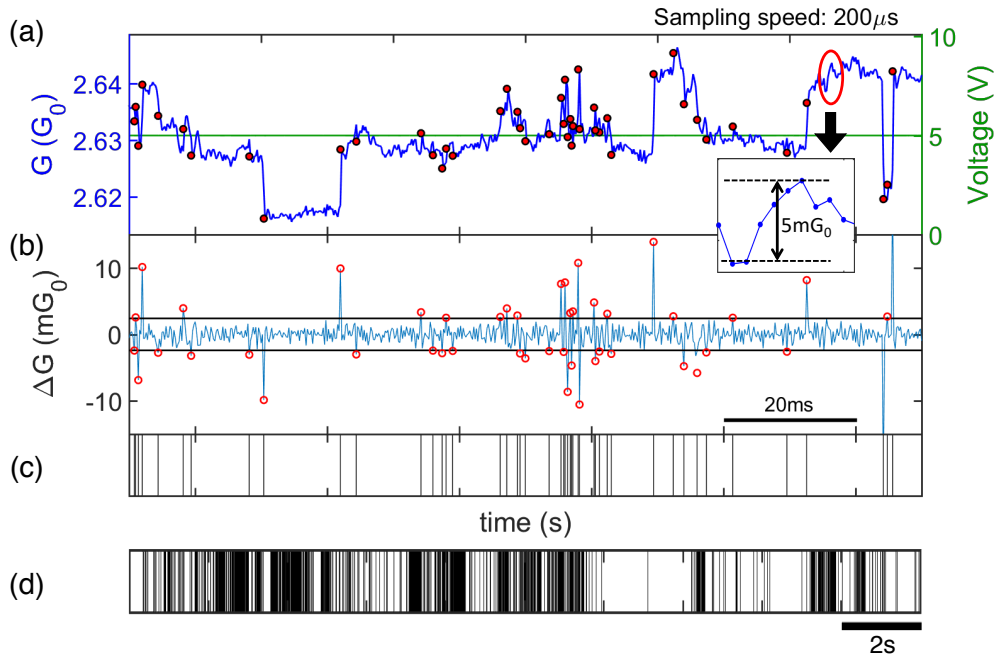

Fig. 4.7. Typical results of event detection for 200 μs fast sampling data with $|\Delta G|_{\text{noise}} = 2.6\text{mG}_0$ (B189(R03), V = 5 V). Switching events (red markers) are shown as either clear discrete steps of device conductance (G) in (a) or big spikes in changes of G (ΔG) in (b). Inset in (a) shows an example of the "discrete" change consisting of multiple steps smaller than the threshold value. This kind of the change cannot be detected. The obtained event-train for the same data segment of (a, b) is shown in (c). (d) the event-train for longer time window (20 s) exhibit "burst" activity in the switching events.

4.3.1 Measurement Noise-floor and Threshold

Thresholding is an important step in the analysis of the time series data. In neuroscience, detection thresholds are used to detect spikes in records of action potentials and to generate spike-trains, as shown in Fig. 4.1(a). One of the well-known methods to determine threshold values in neuronal signals is to use the standard deviation of the signal noise (σ_{noise}) [230]. The threshold value is usually set to be as $k * \sigma_{\text{noise}}$ where k is an integer chosen according to the S/N ratio [229, 230] (see an example in Fig. 4.6(a)). This method allows automation of thresholding for spike detection and corresponding analysis, but is valid only when the number of spikes is a small fraction of the number of measurement points [230].

In order to implement thresholding for event detection in our neuromorphic devices, the noise-floor in our system is determined by measuring ordinary resistors. By comparing data for different voltages, it was found that the electrical current is the dominant source of the noise. As shown in Fig. 4.6(b, c), the noise amplitudes depend on the sampling speeds

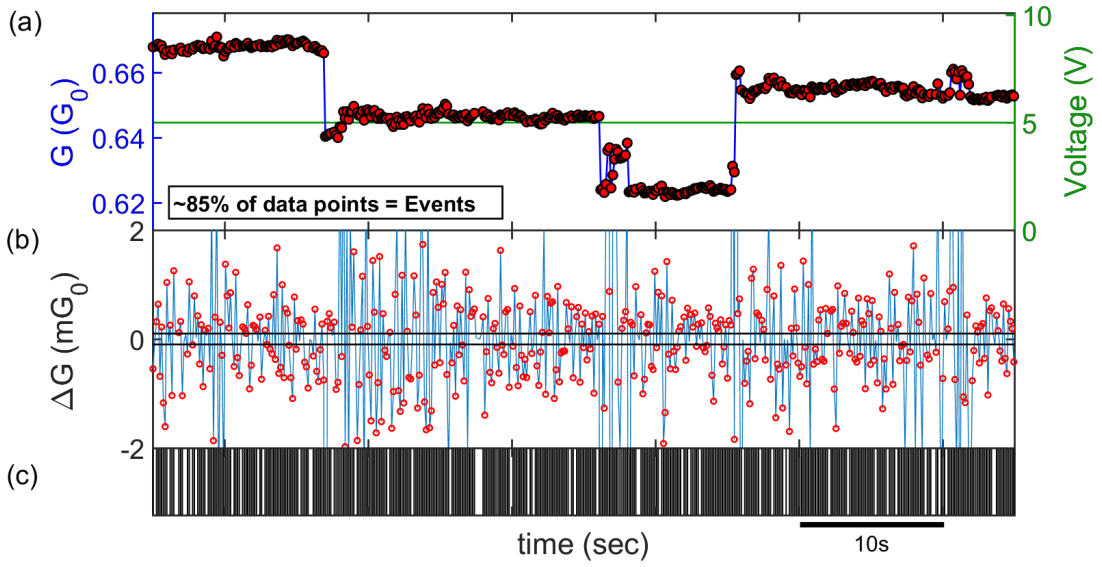

Fig. 4.8. A typical result of the event detection in slow measurement at the noise-floor ($|\Delta G|_{\text{noise}}$). (a) G and (b) ΔG are obtained in the device B189(R04) (120 ms, V = 5 V). The detected events above $|\Delta G|_{\text{noise}}$ ($\sim 0.1\text{mG}_0$) are shown with red markers and the obtained event-train is shown in (c). At the noise-floor, 85% of the data points are assigned as "event" and the event-train in (c) shows the saturation due to inadequate time resolution of 120 ms sampling speed. This saturated event-train obviously cannot characterize the temporal activity and is not used for the analysis.

and conservative estimates of the noise-floor in the current are 40 nA at 120 ms "slow" sampling speed and 1 μA at 200 μs "fast" sampling speed.

Since the noise amplitude is consistent across the measurements for normal range of conductance (0.5G_0 – 3G_0) and applied voltages (up to 10 V), the current noise represents the measurement noise-floor for each sampling speed. The noise in conductance (G) equivalent to the noise in the current of 40 nA and 1 μA are calculated by Eq. (2.1) e.g. for V = 5 V, $\sim 0.1\text{mG}_0$ and $\sim 2.6\text{mG}_0$ at 120 ms and 200μs fast sampling, respectively. All changes in the device conductance ($|\Delta G|$) above the noise-floor ($|\Delta G|_{\text{noise}}$) are a consequence of the network activity and should be recognised as switching events.

Fig. 4.7 shows a typical example of (a) the device conductance (G) and (b) the changes in G (ΔG) at 200 μs fast sampling (V= 5 V) for 120 ms data segments. Switching events detected above $|\Delta G|_{\text{noise}}$ (2.6mG_0, shown as black lines in (b)) are shown with red markers in (a, b) and the obtained event-train is shown in (c). The switching events are well distinguished from the noise and are shown as either discrete changes in G or big "spike" in ΔG. Also, data obtained from the fast sampling exhibits that there are multiple events even within 120ms (= slow sampling speed), which means data obtained from the slow sam-

pling is sub-sampled. Note that some "discrete" changes in G consisting of multiple changes smaller than $|\Delta G|_{\text{thresh}}$ cannot be detected (inset in Fig. 4.7), but these missing events do not affect the analysis (see Section 4.4).

Fig. 4.7(d) shows an overview of the event-train for a much longer data segment (20 s). The event-train is *bursty*, which means that there are different regions where the rate of events is either high or low. This burst activity is quantified in Section 4.3.3 and further details are discussed in Section 4.6 and 4.7.

In slow measurements, thresholding is a critical issue for the analysis. Fig. 4.8 shows a result of event detection with $|\Delta G|_{\text{noise}} = 0.1\text{mG}_0$ at 5 V. As shown in (a) G and (b) ΔG, high fractions of data points (∼85%) are recognised as events, leading to "saturation" in the event-train in (c) whereas fast measurement in Fig. 4.7 recognises only ∼4.7% of data points as events (typically less than 10% across voltages).

The saturated event-train originates from highly sub-sampled data which is measured with inadequate time resolution of 120 ms sampling speed (see Fig. 4.7). Unresolved fast and small events within 120 ms (see Fig. 4.8) induce saturation of the event-train which obviously does not characterise the temporal pattern successfully, i.e. most of "events" are separated by t_{ie} = 120 ms. For this reason, these detected events cannot be used for the time series analysis. In order to avoid the time resolution issue in slow measurements, an alternative threshold value is needed, as introduced in the next section.

4.3.2 Threshold Selection for Slow Sampling

As shown in the previous section, the noise-floor in slow measurements is 25 times lower than that in fast measurements (Fig. 4.6(c, b)), but a high fractions of measured points are recognised as events and the event-train saturates (Fig. 4.8). An alternative method to select the threshold value is introduced below.

1. Generate a multi-barcode plot

A multi-barcode plot is multi-panel plot of event-trains for threshold values which are varied typically from 10mG_0 to 0.5mG_0 (5 times larger than $|\Delta G|_{\text{noise}}$ at 120 ms sampling and V = 5 V). Fig. 4.9 is an example of a multi-barcode plot for the data in Fig. 4.8. Each panel shows events that have a switching size in a range of 1mG_0 (top panel: above 10mG_0, bot-

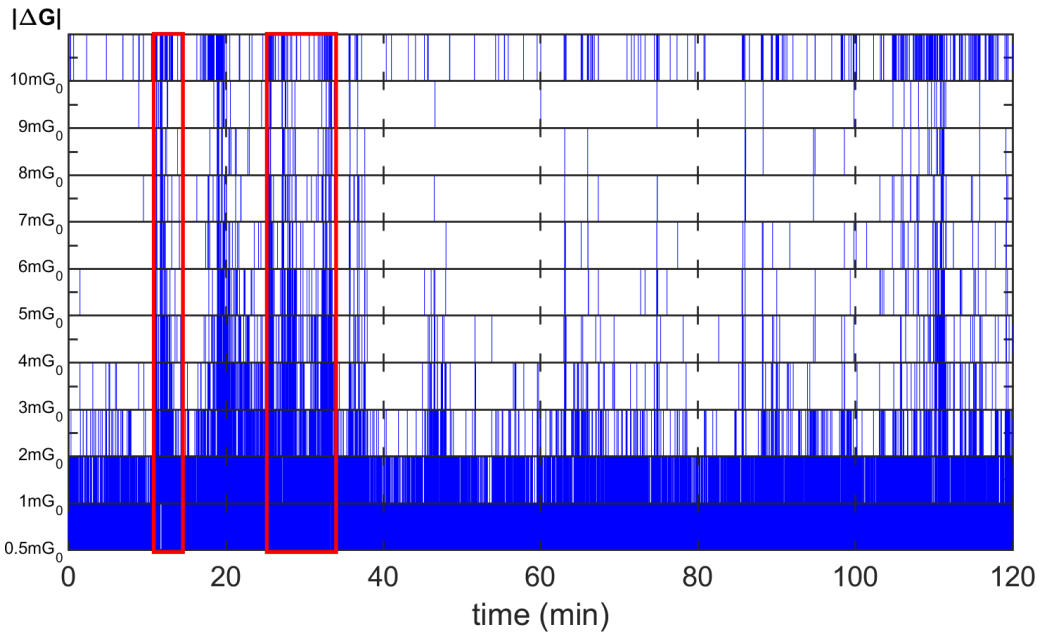

Fig. 4.9. An example of a multi-barcode plot for the same data in Fig. 4.8 (B189(R04), 120 ms sampling, V = 5 V). Threshold values typically vary from 10mG_0 to 0.5mG_0 and each panel shows the events which have a size in a range of 1mG_0 (top panel: above 10mG_0 and bottom panel: 0.5mG_0 to 1mG_0). The event-train below 2mG_0 shows saturation even though 2mG_0 is a 20 times larger threshold value than $|\Delta G|_{\text{noise}} = 0.1\text{mG}_0$. The bigger events above 2mG_0 exhibit *bursty* across $|\Delta G|$ (see red box as an example). The minimum value which can resolve the temporal activity (e.g. bursty activity) is chosen as the alternative threshold value.

tom panel: 0.5mG_0 to 1mG_0), e.g. the third panel from the top is for the switching events with sizes between 8mG_0 and 9mG_0.

2. Define an optimised threshold $|\Delta G|_{\text{thresh}}$

The multi-barcode plot reveals the network activity is bursty, similar to the event-train in fast sampling data shown in Fig. 4.7(d). Note that in the panels below 10mG_0, switching activity is observed at similar times as in the top panel (see the red box as an example). The switching activity with bursts becomes unclear below 2mG_0 (the 2nd panel from the bottom panel in Fig. 4.9) even though 2mG_0 is ~20 times larger than $|\Delta G|_{\text{noise}} = 0.1\text{mG}_0$ at V = 5V. This unclear pattern is probably induced by saturation of the event-train.

In order to avoid saturation due to small and fast changes in the network, an alternative threshold value ($|\Delta G|_{\text{thresh}}$) is chosen to analyse the time series data at slow sampling ($|\Delta G|_{\text{thresh}} = 2\text{mG}_0$ in the example in Fig. 4.9). In the next section, the validity of the event detection for slow measurement and the reliability of the thresholding procedures are

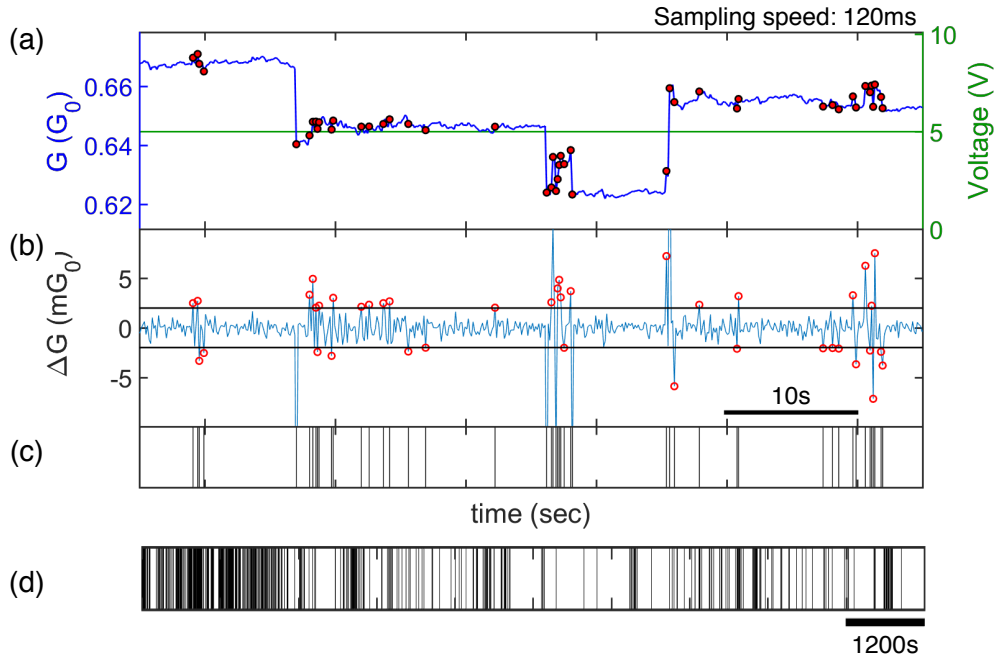

Fig. 4.10. A result of the event detection with an alternative choice of the threshold value and the generated event-train for the data segment in Fig. 4.8 (B189(R04), 120 ms sampling, V = 5 V). Detected events ($|\Delta G|_{\text{thresh}} = 2\text{mG}_0$) are shown as red markers in (a) G and (b) ΔG trace and the event-train is depicted in (c). At this threshold value, only the clear discrete changes in G or big spikes in ΔG are recognised as events and the event-train does not saturate. The event-train for 200 min in (d) exhibits the burst of activity similar to the fast sampling data shown in Fig. 4.7(d).

discussed in relation to the IEI distributions.

4.3.3 Results of Event Detection

This section qualitatively and quantitatively describes results of the event detection for data obtained from fast and slow sampling.

In order to qualify the event detection for slow measurement in the previous section, Fig. 4.10(a-c) are obtained for the same data segment in Fig. 4.8. As shown in (a) G and (b) ΔG, this alternative choice of threshold value ($|\Delta G|_{\text{thresh}} = 2\text{mG}_0$) detects significant switching events showing changes in G and ΔG. The event-train in (c) does not show the saturation like in Fig. 4.8(c).

The IEI distribution is used to quantify activity patterns in the event-train in Fig. 4.10(d). Fig. 4.11(a) shows the IEI distributions for the selected threshold (red line: $|\Delta G|_{\text{thresh}} = 2\text{mG}_0$) as well as for larger and smaller threshold values. The IEI distribution for $|\Delta G|_{\text{thresh}} = 2\text{mG}_0$ has a heavy-tail and spans ~4 orders of magnitude in time. The IEI distributions

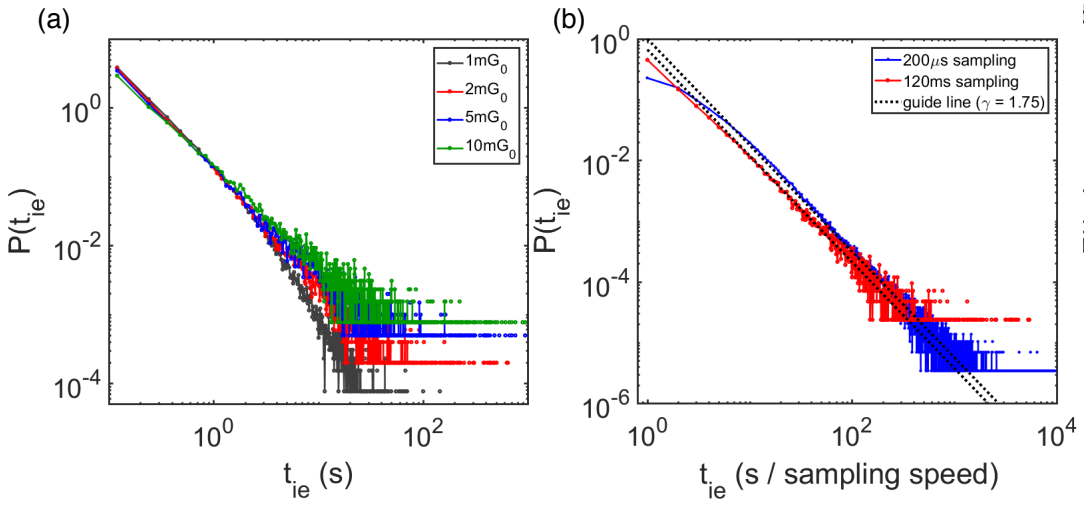

Fig. 4.11. (a) The IEI distributions for threshold values from $1\mathrm{mG}_0$ to $10\mathrm{mG}_0$ in the same data in Fig. 4.9 (B189(R04), 120 ms sampling, V = 5 V). The distribution for $|\Delta G|_{\mathrm{thresh}} = 2\mathrm{mG}_0$ (red) shows heavy-tail and spans ∼4 orders of magnitude in time. The IEI distributions for larger threshold values ($5\mathrm{mG}_0$ (blue) and $10\mathrm{mG}_0$ (green)) does not show significant changes in shapes and time range compared to that of $|\Delta G|_{\mathrm{thresh}} = 2\mathrm{mG}_0$. On the other hand, the threshold value of $1\mathrm{mG}_0$ shows the cut-off on the tail of the distribution. This is caused by the saturation observed in Fig. 4.9. (b) The IEI distributions for two different sampling speeds (blue: 200 μs fast (B189(R03), V = 5 V, $|\Delta G|_{\mathrm{thresh}} = 2.6\mathrm{mG}_0$), red: 120 ms slow (B189(R04), V = 5 V, $|\Delta G|_{\mathrm{thresh}} = 2\mathrm{mG}_0$)) have similar slopes (see the dotted line of the power-law with an exponent of $\gamma = 1.75$) and span ∼4 orders of magnitude in time. (To make comparison easier, t_{ie} is normalised by sampling speeds in (b)). These results infer sub-sampling does not notably change the IEI distribution.

for larger threshold values (blue line: $5\mathrm{mG}_0$ and green line: $10\mathrm{mG}_0$) do not differ significantly from that of $|\Delta G|_{\mathrm{thresh}} = 2\mathrm{mG}_0$ in terms of the shapes and the ranges in time even while the number of events at the threshold value of $2\mathrm{mG}_0$ is ∼4 times higher than at the threshold value of $10\mathrm{mG}_0$. This result is consistent with the fact that the bursty activity is observed at similar time across $|\Delta G|$ (Fig. 4.9). In contrast, the IEI distribution for the threshold of $1\mathrm{mG}_0$ shows the tail dropping away after ∼5 s. The cut-off of the tail can be understood as a consequence of the saturation of the event-train, as shown in Fig. 4.9.

Fig. 4.11(b) compares the IEI distributions between fast sampling (blue) and slow sampling (red) with guide lines (dotted line) showing a power-law (the exponent of $\gamma = 1.75$). The threshold values are $2.6\mathrm{mG}_0$ for fast sampling data and $2\mathrm{mG}_0$ for slow sampling data. Interestingly, the IEI distributions obtained with both sampling speeds have heavy-tails with similar slopes and span ∼4 orders of magnitude in time (t_{ie} is normalised by the sampling

speeds for comparison). Hence, even though 120 ms sampling speed misses a lot of events faster than 120 ms (see Fig. 4.7), the IEI distribution is not affected.

These results infer that sub-sampling does not strongly change the IEI distribution as shown in Fig. 4.11(b) whereas the saturated event-train induce the exponential cut-off in the tail of the IEI distributions. However, the individual atomic switches are known to operate at ∼nano-second or lower time scale [129, 159, 231] and thus even 200 μs sampling speed cannot detect the individual switching event, i.e. fast sampling data is also "sub-sampled". Also, real switching events below the threshold value are missed in both fast and slow sampling speeds. The effect of these missed events from the underlying "true" IEI distribution is still not clear and they are potentially obstacles to characterise the temporal activity in the switching events. In order to investigate the effect of missed events due to small ΔG and sub-sampling in the analysis, the simulation is implemented in the following sections.

4.4 Simulation of Effects of Sub-sampling and Thresholding

In this section, a simulation is used to examine the effect of sub-sampling and thresholding which may discard real switching events from the underlying distributions of IEIs and ΔG.

4.4.1 Construction of Simulated G trace

The simulation is operated with defined synthetic switching events based on our experimental data. Simulated data (i.e. conductance (G_{sim})) is generated from power-law distributed IEIs ($\mathrm{IEI}_{\mathrm{sim}}$) and ΔG (ΔG_{sim}) for 3 million switching events (see Fig. 4.12(a, b)). The power-law distributions represent a typical experimental result (inset in Fig. 4.12(a, b)) and the exponents are set to be 1.8 and 2.3 for IEI and ΔG, respectively. Generated $\mathrm{IEI}_{\mathrm{sim}}$ are discrete (representing the sampling interval in the experiment) and ΔG_{sim} are continuous. The distribution spans 6 orders of magnitude in $\mathrm{IEI}_{\mathrm{sim}}$ and 4 orders in ΔG_{sim} from $0.1\mathrm{mG}_0$ to $1\mathrm{G}_0$. The range of the IEI distribution is set to be wider than that in the experimental distribution to allow a discussion of sub-sampling in the next section. $\mathrm{IEI}_{\mathrm{sim}}$ and ΔG_{sim} are not correlated in the generated data. The signs of ΔG_{sim} values (Up events: positive, Down events: negative) are randomly assigned in this simulation.

To investigate the effects of thresholding and sub-sampling, two models are considered:

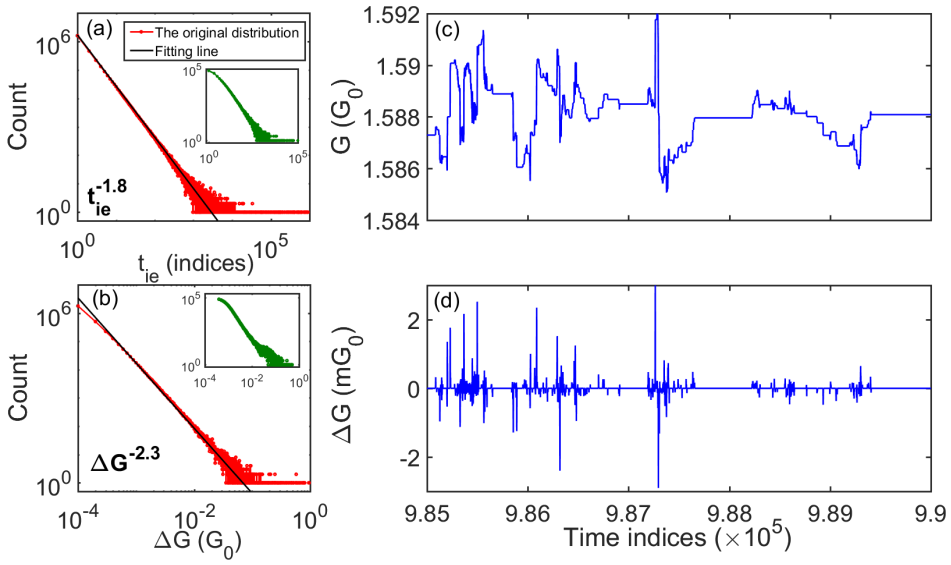

Fig. 4.12. Simulated data (G_{sim}) is constructed from power-law distributed IEIs in (a) and ΔG in (b) with exponents of 1.8 and 2.3, respectively. The power-law distributions represent a typical experimental IEI and ΔG distributions (see inset in (a, b) for B189R04, 120 ms sampling, V = 5 V). Constructed G_{sim} and ΔG_{sim} are shown in (c, d) for model 2. (On this scale, bursty behaviour is not visible and there is no notable difference between model 1 and model 2).

1. Shuffled $\mathrm{IEI}_{\mathrm{sim}}$ + Shuffled ΔG_{sim} (Non-bursty)
2. Correlated $\mathrm{IEI}_{\mathrm{sim}}$ + Shuffled ΔG_{sim} (Bursty)

Bursty activity originates from the correlation among IEIs (also see detail in Section 4.7.2) [189, 191, 214] and these models allow investigation of the effect of underlying bursty activity.

Fig. 4.12(c, d) shows an example of G_{sim} and ΔG_{sim} traces, respectively, for model 2 (On this scale, the bursty are not visible and there is no obvious difference of G_{sim} and ΔG_{sim} between model 1 and model 2). Based on the constructed G_{sim}, the effect of sub-sampling and thresholding is examined in the following sections.

4.4.2 Effects of Sub-sampling

Sub-sampling is implemented in G_{sim} and a new G (G_{sub}) is obtained by collecting every $\mathrm{N}_{\mathrm{sub}}$ points of G_{sim}. Since there is no noise in the simulated data, all non-zero changes in G_{sub} (ΔG_{sub}) are detected as events. Fig. 4.13 shows a typical result of sub-sampling using different $\mathrm{N}_{\mathrm{sub}}$ (= 10 (blue), 100 (green), 500 (light blue) and 1000 (black)) with G_{sim} and ΔG_{sim} (red lines). Obviously, the bigger switching events on G_{sim} are still detected after

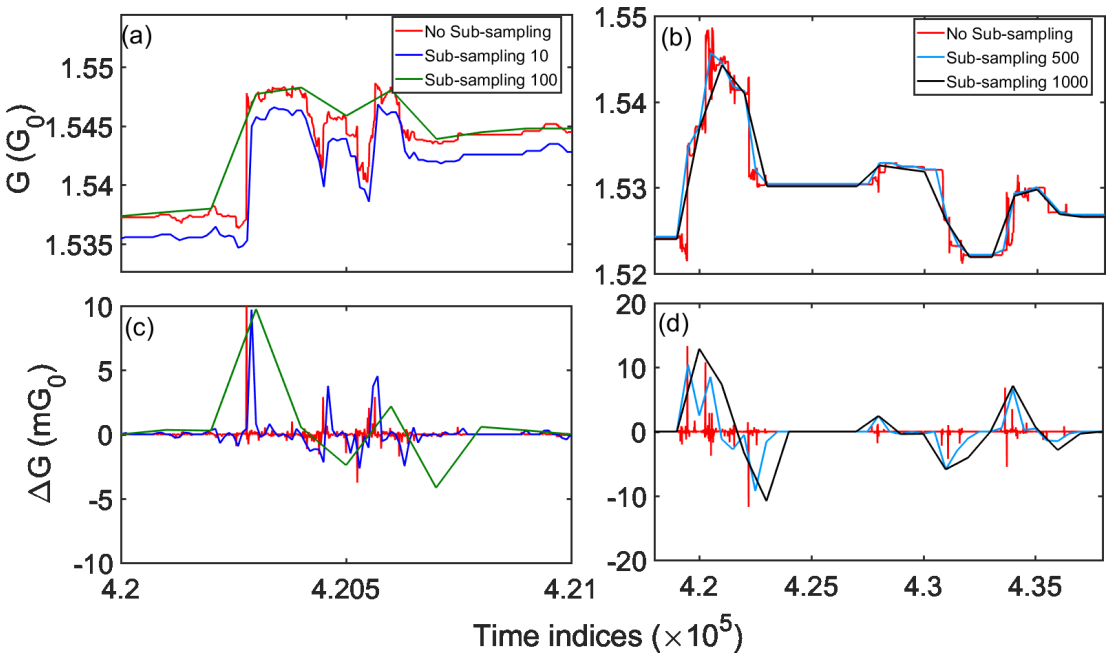

Fig. 4.13. The effect of sub-sampling in (a, b) G_{sim} (red: no sub-sampling) and (c, d) ΔG_{sim} (red: no sub-sampling) in Fig. 4.12(c, d). Sub-sampled G (G_{sub}) and ΔG (ΔG_{sub}) for smaller $\mathrm{N_{sub}}$ (blue: 10, green: 100) are shown in (a, c) and for larger $\mathrm{N_{sub}}$ (light blue: 500, black: 1000) in (b, d). The bigger size of events are still reflected in the conductance and thus even after sub-sampling, these changes can be detected. In contrast, smaller events between sub-sampling points are smoothed out and missed in the event detection.

sub-sampling while many smaller changes originally shown in G_{sim} are not detected on G_{sub}. The number of events after sub-sampling decreases from the original 3 millions to ∼53000 at $\mathrm{N_{sub}} = 500$ in both of models.

From the reconstructed ΔG_{sub} trace, the distribution of IEIs and ΔG are obtained as shown in Fig. 4.14. To make comparison easier, the histograms of counts are plotted instead of PDFs. As shown in Fig. 4.14, apart from the first few points the slope of the IEI distribution does not change for both (a) model 1 (Non-bursty) and (c) model 2 (Bursty). In contrast, the ΔG distributions deviate more strongly for higher $\mathrm{N_{sub}}$ for both of models as depicted in Fig. 4.14(b, d), but the slope of the tail is only strongly affected for very large $\mathrm{N_{sub}}$.

In short, sub-sampling does not affect the slope of the underlying IEI distribution while the ΔG distribution is affected only by higher $\mathrm{N_{sub}}$. The next section examines the effect of thresholding for simulated data before and after sub-sampling.

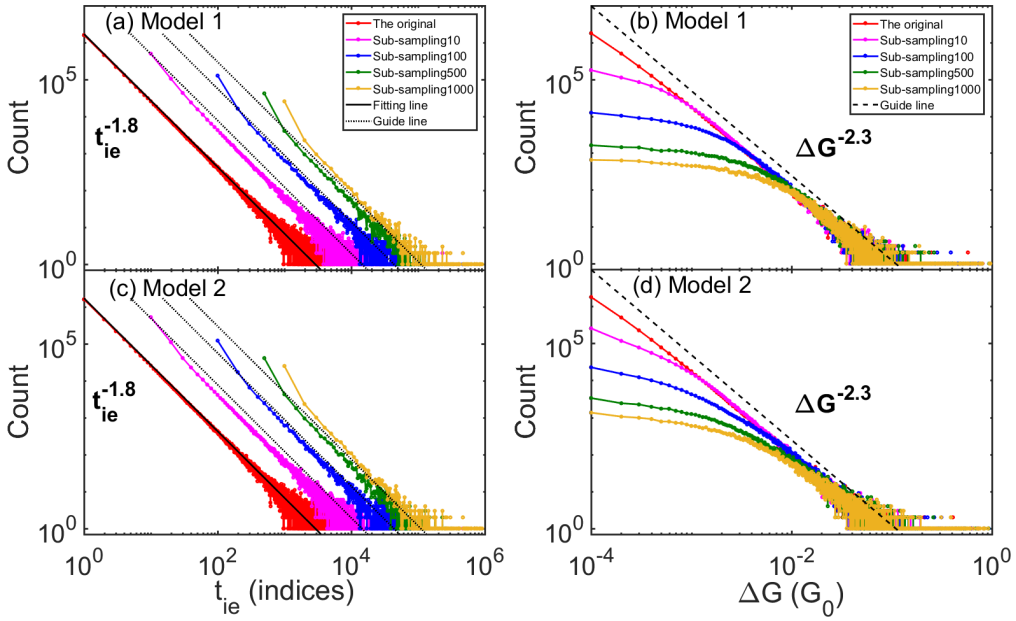

Fig. 4.14. The effect of sub-sampling in distributions of IEI and ΔG for model 1 (a, b) and model 2 (c, d). The solid lines and doted lines follows power-law with exponents of 1.8 for IEI and 2.3 for ΔG. The trend of the IEI distributions do not change before and after sub-sampling for both model 1 and model 2. On the other hand, the ΔG distribution deviates further with increase of N_{sub} while the slope of the tail is only strongly affected for very large N_{sub}. The IEI distributions in (a, c) are horizontally shifted by sub-sampling, depending on N_{sub}.

4.4.3 Effects of Thresholding

Thresholding is now applied to the same simulated data shown in Fig. 4.14. Threshold values are varied from $0.2mG_0$ to $5mG_0$. The number of events at the threshold value of $5mG_0$ is ∼18000 at $N_{sub} = 500$, whereas the original value was 3 millions.

Fig. 4.15 shows the effect of the choice of thresholds on the IEI distributions for each value of N_{sub} and for (a) model 1 and (b) model 2. Note that to make comparison easier for different N_{sub}, the minimum t_{ie} is rescaled to be 1. For higher N_{sub}, the IEI_{sub} distribution is not strongly influenced by the choice of the threshold values. For lower N_{sub}, many smaller events below threshold values are discarded, which means that the temporal activity pattern is changed, leading to a strong change in the IEI distribution. These are consistent in the two different models. The IEI distributions for highly sub-sampled data retain the same slope as the original distribution for all threshold values, regardless of whether the data is bursty or non-bursty. This result indicates that even though our experimental data is sub-sampled, the slopes of the IEI distribution still reflect the underlying IEI distribution

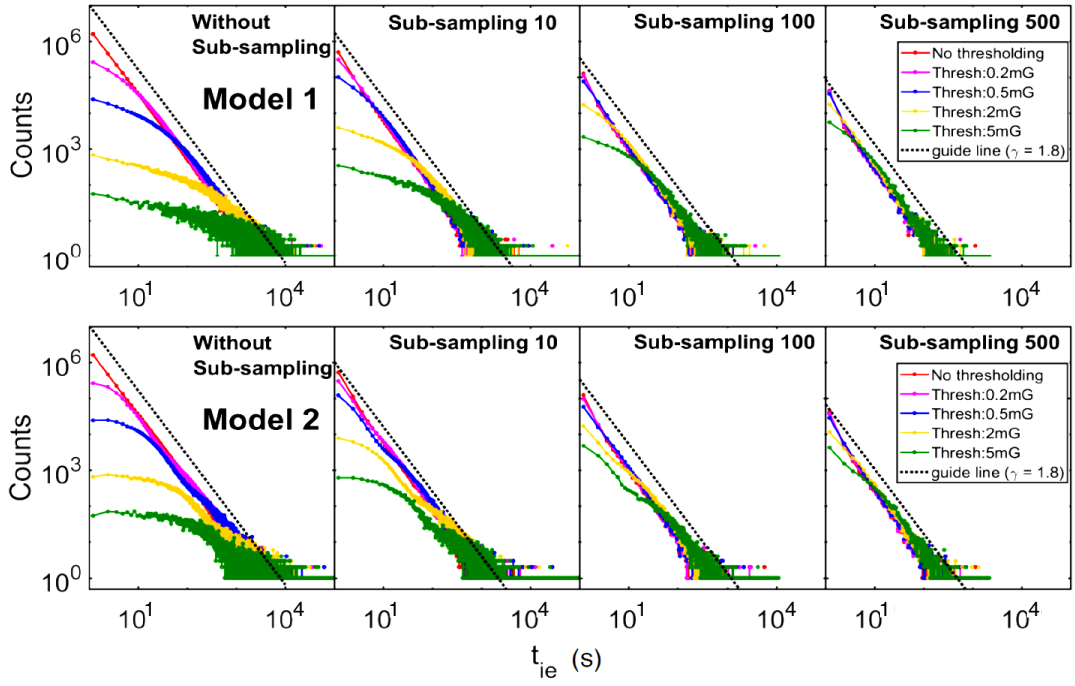

Fig. 4.15. The effect of choice of threshold values before and after sub-sampling for (a) model 1 and (b) model 2. N_{sub} = 1000 cannot be analysed due to the lower number of events and thus only N_{sub} = 10-500 are used. For sub-sampled data with larger N_{sub}, the slopes of the IEI distributions are similar to the underlying slope for different threshold values while the distributions for smaller N_{sub}, the IEI distributions are strongly affected by thresholding. Regardless of the non-bursty (model 1) and the bursty (model 2), the highly sub-sampled data retains the underlying slope of the IEI distribution.

corresponding to the temporal dynamics in our neuromorphic networks.

4.4.4 Summary of Effect of Thresholding

The thresholding procedure for the time series analysis was considered in Section 4.3 and the effect of sub-sampling and thresholding was discussed in Section 4.4 using simulations.

Since the individual switching speed is much faster than the sampling speeds in our experiment, sub-sampling is inevitable even with 200 μs fast sampling. The sub-sampling effect appears in the ΔG distribution, but the slope of the IEI distributions are not affected by the sub-sampling (see Fig. 4.14). In addition, thresholding is necessary to distinguish switching events from the noise and to avoid the saturation of the event-train in slow sampling data. As pointed out in the neuroscience literature [232], picking noise in signals and missing events are trade-offs and the missing events are inevitable. As shown in the exper-

imental results (Fig. 4.11) and the simulation results (Fig. 4.15), the highly sub-sampled data is not strongly affected by the choice of threshold values, and the slopes of the IEI distributions correspond to those of the underlying distribution.

In conclusion, the analysis of the experimental data is not significantly dependent on sub-sampling or thresholding effects while the event-train should not be saturated for the temporal analysis. The following sections describe the detailed analysis of the temporal characteristics of the neuromorphic network dynamics based on the described thresholding procedure. The IEI distributions obtained using optimised threshold values are evaluated in Section 4.6 while the next section describes the switching activity on the underlying network structure.

4.5 Switching Activity and Network Structure

This section describes the switching activity in PNNs on multiple scales in time as well as switching size and investigates the distribution of switching sizes with the numerical simulation for the underlying network structure.

4.5.1 Self-similar Switching Activity

Switching activity in PNNs is recorded as changes in conductance and detected as switching events with the thresholding procedure as discussed in Section 4.3. Fig. 4.16 shows a typical example of the temporal evolution of switching events in ΔG for three different time scales and switching size, i.e. the middle panel and the bottom panel respectively show segments of the top panel (2000 s) with 10 and 100 times, both in temporal and vertical (switching size) scale. The switching activity patterns are not readily distinguishable in three panels, suggesting the existence of a *self-similar* switching activity. Self-similar temporal patterns are observed in electrophysiological signals from the cortex of the human brain [70] and biological physiological measurements such as temporal heartbeat patterns [90] (see Fig. 1.8). These patterns have been discussed in terms of the underlying fractal physical structure.

Fig. 4.17 shows the PDF of the distribution of ΔG obtained with $|\Delta G|_{\text{noise}}$= 0.1mG$_0$. The ΔG distribution does not consider the temporal pattern of the switching events and even in 120 ms slow sampling data, $|\Delta G|_{\text{noise}}$ can be used as the threshold value. However,

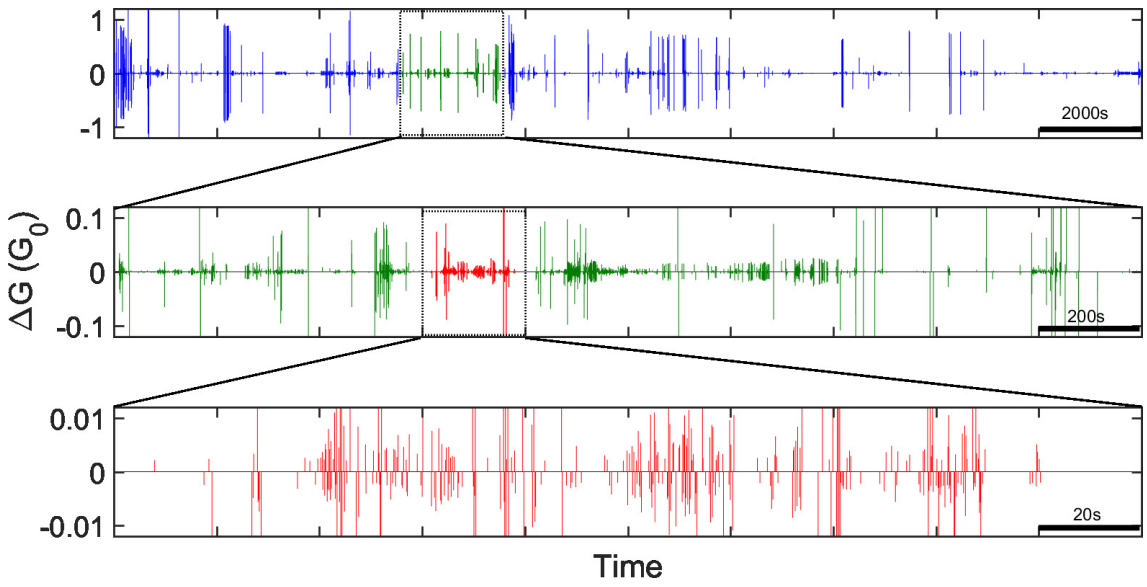

Fig. 4.16. Typical switching activity in multiple time scales (B135R07, 120 ms sampling, V = 7 V, $|\Delta G|_{\text{thresh}} = 2\text{mG}_0$). The top panel shows 2000 s of data and the lower panels present segments of the data with 10 and 100 times greater magnification on temporal and the vertical scale. The activity patterns are not readily distinguishable from each other, indicating *self-similar* network dynamics.

the effect of sub-sampling appears as the roll-off in the small ΔG of the distribution (grey shaded region). The same feature in the ΔG distribution is observed in the sub-sampled simulation data shown in Fig. 4.14.

The ΔG distribution in Fig. 4.17 spans ∼4 orders of magnitude in switching size and exhibits a heavy-tail (dotted line shows a power-law with an exponent of 2.5). The different switching sizes are believed to reflect the configuration of the network and location of the switching sites within the network. While each atomic-scale wire has the same conductance [52], the contribution to the overall conductance can vary over several orders of magnitude. When the switching occurs on "main branches" that have few parallel pathways (the blue branch in the inset in Fig. 4.17), large ΔG are observed (e.g. blue shaded region in Fig. 4.17). Conversely, switches on "higher order branches" which have many parallel pathways (e.g. the red or black branches in the inset) result in small ΔG (pink-grey shaded regions in Fig. 4.17). The similar sizes of the switching events can be the result of either repeated switching at a single site or switching at different sites on the similar order branches. It is important to note that the switching events induce a dynamic change in the network configuration and the switching site can be found on different order branches following the occurrence of a switching event at different sites.

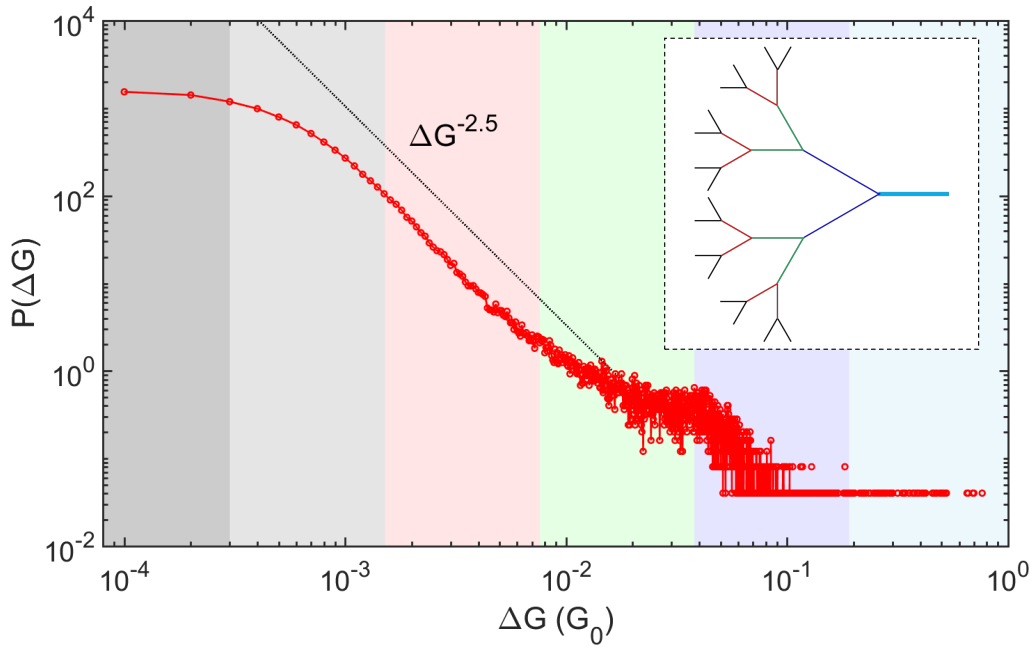

Fig. 4.17. A typical probability density function (PDF) of changes of the device conductance exhibits a heavy-tail (B189R04, 120 ms sampling, V = 5 V, $|\Delta G|_{\text{thresh}} = 0.1\text{mG}_0$). The roll-off in the small ΔG (grey shaded regions) can be understood as the effect of sub-sampling observed in the simulated data in Fig. 4.14. Switching sizes perhaps reflects the locations of the switching sites in the network. The inset shows a schematic illustration of a highly branched fractal network. The larger ΔG (blue shaded region) corresponds to the "main branches" where there are few parallel pathways (e.g. blue branch) whereas smaller ΔG (e.g. pink-grey shaded regions) corresponds to "higher branches" which possess a lot of parallel pathways (red or black branches in the inset).

Although the literature [70, 90] and the experimental results infer that the self-similar temporal activity occurs on the underlying fractal network, the percolating tunnelling networks have been the subject of limited number of studies [79, 80]. The network structure in PNNs is difficult to investigate in the experimental system and thus numerical simulations are used, as explained in the next section.

4.5.2 Network Structure

Numerical simulations have been operated by M. D. Pike at UC and provide valuable insight into the underlying network structure of PNNs. The simulation is based on 2D continuum percolating tunnelling models [79] (see Fig. 1.7(e, f)) and generates the network structures for different surface coverages (p). In this model, the conducting objects (uniform discs) are allowed to overlap and form groups of particles [79, 80] where the particles are considered to be ohmically connected. While the well-established percolation threshold value (p_c) is

0.676336 [76], the primary focus of the surface coverage is $p = 0.65(< p_c)$ to consider the network with tunnelling gaps. Further details of the simulations are described in the literature [79, 80].

Fig. 4.18(a-c) show simulated networks at three different surface coverages, i.e. 0.60 ($<< p_c$), 0.65 ($< p_c$) and 0.67 ($\sim p_c$)). A different colour represents each group of particles. For $p = 0.60$ in (a), only small groups are observed, but for $p = 0.65$ and $p = 0.67$ in (b, c) some groups become large and various sizes of groups are observed. For $p \sim p_c$ in (c), a few huge groups of particles start occupying the network. Fig. 4.18(g) is the post-deposition colourised SEM image of the device (colourisation enhances visualisation of connected groups of particles). The map of groups for the primary focus of $p = 0.65$ in (b) is qualitatively similar to the experimental network showing the groups have various sizes and fractal geometries.

To visualise the network connectivity, maps of connection between different groups of particles are obtained for (a-c) as shown in Fig. 4.18(d-f). The connection maps indicate which groups are connected together via tunnelling gaps. The maps for $p < p_c$ and $p \sim p_c$ exhibit highly inhomogeneous connections, i.e. a few groups of particles have a lot of connections with their neighbours while the maps for $p << p_c$ shows only a small number of connections for each group.

These connection maps are quantified by counting the number of connections from each *node* (group of particles) to other nodes, which is called the *degree* (k) of the node [84, 233]. The degree distribution $P(k)$ is a fundamental characteristic of the network [84, 106, 234]. For lower surface coverage ($p < 0.63$) there are exponential cut-offs in the tail of the distributions. In contrast, near the percolation threshold (0.65 and 0.67) the distributions show heavy-tails and are close to a power-law $P(k) \sim k^{-\varphi}$ with $\varphi \sim 2.5$, indicating that PNNs are scale-free networks [84, 106]. For many complex networks (e.g. biological neuronal network) φ is reported to be between 2.0 and 3.0 [233] and the scale-free networks ensure that there is a small number of heavily-connected nodes which promote global connections across the system [5].

The inset in Fig. 4.18 shows the degree distributions for choice of the network sizes for $p = 0.65$. The primary focus of the board size is 200×200 particle diameters, which is chosen

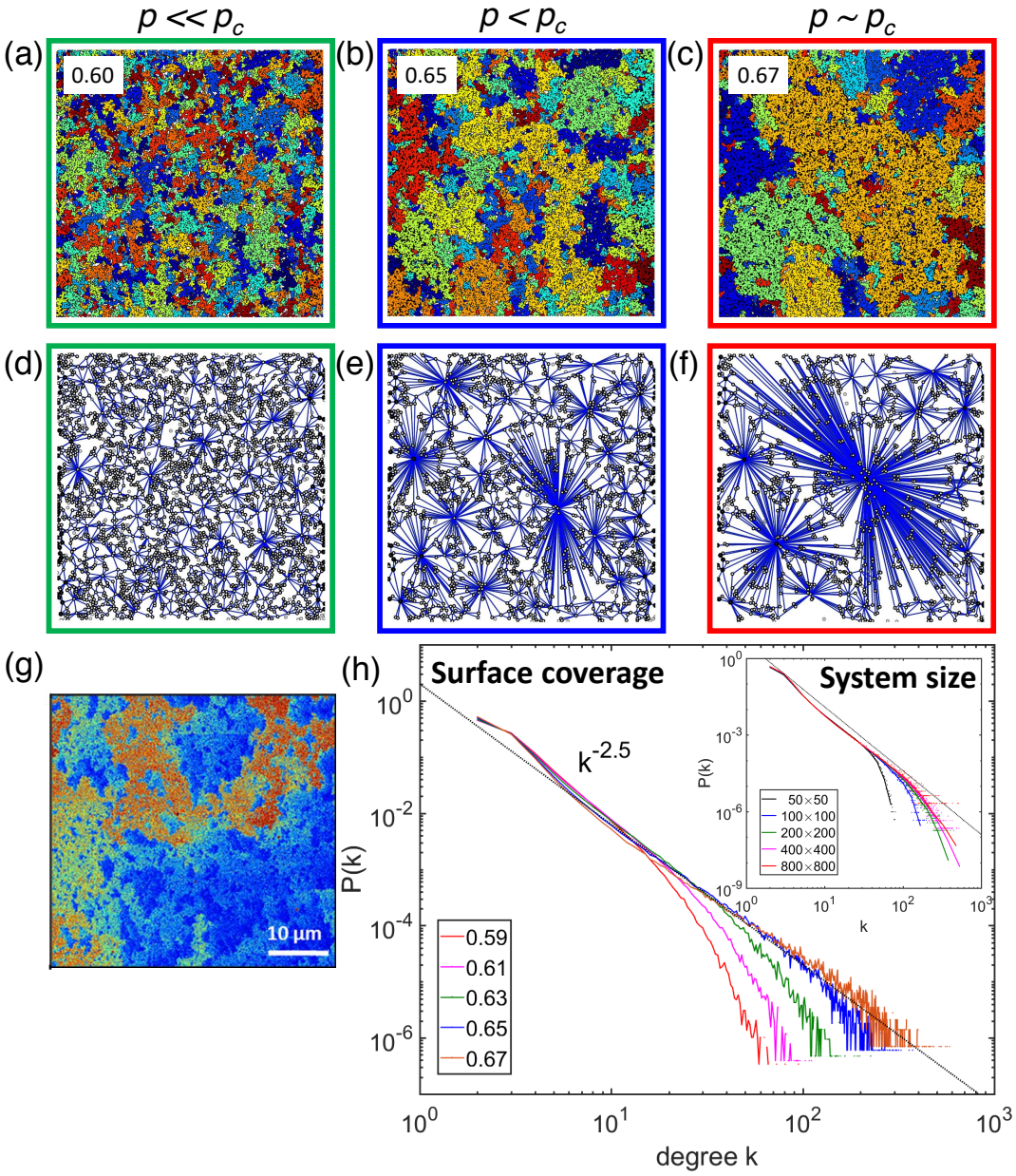

Fig. 4.18. The network structure and the degree distributions obtained from the numerical simulation. (a-c) The simulated networks of 200×200 particle diameters shows groups of particles (represented by different colour) that are separated by tunnel gaps. For $p << p_c$ ($p_c = 0.676336$ [76]) in (a), there are only small sizes of groups, but for $p < p_c$ and $p \sim p_c$, some bigger groups of particles appears. (d-f) Maps of connections between groups are obtained from (a-c). While the maps for $p << p_c$ in (d) shows each group only has a small number of connections, the map for $p < p_c$ and $p \sim p_c$ in (e. f) exhibits a highly inhomogeneous connections i.e. some groups are heavily connected to neighbouring groups. (g) The colourised SEM image of a PNN shows a fractal network topography similar to the simulated network for $p = p_c$ in (b). Colourisation enhances visualisation of the groups of particles. (h) The degree distributions near the percolation threshold (0.65 and 0.67) show heavy-tails close to a power-law $P(k) \sim k^{-\varphi}$ with $\varphi \sim 2.5$, indicating the PNNs are *scale-free network* whereas the distributions for lower surface coverage ($p < 0.63$) have exponential cut-offs. The inset shows the system size dependence of the degree distribution for $p = 0.65$, indicating the degree distributions are not significantly affected by the system sizes above 200×200 particle diameters. (The inset is provided by M. D. Arnold in University of Technology Sydney)

to provide the best trade off between computational time and the finite size effect. As shown in the inset, the system sizes bigger than 200×200, the finite size effect is negligible and it does not affect the exponent φ.

The simulation results suggest that PNNs near the percolation threshold have a scale-free network structure, and that the self-similar switching activity and the heavy-tailed ΔG distribution may originate from the underlying scale-free network structure. Further details of the temporal activity are discussed in the following sections. Note that since the switching dynamics in the simulated network are still under investigation, the temporal switching activity on the network is not available in this work.

4.6 Fits to IEI Distributions

As shown in the previous section, the switching activity exhibits self-similar temporal activity along with bursts. Also, the preliminary plots of the IEI distributions in Fig. 4.11 exhibit heavy-tails consistent with the hypothesis that the IEI distribution is a power-law [70, 189]. This section examines the power-law hypothesis as well as the other heavy-tailed distributions [88, 183, 235].

4.6.1 Power-law

The power-law hypothesis for the IEI distribution is examined by MLE and the KS test described in Section 4.2. Power-law exponents are estimated for various lower ($t_{\min}$) and upper ($t_{\max}$) cut-off values in IEIs and the p-values of the KS test for the data range are calculated. The $t_{\min}$ and $t_{\max}$ allow the data to be truncated [184, 215]. The minimum requirement of the range between $t_{\min}$ and $t_{\max}$ is set to be 2 orders of magnitude in time to avoid a fit for very small subsection of the distribution [228]. Fig. 4.19 shows colour maps of (a) the estimated exponents and (b) the p-values from the KS test for various choices of cut-offs in the IEI distribution for the same data shown in Fig. 4.11(a). As shown in Fig. 4.19(a), the typical range of the exponents is between 1.5 (blue markers) and 2 (green markers) for all selected cut-off values. Areas covered by blue and white markers in (b) suggests the plausibility of the power-law hypothesis (p-value > 0.2) whereas the red markers indicate the data range where the power-law hypothesis is rejected (p-value < 0.2).

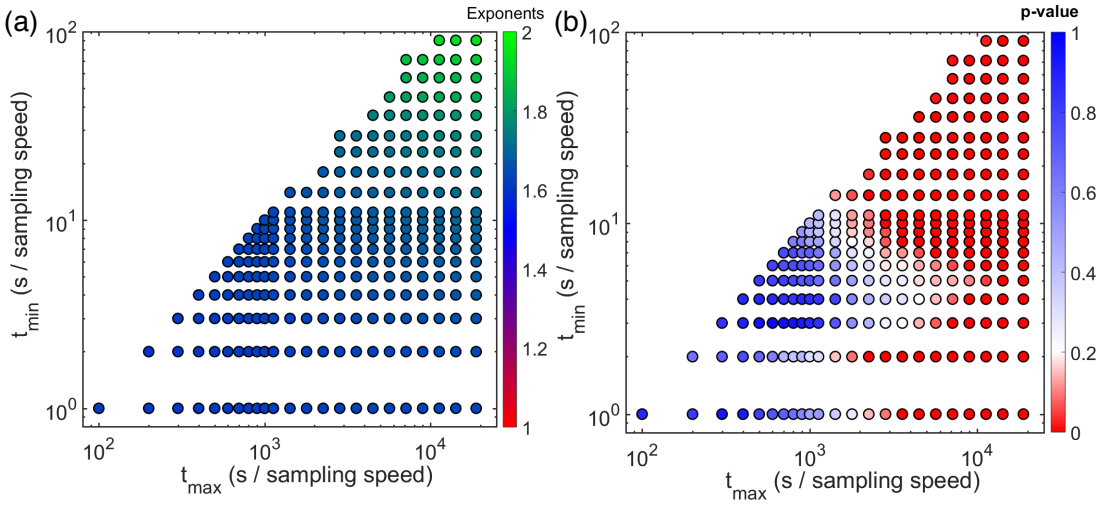

Fig. 4.19. Maps of (a) exponents estimated by MLE and (b) p-values of KS test for various lower (t_{min}) and higher (t_{max}) cut-off values (B189R04, 120 ms sampling, V = 5 V, $|\Delta G|_{\mathrm{thresh}} = 3\mathrm{mG}_0$). t_{min} and t_{max} are scaled by sampling speeds and allow the data to be truncated. The typical exponent range is between 1.5 (blue dots in (a)) and 2 (green dots in (a)) for all selected t_{min} and t_{max}. The obtained exponents are examined by the KS test. The areas covered by blue and white dots suggest plausibility of the power-law hypothesis (p-value > 0.2), while the area covered by red dots indicates the power-law hypothesis is rejected (p-value < 0.2). Although the tail failed the KS test, a wide range of the distributions (> 3 orders of magnitude in this example) could pass the KS test with p-value > 0.2. The widest range of the distribution that could pass the KS test is selected to determine the exponent, as the exponents estimated by MLE does not significantly change with variations of t_{min} and t_{max}, as shown in (a).

Fig. 4.20(a) shows an example of the IEI distribution and the power-law fit (blue line) obtained from the MLE procedure. While the KS test is extremely sensitive to small deviation from a mathematical power-law [183, 184, 215], the experimental data passes the KS test for more than 2 orders of magnitude in time. This is consistent across multiple devices as shown in Fig. 4.20(b) while the exponent values obtained from more devices are shown in Section 4.7.4. Also, the IEI distributions for different choice of threshold value were investigated and all selected threshold values (Fig. 4.20(c)) passed the KS test. Fig. 4.20(d) shows that the estimated exponents are within the typical range between 1.5 and 2 whereas the switching rate for $|\Delta G|_{\mathrm{thresh}} = 2\mathrm{mG}_0$ is more than double of $|\Delta G|_{\mathrm{thresh}} = 5\mathrm{mG}_0$. This shows that the choice of threshold value does not significantly affect the IEI distributions as long as the event-train is not saturated.

To compare with the power-law, the hypothesis that the IEI distribution is exponential is also examined with MLE and the KS test was performed for the same data range as

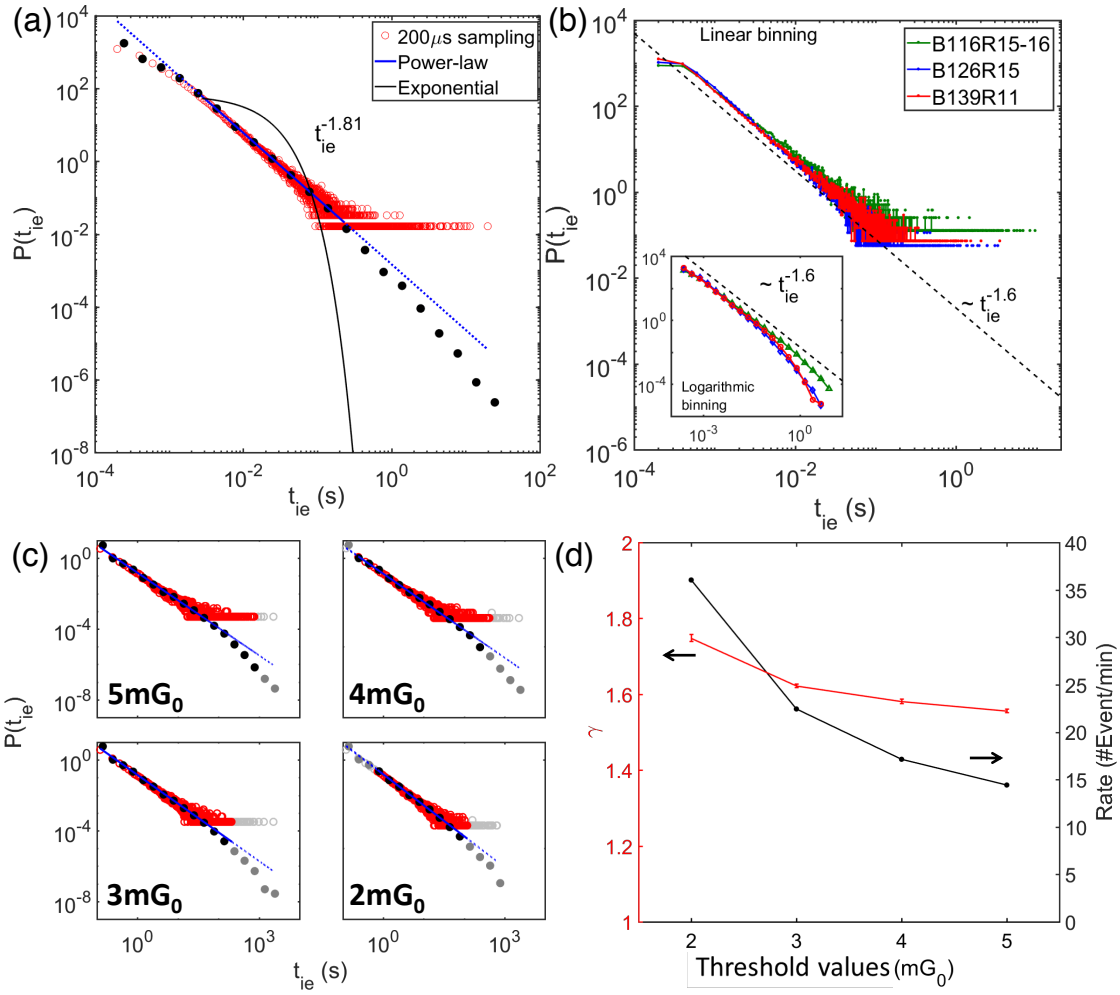

Fig. 4.20. (a) The IEI distribution (B189R03, 200 μs sampling, V = 5 V, $|\Delta G|_{\text{thresh}}$= 2.6mG$_0$) follows a power-law (blue line) with the exponent of 1.81 (p-value of the KS test > 0.2 for more than 2 orders of magnitude in time). Red markers and black markers shows linear binning and logarithmic binning, respectively. The exponential fit (black line) does not match the experimental data and fails the KS test (p-value < 0.01) (b) The power-law distributed IEIs are observed across multiple devices (B116R15-16, B126R15, B139R11) for the identical voltage (V = 6 V), suggesting the power-law IEI distributions are an inherent feature of the switching activity. The dashed line shows a power-law with the averaged exponent of 1.6 while all devices pass the KS test for more than 2 orders of magnitude in time. The inset shows logarithmically binned distribution. (c) Different threshold values (2-5mG$_0$) are used to obtained the IEI distributions of the data shown in Section 4.3.3 (B189R04, 120 ms sampling, V = 5 V). For all of the selected threshold values, the power-law hypothesis is not rejected by the KS test (i.e. p-value > 0.2). As shown in (d), the estimated exponents are within the typical range between 1.5 and 2 across different threshold values even though the switching rate for $|\Delta G|_{\text{thresh}}$ = 2mG$_0$ is twice higher than that for $|\Delta G|_{\text{thresh}}$ = 5mG$_0$.

the power-law. The exponential fit (black line in Fig. 4.20(a)) obviously does not match the experimental data and the hypothesis is rejected with p-value < 0.01. The information criteria (AIC and BIC) discussed in Section 4.2.4 also suggests the preferable model is the

power-law (the weights in AIC and BIC are ∼1 for power-law). In order to confirm the power-law hypothesis, other heavy-tailed distributions are examined in the next section.

4.6.2 Other Heavy-tailed Distributions

The previous section shows the power-law hypothesis passed the KS test for more than 2 orders magnitude in time, but other heavy-tailed distributions should also be considered [88, 183]. In addition, presenting complimentary cumulative density function (CDF) plots with slopes estimated in MLE is considered as the standard in some studies [183, 235, 236]. The CDF plots are sensitive for the deviation of the data from the mathematical distribution and even if one point deviates in the PDF, the CDF changes. This section presents the estimated parameters in MLE for *log-normal* and *Weibull* distributions and discusses the reliability.

In order to implement MLE and the KS test for log-normal and Weibull distributions [183], the MATLAB codes (`lnmle` and `wbmle` in Appendix A.1) are used:

$$\text{(Log-normal)} \quad f(x) = C\frac{1}{x}\exp\left[\frac{-(\ln x-\mu)^2}{2\sigma^2}\right] \tag{4.22}$$

$$\text{(Weibull)} \quad f(x) = Cx^{\varepsilon-1}\exp(-\eta x^{\varepsilon}) \tag{4.23}$$

where C is the normalisation factor calculated from Eq.(4.3).

Fig. 4.21 presents (left) PDF, (centre) corresponding CDF and (right) tables of fitted parameters with the mean values for (a) 200 μs fast and (b) 120 ms slow sampling data. Note that the IEI values in Fig. 4.21 are scaled by the sampling speeds for convenience. The log-normal distribution and Weibull distribution also pass the KS test for the data range where the power-law hypothesis passes the test. However, when mean values are calculated from equations [237, 238]:

$$\text{(Log-normal)} \quad \exp\left(\mu+\frac{\sigma^2}{2}\right) \tag{4.24}$$

$$\text{(Weibull)} \quad \eta^{-1/\varepsilon}\Gamma\left(1+\frac{1}{\varepsilon}\right) \tag{4.25}$$

where Γ is a gamma function, the mean values shown in Fig. 4.21(a, b)(right) are unphysical, i.e. smaller than 1. The log-normal and Weibull distributions are therefore discarded. In

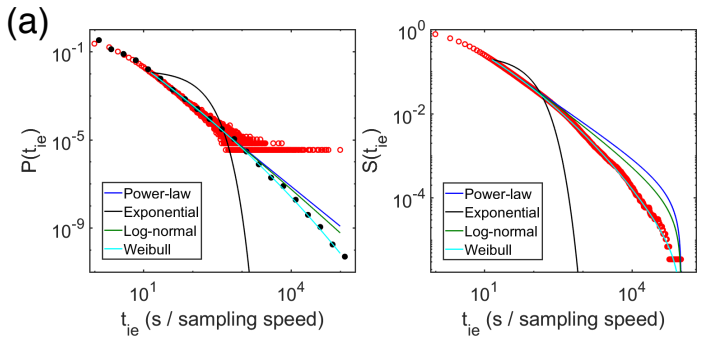

	Distribution	Estimated parameters	Mean value
B189R03 (Fast5V)	Power-law	$\gamma = 1.81$	-
	Exponential	$\lambda = 0.015$	66.67
	Log-normal	$\mu = -23.63$ $\sigma^2 = 34.52$	1.7×10^{-3}
	Weibull	$\varepsilon = 0.10$ $\eta = 5.87$	7.5×10^{-3}

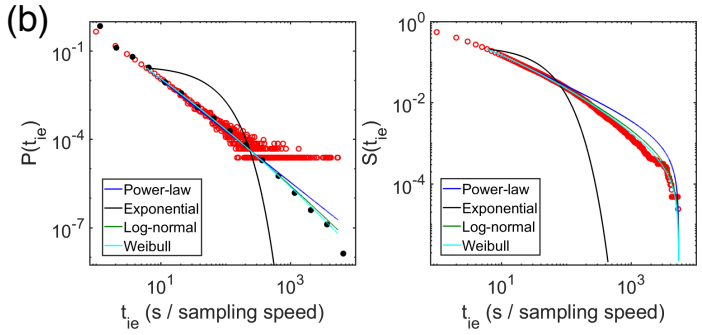

	Distribution	Estimated parameters	Mean value
B189R04 (Slow5V)	Power-law	$\gamma = 1.75$	-
	Exponential	$\lambda = 0.028$	35.71
	Log-normal	$\mu = -6.74$ $\sigma^2 = 13.82$	1.18
	Weibull	$\varepsilon = 0.10$ $\eta = 5.88$	7.3×10^{-3}

Fig. 4.21. The summary of parameters estimated by MLE for the power-law, exponential, log-normal and Weibull distributions: (left) Probability density functions (PDF: $P(t_{ie})$), (centre) corresponding complementary cumulative density functions (CDF: $S(t_{ie})$) and (right) tables of fitted parameters. For convenience of discussion about the estimated parameters, the sampling speed is rescaled to be 1. (a) and (b) are obtained for 200 μs fast and 120 ms slow sampling data, respectively. The MLE are implemented for (blue) the power-law, (black) the exponential, (green) log-normal and (light blue) Weibull in the range where the power-law hypothesis passes the KS test with more than 2 orders of magnitude in time. The power-law exponents are consistent across devices and sampling speeds (200 μs and 120 ms) as discussed in Section 4.7. On the other hand, the parameters estimated in MLE for log-normal and Weibull are unphysical values i.e. the mean values are either smaller than 1 or out of fitting range.

contrast, the power-law hypothesis is qualitatively (Fig. 4.16) and quantitatively (Fig. 4.20) supported, and thus the power-law is adopted as the valid fitting model to discuss the switching dynamics in the following sections. The results of the power-law fits for different datasets obtained from the multiple devices are shown in Section 4.7.4.

4.7 Scale-free Temporal Dynamics and Correlations

The power-law IEI distribution suggests scale-free temporal dynamics in PNNs. This section investigates the correlation between events and discusses the origin of the scale-free switching behaviour with the underlying physical network structure.

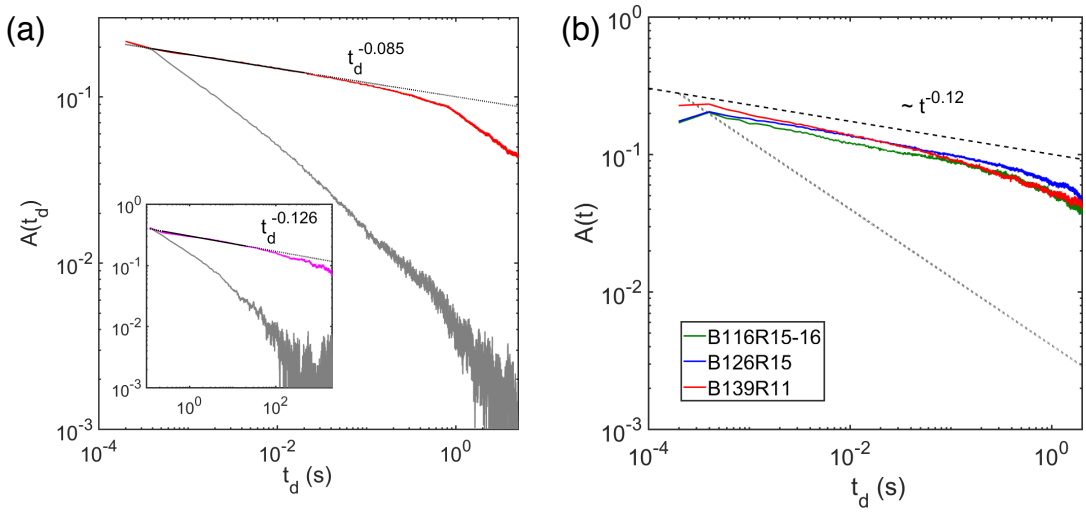

Fig. 4.22. (a) The ACFs show a power-law decay for more than 3.5 orders of magnitude in time for both 200 μs sampling data (B189R03, V = 5 V, $|\Delta G|_{\text{thresh}} = 2.6\text{mG}_0$) and (the inset) 120 ms sampling data (B189R04, V = 5 V, $|\Delta G|_{\text{thresh}} = 2\text{mG}_0$). To distinguish the slope from renewal process, the correlation among events is destroyed by shuffling the IEI values. Our experimental ACFs (red and magenta lines) shows slower decay than the uncorrelated ACFs (grey shading), indicating existence of LRTC in our switching activity. (b) The LRTCs are observed across multiple devices(B116R15-16, B126R15, B139R11,(200 μs sampling)) for the identical voltage (6 V). The black dashed line shows a power-law with the averaged exponent of 0.12 and grey dotted line shows the slope of the uncorrelated ACF. These results suggest that LRTC is the inherent feature of the switching activity in PNNs

4.7.1 Long-range Temporal Correlation (LRTC)

The correlation between the switching events is characterised using autocorrelation functions (ACFs) as described in Section 4.1.3. Fig. 4.22(a) shows the ACF for data obtained with 200 μs sampling speed (the inset for data obtained with 120 ms sampling speed). The ACFs for data obtained with both sampling speeds exhibit a power-law decay for more than 3.5 orders of magnitude in time with almost identical slope of $\beta \sim 0.1$, suggesting the existence of a *long-range temporal correlation* (*LRTC*). In order to distinguish the slope from the renewal processes (see Section 4.1.4) and verify the LRTC, the correlation among switching events is destroyed by shuffling IEIs [189, 193, 214]. This approach preserves the total number of events and the power-law IEI distribution, but removes any temporal correlations between events. The ACF obtained from the shuffled IEI data (grey line) decays much faster than the experimental ACFs, which demonstrates that the original switching events are strongly correlated. Fig. 4.22(b) shows a representative example of the ACFs in three different

devices at the identical voltage of 6 V. Further detail of the LRTCs in multiple devices is shown in Section 4.7.4

The presence of LRTC indicates that each burst is only a part of a series of correlated events and the self-similar temporal activity pattern represents bursts within bursts (i.e. hierarchical burst) [83, 203]. To demonstrate the LRTC, the numerical simulation with a hierarchy of bursts is implemented as described in the next section.

4.7.2 Hierarchical Burst Model

The switching activity in PNNs shows self-similar switching activity on multiple time scales as well as bursts (Fig. 4.16). The LRTC suggests that the fractal structure of the temporal activity which reflects a hierarchy of bursts within bursts rather than individually distributed independent burst [203]. In order to demonstrate LRTC, the hierarchically organised bursty time series is generated with inspiration from the literature [214], as described below.

A burst is defined as a collection of successive switching events with IEIs $< \text{IEI}_{\text{mean}}$ (the mean IEI value). Conversely, each successive burst is separated by IEIs $> \text{IEI}_{\text{mean}}$ [189]. Fig. 4.23(a) shows a segment of an experimental event-train with defined burst sections (highlighted by orange shading). The data is characterised by the distribution of burst sizes (S) [189, 214], which is the number of events in a single burst. The burst size distribution in the experimental data typically follows a power-law with the exponent of $\sim$2, as shown in Fig. 4.23(b). Also, the power-law distributed burst sizes indicate critical dynamics of switching activity [75] (see Section 4.8).

The simulated time series is constructed from power-law distributed IEIs and burst sizes (generated from `gendata` in Appendix A.1). The power-law exponents are set to be 1.8 for IEIs and 2 for the burst sizes, based on the typical experimental result shown in Fig. 4.20 and Fig. 4.23(b). In the hierarchical burst model, generated burst sizes serve as the topmost layer of the hierarchy, shown as S_1 in Fig. 4.23(c). Accordingly, these bursts are separated by the longest intervals in the IEI distribution, which are shaded in red in Fig. 4.23(c). The second layer S_2 of the hierarchy is created by subdividing every burst in S_1 which has $S > 1$ into smaller bursts by drawing again from the same power-law. The bursts in S_2 are separated by IEIs shorter than those used to separate the bursts in S_1, which are shaded in blue in Fig. 4.23(c). From one layer to the next, bursts are partitioned

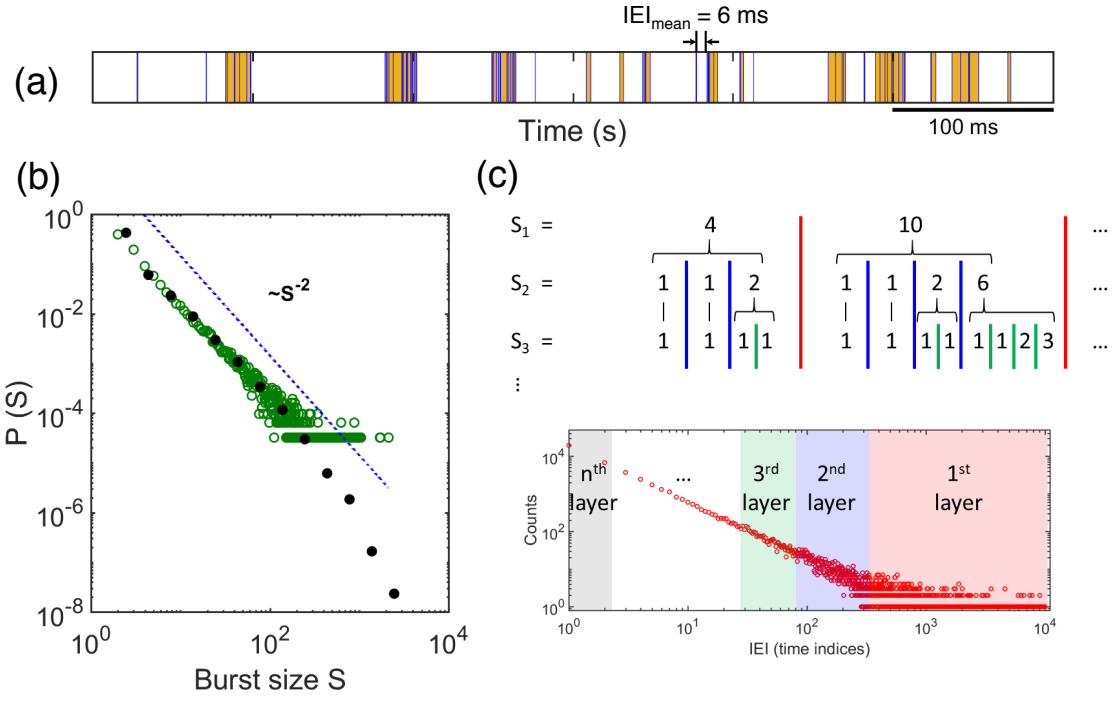

Fig. 4.23. The bursty activity pattern in our experimental data (B189R04, 120 ms sampling, V = 5 V, $|\Delta G|_{\text{thresh}} = 2\text{mG}_0$) and the hierarchical burst model. (a) The burst section (highlighted by orange shade) is a collection of successive events with IEI $<$ $\text{IEI}_{\text{mean}} = 6$ ms (the mean value of IEIs). (b) The burst size distribution ($P(S)$) shows heavy-tail and spans for more than 3 orders of magnitude of size. The blue dashed line shows a power law with the exponent of $\gamma = 2$. (c) Schematics of the hierarchical burst model. The burst on the layer n has a further burst structure created in the next layer $n+1$ i.e. the bursts are themselves made up of bursts. The created burst is separated by smaller IEIs for each successive layer.

into smaller and smaller bursts which are separated by smaller and smaller intervals. This process is repeated until the n_{th} layer features no bursts with $S > 1$. It is important to note that this model does not change the number of events or the IEI distribution, but arranges the order of successive IEIs.

Fig. 4.24(a) shows the event-train generated using the hierarchical burst model on multiple different time scales. The event-trains in the four panels are not readily distinguished and show self-similar activity. As shown in 4.24(b), ACF for this hierarchical burst model (blue line) match the experimental ACF and show the power-law decay over ∼4 orders of the magnitude in time.

To compare with the hierarchical burst model, a non-hierarchical burst model is also examined. In this model, the burst size distribution and the IEI distribution still follow

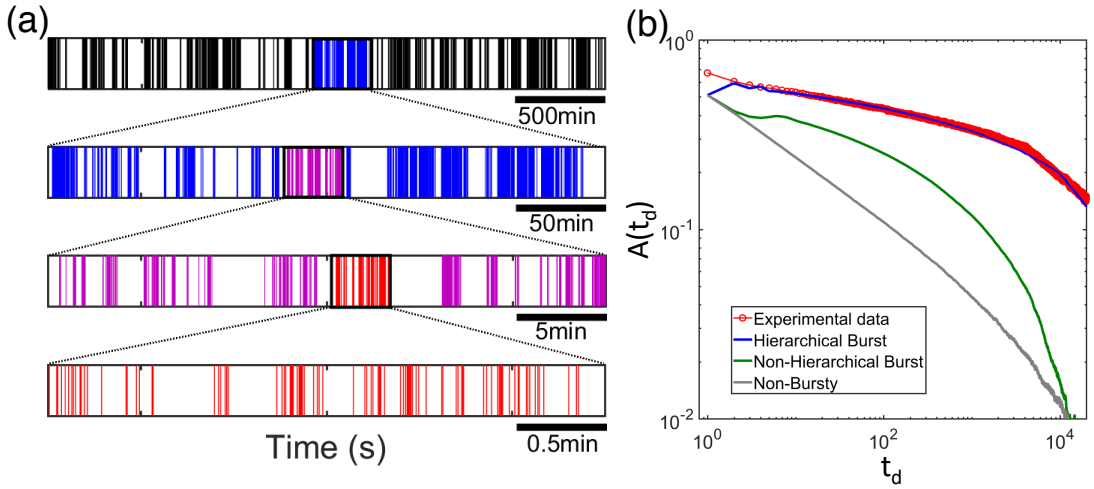

Fig. 4.24. (a) the event-train for different time scales in the hierarchical burst model (sampling speed is scaled as 120 ms). The event-trains feature bursty patterns which are qualitatively the same across different time scales, demonstrating that large bursts of activity are comprised of smaller burst of activity, i.e. the bursts of activity are temporally self-similar. This self-similar structure induces the LRTC in the ACF. (b) Only the ACF of the hierarchical burst model (blue line) can successfully replicate the experimental ACF (red markers). Although the non-hierarchical burst model (green line) has a smaller slope than the ACF of the uncorrelated IEI (gray line), the slope is much greater than that obtained from the hierarchical burst model.

the same power-laws as the hierarchical burst model, but in the bursts which are separated by IEIs $>$ IEI_{mean}, the events with IEIs $<$ IEI_{mean} are randomly distributed. The non-hierarchical burst model cannot successfully explain the LRTC and as shown in Fig. 4.24(b), the ACF (green line) decays quickly compared to that of the hierarchical burst model.

The next section discusses the origin of the LRTC in terms of the signal propagation on the underlying network structure.

4.7.3 LRTC and Underlying Network Structure

LRTC is the inherent feature in PNNs that arises from the hierarchically organised burst structure in the time series data. According to the literature [239], long-range spatial and temporal correlations are different sides of the same coin, i.e. they are interdependent. Long-range spatial correlations ensure that local interactions can propagate to the network on multiple time scales, resulting in LRTC [203]. In PNN devices fabricated with deposition near the percolation threshold, the correlation length diverges [60] and long-range spatial correlation is naturally introduced to the system.

In the brain, synapses connect and transmit the information between neurons. In PNNs,

switching events occur in tunnelling gaps [50–52] distributed on the highly branched fractal network structure (see Fig. 4.18). Under external stimuli, the formation or annihilation of an atomic scale wire at the tunnelling gaps redistributes electrical current across the network, thereby modifying local electric field across other tunnelling gaps. This reconfiguration of the network due to the switching influences subsequent switching events through internal feedforward and feedback networks. Therefore, the switching events can propagate over long distances in time and space, resulting in the LRTC [92, 203]. In short, similar to biological brains, PNNs consist of a network of non-linearly interacting nodes (groups of particles) and temporal correlations emerge from the underlying scale-free network structure and local processes that connect the nodes.

The consistency of the scale-free dynamics and the LRTC in multiple devices are investigated in the next section.

4.7.4 Scale-free Dynamics and LRTC in Multiple Devices

To quantify scale-free dynamics and the LRTCs across multiple devices, the power-law exponents of the IEI distributions (γ) and the ACFs (β) were obtained from 30 measurements in 8 independent devices. While the total number of the stable devices fabricated in this work is ~ 200, the analysis of the IEI distributions and the ACFs require a large number of events (> 2000) and very long dataset ($> 1 \times 10^5$ data points) to avoid finite size effects [240] and so the data presented here is limited to those that meet criteria.

Fig. 4.25 shows the power-law exponents of (a) the IEI distributions and (b) the ACF slopes as a function of the applied voltage. Corresponding exponent values are summarised in Table 4.2. The power-law exponents in the IEI distributions were estimated using MLE and passed the KS test (p-value > 0.2) whereas the data obtained at higher voltages (9-10V) could not pass the KS test (also see Table 4.2). As shown in Fig. 4.25(a), the majority of exponent values in the IEI distributions are in the range between 1.5 and 2 (green shaded band). While the physical meaning of the power-law exponents in the IEI distributions is still not clear and further research is required, the exponents in the range might indicate switching activity in the well balanced network states between excitation and inhibition [241].

(a)

Devices	No.	Voltage (V)	γ	β
B133	R09	5	1.70	0.13
B135	R05	5	1.76	0.25
	R06	6	1.72	0.23
	R07	7	1.68	0.14
	R08	8	---	0.21
	R09	9	---	0.19
	R10	10	---	0.24
B136	R05	5	1.63	0.19
	R09	6	1.86	0.10
	R12	7	1.76	0.21
	R15	8	1.91	0.14
	R19	9	---	0.17
	R22	10	---	0.25
B149	R04	4	1.63	0.13
	R04	5	1.42	0.23
B189	R04	5	1.75	0.10

(b)

Devices	No.	Voltage (V)	γ	β
B116	R06 – R07	5	1.78	0.10
	R15 - R16	6	1.51	0.15
	R22 - R23	7	1.40	0.23
B126	R14	5	1.72	0.09
	R15	6	1.73	0.13
	R16	7	1.81	0.09
	R17	8	1.74	0.11
	R18	9	---	0.17
	R19	10	---	0.25
B139	R11	6	1.61	0.15
B189	R03	5	1.81	0.09

Table 4.2: Tables of power-law exponents values in the IEI distributions (γ) and the values of the ACF slopes (β) for data obtained from (a) 120 ms sampling speed and (b) 200 μs sampling speed. γ for some data sets obtained at higher voltages (9 - 10V) are not shown because there is no data range which could pass the KS test [2].

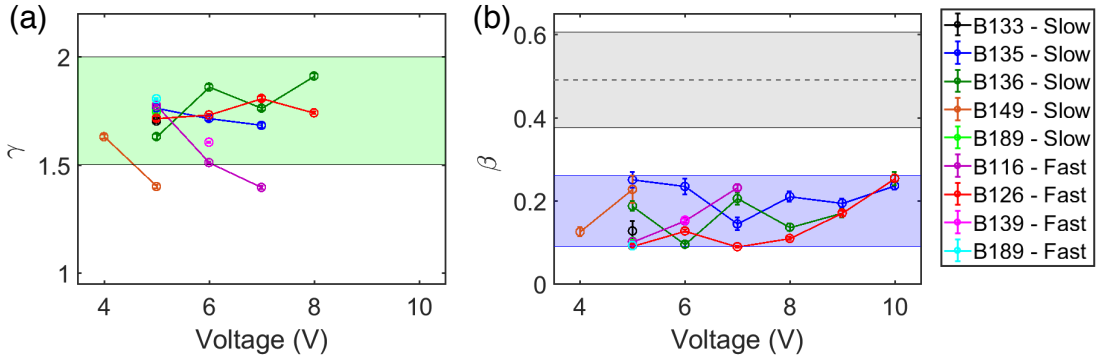

Fig. 4.25. (a) Power-law exponents (γ) of the IEI distributions obtained in multiple devices and for a range of voltage stimuli. The exponents are typically found to be in the range between 1.5 and 2 (highlighted by green shade). Since the data obtained at higher voltages (9-10 V) could not pass the KS test, there is not data point (also see Table 4.2). (b) Power-law exponents (β) of the ACFs for the data obtained in the same data as in (a). The grey shaded band and dashed line indicate the range of β obtained from shuffled IEI data and the mean value of the exponents ($\beta \sim 0.5$), respectively. All values of β are within the range between 0.1 and 0.3 (highlighted by blue shade) and also are lower than the slope of the ACF obtained from shuffled IEI data (gray band), indicating the existence of LRTCs in all the measurements.

As shown in Fig. 4.25(b), all values of the original ACF slopes are within the range from ∼0.1 to 0.3 (blue shaded band) and are smaller than those of the ACFs obtained from shuffled IEI data (grey shaded band), suggesting the existence of the LRTCs across devices.

In summary, the scale-free dynamics and the LRTCs are observed in a number of devices, for a range of stimuli and for independent measurements. Also, these results indicate the reproduciblility of the switching dynamics in independently fabricated PNN devices. As shown in Table 4.2, some data at higher voltages does not have power-law exponents and fail the KS test [2]. The next section investigates the scale-free dynamics and correlations for different DC voltages.

4.7.5 Voltage Dependence of Scale-free Dynamics

In order to investigate the stimulus dependence of the scale-free network activity and the LRTC, a range of voltages between 5 V (slightly above the switching threshold voltage) and 10 V was applied to the devices. As described in Section 3.3.1 (III), the switching activity in PNNs has shown that higher voltages enhance the switching activity due to activation of new switching sites on the higher order branches in the network, whereas it is possible to

[2]The minimum range required to estimate the power-law exponents is 2 orders of magnitude in time to avoid fitting for very narrow data range [228].

increase the activity at the same switching sites [50, 51].

Fig. 4.26 shows (a) the IEI distributions and (b) ACFs for a range of stimulus. For all applied voltages, the IEI distributions span ∼4 orders of magnitude in time with heavy-tail and the ACFs exhibit LRTC with decay for over ∼4 orders of magnitude in time. The power-law hypothesis for the IEI distributions is examined by MLE and the KS test. Power-law fits for lower voltages (5-8V) pass the KS test over a range of more than 2 orders of magnitudes in time and the estimated slopes are almost identical as shown in Fig. 4.26(c).

To quantify the voltage dependence of the ACFs, the correlation strength and the slopes of the ACFs are obtained as shown in Fig. 4.26(d). While the correlation strength is usually indicated by the ACF at lag-1 (i.e.$A(t_1)$) (see Section 4.1.3), in the experimental data the lag-2 is used to avoid issues in data sampling (discussed in Section 4.3). The lag-2 correlations and the ACF slopes also weakly vary from 5 V to 8 V, implying the correlation strength and LRTC are completely independent of applied voltage up to 8 V.

Interestingly, at higher voltages (9-10 V), the IEI distribution deviates from a strict power-law, the correlation strength at lag-2 is significantly lower than that at lower voltages and the ACF slope increases. Hence, there is a clear decrease in correlation at voltages higher than 8 V. While the switching rate decreases at 9 V and 10 V in Fig. 4.26(d), a decrease in activity is generally associated with an increase in the correlation strength [195]. Therefore, the decrease of correlation at higher voltages cannot be attributed to the switching rate.

In neuroscience, a decline in LRTC has been investigated as an indicator of neurological conditions related to disease [200, 242], in addition to a number of cognitive alternations [194, 243]. The decrease in correlation of the neuronal signals is caused by a “disconnection” in large-scale networks and fatigue in the brain [194]. In PNNs, a similar fatiguing process may induce the decline in LRTC observed at the higher voltages (9-10 V): higher applied voltages lead to larger currents which may break the atomic filaments at the switching sites due to excessive Joule heating. Since such large currents are distributed across the switching sites in the network, network-wide fatigue may occur, which result in disconnections between different parts of the network. This would disrupt the propagation of local interaction to global scale, leading to an observation of decrease in correlation. Nonetheless, the

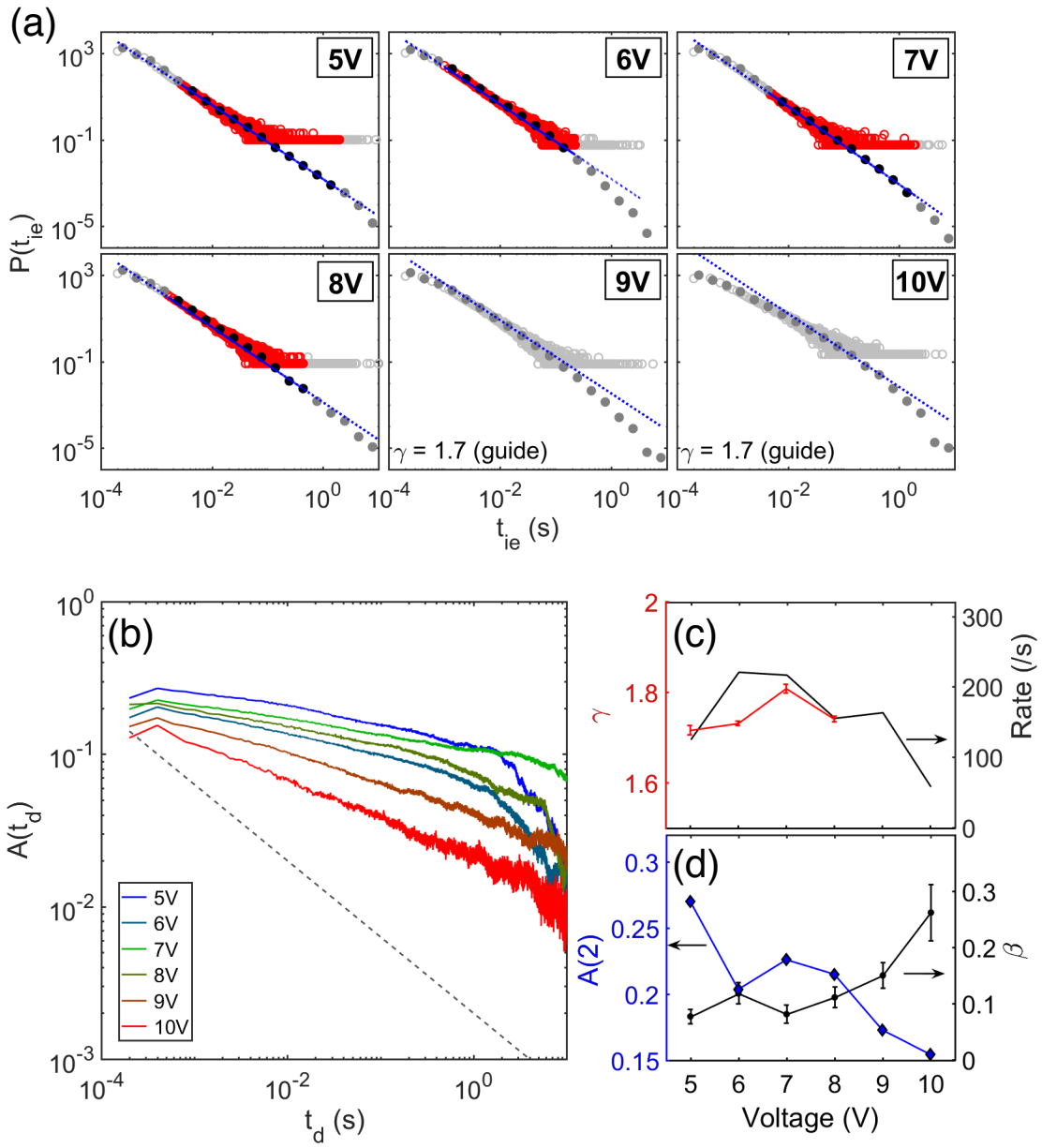

Fig. 4.26. Evolution of switching dynamics and LRTC with applied voltages (B126R12-19, 200 μs sampling, $|\Delta G|_{\text{thresh}} = 1\text{mG}_0$). (a) The IEI distributions for a range of applied voltages between 5 V and 10 V shows heavy-tails.The red markers (linear binning) and black markers (logarithmic binning) indicate the range of the distribution used for estimation of the power-law exponents in MLE. For lower voltages (5-8 V), the power-law hypothesis pass the KS test with slope ∼1.7, but at higher voltages (9-10 V) the power-law hypothesis is rejected (p-value < 0.2). (b) ACFs for all applied voltages show LRTCs with the decay slower than that expected in the renewal process (grey dashed line for the averaged slope ($\beta \sim 0.5$)). (c) The estimated exponents (red line) are consistent between 5V and 8V, while the exponents for 9 V and 10 V are not available the KS test was failed. Switching rate varies with different applied voltages. (d) The voltage dependence of ACFs is quantified with lag-2 of the ACFs (i.e. $A(t_2)$) shown as blue line and the decay exponents (β) represented by the black line. The lower operating voltages (5 V) maximise the correlation in the switching events.

correlations in switching events in PNNs are maximised at the low voltages, which would be the operating point of our devices.

4.8 Correlations and Critical Dynamics

In the neuroscience literature, LRTC is explained within the theoretical framework of self-organised criticality [201, 203, 244]. In the brain, criticality leads to optimised information transfer, learning and information processing [95, 100, 245, 246]. Criticality in neuromorphic hardware is also an important property as discussed in previous research on silver nanowire networks [48, 49]. In the most recent work [75], the criticality of Sn-based PNNs has been systematically demonstrated using rigorous criteria with similar methodology used in the analysis of avalanches in neural recordings [96, 215]. Critical dynamics have been demonstrated by the agreement between three independent estimates of a characteristic exponent ($1/\sigma\nu z$) [247], as briefly described below. Note that in this section, the term "avalanche" is used to describe a burst of switching events [75].

In critical systems, the sizes and durations of avalanches have power-law PDFs as shown in Fig. 4.27(a, b, e, f). The power-law exponents of the size (α) and the duration (τ) are estimated by MLE and validated by the KS test as described in Section 4.6.1. As the demonstration of criticality hinges on correct estimation of PDF exponents, the MLE procedure is an essential part of the analysis. The average size of an avalanche of a particular duration ($\langle S \rangle(T)$) is a power-law function of its duration with the characteristic exponent [247], which is denoted as:

$$\langle S \rangle(T) \sim T^{1/\sigma\nu z} \tag{4.26}$$

In the experimental data shown in Fig. 4.27(c, g), the characteristic exponents were found to be ∼1.6 in data obtained with both 120 ms and 200 μs sampling.

The second estimate of the characteristic exponent is given by α and τ with the following equation, which is known as the *crackling relationship* [247]:

$$\frac{1}{\sigma\nu z} = \frac{\alpha - 1}{\tau - 1} \tag{4.27}$$

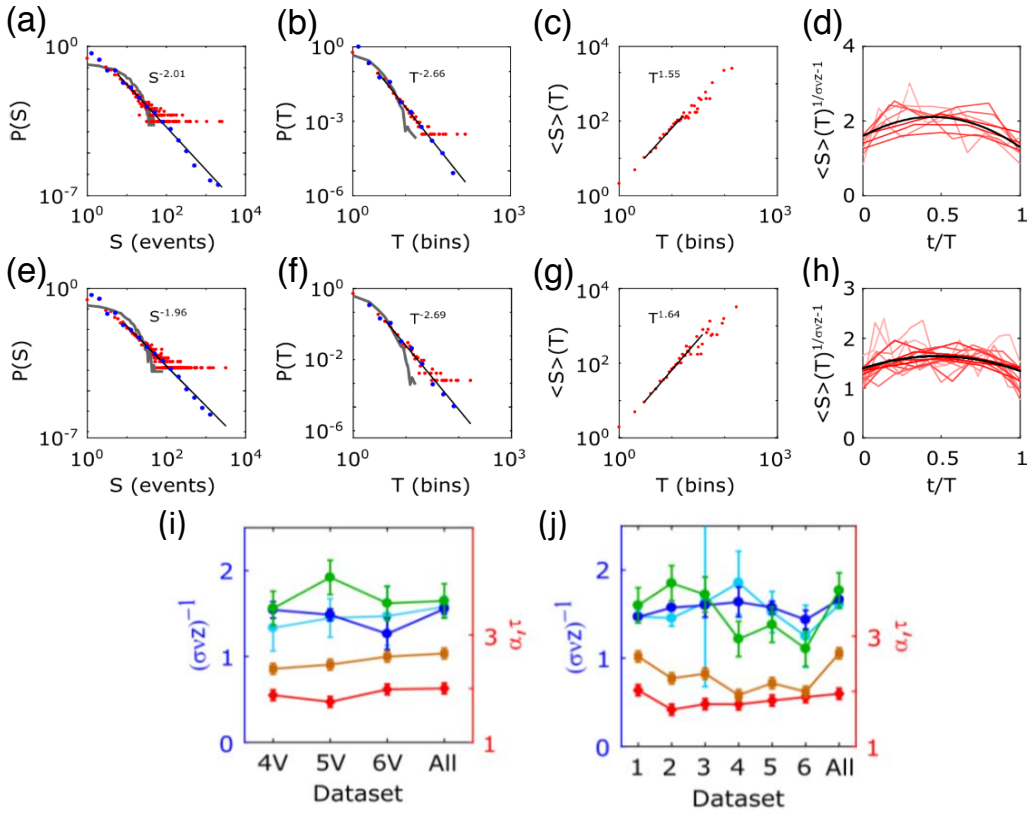

Fig. 4.27. The avalanche profiles and the characteristic exponents ($1/\sigma\nu z$) for data obtained with (a-d, i) 120 ms sampling speed and (e-h, j) 200 μs sampling speed (adapted from ref. [75]). The distributions of (a, e) size and (b, f) duration of avalanche follow power-laws with exponents of $\alpha \sim 2$ and $\tau \sim 2.7$, respectively. The exponents are estimated using MLE procedure and validated by the KS test. The *crackling relationship* calculated from α and τ provides an estimate of $1/\sigma\nu z$. (c, g) The mean size of the avalanche ($\langle S \rangle(T)$) as a function of their relation independently provides an estimate of $1/\sigma\nu z$. (d, h) The mean avalanche shape for each duration exhibits a characteristic "collapse" on to a single parabolic scaling function (black lines), which gives the third estimate of $1/\sigma\nu z$. (i, j) Values of $1/\sigma\nu z$ obtained from three independent estimates: (green) crackling relationship, (blue) exponents of mean avalanche size given duration and (cyan) avalanche shape collapse. The right axes represent the power-law exponents of (amber) α and (red) τ. In almost every case in (i, j), the three estimates agree within the measurement uncertainty, which is strong evidence of the critical dynamics in PNNs. This is consistent in the data obtained from both (i) 120 ms slow sampling and (j) 200 μs fast sampling, suggesting the presence of scale-free temporal dynamics.

The third estimate of $1/\sigma\nu z$ is given by the collapse of the mean temporal profile (average avalanche shape) for each unique avalanche duration on to a single parabolic scaling function [96, 247], as shown in Fig. 4.27(d, h). Because the durations of avalanches are power-law distributed, very long avalanches are rare, and their mean temporal profiles are hence the average of only a small number of occurrences. This results in more deviation from the scaling function for longer durations and an associated increase in the uncertainty of the

estimate of $1/\sigma\nu z$, compared to the other two methods used to estimate the characteristic exponent [75].

Fig. 4.27 shows the three independent estimates of $1/\sigma\nu z$ (blue, cyan and green symbols) for (i) a range of applied voltage and (j) successive measurements at the same applied voltage. All three estimates obtained in the experimental data agree within the uncertainties for most cases. Deviation from agreement between the $1/\sigma\nu z$ values arises due to statistical variance between data sets, as exemplified by the superb agreement between the $1/\sigma\nu z$ estimates when successive measurements are concatenated into a single data set ("All" in Fig. 4.27(i, j)). The agreement between estimates of the critical exponent for a range of applied voltage and repeated measurements is strong evidence of criticality in PNNs [248]. Criticality originating from long-range spatiotemporal correlation is consistent with the observation of LRTC in the scale-free network structure as discussed in the previous sections. Further details on the critical dynamics in PNNs can be found in the literature [75].

4.9 Summary

This chapter explored the temporal dynamics and correlation in the Sn-based PNNs using time series analysis such as IEI distributions and the ACFs. The DC voltage measurements provided better signal-to-noise ratio than the pulsed measurement, allowing the detection threshold to be lowered. The threshold values were carefully assessed in data obtained with 200 μs "fast" sampling and 120 ms "slow" sampling speeds. While the estimated noise originating from the electric current was used as the thresholding value in the fast sampling, in data obtained with the slow sampling, an alternative threshold value was selected from the multi-barcode plot to avoid saturation of the event-train due to unresolved fast and small events. While the IEI distributions were not affected by the threshold values above the selected value, the smaller threshold values for data obtained with the slow sampling speed induced the cut-off in the tail because of the saturation of the event-train. Moreover, in the simulation model to investigate the effect of sub-sampling and thresholding showed when the underlying distributions of IEIs and ΔG follow power-laws, the power-law slopes of the IEI distributions in highly sub-sampled data do not significantly change with the threshold

values.

Based on event detection, the temporal switching activity in PNNs was investigated. The switching activity exhibited bursty and self-similar pattern in different scales in time and switching size. The ΔG distribution showed a heavy-tailed distribution spanning $\sim$4 orders of magnitudes in switching size. The heavy-tailed ΔG distribution was discussed in terms of the underlying network structure obtained from numerical simulations based on 2D continuum percolating tunnelling models. The network structure near the percolation threshold is highly branched, and the degree distributions showed heavy-tail close to the power-law which is an indication of scale-free networks. The different event sizes were assumed to reflect the configuration of the network and location of the switching sites, i.e. big ΔG originate from events on the main branch which have few parallel pathways and the small ΔG is caused by events on higher order branches that have many parallel pathways.

Self-similar patterns are usually characterised by power-laws (Section 1.3). A hypothesis for power-law IEI distributions was examined by rigorous criteria of MLE and the KS test. The IEI distribution could pass the KS test with the power-law exponent obtained from MLE procedure for more than 2 orders of magnitude in time even while the KS test is extremely sensitive to small deviation from a mathematical power-law. Weibull and log-normal distributions were also examined, but the estimated parameters for these distributions were unphysical and thus were discarded.

Temporal correlations between switching events were investigated using the ACFs. The data obtained with both fast and slow sampling speed exhibited power-law decays of the ACFs with the slopes smaller than that of the ACF in uncorrelated events, indicating the existence of LRTCs. The numerical simulation for the hierarchical burst model could successfully demonstrate the LRTC with a similar decay slope of the ACF whereas the simulated data which is for non-burst or burst without the hierarchy showed faster decay of the correlation. The origin of the LRTC in PNNs was discussed in terms of the underlying scale-free network structure. Since the switching events reconfigure the network and influence subsequent switching events through internal feedforward and feedback network, the switching events can propagate in multiple scale of time and space, leading to the LRTC. Furthermore, the presence of the LRTCs is consistent with critical dynamics in PNNs, which is a natural

extension of correlated switching dynamics.

The voltage dependence of the network activity and temporal correlation were also examined with a range of voltage between 5 V and 10 V. The IEI distributions showed heavy-tails for all voltages, but only for lower voltages (5-8 V), the power-law hypothesis for the IEI distributions passed the KS test. In the ACFs, although data for all voltages showed LRTC with slow power-law decays of the ACFs, the lag-2 correlation and the ACF slopes varied at higher voltages (9-10 V). With analogies to the large-scale networks in the brain, this was understood as a consequence that the network is fragmented into different parts due to excessive Joule heating, resulting in disruption of the propagation of the local interaction to the network. This result indicated that the operating point of the PNN devices is low voltage, which would be an advantage in energy efficient computation.

In neuroscience, the observation of LRTC has several implications for information processing in the brain. For examples, LRTCs are associated with extended timescales and memory effects, which are thought to provide favourable neuronal substrates for the integration of information across time and across different cortical areas in order to increase the signal-to-noise ratio during cognitive tasks (e.g. during decision making [194]). Also, information processing and learning in the human brain is believed to be carried out by correlated firing patterns of neuronal populations [249].

The correlated network dynamics discussed above might be exploited within the context of a practically implementable neuromorphic computational framework such as Reservoir Computing (RC) [29, 30, 49] (see Section 1.1.2). Software simulations of RC have acknowledged the importance of utilising the rich topological features of biological neuronal networks. According to the literature [250], the use of a scale-free network as reservoir in RC leads to improved performance in chaotic time series predictions, particularly processing time series with multi-scale characteristics such as speech, text and gestures [30], compared to a random reservoir [251]. Therefore, the percolating network devices, which have several topological features of biological neuronal networks and exhibit scale-free and self-similar temporal dynamics, LRTC, and criticality may provide an interesting alternative platform for neuromorphic hardware implementation.

Chapter 5

Ag/Ag_2S-based PNNs

Sn-based PNNs are charactersed by their self-similar switching activity with scale-free temporal dynamics and LRTC, as discussed in Chapter 4. In this chapter, the objective is to investigate whether the same fabrication technique can be applied for other materials which have different properties, such as memristive behaviour. Different switching junctions are expected to provide other functionalities in the PNNs.

This chapter presents preliminary data for Ag/Ag_2S devices, which show switching behaviour based on a nanoscale solid-state electrochemical reaction [156, 157]. Ag_2S is well-known as an ionic conductive material [156] and has attracted a lot of attention since synapse-like behaviour was observed in a single atomic switch [142]. Although similar behaviour is observed in other materials such as Cu_2S [143, 144], TiO_2 [154, 252] and Ta_2O_5 [253], the use of Ag_2S in this work was motivated by its fast switching speed [157, 159] and low operation voltage [157, 254].

This chapter consists of the following sections. Section 5.1 introduces memristors and the previous research on Ag/Ag_2S atomic switches in a single junction and in networks. Section 5.2 describes fabrication of the first Ag/Ag_2S-based PNNs at UC and Section 5.3 discusses important properties of the PNNs for neuromorphic application. The conclusion and future prospects are given in Section 5.4.

5.1 Previous Research of Memristive Ag/Ag$_2$S Devices

The Ag/Ag$_2$S atomic switch was serendipitously discovered in research on novel electronic devices [129, 255, 256]. Since then, the Ag/Ag$_2$S-based atomic switch has been widely investigated in single atomic junctions [129, 142, 254–258] as well as in complex networks [48, 49, 158, 259–262]. It has been shown that Ag/Ag$_2$Satomic switches exhibit various functionalities, including memristive switching behaviour [156–158, 262] and memory capabilities [48, 142, 258]. This section introduces the concept of the memristor and summarises the previous research for Ag/Ag$_2$S devices with the switching mechanism based on electrochemical reaction.

5.1.1 Memristor

In circuit theory, it is well-known that there are the four fundamental circuit elements: *current* (i), *voltage* (v), *charge* (q) and *magnetic flux* (ϕ). Pair combinations of these elements are related to two basic terminal elements, as shown in Fig. 5.1(a). The three classical circuit elements defined in between the 1740s to 1830s are the *resistor* (R), the *capacitor* (C) and the *inductor* (L). These components are defined using the four circuit elements as $R = dv/di$, $C = dq/dv$, and $L = d\phi/di$. These three had been used as the fundamental elements for a long time until the fourth circuit element, referred to as *memristor*, was proposed by L. Chua in 1971 [263].

The memristor is defined from the "missing" relationship between two elements i.e. q and ϕ (right bottom in Fig. 5.1(a)) and the *memristance* (M), which is the "resistance" of memristor, is denoted as $M = d\phi/dq$. The term "memristor" is the compression of memory and resistor and this name originates from the unique property that the memristor stores information as a resistance level even in the absence of the electrical power. The memristance is a function of the current that was passed through the device at previous time.

The first experimental demonstration of a memristor was reported in 2008 using a nanoscale titanium dioxide thin-film [264]. One of the significant properties of memristors is the characteristic of the current-voltage (I-V) relation showing the pinched hysteresis loop for any bipolar periodic voltage or current independent of the initial condition [265].

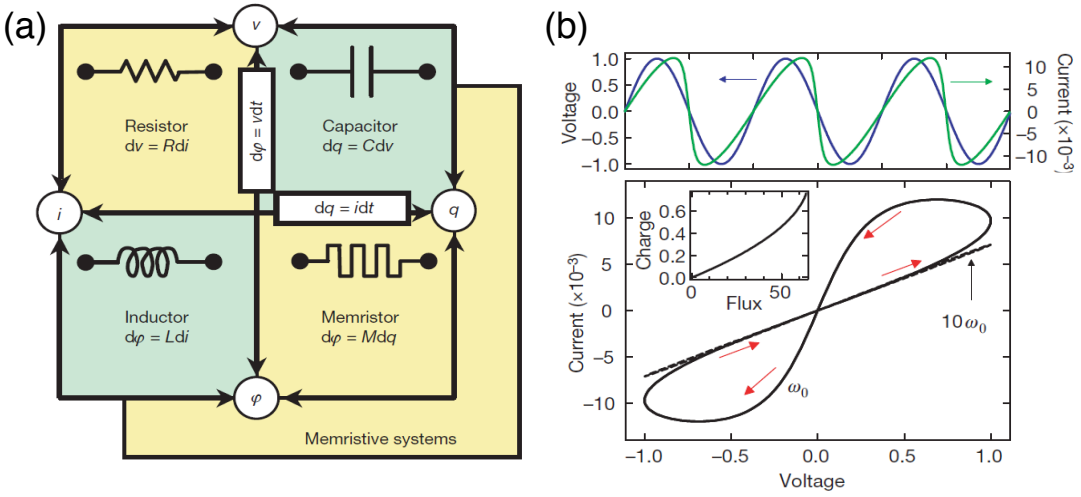

Fig. 5.1. (a) A circuit diagram shows the relationship between four fundamental circuit elements and constructed two terminal elements. The *memristor* is considered as the fourth "missing" relationship. (b: top) Applied input voltage (blue lines) and the current (green line) as a response to the applied bias. The pinched-hysteresis in I-V characteristic shown in (b: bottom) is the signature of a memristor (adapted from ref.[264])

Since then, memristors have attracted a lot of attention and the concept of memristors has been expanded to a broader class of nonlinear systems, called *memristive systems*. Nowadays, various types of memristors, including molecular and ionic thin films [266, 267] as well as spin-based and magnetic memristive systems [267–269], have been fabricated with a wide array of materials [270]. One of the most attractive behaviours of memristors is that they exhibit similar behaviour to the synaptic behaviour in brains. Because of this, many neuromorphic devices have been fabricated with memristors [270–272]. The properties of the Ag/Ag$_2$S system, one of the memristive systems, are described in the following sections.

5.1.2 Ag/Ag$_2$S-based Single Atomic Switches

The fundamental properties of the Ag/Ag$_2$S systems have been studied in a single atomic junction, which is a sandwich structure of metal/insulator (i.e. Ag$_2$S)/metal (MIM). In the MIM of a single junction, while one side of the metal is Ag, the other side of the metal is an inert metal (e.g. Pt or W). Also, a STM tip is often used as the inert metal electrode, which allows to precisely control a vacuum gap distance between Ag$_2$S and the electrode (see Fig. 5.2(d)). The MIM with a vacuum gap is called a *gap-type* atomic switch [157]. In essence, the synapse-like behaviour is a consequence of the electrochemical reaction

which allows for Ag filament formation and dissolution in the junction. Details of the mechanism are provided in Section 5.1.4. The great advantage of the Ag/Ag$_2$S system is its low operation bias (∼0.05 V) [157, 254] and fast switching speed (< 10 ns) [129, 159]. The conductance quantisation and demonstration of a logic gate configuration have been reported [129]. This section mainly focuses on the switching behaviour related to neuromorphic device application.

(I) Memristive Switching Behaviour

As shown in Fig. 5.2(a), the I-V characteristics of an Ag/Ag$_2$S atomic switch exhibit pinched hysteresis which is recognised as the signature of memristors. Memristive behaviour is explained with the Ag filament formation and dissolution in a gap between Ag$_2$S and a counter inert electrode (e.g. Pt) as shown in Fig. 5.2(d): (i) The application of positive bias to Ag$_2$S induces the precipitation of Ag atoms from the Ag$_2$S and (ii) creates an Ag protrusion (also see Fig. 5.2(c)). (iii) Completion of the Ag filament formation results in the switch being ON, i.e. the current is high. (iv) Applying a negative bias causes a dissolution of the Ag filament into Ag$_2$S, leading to shrinkage of the protrusion and (v) finally the switch returns to low current state (Off state). It has been reported that many voltage sweeps ($\sim 10^5$ times) reproduce a similar I-V trace [157, 254]. In the pinched hysteresis loops, the area of the loop for the negative bias application is smaller than that of the positive bias. This is because of the difference of speeds between filament formation and dissolution, i.e. the dissolution is faster [257].

Multiple application of the bias for the filament formation (i.e. the cycle of (i-iii) in 5.2(d)) results in the gradual increase in the current as shown in Fig. 5.2(b). This result indicates that repetition of stimuli causes the further filament formation with the history of subsequent sweeps and the atomic switch has a learning ability that has been reported in memristive devices [156, 272]. Unlearning ability, where the switching state returns to the initial condition, is also achieved with a bias voltage of opposite polarity (i.e. the cycle of (iii-v) in 5.2(d)) [156]. This learning-unlearning process shows potential in the development of controllable artificial neural switching element [156, 157].

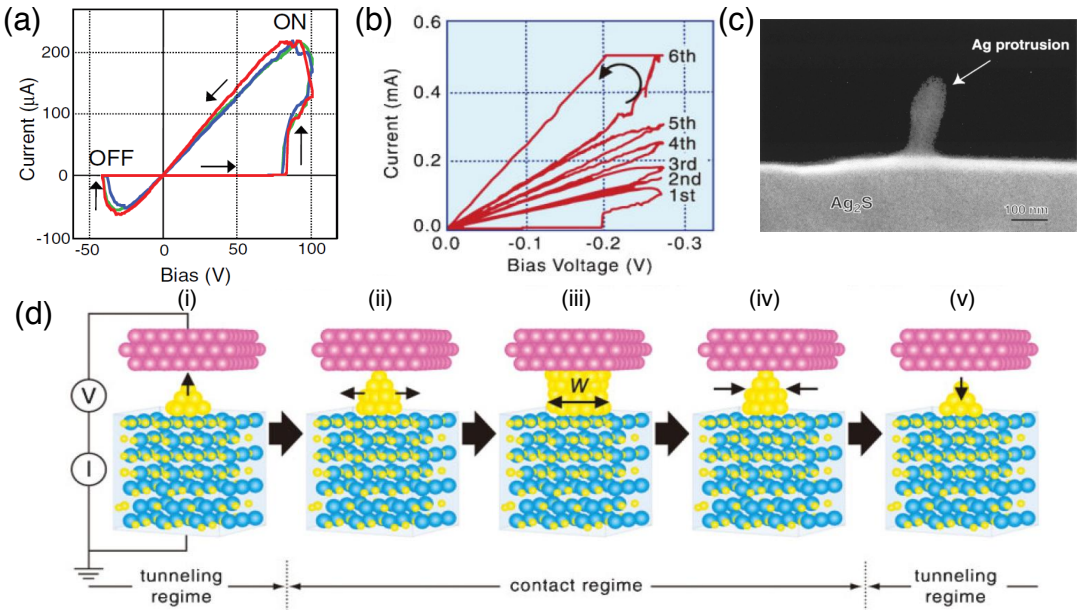

Fig. 5.2. (a) I-V characteristic of a single atomic switch (Pt/Ag_2S/Ag) shows the pinched hysteresis, which is the signature of the memristive devices. The positive bias applied to the Ag_2S grows a Ag protrusion, leading to the switch being turned on with higher current. In contrast, the reverse bias cause dissolution of the filament into Ag_2S, resulting in the switch being turned off. (b) The multiple application of negative bias to the counter electrode (equivalent for the positive bias application to Ag_2S) causes a gradual increase in current, which results in every stimulus growing Ag filaments. This behaviour is consistent with the learning abilities observed in the other memristive systems [272]. (c) The SEM image of the Ag protrusion grown during the experiment (adapted from ref.[255]). (d) Ag filament formation and dissolution process in a single junction consisting of Ag/Ag_2S inert metal (Pt or W): (i) precipitation of Ag atoms with voltage bias, (ii) formation of a Ag protrusion (iii) the complete filament formation between two electrodes, resulting in the switch being turned on (iv) the opposite bias application causes the dissolution of the formed filament into Ag_2S (v) the switch is turned off. (adapted from [157])

(II) Short-term Plasticity (STP) and Long-term Potentiation (LTP)

A single atomic switch exhibits two characteristics of memory related to the Ag filament formation with respect to the applied bias, i.e. *short-term plasticity* (*STP*) and *long-term potentiation* (*LTP*) [156]. Fig. 5.3 shows (a) a schematic illustration of a single junction configuration with a process of filament formation and (b, c) changes of G for two different stimulus intervals (τ_{int}) [142]. Applied voltage stimuli are $V_p = 80$ mV with $\tau_p = 0.5$. For a longer stimulus interval ($\tau_{\text{int}} = 20$ s) in (b), while the G increased to $\sim 1G_0$ ($= 77.5$ μS) for each applied pulse, the G decays with time back to the initial low G for each pulse interval. Interestingly, this decay is observed without any applied voltage stimuli whereas other ionic

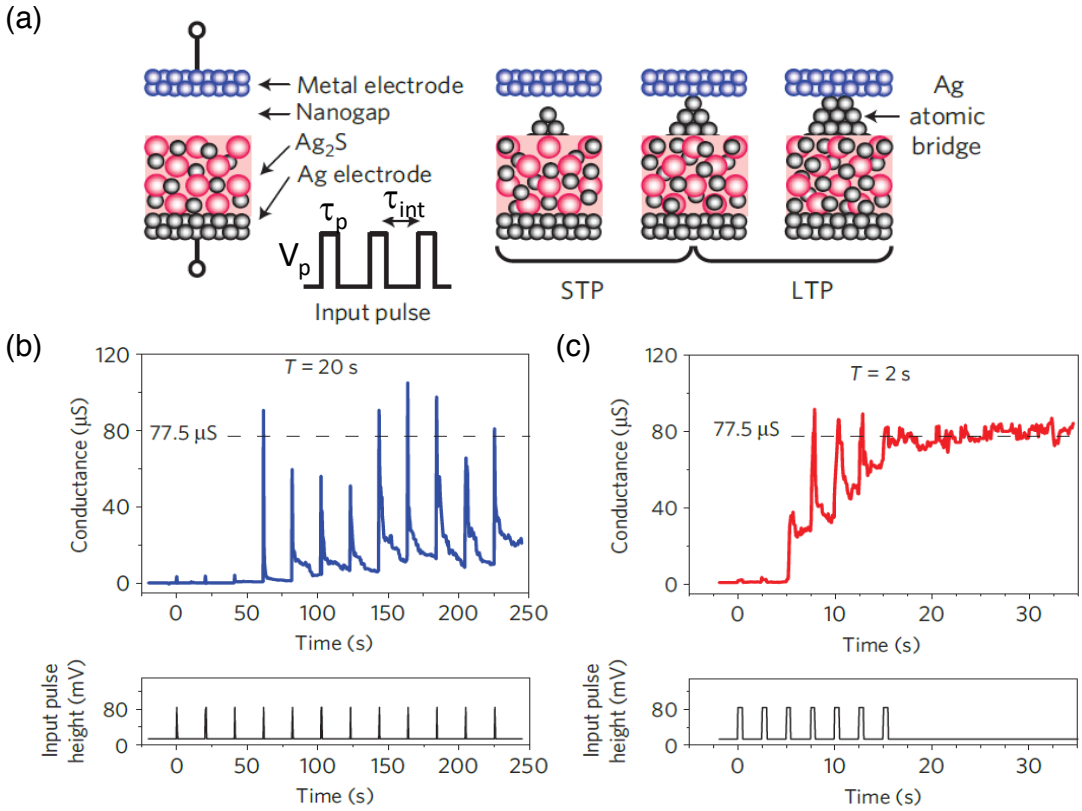

Fig. 5.3. Inorganic synaptic behaviour in the Ag/Ag$_2$S single atomic junction. (a) A schematic illustration of (left) the experimental setup and input pulses, (right) Ag atomic bridge formation process in respect to the repetition of voltage stimuli. Applied input pulses (V = 80 mV, τ_p = 0.5 s) induce the Ag filament within the gap, resulting in transition to the higher conductance state (> $1G_0$). (b) In longer pulse intervals (τ_{int} = 20 s), the G quickly decays during the interval without voltage stimuli, i.e. *short-term plasticity* (*STP*). In contrast, the voltage pulse stimuli with the short interval (τ_{int} = 2 s) induces *long-term potentiation* (*LTP*), where the Ag atomic bridge is formed, resulting in the transition from low G to high G state. Once the bridge is formed, the G stays on the high G values without additional voltage stimuli (adapted from ref.[142]).

devices require the external stimulation [270–272]. In the pulsed stimuli with the longer interval, the precipitated Ag atoms cannot accomplish the formation of a Ag bridge between Ag$_2$S and a counter electrode (see Fig. 5.3(a)). Thus, a formed protrusion is resolved back to the Ag$_2$S layer, resulting in low G states. This phenomenon, which fades away after the input pulse, is called STP.

In contrast, frequent voltage stimuli with shorter pulse intervals (τ_{int} = 2 s) induce a permanent transition from low G to high G states. As shown in Fig. 5.3(c), the decay of the G between input pulses becomes smaller with the application of the voltage pulses and the G values gradually increase. Finally, the G reached 1G$_0$, indicating a single atomic contact

[130, 135], and stay at the same states without applied stimuli. The LTP originates from a complete Ag atomic bridge formation, resulting in the permanent transition to the higher G of 1G$_0$ (see Fig. 5.3(a)). Once, the atomic bridge is formed within the gap, the lifetime of the junction is several years [157, 273].

The results in Fig. 5.3 demonstrate a single inorganic synapse in the Ag/Ag$_2$S single junction [142], which has interesting characteristics analogous to the biological organic synapses and memory in brains [274] for the application to the dynamic memorization without the external programming. Based on the insight given in the single atomic junction, atomic switch networks are described in the next section.

5.1.3 Atomic Switch Networks

Atomic switch networks (ASNs) are complex networks fabricated with self-assembled Ag nanowires with Ag$_2$S shells which work as memristive switching junctions. The estimated density of the controllable junctions is $\sim 10^9$ junctions/cm^2 and these switching junctions are distributed across the network [48, 260]. The features in ASNs described below are discussed as the collective behaviour of multiple switching activity [48, 49, 260].

The fabricated ASNs are initially at high resistance states and the networks need to be activated with voltage stimuli. Fig. 5.4(a) shows the electric current gradually increasing with applied voltage sweeps which leads to the Ag filament formation, resulting in the change in resistance from ∼10 MΩ to ∼500 Ω [260]. The I-V characteristic of the activated ASNs exhibits a pinched hysteresis (i.e. memristive behaviour [48]) as shown in Fig. 5.4(b). The existence of the hysteresis suggests that even though the MIM structure is symmetric (i.e. Ag/Ag$_2$S/Ag), which allows the Ag filament formation from both Ag electrodes, the dissolution process is faster which means that existing filaments are destroyed before another filament is formed [257]. Therefore, the I-V characteristic shows the memristive pinched hysteresis similar to that of the single atomic switch (Fig. 5.2(a)).

The nanowire networks exhibit higher harmonics generation. Fig. 5.4(c) shows a network response to a 10 Hz sinusoidal voltage signal with an amplitude of 2 V for activated ASNs. In addition to the 1st peak of the original input frequency, large peaks in higher frequency components (e.g. 2nd and 3rd) are also observed. Higher harmonic generation indicates the non-linearity of the switching junction required for deformation of an input

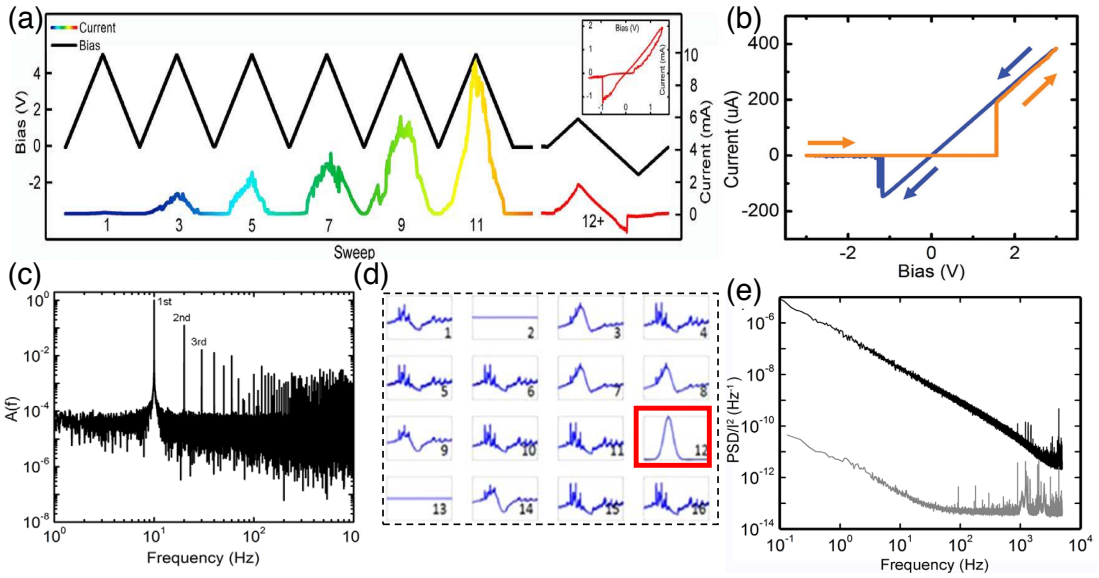

Fig. 5.4. (a) Activation of the network. Multiple voltage sweeps grow Ag filaments in the ASN, leading to the gradual increase in the current. (b) I-V characteristic obtained in ASNs shows pinched hysteresis, which is a memristive behaviour (adapted from ref.[48]). (c) Amplitude spectrum from the Fourier transform of the activated network response to a sinusoidal signal (2V, 10Hz). The observation of higher harmonics (2nd and 3rd) indicates the existence of the non-linearity in the switching junction. (d) The input signal deformation is observed in the multiple output signals (adapted from ref.[261]). The input signal is a Gaussian pulse and is applied to the electrode-12 (red box). Each output signal corresponding to the physical location exhibits the deformation of the input waveform depending on the network pathways. The transformation of the input signal into the high-dimensional output representations is a fundamental function required in reservoir computing (see the detail in Section 1.1.2). (e) The power spectral density (PSD) for the activated device (black) and non-activated Ag wire device (grey). The PSD of the activated device in (a) shows $1/f^{\beta}$ power law which indicates the existence of the recurrent delayed feedback loop in the ASNs. ((a, c, e) adapted from ref.[260]).

signal, as shown in Fig. 5.5(d). The input signal (Gaussian pulse) is applied to an electrode (red box) and output signals are recorded at each electrode corresponding to the physical location. The output signals have different waveform dependent upon the network pathways. Along with the higher harmonic generation, the deformation of the waveform indicates that the input signal is transformed into high dimensional output representations, which is a necessary functionality for reservoir computing [48, 259] (see Section 1.1.2).

Another network property is the power-law ($1/f^{\beta}$) frequency spectrum (Fig. 5.4(e)) for activated ASNs (black line). Note that the power-law behaviour is not observed in the non-activated Ag networks (grey line). The observation of the power-law PSD (power spectral density) indicates the existence of the recurrent delayed feedback loop in the network which

	Counductivity	Stable temperature
Silver (Ag)	$6.3 \times 10^5 (/\Omega\ \mathrm{cm})$	—
Acanthite (α-Ag$_2$S)	$2.5 \times 10^{-3} (/\Omega\ \mathrm{cm})$	$< 451\mathrm{K}$ (178°C)
Argentite (β-Ag$_2$S)	$1.6 \times 10^3 (/\Omega\ \mathrm{cm})$	$> 451\mathrm{K}$ (178°C)

Table 5.1: Electric properties of Ag and Ag$_2$S (α and β phases) [275]. α-Ag$_2$S is electrically and ionically insulating phase and stable at room temperature. However, under application of the bias, the phase transition from α to β becomes possible, and β-Ag$_2$S (which is a superionic conductor where Ag$^+$-ions have high mobility) can exist, leading to the chemical reaction in Eq. 5.1.

leads to complex internal coupling of the signals and constantly evolving network states [48, 262]. In other words, the switching activity has temporal correlations although rigorous analysis is necessary to discuss the correlation (Section 4.1).

The next section describes the detail of the switching mechanism with focus on the metals comprising the MIM junctions.

5.1.4 Switching Mechanisms

The Ag/Ag$_2$S-based atomic switch and ASNs exhibit brain-like properties as described in the previous sections. This behaviour originates from unique electrochemical properties of Ag$_2$S, as described in this section.

The switching activity in Ag/Ag$_2$S devices originates from the following chemical reaction leading to the Ag filament formation and dissolution in Ag$_2$S:

$$\mathrm{Ag}^+_{(\mathrm{Ag_2S})} + e^- \underset{\text{Oxidation}}{\overset{\text{Reduction}}{\rightleftarrows}} \mathrm{Ag}_{(\mathrm{metal})} \tag{5.1}$$

where $\mathrm{Ag}^+_{(\mathrm{Ag_2S})}$ is the Ag$^+$-ion in Ag$_2$S and e^- is an electron. The reduction process (i.e. the filament formation) occurs in the cathode electrode and the oxidation process (i.e. the filament dissolution) is induced in an anode electrode.

As shown in Table 5.1, while α-Ag$_2$S (Acanthite) is electrically and ionically insulating, β-Ag$_2$S (Argentite) is electrically semiconductive and ionically conductive (known as *superionic conductor*), where Ag$^+$-ions have a high mobility [275]. The α/β transition temperature is 451 K (178 °C) and thus, at room temperature, the α phase is stable, i.e. Ag$_2$S is electrically insulating. However, the transition temperature decreases under applied bias,

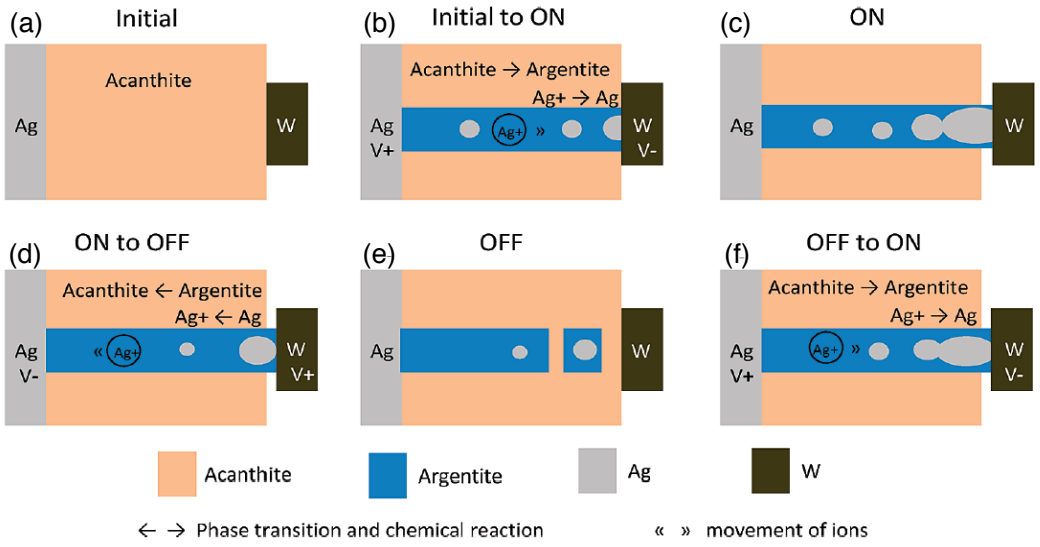

Fig. 5.5. Schematics of the electrochemical process for Ag filament formation process in the Ag/Ag$_2$S/W single junction (adapted from ref.[275]). (a) Acanthite (α-Ag$_2$S) phase before voltage application. (b) bias driven phase transition ($\alpha \rightarrow \beta$) allows migration of Ag$^+$-ions in Argentite (β-Ag$_2$S) toward a cathode (W in this example). (c) the high conductivity and the complete filament formation. (d) The opposite bias induces dissolution of the Ag filament into Ag$_2$S. (e) the switch is turned off while β-Ag$_2$Sand Ag nano-crystals can survive due to locally Ag-rich environment. (f) the switch can be turned on faster than the first bias application because the "frozen" β-Ag$_2$S and Ag nano-crystals contribute the filament formation.

and the bias driven phase transition, caused by the change of the crystal structure in Ag$_2$S [275], allows the Ag$^+$-ions to migrate in the Ag$_2$S layer.

The MIM switching junctions are classified into two types (i.e. type I and type II) according to the electrode metals. The junction configuration of type I is Ag / Ag$_2$S / an inert metal (e.g. Pt or W), which is often used in the two-terminal single atomic switch configuration [129, 142, 157]. The inert metal is electrochemically stable and does not contribute to the filament formation. Fig. 5.5 shows schematic illustrations of the electrical chemical process in the Ag/Ag$_2$S/W single junction: (a) The initial state is insulating α-Ag$_2$S. (b) The applied voltage induces a phase transition and Ag$^+$-ions migrate in β-Ag$_2$S towards a cathode. (c) Oxidation on the cathode (Ag$^+ + e^- \rightarrow$ Ag) cause the Ag filament formation. (d) An opposite bias induces the dissolution of the filament (Ag $\rightarrow$ Ag$^+ + e^-$). (e) Even in the "off" state of the atomic switch, Ag-rich environment maintains locally "frozen" states of β-Ag$_2$S without applied voltage while the switch can be fully turned off by continuous

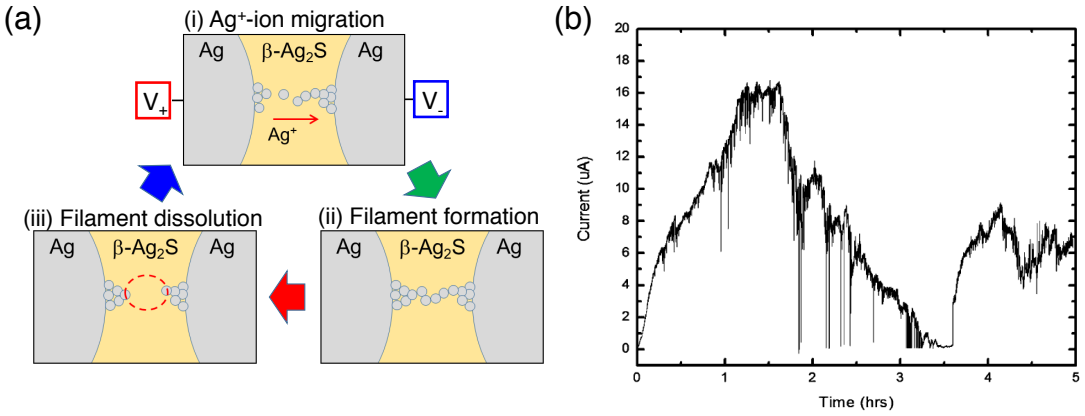

Fig. 5.6. (a) Schematic illustrations of Ag filament formation and self-dissolution process in the Ag/Ag_2S/Ag junction and (b) corresponding current fluctuation under constant DC bias (adapted from ref.[260]). Under applied bias, the bias driven phase transition of Ag_2S ($\alpha \rightarrow \beta$) and Ag^+-ions can migrate from higher potential electrode to the opposite side of the electrode as shown in (i). Once the complete filament is formed in Ag_2S like (ii), the potential difference between electrodes decreases, resulting in the thermodynamically driven dissolution of the filament, which result in filament destruction in (iii: dashed red circle). Then, the gap again appears and the formation process starts again. As shown in (b), repetition of the cycle of (i - iii) is a cause of the observed fluctuation in the electric current. Also, the various magnitude of the current change indicates the Ag/Ag_2S/Ag junctions are spatially distributed in ASNs.

application of the opposite bias. (f) The "frozen" β-Ag_2S and Ag nano-crystals contribute to the rapid filament formation during the next applied bias. This is the mechanism of the transition from STP to LTP discussed in Section 5.1.2.

On the other hand, the type II has a symmetric configuration, i.e. electrochemically active metals for both electrodes (i.e. Ag/Ag_2S/Ag) which are composed of the ASNs described in the previous section. The formation process of an Ag filament is assumed to be the same as the type I [49, 259, 261], but the opposite bias also forms an Ag filament from the other side of the electrode.

In type I, there is a natural difference in the electrochemical potential between Ag and the counter electrode (e.g. Pt or W), leading to a sustained filament without applied bias [273]. However, in the type II junction, there is no potential difference between the two Ag electrodes and the driving force for the filament formation is only the external applied bias. Thus, once the metallic filament is formed between Ag electrodes, the potential energy to drive Ag^+-ion migrations decrease. In the absence of potential difference between two Ag electrodes (see Fig. 5.6(a)-(ii)), the Ag filament in the Ag_2S is thermodynamically unstable

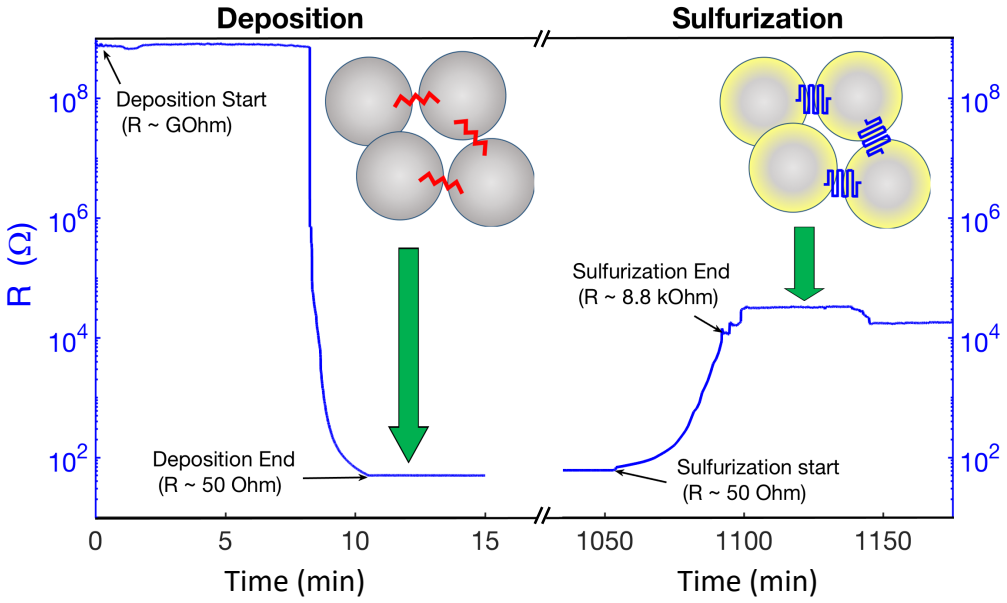

Fig. 5.7. Changes of the device resistance during fabrication process: consisting of Ag NP deposition and sulphidisation of deposited Ag NPs. NPs are deposited until R∼50 Ω where there are conducting pathways and tunnelling junctions. Then the device is sulphidised until resistance reaches 10 kΩ. Note that the resistance naturally proceeds to ∼MΩ even after the termination of sulphidisation.

[261, 262] and dissolves back into insulating high resistance states of α-Ag$_2$S without Ag filaments. When the filament is destroyed, the potential difference appears and the filament formation starts again. As shown in Fig. 5.6(a), repetition of the cycle, i.e. (i) Ag^+-ion migration → (ii) Ag filament formations → (iii) The filaments dissolution, results in a fluctuation of the electric current under constant DC bias, as shown in Fig. 5.6(b).

While there is a difference between two types of MIM when the filament is formed, the switching mechanism is believed to be the same [261, 262]. Based on the knowledge obtained in the previous research for Ag/Ag$_2$S systems, Ag/Ag$_2$S-based PNNs are fabricated, as described in the following sections.

5.2 Fabrication of Ag/Ag$_2$S-based PNNs

This section describes the fabrication procedure for the first Ag/Ag$_2$S-based PNNs at UC. In brief, the fabrication process consists of two steps: deposition of Ag NPs and then sulphidisation of them. In the following sections, the device resistance (R), instead of G, represents the network state for convenience. Fig. 5.7 shows the change in resistance

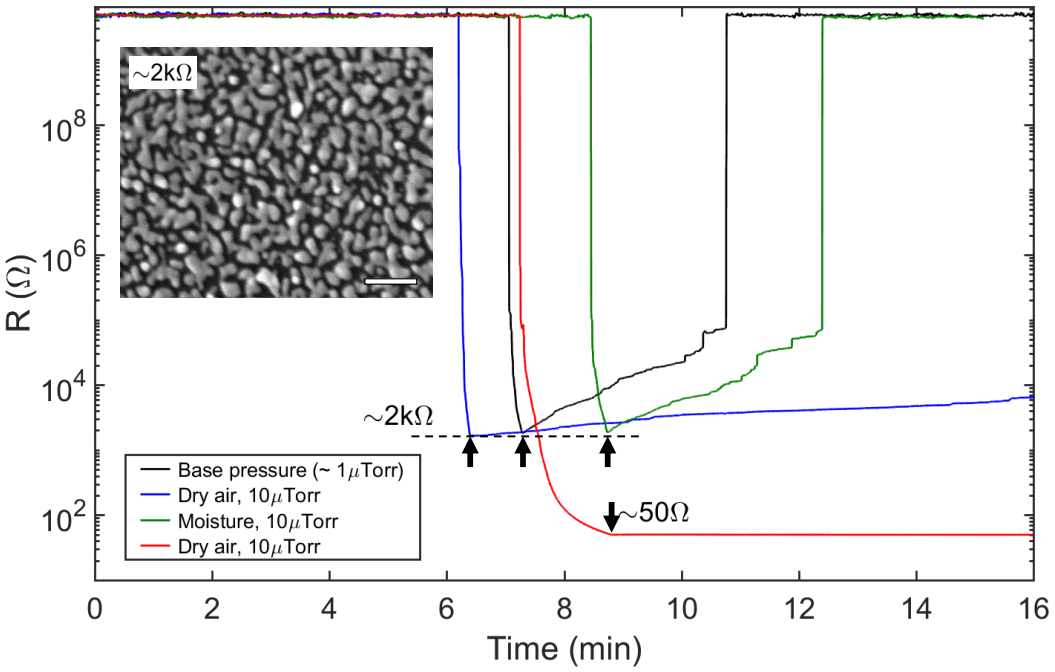

Fig. 5.8. Onset curves of resistance for different deposition conditions: (black: Ag01) Base pressure ($\sim$ 1 μTorr), (blue: Ag02) Dry air, $P_{\text{dep}} = 10$ μTorr, $R_{\text{stop}} = 2$ kΩ (green: Ag03) ambient air with moisture, $P_{\text{dep}} = 10$ μTorr, $R_{\text{stop}} = 2$ kΩ and (red: Ag13) Dry air, $P_{\text{dep}} = 10$ μTorr, $R_{\text{stop}} = 50$ Ω. All of the 2 kΩ devices were spontaneously opened before the voltage applications, but 50 Ω devises were very much stable and did not change in the resistance.

of the device during fabrication. The schematic illustrations in Fig. 5.7 depict change of the switching junctions between NPs before and after sulphidisation, i.e. from tunneling junctions (Chapter 3) to memristive Ag_2S junctions (Section 5.1). The following sections summarise the conditions for deposition and sulphidisation of Ag NPs.

5.2.1 Deposition of Ag NPs

The Ag NP deposition is performed in the same deposition system (Section 2.3) with a sputter target of Ag (99.999% pure Ag supplied by Kurt J. Lesker). In the first attempt, Ag NPs were deposited with three conditions based on Sn NP deposition, as discussed in Section 3.2. Fig. 5.8 shows the onset curves of resistance for different conditions i.e.under the base pressure ($\sim$ 1 μTorr) (black line), $P_{\text{dep}} = 10$ μTorr without moisture (blue line), and $P_{\text{dep}} = 10$ μTorr with moisture (green line). The deposition was terminated at $R_{\text{stop}} \sim 2$ kΩ (black arrows), which is the typical resistance value in the deposition of Sn NPs. As shown in Fig. 5.8, two of the 2 kΩ devices (black and green) spontaneously died after the deposition,

which means the resistance went to ∼GΩ. The device represented by the blue line also died 30 minutes after the deposition. High P_{dep} and moisture, which disrupt the coalescence in Sn NPs, do not work to stabilize the Ag NP devices. A representative SEM image of R_{stop} ∼2 kΩ in Fig. 5.8(the inset) shows the deposited Ag NPs are isolated, resulting in the disconnection of the network.

To deposit more NPs to prevent coalescence breaking up the network, the deposition was terminated at R_{stop} ∼50 Ω (red line in Fig. 5.8). Fig. 5.9(c) shows a SEM image of the 50 Ω devices which are very stable even in the ambient condition, allowing sulphidisation before oxidation of Ag NPs (also see Fig. 5.7). In short, the stability of the Ag NP devices relies on the amount of the Ag NPs rather than such factors as the P_{dep} and the amount of moisture.

5.2.2 Sulphidisation of Ag NPs

The deposited Ag NPs are sulphidised in a sulphidisation chamber in the fume hood with the *in-situ* measurement of the device resistance. Fig. 5.9(a) shows the schematic illustration of the sulphidisation setup. The Ag NP device is located 10 cm above from the hotplate and is not heated except by radiation from the hotplate. To measure the resistance during sulphidisation process, the electrodes are connected to a multimeter through copper wires with silver paste. Since the volume of silver paste is bigger than that of the deposited Ag NPs, the sulphidisation of silver paste does not affect the measured resistance of the network, i.e. the resistance between a copper wire connecting Ag paste and the same gold electrode is negligibly small. The hotplate is heated up to vaporize the sulphur powder (99.5% purity, supplied by PanReac, the melting point of S: 388K (115 °C) [108]) in the small heating boat (5mm dimple on a tungsten boat).

The sulphidisation rate is very sensitive to the hotplate temperature. Fig. 5.9(b) shows the change in resistance during the sulphidisation process for three different hotplate temperatures in 50 Ω Ag NP devices. At high temperatures (140 °C and 145 °C), the sulphidisation rate is high and the resistance of the device immediately reaches ∼MΩ and eventually rises to ∼GΩ. These over-sulphidised devices (fast sulphidisation rate) are not active when a voltage is applied, which is believed to be because there is no Ag NP, needed to form Ag filaments in the Ag/Ag$_2$S NPs, and only exists Ag$_2$S NPs.

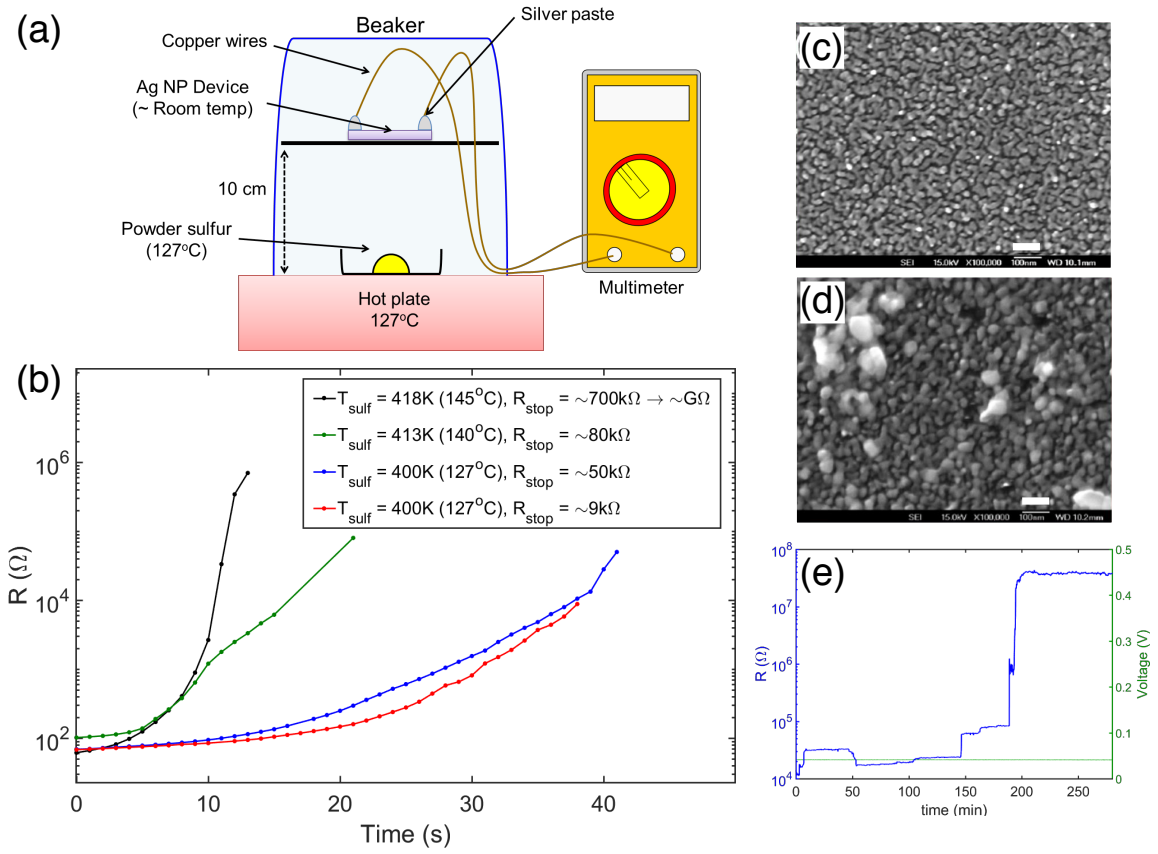

Fig. 5.9. (a) Schematic illustration of the sulphidisation chamber. The Ag NP device is located 10 cm above the hot plate and sulphidised near room temperature. The temperature of the hot plate is measured with a temperature sensor near the sulphur powder and the resistance change is monitored using the multimeter connected to the electrodes of the devices through copper wires and silver paste. The volume of the silver paste is bigger than that of NPs and the sulphidisation of the silver paste does not affect the measured resistance. (b) Changes of resistance for different temperature and termination resistance (R_{stop}) (black: AgS10, green: AgS11, blue: AgS12, red: AgS13). Sulphidisation is started after pre-heating of the hot plate (∼30 min). The sulphidisation speed is very sensitive to slight changes in temperature and high temperature (> 140 °C : black and green lines) over-sulphidise the Ag NPs, resulting in no change in resistance for applied stimuli. The lower temperature of 400K (127 °C), which is slightly above the melting point of sulphur (388 K (= 115 °C)), shows very slow resistance change. The devices fabricated with slow sulphidisation and lower R_{stop} (∼10 kΩ) can sustain various voltage stimuli. SEM images of the Ag NPs (c)before and (d) after sulphidisation in the same device. The size of NPs after sulphidisation in (d) becomes bigger than that before sulphidisation in (c). (e) The change in resistance after the termination of the sulphidisation (AgS13R03). The sulphidisation process continues on the device even without sulphur gas condition. The resistance finally stabilised around MΩ.

On the other hand, a lower hotplate temperature (127 °C) allows the Ag NPs to be slowly sulphidised whereas resistance increases quickly above 10 kΩ. The SEM images in Fig. 5.9 shows the morphology changes (c) before and (d) after sulphidisation for the slow

rate in the same device. Particle size after sulphidisation increases due to the formation of the Ag_2S shell [276]. As shown in Fig. 5.9(e), since the sulphidisation process in sulphur gas still proceeds on the devices even after termination of the sulphidisation, the resistance increases (>MΩ) and the measurements in the following sections were performed after the resistance stabilized at high values.

5.3 Properties of Ag/Ag_2S-based PNNs

Successfully sulphidised devices respond to applied voltage stimuli and show changes in resistance. This section describes the preliminary results showing network properties of Ag/Ag_2S devices and discusses the functionality compared to the previous research described in Section 5.1.

5.3.1 Network Activation

To investigate activation of the network, voltage pulses are applied in the range of voltage amplitude (V_p) from 0.1 V to 3 V with a read voltage of 50 mV (in between the pulses). Fig. 5.10 shows changes in the resistance under the applied voltage stimuli. Significant drops of the resistance were observed at $V_p = 0.4$ V. This voltage is determined as the activation voltage in the device and is ∼10 times lower than that of Sn-based device (Section 3.3.1), which implies the Ag/Ag_2S networks can be operated at lower voltage.

When the read voltage is applied between pulses, the network returns to a high resistance state, indicating Ag filament dissolution in Ag_2S layers in the switching junctions. As described in Section 5.1.4, in the symmetric MIM junctions, the formed Ag filaments dissolved back into α-Ag_2S when the applied bias is insufficient to form Ag filaments [261, 262].

To quantify the network response, average resistances during the network stimulation (R_V) and application of the read voltages (R_{int}) were obtained. Fig. 5.10(b) shows (red) R_V and (black) R_{int} as a function of the voltage amplitude. Around $V_p = 0.5$ V, both R_V and R_{int} show the significant changes to lower values. This can be understood as a consequence of the fact that higher applied voltages activate additional switching sites (Section 3.3.1) allowing formation of additional Ag filaments and also induce fast filament formation [159]. Formed filaments in the network can still exist even during application of the read voltage,

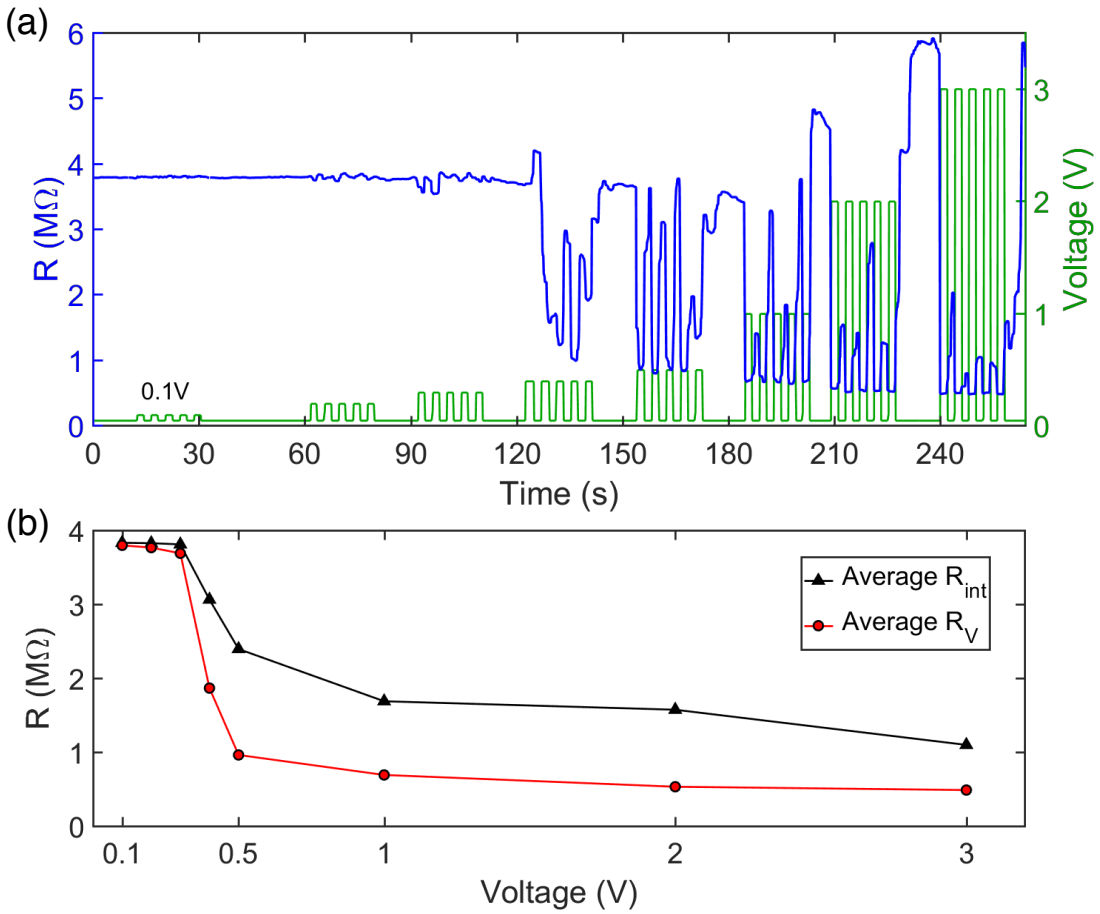

Fig. 5.10. The network response to the applied voltage pulse ($\tau_p = \tau_{\text{int}} = 2$ s, 5 pulses for each V_p) and the activation voltage (V_{th}) in this device is found to be 0.4 V which is ∼10 times lower than that of Sn-based devices (AgS11R28). (a) Resistance changes for applied voltage pulses of V_p in the range between 0.1 V and 3 V. (The read voltage is 50 mV) At $V_p = 0.4$ V, the remarkable resistance drop is observed, indicating Ag filaments are formed within the gaps in the network. (b) Averaged resistance during stimulus with V_p (R_V: red) and intervals between pulses (R_{int}: black). Above $V_p = 0.5$ V, both R_V and R_{int} saturates.

resulting in lower R_{int}.

This result indicates that one of the parameters which controls the network state is voltage amplitude. In the next section, the bias polarity of the network state is explored as another control parameter.

5.3.2 Bias Polarity Dependence of the Filament Formation

The memristive behaviour in the Ag/Ag$_2$S systems (Section 3.1) originates from the polarity dependence of the Ag filament formation and dissolution, i.e. opposite voltage enhances the

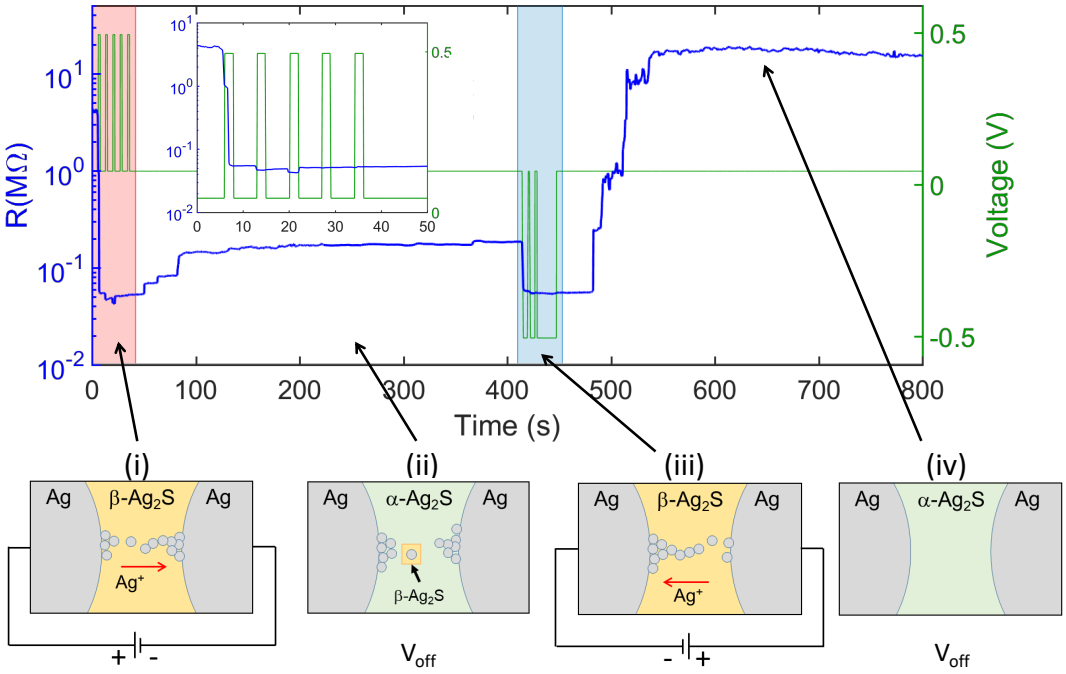

Fig. 5.11. Resistance changes for applied positive (red shaded region) and negative (blue shaded region) voltage stimuli (AgS13R06, $\tau_p = 2$ s, $\tau_{\text{int}} = 5$ s, $V_p = \pm 0.5$ V). The inset shows the first 5 positive voltage pulses and the resistance drops to ∼50 kΩ in the first pulse. Three schematic illustrations depict the Ag^+-ion movement and filament formation with respect to the applied bias. (i) the bias driven $\alpha \rightarrow \beta$ phase transition and filament formation. (ii) the filament dissolution and locally frozen β-Ag_2S. (iii) reformation of the filament with the opposite bias. (iv) back to the initial high resistance state (α-Ag_2S without filaments)

filament dissolution, leading to the high resistance state. This section examines the network response to the different polarity of the applied bias in Ag/Ag_2S-based PNNs.

Fig. 5.11 shows changes in the device resistance for applied positive (red shaded) and negative (blue shaded) voltage stimuli. The schematic illustration (i-iv) shows the states of Ag/Ag_2S junctions for each network state. The initial resistance was ∼MΩ and during the first sequence of applied voltage pulses, the resistance decreased to 50 kΩ due to Ag filament formation (see the inset and (i) in Fig. 5.11). Under a read voltage of 50 mV, the resistance of the network slowly increased, but the resistance is still lower than the initial value. This could be because some robust filaments and "frozen" β-Ag_2S [275] in the network may exist even during the application of the read voltage (see Fig. 5.11(ii)).

Negative bias was then applied with the expectation of accelerating filament dissolution leading to high resistance states in the network, as previously reported in the literature [260]. However, as shown in Fig. 5.11(blue shaded region), the resistance decreased to 50 kΩ with

negative bias stimuli, indicating another Ag filament formation from the opposite side of Ag particle. (see Fig. 5.11(iii)). When the negative bias was applied to the networks with the previously formed Ag filaments, dissolution of the filaments and formation of new filaments might occur at the same time. The observation of decrease in the resistance under negative bias stimuli implies that the filament formation is faster than the filament dissolution. A hypothesis to explain the rapid formation is that the "frozen" states of β-Ag$_2$S and Ag crystals in Ag$_2$S layer (Fig. 5.11(ii)) assist the new filament formation, resulting in the rapid filament formation in the Ag$_2$S layer [275] (also see Fig. 5.5). The network state returned to high resistance state under application of the read voltage (Fig. 5.11(iv)) due to thermodynamically driven filament dissolution [261, 262].

Although no dependence on the bias polarity in Ag/Ag$_2$S-based PNNs is observed, the fast filament formation after the first stimuli suggests the existence of system memory formed by Ag filaments and β-Ag$_2$S in the network. The stimulus frequency dependence of the network state [142] is explored in the next section.

5.3.3 Stimulus Frequency Dependent Plasticity

To investigate the stimulus frequency dependence of the network activity, short voltage pulses ($\tau_p = 0.5$ s) were applied with various intervals between the pulses (τ_{int}) in the range between 0.5 s and 5 s. Fig. 5.12 shows (a) changes in the network resistance under voltage stimuli and (b) change in R_V and R_{int} (defined in Section 5.3.1) as a function of the intervals. For voltage stimuli with longer intervals ($\tau = 3$ s and 5 s), the network returned to high resistance states during the intervals, leading to high R_{int} ($\sim$4 MΩ) in Fig. 5.12(b). In contrast, for the voltage pulse with shorter pulse intervals ($\tau = 0.5$ s and 1 s), the increase in the resistance during intervals becomes smaller, resulting in lower R_{int} in Fig. 5.12(b). This can be considered STP-like network activity with the analogy of a single Ag/Ag$_2$S junction [142], as described in Section 5.1.2. In longer pulse interval stimuli, the formed filaments can be dissolved during each interval. In contrast, the voltage pulse stimuli with shorter intervals allow additional filament formation before the previous filaments are dissolved, resulting in the enhancement of the network connectivity. This effect can be seen in the difference between R_V and R_{int}, which becomes smaller with decreases in the time intervals.

In these measurements, the transition from STP to LTP [142] was not observed and the

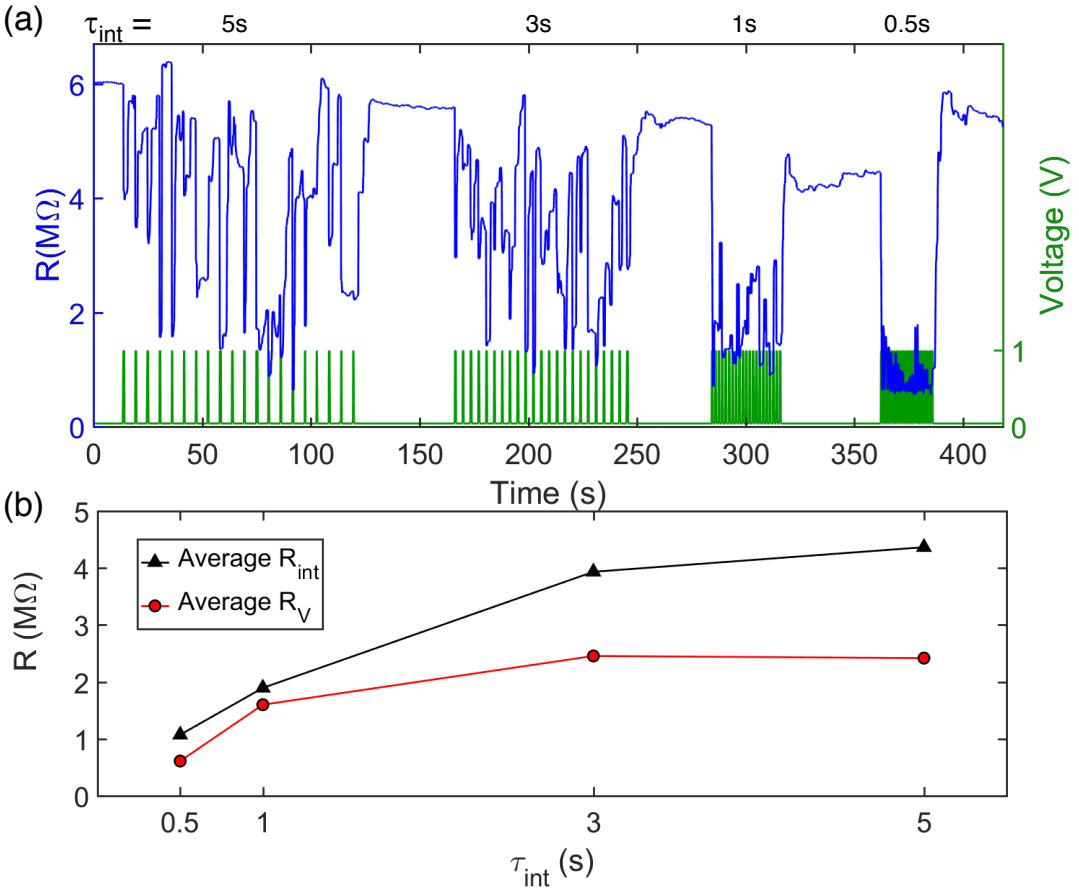

Fig. 5.12. (a) The pulse interval (τ_{int}) dependence of resistance change with fixed τ_p = 0.5 s (AgS11R26,V_p = 1V) and (b) average resistance for "on" phase (R_{on}: red) and "off" phase (R_{off}: black) of the pulses. τ_{int} is varied in the range from 0.5 s to 5 s and 20 pulses are applied for each τ_{int}. Voltage stimuli with longer τ_{int} (e.g. 3 s and 5 s) cause the Ag filaments dissolution during each interval, resulting in higher R_{int}. In contrast, voltage pulsed stimuli with shorter τ_{int} allow formation of additional filaments before previous filaments are dissolved, leading to lower R_V and R_{int} and smaller differences between them.

network quickly returned to high resistance state after stimuli. In LTP state, the strong Ag filaments are formed and the network can maintain the lower network state even during application of the read voltage [142] (also see Fig. 5.3). As shown in Fig. 5.12(b), R_V and R_{int} decreases with smaller intervals between the pulses and also the difference between R_V and R_{int} becomes smaller. This indicates more frequent stimuli ($\tau_{\text{int}} < 0.5$ s) could induce the transition to the LTP state of the network. However, in this work, 120 ms sampling speed is used in measurements with voltage pulse (Section 2.5), shorter intervals between pulses could not be used due to low time resolution.

Although further investigation is needed to characterise the network activity with re-

spect to the stimulus frequency, this result indicates the network state can be controlled by different frequency of stimuli as well as the voltage amplitude, as discussed in Section 5.3.1.

5.4 Summary

This chapter described the preliminary results for the properties of the first Ag/Ag_2S-based PNNs at UC. Stable Ag NP films were fabricated and then sulphidised. The crucial factor in the device fabrication was the control of the sulphidisation process. The successfully fabricated devices responded to voltage pulse stimuli. The activation voltage of the network was found to be ∼0.5 V, which is 10 times lower than that of Sn-based devices. The network activity was observed as a reduction in the resistance caused by the formation of Ag filaments. Also, the network activity showed stimuli frequency dependence which is related to STP in neuroscience and is indicative of the modulation of synaptic connections in the brain.

Although the basic properties of the networks have been successfully characterised, the devices were fatigued after several voltage stimuli and the network response smaller, i.e. the resistance does not significantly change (not shown). The device stability can be related to the sulphidisation condition. In this work, Ag NPs were sulphidised in the vaporized sulphur gas. While the sulphidisation rate can be controlled by temperature, it is feasible that the device might still get over-sulphidised. In over-sulphidised NPs, the Ag core, which supplies Ag^+-ions to the Ag_2S layer, is not large enough and during measurements, the core can be lost due to ion migrations. One possible solution is the use of moderate sulphidisation techniques, such as wet chemical process [277] and hydrogen sulfide (H_2S) gas sulphidisation [276]. These sulphidisation techniques proceed more slowly than the vaporized sulphur method, which also means the more controllability of the sulphidisation process is better. Another possible method is co-deposition of Ag and Ag_2S NPs [278]. This method can be achieved by introducing H_2S gas during Ag NP deposition. There is less chance of losing the Ag cores in the NPs when using this technique because the Ag NPs with an Ag_2S shell are supplied as well as bare Ag NPs.

Stabilized Ag/Ag_2S-based PNNs will provide researchers with further opportunities to investigate the network activity, including the reported deformation of the input signal

and temporal correlation in the networks [259, 261, 262]. It is expected to provide new insight into the network activity for the long term purpose of implementing neuromorphic computing.

Chapter 6

Conclusion and Future Work

Neuromorphic computing which emulates the functionalities of biological brains is at the centre of the research focus in unconventional computing frameworks. Neuromorphic hardware is expected to operate with lower energy consumption and show greater performance in such computational tasks as pattern recognition and chaotic time series predictions. Hence, there has been a surge in research efforts to develop neuromorphic hardware based on the restructuring of conventional CMOS chips and also novel functional materials.

Percolating systems poised at a critical point are promising candidates for the investigation of neuromorphic architecture. This is because the concept of percolation is a central focus of criticality and the neural networks in the brain. This thesis focused on PNNs as a platform of neuromorphic hardware implementation and investigated the network properties under external stimuli. The PNN devices were fabricated with metal NPs of Sn and Ag, which were deposited near the percolation threshold.

The primary focus of this thesis was to investigate properties of Sn-based PNN devices fabricated under optimised deposition conditions. The stable devices were activated with external voltage stimuli and presented switching events in the network observed as changes in conductance. The pulsed voltage stimuli allowed the network state to be controlled, i.e. shorter pulses enhance connectivity, resulting in higher conductance states, and in contrast, longer voltage pulses decrease conductance due to atomic wire destruction. The modulation of the network with respect to the applied stimuli is an important requirement for neuromorphic hardware.

The switching rate was controlled by the applied voltage amplitude. Higher voltages activate more switching sites in the network, and at the same time, enhance the switching activity at a single switching site, resulting in an increase in the switching rate. Switching rate was independent of the temperature near room temperature whereas there is no switching event at low temperature below ∼200K.

Under external DC voltage stimuli in Sn-based PNNs, it became clear that the switching events are bursty as well as self-similar both in time and switching event size. The IEI distributions which characterise the temporal structure of the switching events exhibited power-laws, suggesting scale-free dynamics in PNNs. The power-law hypothesis was rigorously validated with the MLE procedure and the KS test in a number of devices, for a range of stimuli and for independent measurements. The correlations among the switching events were quantified by ACFs. The ACFs obtained from the experimental data exhibited a power-law decay which is evidence of the existence of LRTCs. The LRTC in Sn-based PNNs originates from the highly correlated switching events in the underlying scale-free network structure. In neuroscience, the presence of LRTCs is related to learning ability, the maximization of the memory and the adaptability of the human brains. Furthermore, demonstration of critical dynamics is consistent with maximisation of computational performance and optimisation of information processing in PNNs.

To explore other device functionalities, Ag/AgS-based PNNs were fabricated by the sulphidisation of Ag NPs. The critical factor to stabilise the devices was found to be sulphidisation rate which is controlled by the temperature of the hot plate. Only the slow sulphidisation processes succeeded in stabilising the devices. The fabricated Ag/Ag_2S-based PNNs responded to the voltage pulse stimuli and resulted in a reduction in the device resistance due to Ag filament formation. Stimulus frequency dependent plasticity, similar to STP observed in biological synapse is an important functionality for training the Ag/Ag_2S-based network with respect to type of input stimuli.

The brain-like topographical and functional features of PNNs discussed in this work provide a platform for the development of neuromorphic hardware and open possibilities for real-world implementation within neuromorphic computing frameworks, such as reservoir computing (RC). In RC, temporal correlation is an essential requirement to project input

signals into higher dimensional spaces. Signals obtained from multiple output terminal devices can be processed by linear regression in order to implement complex computational tasks such as time series prediction and pattern recognition.

Although a number of studies have demonstrated hardware-based RC in various physical systems such as memristive cross-bar arrays and silicon-based neurons, they have still relied on a small number of device elements due to the complicated fabrication process and high research costs. In contrast, the PNNs are naturally suited for use as hardware for RC because deposition onto multi-contact-electrode arrays allows the fabrication of PNN devices with multiple inputs and outputs which are required to process the signals. Therefore, it is suggested that the focus of future work should be on computation in the framework of RC.

The ultimate aim would be to build a neuromorphic chip integrated with a CMOS processing unit and implement computational tasks on the chip. There still remains several questions such as optimisation for processing input/output signals for particular computational tasks in RC. These problems can be addressed initially by attempting simple computational tasks such as the classification between a square wave and a sinusoidal wave, and then moving to more complex tasks such as spoken-digit recognition.

Also, the insight obtained from this study could provide opportunities for the further development of percolating systems, including building of 3D percolating systems with additional complexity in the networks and introducing alternative functional materials including oxide-memristor and phase change materials. The unconventional computing hardware using PNNs could be the key to overcome the limitations of traditional hardware architecture and has potential to open new computational paradigms.

Bibliography

[1] Gordon E. Moore. Cramming more components onto integrated circuits. *Electronics*, 38:114, 1965.

[2] Christos A. Thraskias, Eythimios N. Lallas, Niels Neumann, Laurent Schares, Bert J. Offrein, Ronny Henker, Dirk Plettemeier, Frank Ellinger, Juerg Leuthold, and Ioannis Tomkos. Survey of photonic and plasmonic interconnect technologies for intra-datacenter and high-performance computing communications. *IEEE Communications Surveys and Tutorials*, 20:2758–2783, 2018.

[3] Paul A Merolla, John V Arthur, R. Alvarez-Icaza, Andrew S Cassidy, Jun Sawada, Filipp Akopyan, Bryan L Jackson, Nabil Imam, Chen Guo, Yutaka Nakamura, Bernard Brezzo, Ivan Vo, Steven K Esser, Rathinakumar Appuswamy, Brian Taba, Arnon Amir, Myron D Flickner, William P Risk, Rajit Manohar, and Dharmendra S Modha. A million spiking-neuron integrated circuit with a scalable communication network and interface. *Science*, 345:668–673, 2014.

[4] Eric R. Kandel, James H. Schwartz, and Thomas M. Jessell. *Principles of Neural Science*. McGraw-Hill, 4th edition, 2000.

[5] Hae-Jeong Park and Karl Friston. Structural and Functional Brain Networks: From Connections to Cognition. *Science*, 342:1238411–1238411, 2013.

[6] Olaf Sporns, Dante R. Chialvo, Marcus Kaiser, and Claus C. Hilgetag. Organization, development and function of complex brain networks. *Trends in Cognitive Sciences*, 8:418–425, 2004.

[7] Susana Cohen-Cory. The Developing Synapse: Construction and Modulation of Synaptic Structures and Circuits. *Science*, 298:770–776, 2002.

[8] Andrea Avena-Koenigsberger, Bratislav Misic, and Olaf Sporns. Communication dynamics in complex brain networks. *Nature Reviews Neuroscience*, 19:17–33, 2017.

[9] Domagoj Džaja, Ana Hladnik, Ivana Bičanić, Marija Baković, and Zdravko Petanjek. Neocortical calretinin neurons in primates: increase in proportion and microcircuitry structure. *Frontiers in Neuroanatomy*, 8:1–6, 2014.

[10] Robert W. Williams and Karl Herrup. The Control Of Neuron Number. *Annual Review of Neuroscience*, 11:423–453, 1988.

[11] Frederico A.C. Azevedo, Ludmila R.B. Carvalho, Lea T. Grinberg, José Marcelo Farfel, Renata E.L. Ferretti, Renata E.P. Leite, Wilson Jacob Filho, Roberto Lent, and Suzana Herculano-Houzel. Equal numbers of neuronal and nonneuronal cells make the human brain an isometrically scaled-up primate brain. *Journal of Comparative Neurology*, 513:532–541, 2009.

[12] Gerhard Roth and Ursula Dicke. Evolution of the brain and intelligence. *Trends in Cognitive Sciences*, 9:250–257, 2005.

[13] Kathleen Fitzpatrick and Nicole Tunbridge. Neurons, Synapses, and Signaling. *Pearson Education, Inc.*, 2016.

[14] Mark Mayford, Steven A. Siegelbaum, and Eric R. Kandel. Synapses and memory storage. *Cold Spring Harbor Perspectives in Biology*, 4:1–18, 2012.

[15] Timothy V.P. Bliss and Graham L. Collingridge. A synaptic model of memory: long-term potentiation in the hippocampus. *Nature*, 361:31–39, 1993.

[16] Mark F. Bear and Robert C. Malenka. Synaptic plasticity: LTP and LTD. *Current Opinion in Neurobiology*, 4:389–399, 1994.

[17] Henry Markram, Joachim Lübke, Michael Frotscher, and Bert Sakmann. Regulation of synaptic efficacy by coincidence of postsynaptic APs and EPSPs. *Science*, 275:213–215, 1997.

[18] Daniel E. Feldman. The Spike-Timing Dependence of Plasticity. *Neuron*, 75:556–571, 2012.

[19] Timothy V.P. Bliss and Sam F. Cooke. Long-term potentiation and long-term depression: a clinical perspective. *Clinics*, 66:3–17, 2011.

[20] Thomas H. Brown, Paul F. Chapman, Edward W. Kairiss, and Claude L. Keenan. Long-term synaptic potentiation. *Science*, 242:724–728, 1988.

[21] M. A. Lynch. Long-Term Potentiation and Memory. *Physiological Reviews*, 84:87–136, 2004.

[22] Dante R. Chialvo. Emergent complex neural dynamics. *Nature Physics*, 6:744–750, 2010.

[23] Rafael Yuste. From the neuron doctrine to neural networks. *Nature Reviews Neuroscience*, 16:487–497, 2015.

[24] Kevin Gurney. *An Introduction to Neural Networks*. CRC Press, 1st edition, 1997.

[25] Raúl Rojas. *Neural Networks*. Springer-Verlag Berlin Heidelberg, 1996.

[26] Jürgen Schmidhuber. Deep Learning in neural networks: An overview. *Neural Networks*, 61:85–117, 2015.

[27] Danilo P Mandic and Jonathon A Chambers. *Recurrent Neural Networks for Prediction*. John Wiley & Sons, Ltd, 2001.

[28] David Silver, Aja Huang, Chris J. Maddison, Arthur Guez, Laurent Sifre, George van den Driessche, Julian Schrittwieser, Ioannis Antonoglou, Veda Panneershelvam, Marc Lanctot, Sander Dieleman, Dominik Grewe, John Nham, Nal Kalchbrenner, Ilya Sutskever, Timothy Lillicrap, Madeleine Leach, Koray Kavukcuoglu, Thore Graepel, and Demis Hassabis. Mastering the game of Go with deep neural networks and tree search. *Nature*, 529:484–489, 2016.

[29] Gouhei Tanaka, Toshiyuki Yamane, Jean Benoit Héroux, Ryosho Nakane, Naoki Kanazawa, Seiji Takeda, Hidetoshi Numata, Daiju Nakano, and Akira Hirose. Recent

advances in physical reservoir computing: A review. *Neural Networks*, 115:100–123, 2019.

[30] Mantas Lukoševičius and Herbert Jaeger. Reservoir computing approaches to recurrent neural network training. *Computer Science Review*, 3:127–149, 2009.

[31] Benjamin Schrauwen, David Verstraeten, and Jan Van Campenhout. An overview of reservoir computing: theory, applications and implementations. *Proceedings of the 15th European Symposium on Artificial Neural Networks*, pages 471–482, 2007.

[32] Guy Van Der Sande, Daniel Brunner, and Miguel C. Soriano. Advances in photonic reservoir computing. *Nanophotonics*, 6:561–576, 2017.

[33] Yannick Viero, David Guérin, Anton Vladyka, Fabien Alibart, Stéphane Lenfant, M. Calame, and Dominique Vuillaume. Light-Stimulatable Molecules/Nanoparticles Networks for Switchable Logical Functions and Reservoir Computing. *Advanced Functional Materials*, 28:1801506, 2018.

[34] François Duport, Anteo Smerieri, Akram Akrout, Marc Haelterman, and Serge Massar. Fully analogue photonic reservoir computer. *Scientific Reports*, 6:22381, 2016.

[35] Kristof Vandoorne, Pauline Mechet, Thomas Van Vaerenbergh, Martin Fiers, Geert Morthier, David Verstraeten, Benjamin Schrauwen, Joni Dambre, and Peter Bienstman. Experimental demonstration of reservoir computing on a silicon photonics chip. *Nature Communications*, 5:3541, 2014.

[36] Chao Du, Fuxi Cai, Mohammed A. Zidan, Wen Ma, Seung Hwan Lee, and Wei D. Lu. Reservoir computing using dynamic memristors for temporal information processing. *Nature Communications*, 8:2204, 2017.

[37] Chrisantha Fernando and Sampsa Sojakka. Pattern Recognition in a Bucket. In *European conference on artificial life*, pages 588–597. 2003.

[38] Janardan Misra and Indranil Saha. Artificial neural networks in hardware: A survey of two decades of progress. *Neurocomputing*, 74:239–255, 2010.

[39] Catherine D. Schuman, Thomas E. Potok, Robert M. Patton, J. Douglas Birdwell, Mark E. Dean, Garrett S. Rose, and James S. Plank. A Survey of Neuromorphic Computing and Neural Networks in Hardware. *arXiv*, 1705:06963v1, 2017.

[40] Johannes Schemmel, Johannes Fieres, and Karlheinz Meier. Wafer-scale integration of analog neural networks. In *2008 IEEE International Joint Conference on Neural Networks (IEEE World Congress on Computational Intelligence)*, pages 431–438. IEEE, 2008.

[41] Steve Furber. Large-scale neuromorphic computing systems. *Journal of Neural Engineering*, 13:051001, 2016.

[42] Michael Hopkins, Garibaldi Pineda-García, Petru A. Bogdan, and Steve B. Furber. Spiking neural networks for computer vision. *Interface Focus*, 8:20180007, 2018.

[43] Ben Varkey Benjamin, Peiran Gao, Emmett McQuinn, Swadesh Choudhary, Anand R. Chandrasekaran, Jean Marie Bussat, Rodrigo Alvarez-Icaza, John V. Arthur, Paul A. Merolla, and Kwabena Boahen. Neurogrid: A mixed-analog-digital multichip system for large-scale neural simulations. *Proceedings of the IEEE*, 102:699–716, 2014.

[44] Robert F. Service. The brain chip. *Science*, 345:614–616, 2014.

[45] Andrea Calimera, Enrico Macii, and Massimo Poncino. The Human Brain Project and neuromorphic computing. *Functional Neurology*, 28:191–196, 2013.

[46] Mike Davies, Narayan Srinivasa, Tsung Han Lin, Gautham Chinya, Yongqiang Cao, Sri Harsha Choday, Georgios Dimou, Prasad Joshi, Nabil Imam, Shweta Jain, Yuyun Liao, Chit Kwan Lin, Andrew Lines, Ruokun Liu, Deepak Mathaikutty, Steven McCoy, Arnab Paul, Jonathan Tse, Guruguhanathan Venkataramanan, Yi Hsin Weng, Andreas Wild, Yoonseok Yang, and Hong Wang. Loihi: A Neuromorphic Manycore Processor with On-Chip Learning. *IEEE Micro*, 38:82–99, 2018.

[47] Sandeep Ravindran. Building a Silicon Brain (The Scientist: https://www.the-scientist.com/features/building-a-silicon-brain-65738), 2019.

[48] Audrius V Avizienis, Henry O Sillin, Cristina Martin-Olmos, Hsien Hang Shieh, Masakazu Aono, Adam Z Stieg, and James K Gimzewski. Neuromorphic atomic switch networks. *PloS one*, 7:e42772, 2012.

[49] Adam Z. Stieg, Audrius V. Avizienis, Henry O. Sillin, Cristina Martin-Olmos, Masakazu Aono, and James K. Gimzewski. Emergent criticality in complex turing B-type atomic switch networks. *Advanced Materials*, 24:286–293, 2012.

[50] Saurabh K. Bose, Joshua B. Mallinson, Rodrigo M. Gazoni, and Simon A. Brown. Stable Self-Assembled Atomic-Switch Networks for Neuromorphic Applications. *IEEE Transactions on Electron Devices*, 64:5194–5201, 2017.

[51] Saurabh K. Bose, Shirai Shota, Joshua B. Mallinson, and Simon A. Brown. Synaptic dynamics in complex self-assembled nanoparticle networks. *Faraday Discussions*, 213:471–485, 2019.

[52] Abdul Sattar, Shawn Fostner, and Simon A. Brown. Quantized Conductance and Switching in Percolating Nanoparticle Films. *Physical Review Letters*, 111:136808, 2013.

[53] Scott M. Woodley and Stefan T. Bromley. *Introduction to modeling nanoclusters and nanoparticles*. Elsevier Ltd., 2019.

[54] Riccardo Ferrando and Francesca Baletto. Structural properties of nanoclusters: Energetic, thermodynamic, and kinetic effects. *Reviews of Modern Physics*, 77:371–423, 2005.

[55] Xi-Feng Zhang, Zhi-Guo Liu, Wei Shen, and Sangiliyandi Gurunathan. Silver Nanoparticles: Synthesis, Characterization, Properties, Applications, and Therapeutic Approaches. *International Journal of Molecular Sciences*, 17:1534, 2016.

[56] J. G. Partridge, R. Reichel, A. Ayesh, D. M. A. Mackenzie, and S. A. Brown. Production and assembly of atomic clusters. *physica status solidi (a)*, 203:1217–1222, 2006.

[57] Kheng Chok Tee, Andreas Lassesson, Joris Van Lith, Simon A. Brown, Jim G. Partridge, Monica Schulze, and Richard J. Blaikie. Selective filling and sintering of copper nanoclusters for interconnect. *IEEE Transactions on Nanotechnology*, 6:556–560, 2007.

[58] R. Reichel, J. G. Partridge, F. Natali, T. Matthewson, S. A. Brown, A. Lassesson, D. M. A. Mackenzie, A. I. Ayesh, K. C. Tee, A. Awasthi, and S. C. Hendy. From the adhesion of atomic clusters to the fabrication of nanodevices. *Applied Physics Letters*, 89:213105, 2006.

[59] S. R. Broadbent and J. M. Hammersley. Percolation processes. *Mathematical Proceedings of the Cambridge Philosophical Society*, 53:629–641, 1957.

[60] Dietrich Stauffer and Amnon Aharony. *Introduction To Percolation Theory.* Taylor & Francis, 2003.

[61] Scott Kirkpatrick. Percolation and Conduction. *Reviews of Modern Physics*, 45:574–588, 1973.

[62] Abbas Ali Saberi. Recent advances in percolation theory and its applications. *Physics Reports*, 578:1–32, 2015.

[63] Ilya A. Gruzberg, Andreas W.W. Ludwig, and N. Read. Exact exponents for the spin quantum hall transition. *Physical Review Letters*, 82:4524–4527, 1999.

[64] Abbas Ali Saberi. Geometrical phase transition on WO3 surface. *Applied Physics Letters*, 97:154102, 2010.

[65] Muhammad Sahimi. Flow phenomena in rocks: From continuum models to fractals, percolation, cellular automata, and simulated annealing. *Reviews of Modern Physics*, 65:1393–1534, 1993.

[66] M. B. Isichenko. Percolation, statistical topography, and transport in random media. *Reviews of Modern Physics*, 64:961–1043, 1992.

[67] Samartha G. Anekal, Pradipkumar Bahukudumbi, and Michael A. Bevan. Dynamic

signature for the equilibrium percolation threshold of attractive colloidal fluids. *Physical Review E*, 73:020403, 2006.

[68] Nicoletta Gnan, Emanuela Zaccarelli, and Francesco Sciortino. Casimir-like forces at the percolation transition. *Nature Communications*, 5:3267, 2014.

[69] Muhammad Sahimi. *Applications of Percolation Theory*. Taylor & Francis, 1994.

[70] Gerhard Werner. Fractals in the nervous system: conceptual implications for theoretical neuroscience. *Frontiers in Physiology*, 1:1–28, 2010.

[71] Joseph W. Larkin, Xiaoling Zhai, Kaito Kikuchi, Samuel E. Redford, Arthur Prindle, Jintao Liu, Sacha Greenfield, Aleksandra M. Walczak, Jordi Garcia-Ojalvo, Andrew Mugler, and Gürol M. Süel. Signal Percolation within a Bacterial Community. *Cell Systems*, 7:137–145, 2018.

[72] Jean-Paul Metzger and Henri Décamps. The structural connectivity threshold: An hypothesis in conservation biology at the landscape scale. *Acta Oecologica*, 18:1–12, 1997.

[73] Imre Derényi, Gergely Palla, and Tamás Vicsek. Clique Percolation in Random Networks. *Physical Review Letters*, 94:160202, 2005.

[74] Duncan S. Callaway, M. E. J. Newman, Steven H. Strogatz, and Duncan J. Watts. Network Robustness and Fragility: Percolation on Random Graphs. *Physical Review Letters*, 85:5468–5471, 2000.

[75] Joshua B. Mallinson, Shota Shirai, Susant K. Acharya, Saurabh K. Bose, Galli Edoard, and Simon A. Brown. Avalanches and criticality in self-organised nanoscale networks. *Science Advances*, 5:eaaw8438, 2019.

[76] Edward. T. Gawlinski and H. Eugene Stanley. Continuum percolation in two dimensions: Monte Carlo tests of scaling and universality for non-interacting discs. *Journal of Physics A: Mathematical and General*, 14:L291–L299, 1981.

[77] Harry Kesten. The critical probability of bond percolation on the square lattice equals 1/2. *Communications in Mathematical Physics*, 74:41–59, 1980.

[78] John C. Wierman. A bond percolation critical probability determination based on the star-triangle transformation. *Journal of Physics A: Mathematical and General*, 17:1525–1530, 1984.

[79] Shawn Fostner, Richard Brown, James Carr, and Simon A. Brown. Continuum percolation with tunneling. *Physical Review B*, 89:075402, 2014.

[80] Shawn Fostner and Simon A. Brown. Neuromorphic behavior in percolating nanoparticle films. *Physical Review E*, 92:052134, 2015.

[81] Benoit B. Mandelbrot. How Long Is the Coast of Britain? Statistical Self-Similarity and Fractional Dimension. *Science*, 156:636–638, 1967.

[82] Antonio Di Ieva, Fabio Grizzi, Herbert Jelinek, Andras J. Pellionisz, and Gabriele Angelo Losa. Fractals in the neurosciences, part I: General principles and basic neurosciences. *Neuroscientist*, 20:403–417, 2014.

[83] Richard Hardstone, Simon-Shlomo Poil, Giuseppina Schiavone, Rick Jansen, Vadim V. Nikulin, Huibert D. Mansvelder, and Klaus Linkenkaer-Hansen. Detrended Fluctuation Analysis: A Scale-Free View on Neuronal Oscillations. *Frontiers in Physiology*, 3:1–13, 2012.

[84] Albert-László Barabási and Réka Albert. Emergence of Scaling in Random Networks. *Science*, 286:509–512, 1999.

[85] M. E. J. Newman. The Structure and Function of Complex Networks. *SIAM Review*, 45:167–256, 2003.

[86] Cornelis J. Stam and Jaap C. Reijneveld. Graph theoretical analysis of complex networks in the brain. *Nonlinear Biomedical Physics*, 1:3, 2007.

[87] Victor M. Eguíluz, Dante R Chialvo, Guillermo A Cecchi, Marwan Baliki, and A Vania Apkarian. Scale-free brain functional networks. *Physical Review Letters*, 94:018102, 2005.

[88] Anna D. Broido and Aaron Clauset. Scale-free networks are rare. *Nature Communications*, 10:1–10, 2019.

[89] Michael Lucy. Fractals in nature (https://cosmosmagazine.com/mathematics/fractals-in-nature).

[90] Ary L. Goldberger, Luis A. N. Amaral, Jeffrey M. Hausdorff, Plamen Ch. Ivanov, C.-K. Peng, and H. Eugene Stanley. Fractal dynamics in physiology: Alterations with disease and aging. *Proceedings of the National Academy of Sciences*, 99:2466–2472, 2002.

[91] Armin Bunde and Jan W. Kantelhardt. Diffusion and Conduction in Percolation Systems. In *Diffusion in Condensed Matter*, pages 895–914. Springer-Verlag, Berlin/Heidelberg, 2005.

[92] James B. Bassingthwaighte, Larry S. Liebovitch, and Bruce J. West. *Fractal Physiology*. Springer New York, 1994.

[93] Bruce J. West and William Deering. Fractal physiology for physicists: Lévy statistics. *Physics Reports*, 246:1–100, 1994.

[94] Bruce J. West. Fractal physiology and the fractional calculus: a perspective. *Frontiers in Physiology*, 1:1–17, 2010.

[95] John M. Beggs. The criticality hypothesis: How local cortical networks might optimize information processing. *Philosophical Transactions of the Royal Society A: Mathematical, Physical and Engineering Sciences*, 366:329–343, 2008.

[96] Nir Friedman, Shinya Ito, Braden A.W. Brinkman, Masanori Shimono, R. E.Lee Deville, Karin A. Dahmen, John M. Beggs, and Thomas C. Butler. Universal critical dynamics in high resolution neuronal avalanche data. *Physical Review Letters*, 108:208102, 2012.

[97] Enzo Tagliazucchi, Pablo Balenzuela, Daniel Fraiman, and Dante R. Chialvo. Criticality in Large-Scale Brain fMRI Dynamics Unveiled by a Novel Point Process Analysis. *Frontiers in Physiology*, 3:1–12, 2012.

[98] David L. Gilden. Cognitive emissions of 1/f noise. *Psychological Review*, 108:33–56, 2001.

[99] Paolo Allegrini, Danilo Menicucci, Remo Bedini, Leone Fronzoni, Angelo Gemignani, Paolo Grigolini, Bruce J. West, and Paolo Paradisi. Spontaneous brain activity as a source of ideal 1/f noise. *Physical Review E*, 80:061914, 2009.

[100] Miguel A. Muñoz. Colloquium : Criticality and dynamical scaling in living systems. *Reviews of Modern Physics*, 90:031001, 2018.

[101] Dietrich Stauffer. Scaling theory of percolation clusters. *Physics Reports*, 54:1–74, 1979.

[102] Mitsunobu Nakamura. Fractal property of two-dimensional continuum percolation clusters. *Physical Review A*, 34:3356–3361, 1986.

[103] Hernán D. Rozenfeld and Hernán A. Makse. Fractality and the percolation transition in complex networks. *Chemical Engineering Science*, 64:4572–4575, 2009.

[104] Richard F. Voss. The fractal dimension of percolation cluster hulls. *Journal of Physics A: Mathematical and General*, 17:L373–L377, 1984.

[105] Jie Liu and Klaus Regenauer-Lieb. Application of percolation theory to microtomography of structured media: Percolation threshold, critical exponents, and upscaling. *Physical Review E*, 83:016106, 2011.

[106] Réka Albert and Albert-László Barabási. Statistical mechanics of complex networks. *Reviews of Modern Physics*, 74:47–97, 2002.

[107] Chloé Minnai, Andrea Bellacicca, Simon A Brown, and Paolo Milani. Facile fabrication of complex networks of memristive devices. *Scientific Reports*, 7:7955, 2017.

[108] David R. Lide. *CRC Handbook of Chemistry and Physics, 84th Edition, 2003-2004*. 2003.

[109] Mel Schwarts. *Encyclopedia of materials, parts, and finishes*. CRC Press, 2nd edition, 2002.

[110] Hideki Masuda. Combined Transmission Electron Microscopy In situ Observation of the Formation Process and Measurement of Physical Properties for Single Atomic-

Sized Metallic Wires. In *Modern Electron Microscopy in Physical and Life Sciences*. InTech, 2016.

[111] Michael Faraday. Experimental Researches in Electricity. Fourth Series. *Philosophical Transactions of the Royal Society*, 123:507–522, 1833.

[112] R. C. Sharma and Y. A. Chang. The AgS (Silver-Sulfur) system. *Bulletin of Alloy Phase Diagrams*, 7:263–269, 1986.

[113] Carl Wagner. Investigations on silver sulfide. *The Journal of Chemical Physics*, 21:1819–1827, 1953.

[114] H. Schmalzried. Ag2S-The physical chemistry of an inorganic material. *Progress in Solid State Chemistry*, 13:119–157, 1980.

[115] H. Ohno and Y. Katano. Electrical Properties of Silicon Nitride. *Materials Science Forum*, 47:215–227, 1991.

[116] Abdul Sattar. *Electrical Characterization of Cluster Devices*. Phd thesis, University of Canterbury, 2011.

[117] Ahmad Ayesh. *Device fabrication using Bi nanoclusters*. Phd thesis, University of Canterbury, 2007.

[118] René Reichel, Jim G. Partridge, Alan D.F. Dunbar, Simon A. Brown, Owen Caughley, and Ahmad Ayesh. Construction and application of a UHV compatible cluster deposition system. *Journal of Nanoparticle Research*, 8:405–416, 2006.

[119] René Reichel. *Nano Scale Cluster Devices*. Phd thesis, University of Canterbury, 2007.

[120] Thomas Francis Watson. *Tin Oxide Cluster Assembled Films: Morphology and Gas Sensor*. PhD thesis, 2009.

[121] B. von Issendorff and R. E. Palmer. A new high transmission infinite range mass selector for cluster and nanoparticle beams. *Review of Scientific Instruments*, 70:4497–4501, 1999.

[122] Ashley R Clarke and Colin N Eberhardt. *Microscopy techniques for materials science*. CRC Press, 2002.

[123] Ludwig Reimer. *Scanning Electron Microscopy - Physics of Image Formation and Microanalysis*. Springer-Verlag Berlin Heidelberg, second edition, 1998.

[124] J. Schmelzer, S. A. Brown, A. Wurl, M. Hyslop, and R. J. Blaikie. Finite-Size Effects in the Conductivity of Cluster Assembled Nanostructures. *Physical Review Letters*, 88:226802, 2002.

[125] M. Schulze, S. Gourley, S. A. Brown, A. Dunbar, J. Partridge, and R. J. Blaikie. Electrical measurements of nanoscale bismuth cluster films. *The European Physical Journal D - Atomic, Molecular and Optical Physics*, 24:291–294, 2003.

[126] P. Y. Convers, D. N. McCarthy, A. Sattar, F. Natali, S. C. Hendy, and S. A. Brown. Electrical signature of nanoscale coalescence in a percolating Bi nanocluster film. *Physical Review B*, 82:115409, 2010.

[127] A. D. F. Dunbar, J. G. Partridge, M. Schulze, and S. A. Brown. Morphological differences between Bi, Ag and Sb nano-particles and how they affect the percolation of current through nano-particle networks. *European Physical Journal D*, 39:415–422, 2006.

[128] A. Lassesson, M. Schulze, J van Lith, and S. A. Brown. Tin oxide nanocluster hydrogen and ammonia sensors. *Nanotechnology*, 19:015502, 2008.

[129] K. Terabe, T. Hasegawa, T. Nakayama, and M. Aono. Quantized conductance atomic switch. *Nature*, 433:47–50, 2005.

[130] B. J. van Wees, H. van Houten, C. W J Beenakker, J. G. Williamson, L. P. Kouwenhoven, D. van der Marel, and C. T. Foxon. Quantized conductance of point contacts in a two-dimensional electron gas. *Physical Review Letters*, 60:848–850, 1988.

[131] Supriyo Datta. *Electronic Transport in Mesoscopic Systems*. Cambridge University Press, 1995.

[132] D A Wharam, T J Thornton, R Newbury, M Pepper, H Ahmed, J E F Frost, D G Hasko, D C Peacock, D A Ritchie, and G A C Jones. One-dimensional transport and the quantisation of the ballistic resistance. *Journal of Physics C: Solid State Physics*, 21:L209–L214, 1988.

[133] R. Tolley, A. Silvidi, C. Little, and K. F. Eid. Conductance quantization: A laboratory experiment in a senior-level nanoscale science and technology course. *American Journal of Physics*, 81:14–19, 2013.

[134] N. Agraït, J. G. Rodrigo, and S. Vieira. Conductance steps and quantization in atomic-size contacts. *Physical Review B*, 47:12345–12348, 1993.

[135] Nicolás Agraït, Alfredo Levy Yeyati, and Jan M. van Ruitenbeek. Quantum properties of atomic-sized conductors. *Physics Reports*, 377:81–279, 2003.

[136] J. M. Krans, J. M. van Ruitenbeek, V. V. Fisun, I. K. Yanson, and L. J. de Jongh. The signature of conductance quantization in metallic point contacts. *Nature*, 375:767–769, 1995.

[137] C. J. Muller, J. M. Krans, T. N. Todorov, and M. A. Reed. Quantization effects in the conductance of metallic contacts at room temperature. *Physical Review B*, 53:1022–1025, 1996.

[138] J. K. Gimzewski and R. Möller. Transition from the tunneling regime to point contact studied using scanning tunneling microscopy. *Physical Review B*, 36:1284–1287, 1987.

[139] C. J. Muller, J. M. van Ruitenbeek, and L. J. de Jongh. Conductance and supercurrent discontinuities in atomic-scale metallic constrictions of variable width. *Physical Review Letters*, 69:140–143, 1992.

[140] A. I. Yanson, G. Rubio Bollinger, H. E. Van Den Brom, N. Agraït, and J. M. Van Ruitenbeek. Formation and manipulation of a metallic wire of single gold atoms. *Nature*, 395:783–785, 1998.

[141] Hideaki Ohnishi, Yukihito Kondo, and Kunio Takayanagi. Quantized conductance through individual rows of suspended gold atoms. *Nature*, 395:780–783, 1998.

[142] Takeo Ohno, Tsuyoshi Hasegawa, Tohru Tsuruoka, Kazuya Terabe, James K. Gimzewski, and Masakazu Aono. Short-term plasticity and long-term potentiation mimicked in single inorganic synapses. *Nature Materials*, 10:591–595, 2011.

[143] Alpana Nayak, Tohru Tsuruoka, Kazuya Terabe, Tsuyoshi Hasegawa, and Masakazu Aono. Switching kinetics of a Cu 2 S-based gap-type atomic switch. *Nanotechnology*, 22:235201, 2011.

[144] Alpana Nayak, Takeo Ohno, Tohru Tsuruoka, Kazuya Terabe, Tsuyoshi Hasegawa, James K. Gimzewski, and Masakazu Aono. Controlling the Synaptic Plasticity of a Cu2S Gap-Type Atomic Switch. *Advanced Functional Materials*, 22:3606–3613, 2012.

[145] Martin Olsen, Magnus Hummelgård, and Håkan Olin. Surface Modifications by Field Induced Diffusion. *PLoS ONE*, 7:e30106, 2012.

[146] Th. Ganetsos, A. W. R. Mair, G. L. R. Mair, L. Bischoff, Ch. Akhmadaliev, and C. J. Aidinis. Can direct field-evaporation of doubly charged ions and post-ionisation from the singly charged state co-exist? *Surface and Interface Analysis*, 39:128–131, 2007.

[147] Paul S. Ho and Thomas Kwok. Electromigration in metals. *Reports on Progress in Physics*, 52:301–348, 1989.

[148] H. C. Yu, S. H. Liu, and Chih Chen. Study of electromigration in thin tin film using edge displacement method. *Journal of Applied Physics*, 98:98–101, 2005.

[149] Kari E.J. Lehtinen and Michael R Zachariah. Effect of coalescence energy release on the temporal shape evolution of nanoparticles. *Physical Review B - Condensed Matter and Materials Physics*, 63:1–7, 2001.

[150] M. José-Yacamán, C. Gutierrez-Wing, M. Miki, D. Q. Yang, K. N. Piyakis, and E. Sacher. Surface diffusion and coalescence of mobile metal nanoparticles. *Journal of Physical Chemistry B*, 109:9703–9711, 2005.

[151] Dorel Moldovan, Vesselin Yamakov, Dieter Wolf, and Simon R. Phillpot. Scaling Behavior of Grain-Rotation-Induced Grain Growth. *Physical Review Letters*, 89:206101, 2002.

[152] Sungil Cho, Jin Yu, Sung K. Kang, and Da Yuan Shih. Oxidation study of pure tin and its alloys via electrochemical reduction analysis. *Journal of Electronic Materials*, 34:635–642, 2005.

[153] Aaron Stockdill. *Neuromorphic Computing with Reservoir Neural Networks on Memristive Hardware*. Cosc460 research project, Universioty of Canterbuty, 2016.

[154] K. Tsunoda, Y. Fukuzumi, J. R. Jameson, Z. Wang, P. B. Griffin, and Y. Nishi. Bipolar resistive switching in polycrystalline TiO2 films. *Applied Physics Letters*, 90:113501, 2007.

[155] G. R. Stewart. Measurement of lowtemperature specific heat. *Review of Scientific Instruments*, 54:1–11, 1983.

[156] Tsuyoshi Hasegawa, Takeo Ohno, Kazuya Terabe, Tohru Tsuruoka, Tomonobu Nakayama, James K. Cimzewski, and Masakazu Aono. Learning abilities achieved by a single solid-state atomic switch. *Advanced Materials*, 22:1831–1834, 2010.

[157] Tsuyoshi Hasegawa, Kazuya Terabe, Tohru Tsuruoka, and Masakazu Aono. Atomic switch: Atom/ion movement controlled devices for beyond von-Neumann computers. *Advanced Materials*, 24:252–267, 2012.

[158] Henry O. Sillin, Eric J. Sandouk, Audrius V. Avizienis, Masakazu Aono, Adam Z. Stieg, and James K. Gimzewski. Benchtop Fabrication of Memristive Atomic Switch Networks. *Journal of Nanoscience and Nanotechnology*, 14:2792–2798, 2014.

[159] Takuro Tamura, Tsuyoshi Hasegawa, Kazuya Terabe, Tomonobu Nakayama, Toshitsugu Sakamoto, Hajime Sunamura, Hisao Kawaura, Sumio Hosaka, and Masakazu Aono. Switching Property of Atomic Switch Controlled by Solid Electrochemical Reaction. *Japanese Journal of Applied Physics*, 45:L364–L366, 2006.

[160] Jonathan R. Whitlock. Learning Induces Long-Term Potentiation in the Hippocampus. *Science*, 313:1093–1097, 2006.

[161] S. J. Martin, P. D. Grimwood, and R. G. M. Morris. Synaptic Plasticity and Memory: An Evaluation of the Hypothesis. *Annual Review of Neuroscience*, 23:649–711, 2000.

[162] Dana H. Ballard. *Brain Computation as Hierarchical Abstraction*. The MIT Press, 2015.

[163] Christopher Chatfield. *Time-Series Forecasting*. Chapman and Hall/CRC, 2000.

[164] George E. P. Box, Gwilym M. Jenkins, Gregory C. Reinsel, and Greta M. Ljung. *Time Series Analysis*. Wiley Series in Probability and Statistics. Wiley, 5th edition, 2015.

[165] Christopher Chatfield. *The Analysis of Time Series*. Chapman and Hall/CRC, 6th edition, 2016.

[166] Newbold Bracewell Ronald. *The Fourier Transform and Its Applications*. McGraw-Hill Kogakusha, Ltd., 3rd edition, 2000.

[167] William H Press, Saul A Teukolsky, William T Vetterling, and Brian P Flannery. *Numerical Recipes in Fortran: The Art of Scientific Computing*. Cambridge University Press, 2nd edition, 1993.

[168] Andrea Vassallo, Michela Chiappalone, Ricardo De Camargos Lopes, Bibiana Scelfo, Antonio Novellino, Enrico Defranchi, Taina Palosaari, Timo Weisschu, Tzutzuy Ramirez, Sergio Martinoia, Andrew F.M. Johnstone, Cina M. Mack, Robert Landsiedel, Maurice Whelan, Anna Bal-Price, and Timothy J. Shafer. A multi-laboratory evaluation of microelectrode array-based measurements of neural network activity for acute neurotoxicity testing. *NeuroToxicology*, 60:280–292, 2017.

[169] M. Abeles, H. Bergman, E. Margalit, and E. Vaadia. Spatiotemporal firing patterns in the frontal cortex of behaving monkeys. *Journal of Neurophysiology*, 70:1629–1638, 1993.

[170] Johnatan Aljadeff, Benjamin J. Lansdell, Adrienne L. Fairhall, and David Kleinfeld. Analysis of Neuronal Spike Trains, Deconstructed. *Neuron*, 91:221–259, 2016.

[171] Malvin C. Teich, Conor Heneghan, Steven B. Lowen, Tsuyoshi Ozaki, and Ehud Kaplan. Fractal character of the neural spike train in the visual system of the cat. *Journal of the Optical Society of America A*, 14:529, 1997.

[172] Jing Hu, Yi Zheng, and Jianbo Gao. Long-Range Temporal Correlations, Multifractality, and the Causal Relation between Neural Inputs and Movements. *Frontiers in Neurology*, 4:1–11, 2013.

[173] S. P. Strong, Roland Köberle, Rob R. de Ruyter van Steveninck, and William Bialek. Entropy and Information in Neural Spike Trains. *Physical Review Letters*, 80:197–200, 1998.

[174] Ilya Nemenman, William Bialek, and Rob de Ruyter van Steveninck. Entropy and information in neural spike trains: Progress on the sampling problem. *Physical Review E*, 69:056111, 2004.

[175] John M Beggs and Dietmar Plenz. Neuronal Avalanches in Neocortical Circuits. *The Journal of Neuroscience*, 23:11167–11177, 2003.

[176] Lubomir Kostal, Petr Lansky, and Jean Pierre Rospars. Neuronal coding and spiking randomness. *European Journal of Neuroscience*, 26:2693–2701, 2007.

[177] Filip Ponulak and Andrzej Kasinski. Introduction to spiking neural networks: Information processing, learning and applications. *Acta neurobiologiae experimentalis*, 71:409–33, 2011.

[178] Albert-László Barabási. The origin of bursts and heavy tails in human dynamics. *Nature*, 435:207–211, 2005.

[179] Frank A Haight. *Handbook of the Poisson distribution*. New York, Wiley, 1967.

[180] Alberto Mazzoni, Frédéric D. Broccard, Elizabeth Garcia-Perez, Paolo Bonifazi, Maria Elisabetta Ruaro, and Vincent Torre. On the Dynamics of the Spontaneous Activity in Neuronal Networks. *PLoS ONE*, 2:e439, 2007.

[181] Rob R. de Ruyter van Steveninck, Geoffrey D. Lewen, Steven P. Strong, Roland Koberle, and William Bialek. Reproducibility and variability in neural spike trains. *Science*, 275:1805–1808, 1997.

[182] M. L. Goldstein, S. A. Morris, and G. G. Yen. Problems with fitting to the power-law distribution. *European Physical Journal B*, 41:255–258, 2004.

[183] Aaron Clauset, Cosma Rohilla Shalizi, and M. E. J. Newman. Power-Law Distributions in Empirical Data. *SIAM Review*, 51:661–703, 2009.

[184] Anna Deluca and Álvaro Corral. Fitting and goodness-of-fit test of non-truncated and truncated power-law distributions. *Acta Geophysica*, 61:1351–1394, 2013.

[185] Ethan P. White, Brian J. Enquist, and Jessica L. Green. ON ESTIMATING THE EXPONENT OF POWER-LAW FREQUENCY DISTRIBUTIONS. *Ecology*, 89:905–912, 2008.

[186] Takehito Kemuriyama, Hiroyuki Ohta, Yoshiaki Sato, Satoshi Maruyama, Megumi Tandai-Hiruma, Kazuo Kato, and Yasuhiro Nishida. A power-law distribution of inter-spike intervals in renal sympathetic nerve activity in salt-sensitive hypertension-induced chronic heart failure. *Biosystems*, 101:144–147, 2010.

[187] Per Bak, Kim Christensen, Leon Danon, and Tim Scanlon. Unified Scaling Law for Earthquakes. *Physical Review Letters*, 88:178501, 2002.

[188] Diego Rybski, Sergey V Buldyrev, Shlomo Havlin, Fredrik Liljeros, and Hernán A Makse. Scaling laws of human interaction activity. *Proceedings of the National Academy of Sciences*, 106:12640–12645, 2009.

[189] Márton Karsai, Kimmo Kaski, Albert-László Barabási, and János Kertész. Universal features of correlated bursty behaviour. *Scientific Reports*, 2:397, 2012.

[190] Hang-Hyun Jo, Juan I. Perotti, Kimmo Kaski, and János Kertész. Correlated bursts and the role of memory range. *Physical Review E*, 92:022814, 2015.

[191] K.-I. Goh and A.-L. Barabási. Burstiness and memory in complex systems. *EPL (Europhysics Letters)*, 81:48002, 2008.

[192] Márton Karsai, Hang-Hyun Jo, and Kimmo Kaski. *Bursty Human Dynamics*. SpringerBriefs in Complexity. Springer International Publishing, 2018.

[193] Szabolcs Vajna, Bálint Tóth, and János Kertész. Modelling bursty time series. *New Journal of Physics*, 15:103023, 2013.

[194] Christian Meisel, Kimberlyn Bailey, Peter Achermann, and Dietmar Plenz. Decline of long-range temporal correlations in the human brain during sustained wakefulness. *Scientific Reports*, 7:11825, 2017.

[195] Marten Scheffer, Jordi Bascompte, William A. Brock, Victor Brovkin, Stephen R. Carpenter, Vasilis Dakos, Hermann Held, Egbert H. Van Nes, Max Rietkerk, and George Sugihara. Early-warning signals for critical transitions. *Nature*, 461:53–59, 2009.

[196] M. Scheffer, S. R. Carpenter, T. M. Lenton, J. Bascompte, W. Brock, V. Dakos, J. van de Koppel, I. A. van de Leemput, S. A. Levin, E. H. van Nes, M. Pascual, and J. Vandermeer. Anticipating Critical Transitions. *Science*, 338:344–348, 2012.

[197] Christian Meisel, Andreas Klaus, Vladyslav V. Vyazovskiy, and Dietmar Plenz. The Interplay between Long- and Short-Range Temporal Correlations Shapes Cortex Dynamics across Vigilance States. *The Journal of Neuroscience*, 37:10114–10124, 2017.

[198] Konglin Zhu, Wenzhong Li, Xiaoming Fu, and Jan Nagler. How Do Online Social Networks Grow? *PLoS ONE*, 9:e100023, 2014.

[199] P.-H. Wu, A. Giri, S. X. Sun, and D. Wirtz. Three-dimensional cell migration does not follow a random walk. *Proceedings of the National Academy of Sciences*, 111:3949–3954, 2014.

[200] V. V. Nikulin and T. Brismar. Long-range temporal correlations in electroencephalographic oscillations: Relation to topography, frequency band, age and gender. *Neuroscience*, 130:549–558, 2005.

[201] L. M. Parish, G. A. Worrell, S. D. Cranstoun, S. M. Stead, P. Pennell, and B. Litt. Long-range temporal correlations in epileptogenic and non-epileptogenic human hippocampus. *Neuroscience*, 125:1069–1076, 2004.

[202] Caroline Hartley, Luc Berthouze, Sean R. Mathieson, Geraldine B. Boylan, Janet M. Rennie, Neil Marlow, and Simon F. Farmer. Long-Range Temporal Correlations in the EEG Bursts of Human Preterm Babies. *PLoS ONE*, 7:e31543, 2012.

[203] Klaus Linkenkaer-Hansen, Vadim V. Nikouline, J. Matias Palva, and Risto J. Ilmoniemi. Long-Range Temporal Correlations and Scaling Behavior in Human Brain Oscillations. *The Journal of Neuroscience*, 21:1370–1377, 2001.

[204] Maria Botcharova, Simon F Farmer, and Luc Berthouze. Markers of criticality in phase synchronization. *Frontiers in Systems Neuroscience*, 8:176, 2014.

[205] Andrew W. Lo. Long-Term Memory in Stock Market Prices. *Econometrica*, 59:1279, 1991.

[206] Thomas Karagiannis, Mart Molle, and Michalis Faloutsos. Long-range dependence ten years of Internet traffic modeling. *IEEE Internet Computing*, 8:57–64, 2004.

[207] C. Varotsos and D Kirk-Davidoff. Long-memory processes in ozone and temperature variations at the region 60 S60 N. *Atmospheric Chemistry and Physics*, 6:4093–4100, 2006.

[208] Horia-Nicolai Teodorescu and Lucian Iulian Fira. DNA Sequence Pattern Identification Using a Combination of Neuro-Fuzzy Predictors. pages 1328–1333. 2004.

[209] D. R. Cox. *Renewal Theory.* Methuen's monographs on applied probability and statistics. Methuen, 1962.

[210] D. L. Gilden, T. Thornton, and M. W. Mallon. 1/f noise in human cognition. *Science*, 267:1837–1839, 1995.

[211] György Buzsáki and Andreas Draguhn. Neuronal olscillations in cortical networks. *Science*, 304:1926–1929, 2004.

[212] Diego Rybski, Sergey V. Buldyrev, Shlomo Havlin, Fredrik Liljeros, and Hernán A. Makse. Communication activity in a social network: relation between long-term correlations and inter-event clustering. *Scientific Reports*, 2:560, 2012.

[213] Jan W Kantelhardt, Eva Koscielny-Bunde, Henio H.A Rego, Shlomo Havlin, and Armin Bunde. Detecting long-range correlations with detrended fluctuation analysis. *Physica A: Statistical Mechanics and its Applications*, 295:441–454, 2001.

[214] Hang-Hyun Jo. Modeling correlated bursts by the bursty-get-burstier mechanism. *Physical Review E*, 96:062131, 2017.

[215] Najja Marshall, Nicholas M. Timme, Nicholas Bennett, Monica Ripp, Edward Lautzenhiser, and John M. Beggs. Analysis of Power Laws, Shape Collapses, and Neural Complexity: New Techniques and MATLAB Support via the NCC Toolbox. *Frontiers in Physiology*, 7:1–18, 2016.

[216] Jeff Alstott, Ed Bullmore, and Dietmar Plenz. powerlaw: A Python Package for Analysis of Heavy-Tailed Distributions. *PLoS ONE*, 9:e85777, 2014.

[217] A. Levina and V. Priesemann. Subsampling scaling. *Nature Communications*, 8:15140, 2017.

[218] Frank J. Massey. The Kolmogorov-Smirnov Test for Goodness of Fit. *Journal of the American Statistical Association*, 46:68–78, 1951.

[219] B. Arnold, Taylor and W. Emerson, John. Nonparametric Goodness-of-Fit Tests for Discrete Null Distributions. *The R Journal*, 3:34, 2011.

[220] H. Bauke. Parameter estimation for power-law distributions by maximum likelihood methods. *The European Physical Journal B*, 58:167–173, 2007.

[221] Mohammad Yaghoubi, Ty de Graaf, Javier G Orlandi, Fernando Girotto, Michael A Colicos, and Jörn Davidsen. Neuronal avalanche dynamics indicates different universality classes in neuronal cultures. *Scientific Reports*, 8:3417, 2018.

[222] Kenneth P. Burnham, David R. Anderson, and Kathryn P. Huyvaert. AIC model selection and multimodel inference in behavioral ecology: some background, observations, and comparisons. *Behavioral Ecology and Sociobiology*, 65:23–35, 2011.

[223] Eric-Jan Wagenmakers and Simon Farrell. AIC model selection using Akaike weights. *Psychonomic Bulletin & Review*, 11:192–196, 2004.

[224] Hirotogu Akaike. *Information Theory and an Extension of the Maximum Likelihood Principle*. Springer Series in Statistics. Springer New York, 1998.

[225] Scott I. Vrieze. Model selection and psychological theory: A discussion of the differences between the Akaike information criterion (AIC) and the Bayesian information criterion (BIC). *Psychological Methods*, 17:228–243, 2012.

[226] Robert E. Kass and Adrian E. Raftery. Bayes Factors. *Journal of the American Statistical Association*, 90:773–795, 1995.

[227] S T Buckland, K P Burnham, and N H Augustin. Model Selection: An Integral Part of Inference. *Biometrics*, 53:603, 1997.

[228] Michael P H Stumpf and M. A. Porter. Critical Truths About Power Laws. *Science*, 335:665–666, 2012.

[229] Woodrow L. Shew, Wesley P. Clawson, Jeff Pobst, Yahya Karimipanah, Nathaniel C. Wright, and Ralf Wessel. Adaptation to sensory input tunes visual cortex to criticality. *Nature Physics*, 11:659–663, 2015.

[230] Hernan Gonzalo Rey, Carlos Pedreira, and Rodrigo Quian Quiroga. Past, present and future of spike sorting techniques. *Brain Research Bulletin*, 119:106–117, 2015.

[231] Nicolas Onofrio, David Guzman, and Alejandro Strachan. Atomic origin of ultrafast resistance switching in nanoscale electrometallization cells. *Nature Materials*, 14:440–446, 2015.

[232] O. Shriki, J. Alstott, F. Carver, T. Holroyd, R. N. A. Henson, M. L. Smith, R. Coppola, E. Bullmore, and D. Plenz. Neuronal Avalanches in the Resting MEG of the Human Brain. *Journal of Neuroscience*, 33:7079–7090, 2013.

[233] Albert-László Barabási and Zoltán N. Oltvai. Network biology: understanding the cell's functional organization. *Nature Reviews Genetics*, 5:101–113, 2004.

[234] Steven H. Strogatz. Exploring complex networks. *Nature*, 410:268–276, 2001.

[235] Justin J. Chapman, James A. Roberts, Vinh T. Nguyen, and Michael Breakspear. Quantification of free-living activity patterns using accelerometry in adults with mental illness. *Scientific Reports*, 7:43174, 2017.

[236] Quang H Vuong. Likelihood Ratio Tests for Model Selection and Non-Nested Hypotheses. *Econometrica*, 57:307, 1989.

[237] Eckhard Limpert, Werner a. Stahel, and Markus Abbt. Log-normal Distributions across the Sciences: Keys and Clues. *BioScience*, 51:341, 2001.

[238] Waloddi Weibull. A Statistical Distribution Function of Wide Applicability. *Journal of applied mechanics*, 103:293–297, 1951.

[239] Per Bak and Kan Chen. The physics of fractals. *Physica D: Nonlinear Phenomena*, 38:5–12, 1989.

[240] Sabine Lennartz and Armin Bunde. Eliminating finite-size effects and detecting the amount of white noise in short records with long-term memory. *Physical Review E*, 79:066101, 2009.

[241] S.-S. Poil, Richard Hardstone, Huibert D. Mansvelder, and Klaus Linkenkaer-Hansen. Critical-State Dynamics of Avalanches and Oscillations Jointly Emerge from Balanced Excitation/Inhibition in Neuronal Networks. *Journal of Neuroscience*, 32:9817–9823, 2012.

[242] T. Montez, S.-S. Poil, B. F. Jones, I. Manshanden, J. P. A. Verbunt, B. W. van Dijk, A. B. Brussaard, A. van Ooyen, C. J. Stam, P. Scheltens, and K. Linkenkaer-Hansen. Altered temporal correlations in parietal alpha and prefrontal theta oscillations in early-stage Alzheimer disease. *Proceedings of the National Academy of Sciences*, 106:1614–1619, 2009.

[243] Mona Irrmischer, Simon J. Houtman, Huibert D. Mansvelder, Michael Tremmel, Ulrich Ott, and Klaus LinkenkaerHansen. Controlling the temporal structure of brain oscillations by focused attention meditation. *Human Brain Mapping*, 39:1825–1838, 2018.

[244] J. Bhattacharya, J. Edwards, A. N. Mamelak, and E. M. Schuman. Long-range temporal correlations in the spontaneous spiking of neurons in the hippocampal-amygdala complex of humans. *Neuroscience*, 131:547–555, 2005.

[245] Woodrow L Shew and Dietmar Plenz. The Functional Benefits of Criticality in the Cortex. *The Neuroscientist*, 19:88–100, 2013.

[246] Luca Cocchi, Leonardo L. Gollo, Andrew Zalesky, and Michael Breakspear. Criticality in the brain: A synthesis of neurobiology, models and cognition. *Progress in Neurobiology*, 158:132–152, 2017.

[247] James P. Sethna, Karin A. Dahmen, and Christopher R. Myers. Crackling noise. *Nature*, 410:242–250, 2001.

[248] Jonathan Touboul and Alain Destexhe. Power-law statistics and universal scaling in the absence of criticality. *Physical Review E*, 95:012413, 2017.

[249] Felix Franke, Michele Fiscella, Maksim Sevelev, Botond Roska, Andreas Hierlemann, and Rava Azeredo da Silveira. Structures of neural correlation and how they favor coding. *Neuron*, 89:409–422, 2016.

[250] Zhidong Deng and Yi Zhang. Collective behavior of a small-world recurrent neural system with scale-free distribution. *IEEE Transactions on Neural Networks*, 18:1364–1375, 2007.

[251] Nathaniel Rodriguez, Eduardo Izquierdo, and Yong-Yeol Ahn. Optimal modularity and memory capacity of neural reservoirs. *Network Neuroscience*, 3:551–566, 2019.

[252] B. J. Choi, D. S. Jeong, S. K. Kim, C. Rohde, S. Choi, J. H. Oh, H. J. Kim, C. S. Hwang, K. Szot, R. Waser, B. Reichenberg, and S. Tiedke. Resistive switching mechanism of TiO2 thin films grown by atomic-layer deposition. *Journal of Applied Physics*, 98:033715, 2005.

[253] Toshitsugu Sakamoto, Kevin Lister, Naoki Banno, Tsuyoshi Hasegawa, Kazuya Terabe, and Masakazu Aono. Electronic transport in Ta2O5 resistive switch. *Applied Physics Letters*, 91:092110, 2007.

[254] Takami Hino, Tsuyoshi Hasegawa, Kazuya Terabe, Tohru Tsuruoka, Alpana Nayak, Takeo Ohno, and Masakazu Aono. Atomic switches: atomic-movement-controlled nanodevices for new types of computing. *Science and Technology of Advanced Materials*, 12:013003, 2011.

[255] K. Terabe, T. Nakayama, T. Hasegawa, and M. Aono. Formation and disappearance of a nanoscale silver cluster realized by solid electrochemical reaction. *Journal of Applied Physics*, 91:10110, 2002.

[256] K. Terabe, T. Nakayama, T. Hasegawa, and M. Aono. Ionic/electronic mixed conductor tip of a scanning tunneling microscope as a metal atom source for nanostructuring. *Applied Physics Letters*, 80:4009–4011, 2002.

[257] Alpana Nayak, Takuro Tamura, Tohru Tsuruoka, Kazuya Terabe, Sumio Hosaka, Tsuyoshi Hasegawa, and Masakazu Aono. Rate-limiting processes determining the switching time in a Ag2S atomic switch. *Journal of Physical Chemistry Letters*, 1:604–608, 2010.

[258] Takeo Ohno, Tsuyoshi Hasegawa, Alpana Nayak, Tohru Tsuruoka, James K. Gimzewski, and Masakazu Aono. Sensory and short-term memory formations observed in a Ag 2 S gap-type atomic switch. *Applied Physics Letters*, 99:203108, 2011.

[259] Henry O. Sillin, Renato Aguilera, Hsien Hang Shieh, Audrius V. Avizienis, Masakazu Aono, Adam Z. Stieg, and James K. Gimzewski. A theoretical and experimental study of neuromorphic atomic switch networks for reservoir computing. *Nanotechnology*, 24:384004, 2013.

[260] Adam Z Stieg, Audrius V Avizienis, Henry O Sillin, Cristina Martin-Olmos, Miuling Lam, Masakazu Aono, and James K. Gimzewski. Self-organized atomic switch networks. *Japanese Journal of Applied Physics*, 53:01AA02, 2014.

[261] E C Demis, R Aguilera, H O Sillin, K Scharnhorst, E J Sandouk, M Aono, A Z Stieg, and J K Gimzewski. Atomic switch networks nanoarchitectonic design of a complex system for natural computing. *Nanotechnology*, 26:204003, 2015.

[262] Eleanor C. Demis, Renato Aguilera, Kelsey Scharnhorst, Masakazu Aono, Adam Z. Stieg, and James K. Gimzewski. Nanoarchitectonic atomic switch networks for unconventional computing. *Japanese Journal of Applied Physics*, 55:1102B2, 2016.

[263] L. Chua. Memristor-The missing circuit element. *IEEE Transactions on Circuit Theory*, 18:507–519, 1971.

[264] Dmitri B. Strukov, Gregory S. Snider, Duncan R. Stewart, and R. Stanley Williams. The missing memristor found. *Nature*, 453:80–83, 2008.

[265] Leon Chua. Everything you wish to know about memristors but are afraid to ask. *Radioengineering*, 24:319–368, 2015.

[266] Yu Chen, Gang Liu, Cheng Wang, Wenbin Zhang, Run-Wei Li, and Luxing Wang. Polymer memristor for information storage and neuromorphic applications. *Materials Horizons*, 1:489, 2014.

[267] Lei Wang, CiHui Yang, Jing Wen, Shan Gai, and YuanXiu Peng. Overview of emerging memristor families from resistive memristor to spintronic memristor. *Journal of Materials Science: Materials in Electronics*, 26:4618–4628, 2015.

[268] Steven Lequeux, Joao Sampaio, Vincent Cros, Kay Yakushiji, Akio Fukushima, Rie Matsumoto, Hitoshi Kubota, Shinji Yuasa, and Julie Grollier. A magnetic synapse: multilevel spin-torque memristor with perpendicular anisotropy. *Scientific Reports*, 6:31510, 2016.

[269] Hammam Al-Bustami, Guy Koplovitz, Darinka Primc, Shira Yochelis, Eyal Capua, Danny Porath, Ron Naaman, and Yossi Paltiel. Single Nanoparticle Magnetic Spin Memristor. *Small*, 14:1–6, 2018.

[270] J. Joshua Yang, Dmitri B. Strukov, and Duncan R. Stewart. Memristive devices for computing. *Nature Nanotechnology*, 8:13–24, 2013.

[271] Giacomo Indiveri, Bernabé Linares-Barranco, Robert Legenstein, George Deligeorgis, and Themistoklis Prodromakis. Integration of nanoscale memristor synapses in neuromorphic computing architectures. *Nanotechnology*, 24:384010, 2013.

[272] Sung Hyun Jo, Ting Chang, Idongesit Ebong, Bhavitavya B Bhadviya, Pinaki Mazumder, and Wei Lu. Nanoscale Memristor Device as Synapse in Neuromorphic Systems. *Nano Letters*, 10:1297–1301, 2010.

[273] N. Banno, T. Sakamoto, S. Fujieda, and M. Aono. On-state reliability of solid-electrolyte switch. *IEEE International Reliability Physics Symposium Proceedings*, pages 707–708, 2008.

[274] Richard C. Atkinson and Richard M. Shiffrin. Human Memory: A proposed system and its control processes BT - The Psychology of Learning and Motivation. *The Psychology of Learning and Motivation*, 2:89–195, 1968.

[275] Zhi Xu, Yoshio Bando, Wenlong Wang, Xuedong Bai, and Dmitri Golberg. Real-Time In Situ HRTEM-Resolved Resistance Switching of Ag 2 S Nanoscale Ionic Conductor. *ACS Nano*, 4:2515–2522, 2010.

[276] Rui Chen, Noel T. Nuhfer, Laura Moussa, Hannah R. Morris, and Paul M. Whitmore. Silver sulfide nanoparticle assembly obtained by reacting an assembled silver nanoparticle template with hydrogen sulfide gas. *Nanotechnology*, 19:455604, 2008.

[277] Hirofumi Tanaka, Tomoki Akai, Daisuke Tanaka, and Takuji Ogawa. Sequential Phase Transition during Fabricating beta-Ag2S Film on Ag Electrode by Wet Chemical Process. *e-Journal of Surface Science and Nanotechnology*, 12:185–188, 2014.

[278] Monica Morales-Masis, Hans-Dieter Wiemhöfer, and Jan M. van Ruitenbeek. Towards a quantitative description of solid electrolyte conductance switches. *Nanoscale*, 2:2275, 2010.

Acknowledgment

This thesis work could not have been completed without supports from many people.

First of all, I would like to thank Prof. Simon Brown for giving me the great opportunity to work on this project and for all the support. All his guidance and feedback during the past three years helped my research and writing of this thesis.

I am also very thankful to my co-supervisor Dr. Saurabh Bose who has helped me and given me a lot of important advice for entire my PhD life from the first day. I learnt an attitude as a researcher from him and could developed my research skills.

Many thanks to my group members: Dr. Susant Acharya, Josh Mallinson, Edoardo Galli and Matthew Pike for fruit-full discussion about experiments, analysis and results. Their broad knowledge and suggestions were essential for solving various problems in research and publishing papers.

Thanks to my lab mates in the STM group: Dr. Ishan Mahajan, Dr. Tobias Maerkl, Dr. Maxime Le Ster and Sara Salehi for their encouragement. Conversations in lunch, tea time and dinner gave me very fun time in the busy days.

I thank my grate friends, Liz Webeck, Miharu Nock and Miguel Reise. In the last stage of my thesis writing, they proofread a whole my thesis and improved readability and prevented grammatical mistakes. Without their support within the very short time, I could not finish my writing before the deadline. Thank you so much.

I thank the MacDiarmid Institute of Advanced Materials and Nanotechnology for providing me with the full scholarship covering my tuition fees and living expenses and I am grateful to the University of Canterbury for allowing me to pursue my Phd degree in Physics.

Also, many thanks to my flatmates, friends and climbing mates. They always supported me and my family. They are very kind, helpful and respectful. I am very glad to meet them.

I would like to say a lot of thank you to my wife, Kaoru, and a son, Hal. I cannot express my gratitude for them with one word. Especially, Kaoru have dedicated her life for me since she came to New Zealand with Hal. Without her daily base supports including great lunch every day and florantans, I could not continue my research work. Hal, you are a wonderful boy. You eat well, sleep well, play well and are grown up well. You are a great gift in my life.

Last, but not the least, I am thankful to my parents. Thanks to their education, emotional support and love, I could reach this stage.

Appendix A

MATLAB codes

The main MATLAB codes and functions used in this thesis are shown in this appendix. Some functions are provided by NCC toolbox [215], but the original source of codes and functions developed in this work belong to the neuromorphic computing research group at UC and can be found in the directory: (/nano/01 - Neromorphic/Shota/MATLAB codes)

A.1 The List of the MATLAB Codes

A.1.1 Raw Data Analysis

- `DataAnalyzer`

  This code is used for the raw data analysis and generate .mat file(s) containing required information (e.g. conductance and results of event detection) for subsequent analyses. The spike-replacement filter and local median filter are also applied in this code. The analysis parameters can be changed on the top part of the main script. (see detail in "ReadMe" document in the code directory)

A.1.2 Analyzing and Plotting Data

All of codes for the data analysis require .mat files generated by `DataAnalyzer`. The output data type is .fig which is a specif file type for MATLAB figures. Some original sub-functions required in the main codes are stored in the function directory "Function_Shota" in the MATLAB code directory.

- `BasicPlot`

  Plot the data on the figure(s) based on the initial analysis in `DataAnalyzer`: $G(t)$ with event detection markers, $G(t)$ and $\Delta G(t)$ with event detection markers, $R(t)$, histograms of the switching event size. Some parameters can be changed on the top part of this code. This code can test event detection with a different value of the threshold.(see detail in "ReadMe" document in the code directory)

- `IEI_ACF_Analysis`

  This code is the main code for implementing all required analysis in IEI distributions and ACFs. In the analysis of IEI distributions, power-law exponents are estimated by MLE procedure for various data range (the minimum range: 2 orders of the magnitude in time by default) and calculate the p-values of the KS test for each estimated exponent. The estimated p-value is plotted as a map as a function of the truncation parameters (see an example in Fig. 4.19(b)) The result of the power-law fit is shown in a figure with a fitting line obtained from the exponent. In the analysis of ACF, the ACF is obtained from experimental data and is plotted on a figure with a slope of the ACF calculated from shuffled IEI data.

A.1.3 Simulation code

- `BurstySimulation`

  This code is used for generating time series data from the hierarchical burst model discussed in Section 4.7.2. The input data is an IEI distribution obtained from either experimental data or `gendata`. Parameters can be chosen on the top part of this code. Non-hierarchical data and non-bursty data are also generated at the same time. The generated data is saved in .mat file and also plotted on figure (see detail in "ReadMe" document in the code directory).

- `SubSampling_Thresholding_IEI_DG`

  This code is used for investigating effects of sub-sampling and thresholding in IEI distributions and ΔG distributions (see Section 4.4). The conductance trace generated in this code and sub-sampled data are saved in .mat file. IEI distributions and ΔG distributions are plotted for each sub-sampled data and thresholding values. The

generated figures are saved as .fig files (see detail in "ReadMe" documjent in the code directory).

A.1.4 Functions

The functions listed below mainly work with the main analysis code above, but can be used for instant analysis on the MATLAB console. detail in the header of the function or type "help (function name)" (Ex. `help gendata`) in the MATLAB console.

- `gendata`

  Random number generator for various distributions. (provided by NCC toolbox [215])
  An examples are shown in the box below i.e. 10000 data points of a power-law distributed random number (discrete) with the exponent of 1.5.

```
IEI_pow = gendata(10000,{'powerlaw',1.5})
```

- `plmle`

  Implement MLE for the power-law distribution with data range between xmin and xmax (provided by NCC toolbox [215]).

```
gamma = plmle(data,'xmin',xmin,'xmax',xmax)
>> gamma = 1.500
```

- `exmle`

  Implement the MLE for the exponential distribution with data range between xmin and xmax.

```
lambda = plmle(data,'xmin',xmin,'xmax',xmax)
>> lambda = 0.301
```

- `lnmle`

  Implement MLE for the log-normal distribution.

```
[mu, sigmaSq] = lnmle(data,'xmin',xmin,'xmax',xmax)
>> mu = -23.632
sigmaSq = 34.521
```

- `wbmle`

  The function implementing the MLE for the (2-parameters) Weibull distribution.

```
[epsilon, eta] = wbmle(data,'xmin',xmin,'xmax',xmax)
>> epsilon = 0.100
eta =  5.875
```

- `pvcalc_pl`

  Calculate a p-value in the KS test with a estimated parameter of a power-law for a specific data range between xmax and xmin. Parallel computing toolbox in MATLAB is available for calculation.

```
p_pl = pvcalc_pl(data, exponent, 'xmin',xmin,'xmax',xmax)
>> p_pl = 0.738
```

- `pvcalc_exp`

  Calculate a p-value in the KS test with a estimated parameter of an exponential for a specific data range between xmax and xmin. Parallel computing toolbox in MATLAB is available for calculation.

```
p_ex = pvcalc_exp(data,exponent,'xmin',xmin,'xmax',xmax)
>> p_ex = 0.016
```

- `pvcalc_ln`

  Calculate a p-value in the KS test with estimated parameters of log-normal for a specific data range between xmax and xmin. Parallel computing toolbox in MATLAB is available for calculation.

```
p_ln = pvcalc_ln(data,exponents,'xmin',xmin,'xmax',xmax)
>> p_ln = 0.456
```

- `pvcalc_wb`

  Calculate a p-value in the KS test with estimated parameters of Weibull (2-parameters) for a specific data range between xmax and xmin. Parallel computing toolbox in MATLAB is available for calculation.

```
p_wb = pvcalc_wb(data,exponents,'xmin',xmin,'xmax',xmax)
>> p_wb = 0.538
```

- `visplparams_exponents`

  Plot a exponent map based on the calculated fitting exponent estimated by MLE as a function of truncated parameters. This function is a sub-function of the main code of `IEI_ACF_Analysis`. See an example in Fig. 4.19(a)

- `visplparams_pvalue`

  Plot a p-value map based on the calculated p-values as a function of truncated parameters. This function is a sub-function of the main code of `IEI_ACF_Analysis`. See an example in Fig. 4.19(b)